Computational and experimental analysis of prestressed concrete railroad ties for large deformation

by

Yu-Szu Chen

B.S., Tamkang University, 2010
M.S., Kansas State University, 2016

AN ABSTRACT OF A DISSERTATION

submitted in partial fulfillment of the requirements for the degree

DOCTOR OF PHILOSOPHY

Department of Civil Engineering
Carl R. Ice College of Engineering

KANSAS STATE UNIVERSITY
Manhattan, Kansas

2023

Abstract

Concrete railroad ties have been used in the United States for over 125 years, and prestressed concrete monoblock ties are most commonly used. In monoblock tie design, flexural strength of the prestressed tie is used to predict the tie capacity. Current tie design procedures vary from manufacturer to manufacturer. American Railway Engineering and Maintenance -of-Way Association (AREMA) sets the flexural design standard for all prestressed ties. AREMA also stipulates critical positions for loading, and limits concrete crack propagation to the outer layer of reinforcement on the tensile surface of the tie. Considering the complexity of prestressed concrete tie behavior especially post-cracking and varying ballast support conditions, a study was conducted to estimate the flexural capacity of monoblock ties under practical load and track system through computational simulation.

A computational tool was built and was verified theoretically and validated experimentally. The program focused on performance of prestressed concrete monoblock tie under flexible design assumption. The tie flexural responses (crack propagation, deflection, and slope) were analyzed by utilizing a moment-curvature relationship and M/EI diagram incorporating moment-area theory. The computational tool is well suited to analyze varying support conditions and is also naturally parameterized to facilitate Monte Carlo analysis of tie behavior. Thus, it is expected that the major outcome of the proposed research will be an uncertainty-informed analysis of concrete monoblock tie flexural behavior that may, in turn, lead to reliability based concrete monoblock tie design.

Computational and experimental analysis of prestressed concrete railroad ties for large deformation

by

Yu-Szu Chen

B.S., Tamkang University, 2010
M.S., Kansas State University, 2016

A DISSERTATION

submitted in partial fulfillment of the requirements for the degree

DOCTOR OF PHILOSOPHY

Department of Civil Engineering
Carl R. Ice College of Engineering

KANSAS STATE UNIVERSITY
Manhattan, Kansas

2023

Approved by:

Co-Major Professor
Dr. Christopher A. Jones

Approved by:

Co-Major Professor
Dr. Robert J. Peterman

Copyright

Abstract

Concrete railroad ties have been used in the United States for over 125 years, and prestressed concrete monoblock ties are most commonly used. In monoblock tie design, flexural strength of the prestressed monoblock tie is used to predict the tie capacity. Current tie design procedures vary from manufacturer to manufacturer. American Railway Engineering and Maintenance -of-Way Association (AREMA) sets the flexural design standard for all prestressed ties. AREMA also stipulates critical positions for loading, and limits concrete crack propagation to the outer layer of reinforcement on the tensile surface of the tie. Considering the complexity of prestressed concrete ties behavior especially post-cracking and varying ballast support conditions, a study was conducted to estimate the flexural capacity of monoblock tie under practical load and track system through computational simulation.

A computational tool was built and was verified theoretically and validated experimentally. The program focused on performance of prestressed concrete monoblock tie under flexible design assumption. The tie flexural responses (crack propagation, deflection, and slope) were analyzed by utilizing a moment-curvature relationship and M/EI diagram incorporating moment-area theory. The computational tool is well suited to analyze varying support conditions and is also naturally parameterized to facilitate Monte Carlo analysis of tie behavior. Thus, it is expected that the major outcome of the proposed research will be an uncertainty-informed analysis of concrete monoblock tie flexural behavior that may, in turn, lead to reliability based concrete monoblock tie design.

Table of Contents

List of Figures

List of Tables

Acknowledgements

I would like to thank Dr. Andresen from the computer science department at Kansas State University for providing an opportunity to improve the efficiency of the code as a class project in CIS 625. Furthermore Dr. Andresen also gave our project another opportunity to be selected as senior project, creating a Python based parameter sweep program running on Beocat. I would like to express my gratitude to Computer Science Department and Beocat at K-State for sharing resources and assistance during the project.

I would like to thank Dr. Robert J. Peterman and Dr. Christopher Jones for their help and guidance with this project. I would also like to extend my acknowledgements to two other members of my committee: Dr. Terry Beck, and Dr. Eric Fitzsimmons.

I would like to acknowledge the help from computer science students: Grant Willford and CIS 625 student team lead by Ali Alhamadah. I would also like to recognize the undergrad students that helped with the research throughout this and extended projects: Joshua Upshaw and Madison Koller.

Thanks to Cody Delaney, Benjamin Thurlow, Andrew Schoenecke, and Clifford Temple for their assistance with laboratory work throughout the research.

Chapter 1 - Introduction

The proposed research deals with the performance of concrete railroad Monoblock ties for use in modern, commercial railroad track installations. The loaded behavior of these ties is fundamentally linked to the condition of the supporting ballast which is known to change over time. As such, the analysis of concrete monoblock tie flexural behavior must be capable of capturing these support effects. In practice, cross tie design procedures do not consider these effects, and this may lead to insufficient prediction of tie performance.

Background

Prestressed concrete monoblock ties are commonly used in North America. As the number of concrete Monoblock ties has increased, safety has been a growing concern. According to the Federal Railroad Administration, Office of Safety Analysis, from January 2016 to the present date, there have been 449 railroad accidents related to rail gauge widening and of the 449,315 are linked to defective or missing cross-ties. Various research has been conducted to gain better understanding of concrete railroad failure mode subsequently to improve rail safety. Furthermore, flexural cracking has been indicated as one of the main railroad tie failure modes in North America. To better understand the flexural behavior of prestressed concrete railroad ties can help to prevent failure due to flexural cracks. According to University of Illinois at Urbana-Champaign (UICUC), flexural cracking is one of the leading failure modes for concrete monoblock ties in North America (Yu, Jeong , Marquis, & Coltman, 2015).

The current concrete railroad tie design standard, AREMA chapter 30, specifies the flexure strength at critical cross-sections as the critical design element. The design flexural strength is required without crack or crack propagation limited to the outermost layer of reinforcement on the tension surface of railroad tie (AREMA, 2020). Accordingly, current concrete monoblock tie design practice involves checking the sectional moment capacity at these critical sections and ensuring the allowable moment capacity can be sustained. Such sectional analysis can be conducted efficiently with simplified methods.

Objectives

Since concrete monoblock tie flexural strength is identified by AREMA (2020) as the critical design element, and because ballast support conditions are fundamentally linked to the flexural behavior of the monoblock ties, an analysis methodology capable of accurately modeling the flexural behavior of the prestressed concrete element and the support condition is required. Consequently, the purpose of this research was to develop a computational tool to predict linear and nonlinear deformations of prestressed concrete monoblock tie under selected ballast conditions and applied loads. The computational tool was further verified theoretically and validated experimentally. The program includes function of design and analysis. To design a new tie, the program can be used to check design criteria before conducting AREMA tie testing for design approval. Furthermore, the program can be used to analyze flexural related failure for monoblock ties which can, in turn, be used to predict tie flexural strength and crack propagation for comparison with AREMA design requirements.

Organization of Dissertation

Chapter 2 gives background on prestressed concrete railroad ties and summarizes the railroad tie correlated research. In addition, this chapter describes the design and analysis considerations including current design specifications.

Chapter 3 details the application of the center negative bending test to the existing and new ties, estimating the load-deflection curve for further used to validate the developed computational program. Additionally, this chapter also details the application of defining key material properties following ASTM standards for further modeling needed.

Chapter 4 introduces the development of the moment curvature based computational program to capture tie response behavior. This chapter goes through the theory of the flexural behavior to code development methodology.

Chapter 5 evaluates the developed numerical program theoretically and experimentally. The program is verified through three stages of comparison, including hand calculation, code to code comparison, and existing example. Furthermore, the validation is conducted through comparison with experimental results.

Chapter 6 describes the method of uncertainty analysis in the tie flexural behavior. The results can help to improve design procedures and increase understanding of observed tie failure.

Chapter 7 concludes the findings throughout this research.

Chapter 2 - Literature Review

Railroad ties are an essential component of railway, integral parts of a railroad track system are fastening systems, rails, railroad ties, and stone ballast. The purposes of ties are transmitting tack load, maintaining position of rail gauge, and resisting lateral and longitudinal movements (Kerr, 2003). Timber and concrete are the commonly used material for railroad ties, other materials (steel and plastic) are also employed. Timber was dominated tie material before the end of World War II in European. Concrete became one of the tie materials due to high demand and supply shrinkage of timber material. There are two types of concrete tie: prestressed monoblock tie and reinforced two-block tie shown in Figure 2.1.

The two-block tie has heavily reinforced concrete blocks connected by a steel rod. The tie has ballast contact area concentrated on the both end which reducing cracking at rail-center, and increasing lateral resistance. Additionally, the tie is more economical in production and handling. The development of the tie began early 20th century, and the tie was adopted and widely used after World War II. (Kerr, 2003)

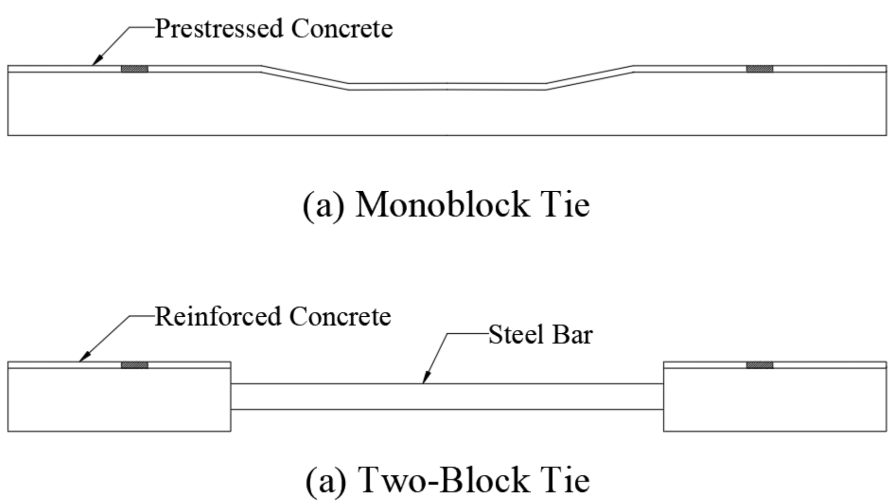

Figure 2.1 Type of Concrete Tie (AREMA, 2020)

In late 19th century, United State and France were seeking to use conventional concrete tie. However, the attempts were failed by the reason of cracks at rail-seat and rail-center, and without proper fastener system. One century later, the conventional reinforced concrete tie was successfully used in Hungarian with wheel load limited to 20,000 lbs and speed up to 50 mph (Kerr, 2003).

The improvement in crack under axial load could be made by employee prestressing method in concrete tie. Prestressed concrete reinforcement has been pre-tensioned prior to concrete casting. The precompression force improves ductility and resistance to external load (Mitchell & Collins, 1991). High strength concrete is used to ensure that the prestressing force is fully transferred to concrete before reaching the rail-seat, and it improves crack resistance and reduces prestress losses (Hanna, 1979). Furthermore, stability and performance of the track system is enhanced when monoblock ties are employed. Germany had an early attempt to utilize prestressing method in crosstie in early 20th century, unfortunately it was not successful due to lacking of advance understanding in prestressed concrete technology. After the finding in behavior of prestressed concrete member subjected axial load, the development in prestressed concrete tie became popular after 1945 in Europe. Concrete ties were first used in 1893 in the United States as recorded (Hanna, 1979), and more interest in utilizing prestressed concrete technology began around 1960 as alternative crosstie option.

Concrete ties are expected to last twice as long as timber ties (Yu, Jeong , Marquis, & Coltman, 2015). However, the concrete tie may not be able to reach its designed service life due to varying failure types (Van Dyk, 2014):

- Rail-Seat Deterioration (RSD)
- Shoulder/Fastening System Wear or Fatigue
- Cracking from Environmental / Chemical Deterioration
- Flexural Cracks (rail-seat crack and rail-center crack)
- Derailment Damage
- Other (e.g., manufacturing defect)
- Tamping Damage

The University of Illinois at Urbana-Champaign (UIUC) conducted a survey internationally and domestically to rank critical issues in concrete monoblock ties showing several distinct concerns. Tamping damage was the critical problem outside of the United States, and RSD and shoulder/fastening system wear or fatigue were the most common issues in North America (Van

Dyk, 2014). UIUC has conducted studies in RSD and fastening system damage by Zeman (2010) and Chen et al. (2014). Flexural cracks are one of the failure modes but limited studies have been conducted (Wolf, 2015). An incident at Bronx, NY in 2013 involved a CSX derailment on the Metro-North track mainly caused by degraded monoblock tie with poor support condition (center-bound support) (Marquis, LeBlanc, Yu, & Jeong, 2014).

Recent research regarding concrete monoblock tie includes rail-seat deterioration, concrete materials, cracks, flexural bending at rail-center, and prestressing transfer length according to Edwards (2019). Ballast support significantly influences monoblock tie performance, and research has been conducted to examine tie failure modes with various ballast supports through experimental work by Bastos (2016) and Finite Element (FE) modeling by Yu et al. (2011). As flexural demand increases it becomes important to focus on tie capacity. Several studies focused on optimization of tie capacity without changing the current tie geometry in order to accommodate heavy-haul railway demand (Lutch, 2019; Harris et al. 2011). However, relatively limited research is focused on monoblock tie behavior under bending especially after cracking. Closely related research was carried out by Wolf (2015). Considering the current empirical design approach, Wolf's research investigated flexural demand at critical locations through varying ballast pressure (Wolf, 2015). Wolf found flexural demand of tie is highly dependent on the ballast condition which is hard to predict. The analysis method used Euler-Bernoulli beam theory and complied with AREMA's recommended analysis approach. From this research Wolf concluded that AREMA's current design recommendation is conservative in assuming rail-seat load as a static point load. AREMA's assumption is further used in this research for developing the design/analysis computational tool.

Prestressed Concrete Monoblock tie Design Consideration

The primary failure mechanisms of concrete monoblock ties are: rail-seat abrasion, flexural at rail-center, and rail fastener failure according to the rail industry in North America (Lutch, 2009). Flexural strength of monoblock ties can be determined if the rail-seat load and ballast support conditions are known. However, tie supporting conditions are variable, and it significantly affects monoblock tie design.

Ballast Supports

As the flexural demand of the monoblock ties vary, it is important to know the tie flexural behavior under various supporting conditions. The ballast support condition is known to change over time due to repetitive loading, and this directly influences tie capacity to resist bending. The track ballast under monoblock ties is tamped regularly to ensure track alignments and ideal ballast support. The ballast is typically tamped under rail-seats and light tamping at rail-center, resulting in lack of center support shown in Figure 2.2 (a). The center support gradually forms after cyclic train traffic in Figure 2.2 (b). Subsequently, ballast support becomes uniform in Figure 2.2 (c). Without proper track maintenance, the center bound condition may occur in Figure 2.2 (d).

Varying ballast support results in diverse pressure between tie and ballast. According to AREMA average ballast pressure is limited to 85 psi for "high-quality abrasion resistant ballast" (AREMA, 2020). The computation of ballast pressure assumes uniform distributed pressure, and it can be calculated by Equation 2.1. The ballast pressure limitation can be reduced depending on ballast material quality.

$$Average\ Ballast\ Pressure = \frac{2P\left[1+\frac{IF}{100}\right]\left(\frac{DF}{100}\right)}{A} \leq 85psi \qquad \textbf{Equation 2.1}$$

P: Wheel load, kips
IF: Impact factor, %
DF: Distribution factor, %
A: Bearing area of concrete monoblock tie, in^2

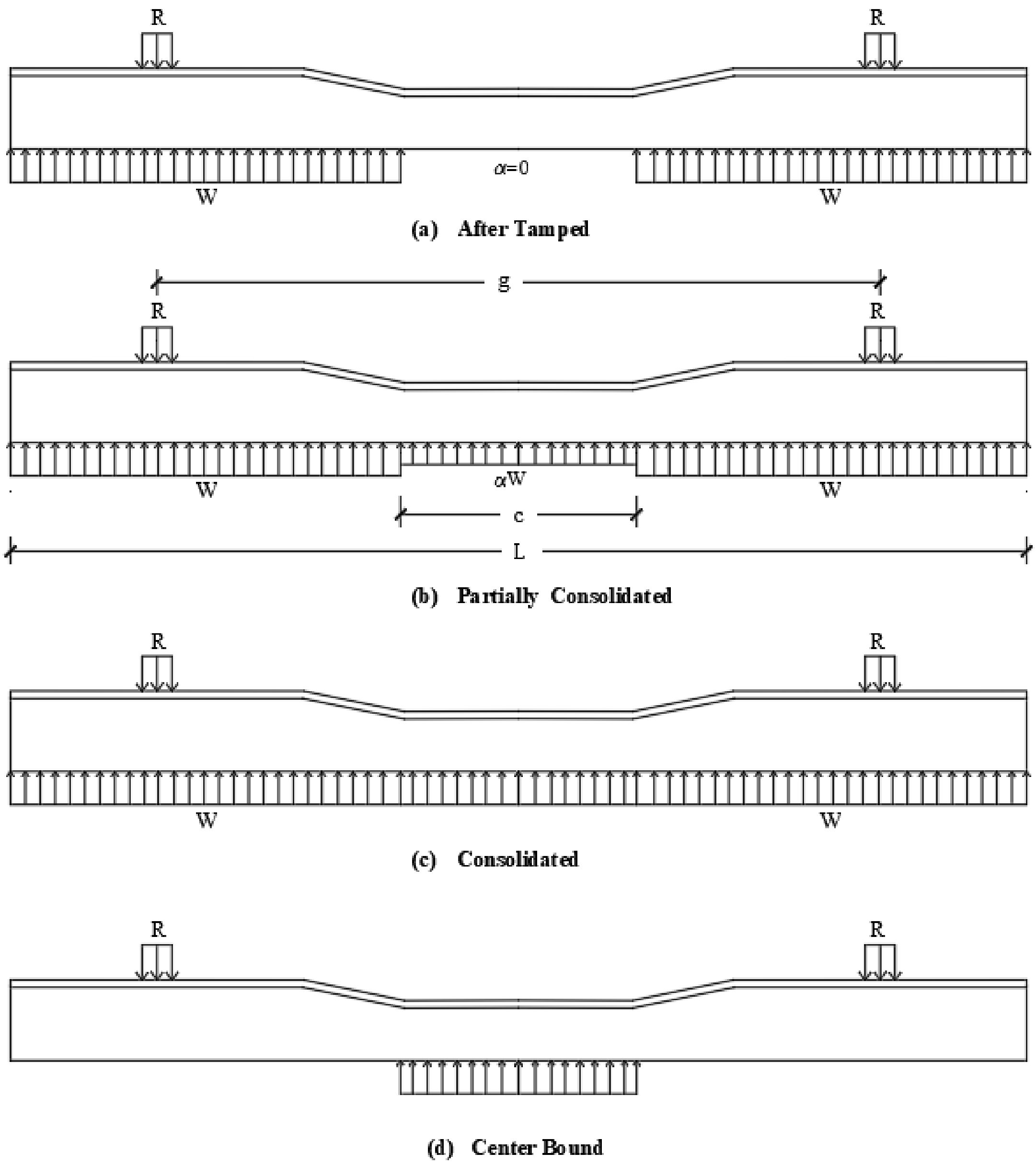

Figure 2.2 Monoblock tie reactions (International Union of Railways, 2004)

Flexural Crack

Flexural cracks can be induced from bending of the tie. Positive bending develops cracks at the bottom, conversely cracks at the top of tie are produced by negative bending. The governing locations in flexural design are rail-seat positive bending and rail-center negative bending (Edwards, 2019). With the track freshly tamped, there is little or no support at center travel way of rail path. The rail-seat has greatest interaction, and the maximum positive moment occurs here. Once the ideal uniform ballast is achieved, without proper track maintenance concentrated pressure arises under the center of monoblock ties where the center bound support condition gradually forms. Subjected to repeated track loads, vertical deformation of railroad tie produces up-and -down pumping action which leads to pulverization of the ballast material underneath rail-seat and tie deterioration (Lutch, 2009). Without proper maintenance, center bound ballast condition may be formed. The large negative moment occurs at center of the tie, resulting flexural failure (Lutch, 2009).

Design Specification -AREMA (2020)

The current railroad tie design specification, AREMA Chapter 30 Part 4 provides recommendations in concrete tie design. The maximum allowable stresses approach is recommended for prestressed monoblock tie design. The recommendation includes materials, dimensions, loads, etc. The requirements for tie dimensions are addressed in Section 4.3 (AREMA, 2020), where

- Length: $8' \leq L \leq 9'$
- Bottom Width: $w_b \geq 8"$
- Top Width: $w_t \geq 6"$ from rail-seat to rail-end
- Depth: $6" \leq d \leq 10"$
- Concrete Cover: min ¾”

The typical governing locations for tie deformation are rail-seat or rail-center, depending on tie ballast condition. These two locations are evaluated for designing flexure of monoblock tie. At the rail-seat, the positive bending moment, B_{RS+}, is the critical case. The governed support condition is without support at center of tie where the track just been tamped. Thus, the AREMA standard recommends zero center reaction factor, α, to determine unfactored design positive rail-seat flexure (Equation 2.2). The standard gauge distance is 60-inches, and is recommended for use in Equation 2.2 and Equation 2.4 (AREMA, 2020). The rail seat load, R, is calculated using Equation 2.3. In Equation 2.3, the recommended axle load (AL) is 82 kips for freight traffic. The distribution factor is defined by Figure 30-4-1 in (AREMA, 2020) with corresponding tie spacing. The tie spacing is suggested between 20-inches to 30-inches, increasing tie spacing results in higher wheel load applied on the tie. The impact factor is incorporating dynamic effects into design load, and a 200% increase is recommended.

$$B_{RS+} = \frac{1}{8}\left[\left(\frac{2R}{2(L-g)+\alpha(2g-L)}\right)(L-g)^2 - Rs\right], (kips-in) \qquad \textbf{Equation 2.2}$$

$$R = 0.5(AL)(DF)(1+IF), (kips) \qquad \textbf{Equation 2.3}$$

L = Length of monoblock tie
g = Rail center-to-center distance
s = Rail-seat width

Another critical case is the negative bending moment, B_{C-}, at rail-center, the tie is lacking support at rail-seats. However, if the track is properly maintained, the center pressure can be reduced. Furthermore, center bound condition can be prevented. Therefore, the ballast condition is assumed partially consolidated for computing design center negative bending moment. Equation 2.4 is used to calculate negative bending moment without including speed and annual tonnage effects (AREMA, 2020). The recommended α can be found in AREMA Table 30-4-1 where the value is within 0.66 to 0.84 depending on tie length (AREMA, 2020).

$$B_{c-} = -\frac{1}{2}R\left[\frac{L^2-(1-\alpha)(2g-L)^2}{2\big(L-(1-\alpha)(2g-L)\big)} - g\right], (kips-in) \qquad \textbf{Equation 2.4}$$

The factored design bending moment is taking speed and annual tonnage (V x T) into design bending moment, and the factor may be determined by Equation 2.5. If the axle load beyond 82 kips, the factor should be taken as 0.7. Also, the factor should be 1.0 for axle load below 35 kips.

$$V \times T = -0.0064(AL) + 1.2234 \qquad \textbf{Equation 2.5}$$

Additional design considerations are recommended for tie flexure design (Table 2.1), and prestressed concrete mono-block ties design is recommended to comply with ACI 318 and PCI design specification (AREMA, 2020). The tie is required to pass testing at critical locations to approve the monoblock tie design. Furthermore, AREMA 2020 defines the capacity limit is the crack propagated to first layer of steel instead of concrete crushing or steel rupture failure (Lutch, 2009).

Table 2.1 Design considerations

Pre-compressive Stress	$\geq$ 500 psi	at rail seat area
Pre-compression	$\leq$ 2500 psi	at any location

Chapter 3 - Experimental Testing of Monoblock Ties

Flexural Test

Rail-seat positive and rail-center negative are the governing cases in flexural design of monoblock ties. Considering the cross-section is generally reduced at center region of tie, the capacity that could be sustained is relatively smaller compared to rail-seat. Additionally, the center bound boundary condition induces large negative bending moment at center region of the tie. Thus, rail-center negative bending test was selected. The purpose of experimental work is to collect load-deflection data at five different locations along the tie to validate the computational tool discussed in this work.

Test Setup

The center negative moment test follows section 4.9.1.6 AREMA Chapter 30 Part 4 (2020) specification. A four-point bending testing setup was followed. Tie was placed upside-down and simply supported at the rail seats. The tie was loaded on a 6-inch spreader beam at center, and maximum constant moment were created between loading points. Deflections were measured at five distances from the center-line of the tie, and a total of 10 liner variable differential transformers (LVDT) were used. These locations were labeled from 1 to 10 following the direction East to West in the testing laboratory. Eight LVDTs were measured from bottom surface of tie with distance 7", 14" and 21" away from center; another two LVDTs (#1 and #10) were located 2" from end of tie. LVDT#5 and #6 were placed under the tie, measuring from top of tie-surface, located at 2.5" from center. Figure 3.1 shown the detail position of LVDTs and schematic of setup.

A 5-power magnifying glass was placed in front of constant-moment region and cracking behavior were recorded by a camera placed behind the magnifying glass (AREMA, 2020). Figure 3.2 shows typical testing setup. A hydraulic actuator with 55-kips capacity used, and a Keithley series 2750 data acquisition system was used to collect load and displacement readings at three-second intervals. The ties were loaded at a rate between 1,000 to 2,000 lbs per minute until first crack occurred; then the tie was loaded at rate of 0.02 inches per minute to failure. The displacement-controlled loading region was intended to promote more controlled failure of the tie.

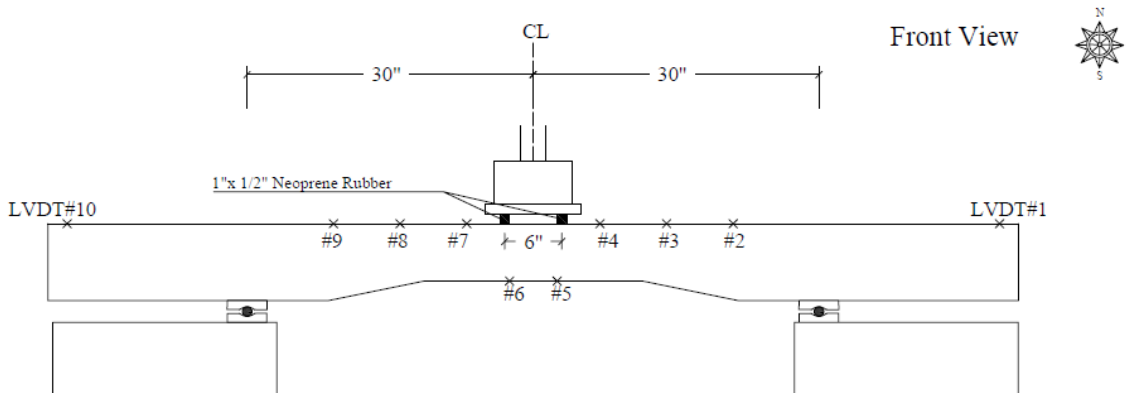

(a) Front view

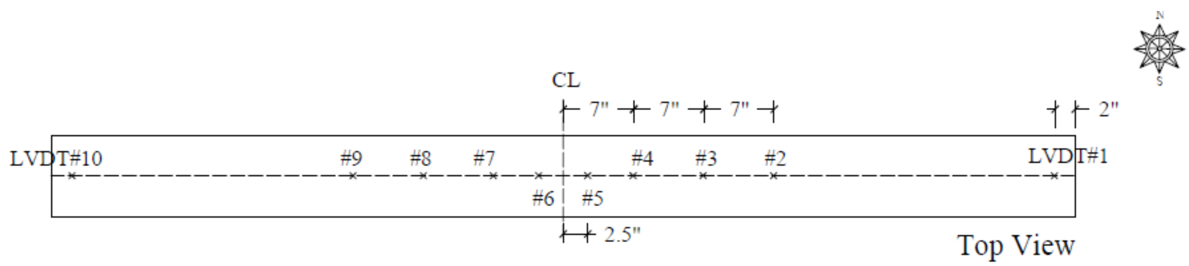

(b) Top view

Figure 3.1 (a) & (b) Schematic of four-point flexural test and LVDT placement

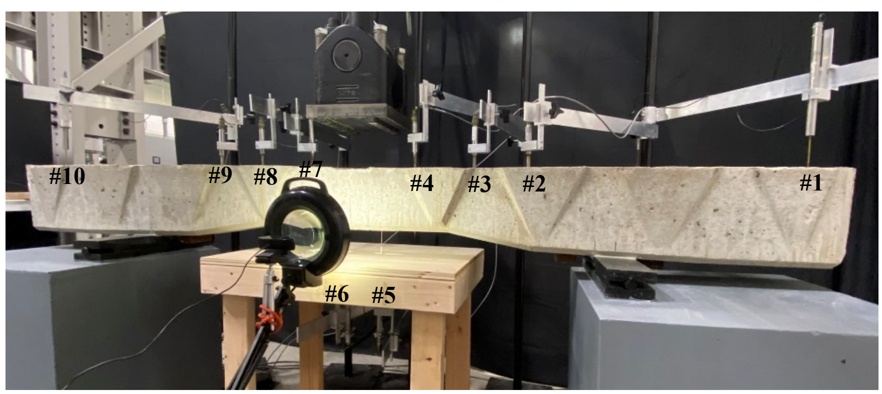

Figure 3.2 Typical flexural test setup

Test Specimen

Ties selected for the test include three ties that were retired from service and six virgin ties. Existing ties are over 25 years old and the material properties are unknown. The retired ties had surface degradation, but overall were in good condition for experiment. New ties were made by previous research at Kansas State University (K-State), and they were stored at K-State and have never been loaded (Scott, 2019). Three types of tie were selected (Table 3.1), in total, 9 ties. There were two type-F ties and one Type-C tie. Moreover, there were six CXT ties, including two of each CXT-WB, CXT-WD, and CXT-WG (WB, WD, and WG referring to type of prestressing wire). The critical cross-section was measured and is reported in Table 3.2. The CXT ties were measured by (Bodapati, 2018). CXT shape tie had the geometry values measured and calculated at each half inch increment, and it is used in Chapter 5 - for program modeling and analysis.

Table 3.1 Description of tie design

	Tie Design	Manufacturer	Scallop	Tendon Type	No. of Tendon	Tendon Diameter
Existing Tie	Type-F	Florida East Coast (F.E.C.)	N.A.	Wire	26	0.191 in.
Existing Tie	Type-C	Con-Force Costain	N.A.	Strand	6	0.375 in.
New Tie	CXT-505S	CXT	Yes	Wire	20	0.209 in.

Table 3.2 Typical cross-section at critical location

Type of Tie	Length, in	Rail-Seat					Center				
		A, in^2	I, in^4	h, in	y_b, in	e,in	A, in^2	I, in^4	h, in	y_b, in	e,in
Type-F	99	73.36	373.97	8.23	4.16	1.48	52.53	131.1	5.88	3.03	0.35
Type-C	108	79.14	381.23	8.5	4.21	0.96	59.56	161.96	5.75	3.36	0.11
CXT-505S	102	87.36	634.72	9.31	4.55	0.64	59.50	278.44	7.5	3.70	-0.22

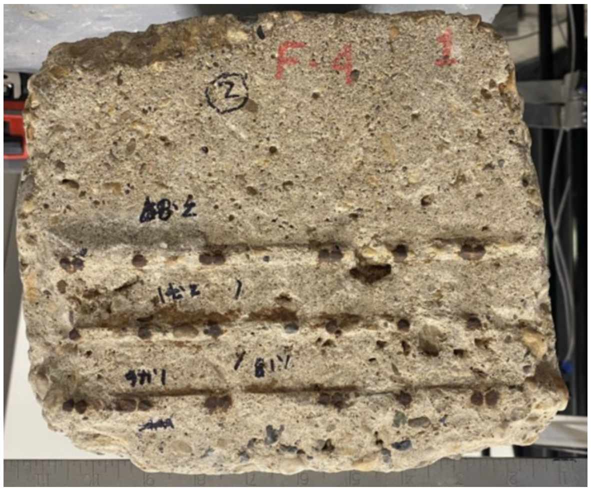

(a) End

(b) Seat

Figure 3.3 Typical type-F tie cross-section

(a) End

(b) Center

Figure 3.4 Typical CXT tie cross-section

(a) Seat

(b) Center

Figure 3.5 Typical type-C tie cross-section

Test Result

The testing results are presented as load versus deflection (P-δ), and can be found in Appendix A. Figure 3.7 to Figure 3.11 show the average results where tie is subjected to maximum moment force. A trial test was conducted on CXT-[WB] tie, and the result was included. It resulted in a total of three experiments for CXT-[WB] tie, and total of 10 tests were performed. The cracking force was determined by visual observation during testing and checked by reviewing recorded video. Figure 3.6 shows the typical flexural cracking pattern. For type-C tie, the initial cracks occurred outside of camera frame, so the value was taken during the test. Table 3.3 presents flexure test results, including force at first crack (P_{cr}) and ultimate (P_{ult}). The experimental result shows the consistency in average P_{cr} and P_{ult} from same tie design group.

Figure 3.6 Flexural cracking pattern

Table 3.3 Crack and ultimate force of each test

	P_{cr}, lbs	Average P_{cr}, lbs	P_{ult}, lbs	Average P_{ult}, lbs	P_{cr} /P_{ult}
CXT_WB_Trial	20,430	21,069	39,999	38,795	0.543
CXT_WB1	21,790		41,010		
CXT_WB2	20,987		35,376		
CXT_WD1	20,524	20,807	37,998	38,337	0.543
CXT_WD2	21,090		38,675		
CXT_WG1	21,000	20,917	38,098	37,833	0.553
CXT_WG2	20,833		37,567		
F-1 (F3)	10,958	10,729	19,005	19,370	0.554
F-2 (F4)	10,500		19,735		
C-1 (C5)	13,500	13,500	23,014	23,014	0.587

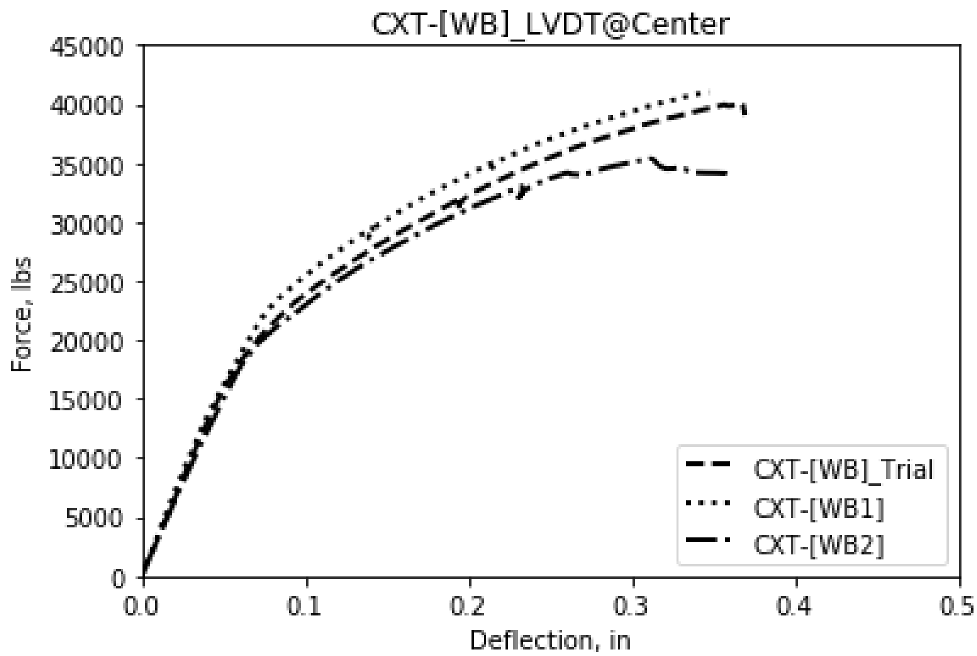

Figure 3.7 Load-Deflection curve for CXT-[WB] ties

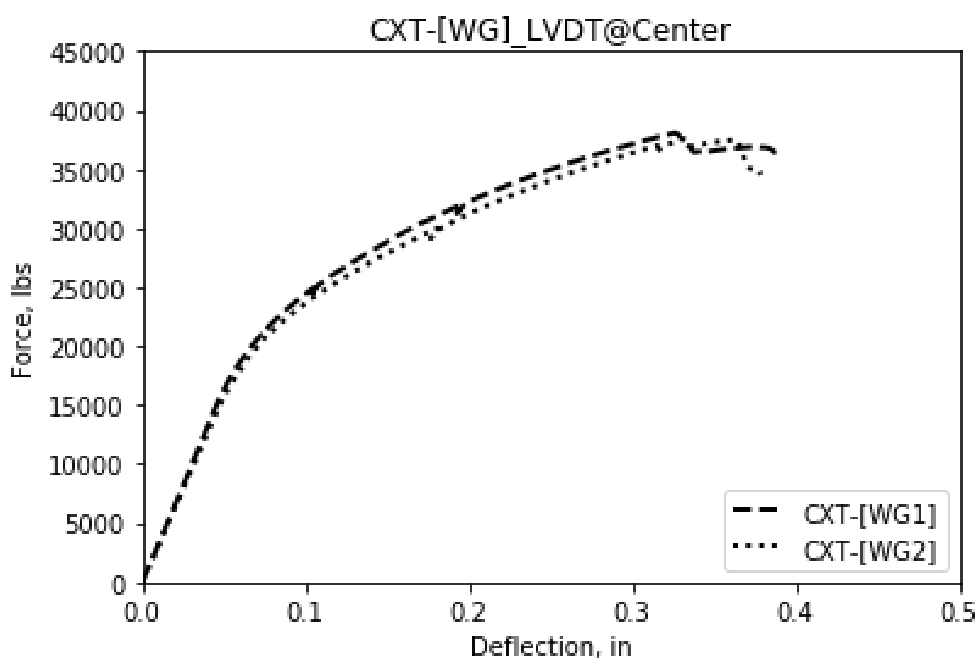

Figure 3.8 Load-Deflection curve for CXT-[WG] ties

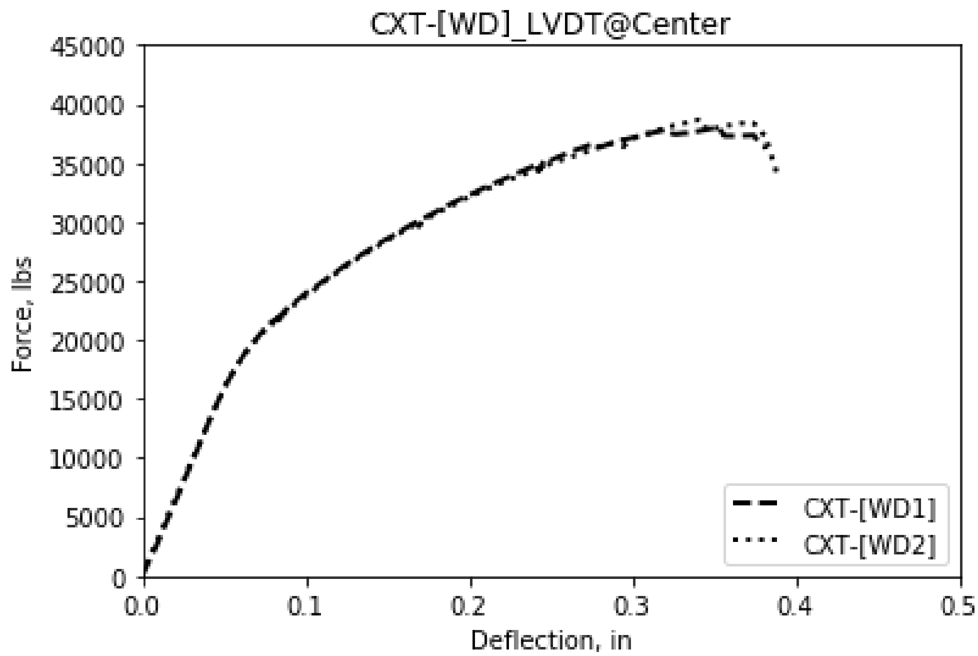

Figure 3.9 Load-Deflection curve for CXT-[WD] ties

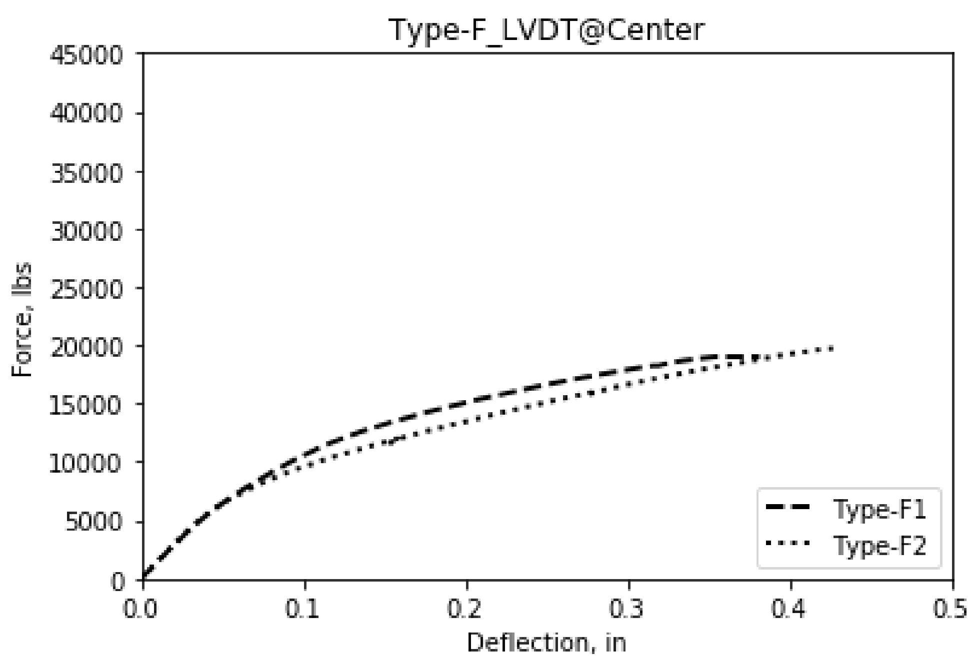

Figure 3.10 Load-Deflection curve for type-F ties

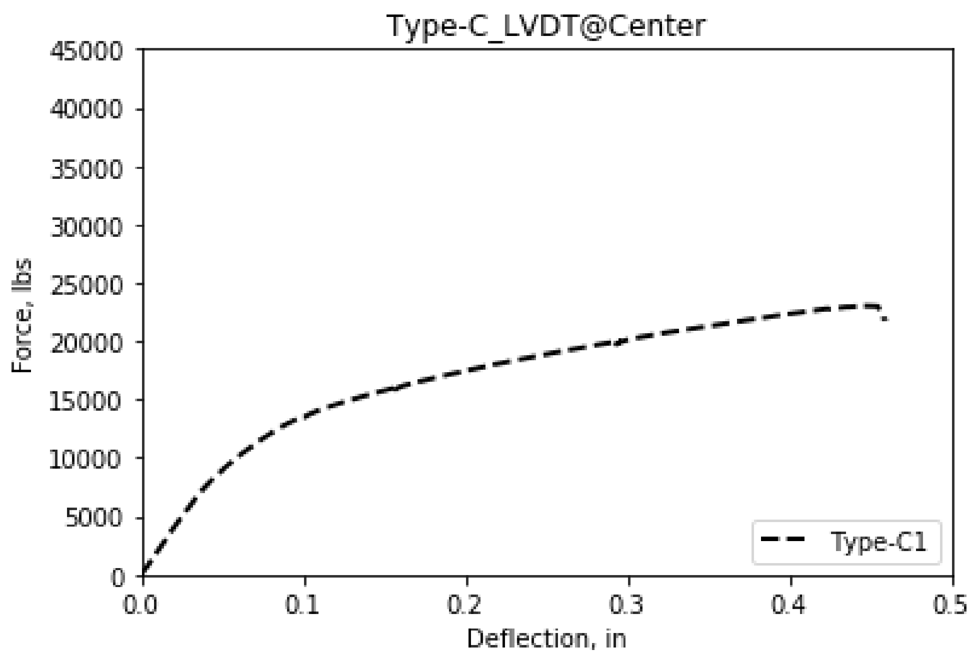

Figure 3.11 Load-Deflection curve for type-C tie

Material Properties

The goal of this section is to obtain concrete compressive strength (f'_c) and Young's modulus of elasticity (E_c) to model tie behavior accurately. The specimens were obtained from ties used in previous flexure tests. The ties were saw cut into a minimum 12-inch length. Then cores were drilled perpendicular to the cross-section of tie between rail-end to rail-seat region where the tie was not damaged from previous experiment, shown in Figure 3.12.

Figure 3.12 Saw cutting and drill coring tie

Due to the reinforcement pattern in railroad tie, the core size is limited to 2-inch diameter. The procedures followed latest ASTM C42/C42M. At least two 2" x 12" cylinders were obtained from each tie. The testing samples were size 2"x4" after being saw cut into preferred length. The samples were capped to ensure the end surfaces were parallel to the plate of compression machine (Figure 3.13).

Figure 3.13 Capped concrete specimens

Concrete Compressive Strength (f'$_c$)

For the concrete compressive strength test, three cylinders were prepared for each tie, a total of 21 concrete cylinders. The specimens were measured prior testing. Diameter was measured at top, middle and bottom. Length was measured three times 120 degrees apart before capped. The measurements are presented in Table 3.4. The overall length to diameter ratio (L/D) is 2.0 which is above 1.75 so the strength correction factor is not required according to ASTM C42/C42M section 7.2.1 (ASTM Standard C42/C42M, 2020).

To determine compressive strength of concrete cylinder, latest ASTM C39/C39M standard was followed. Specimens were loaded at a rate of 35 psi per second to failure, shown in Figure 3.14. The compressive strength was calculated by Equation 3.1 as stated in ASTM C39/C39M (ASTM Standard C39/C39M, 2020).

$$f'_c = \frac{4P_{max}}{\pi D^2} \qquad \textbf{Equation 3.1}$$

Table 3.4 Drilled cores measurement and compressive strength

Specimen	$d_{ave.}$, in	$L_{ave.}$, in	L/D	P_{max}, lbs	f'$_c$, psi
WB-1	1.98	3.97	2.01	33,923	11,040
WB-2	2.01	4.00	1.99	29,712	9,395
WB-3	2.01	4.04	2.01	37,214	11,785
WD-1	2.00	4.03	2.01	21,370	6,794
WD-2	2.00	4.00	2.00	23,744	7,559
WD-3	2.00	4.01	2.01	32,909	10,479
WG1-1	2.01	4.09	2.04	31,251	9,868
WG1-2	2.01	4.03	2.00	33,827	10,669
WG1-3	2.01	4.03	2.00	27,721	8,751
WG2-1	2.01	4.02	2.00	31,768	10,033
WG2-2	2.00	4.00	1.99	28,281	8,968
WG2-3	2.00	4.04	2.02	26,205	8,327
C5-1	2.01	4.02	2.00	21,361	6,762
C5-2	2.01	4.02	2.00	23,218	7,332
C5-3	2.01	4.06	2.02	22,256	7,019
F4-1	2.02	4.05	2.01	18,883	5,918
F4-2	2.01	4.01	1.99	19,877	6,257
F4-4	2.01	4.00	1.99	18,926	5,956
F3-1	2.00	3.98	1.98	21,781	6,901
F3-2	2.00	4.02	2.01	25,343	8,053
F3-3	2.01	4.06	2.02	19,937	6,309

Figure 3.14 Compression test

Detailed testing results could be found in Table 3.4 and the average compressive strength is shown in Figure 3.15. Same tie and same design group show variations in compressive strength which can be observed from testing results.

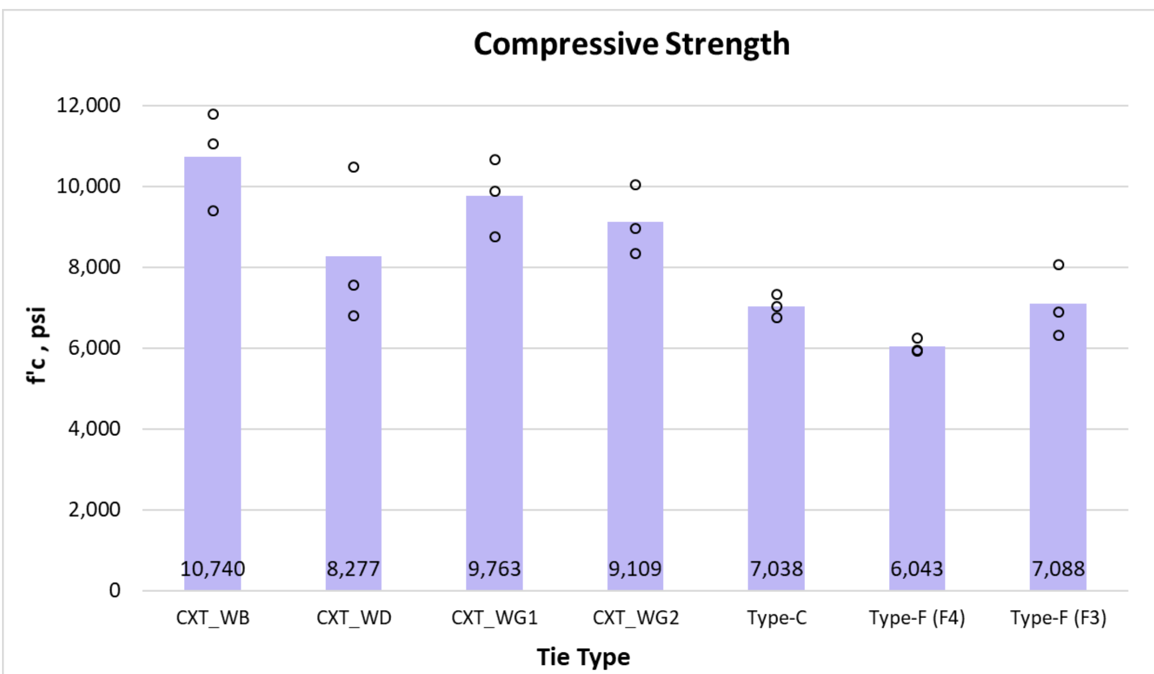

Figure 3.15 Average compressive strength

Concrete Modulus of Elasticity (E_c)

This section includes actual concrete Young's modulus of elasticity obtained through experimental work. The test utilized ASTM C469/C469M specification. The sample was 2-inch by 4-inch concrete cylinder. A total of 14 cylinders were prepared, and each tie had two samples. The samples were measured before being capped, and the dimensions are listed in Table 3.5. The gauge length is 2-inches, as recommended by ASTM C469/C469M. Thus, the yokes were one inch from cylinder end at each side. The cylinders were tested using a Schimaduz Universal machine with loading rate at 0.05 inch per minute. The specimens were loaded to 40% of the average ultimate load (Table 3.6). A LVDT was used to capture displacement, and a Keithley series 2750 data acquisition system was used to collect data readings. The test setup is shown in Figure 3.16.

Table 3.5 Specimen measurement

Specimen	d1	d2	d3	$d_{\_average}$	L1	L2	L3	$L_{\_average}$	L/D
WB-1	2.006	2.007	2.008	2.007	4.016	4.023	4.026	4.022	2.0
WB-2	2.001	2.008	2.002	2.004	4.034	4.035	4.038	4.035	2.0
WD-1	2.001	2.008	2.003	2.004	4.039	4.016	4.019	4.025	2.0
WD-2	2.002	2.001	2.000	2.001	4.383	4.336	4.334	4.351	2.2
WG1-1	2.010	2.009	2.007	2.008	4.014	4.032	4.038	4.028	2.0
WG1-2	2.007	2.005	2.003	2.005	4.0.36	4.026	4.036	4.031	2.0
WG2-1	2.007	2.008	2.012	2.009	4.557	4.537	4.536	4.543	2.3
WG2-2	2.002	2.011	2.007	2.006	4.027	4.016	4.009	4.017	2.0
C5-1	2.006	2.012	2.006	2.008	4.016	3.983	3.999	3.999	2.0
C5-2	2.007	2.008	2.014	2.009	4.022	4.019	4.011	4.017	2.0
F4-1	2.013	2.011	2.023	2.016	4.072	4.093	4.099	4.088	2.0
F4-2	2.013	2.014	2.013	2.013	4.075	4.095	4.069	4.080	2.0
F3-1	1.999	2.009	2.008	2.005	4.019	4.028	4.015	4.021	2.0
F3-2	2.008	2.008	2.013	2.009	3.871	3.867	3.868	3.868	1.9

Table 3.6 40% of the average ultimate loading load

	40%P_{max}, lbs
CXT_WB	4296
CXT_WD	3311
CXT_WG1	3905
CXT_WG2	3644
Type-C	2815
Type-F (F4)	2417
Type-F (F3)	2835

Figure 3.16 Typical Young's modulus of elasticity setup

The Young's modulus of elasticity can be calculated by using Equation 3.2 as below:

$$E = (S_2 - S_1)/(\varepsilon_2 - \varepsilon_1) \qquad \textbf{Equation 3.2}$$

In Equation 3.2, S_2 is the stress at 40% of ultimate load, and corresponding strain is ε_2. ε_1 is strain at 50 millionths, and S_1 is the corresponding stress (ASTM Standard C469/C469M, 2014). The ε_1 may be beyond the specified point as shown in Figure 3.17 to ensure the load is fully applied.

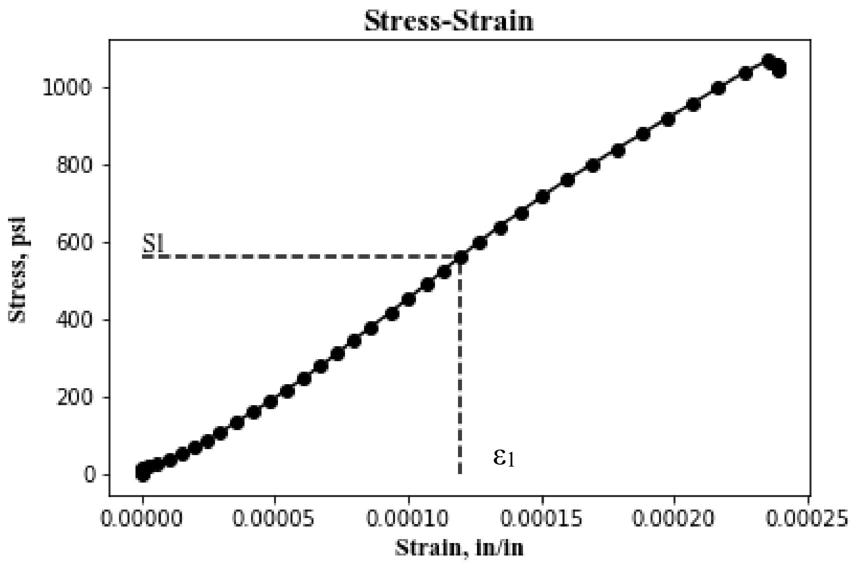

Figure 3.17 Typical testing result in stress versus strain

The calculated E_c is presented in Table 3.7. For sample F3-1, the test data is invalid so it is eliminated, same as first test of WG1 specimen. For new design tie group (CXT), the result shows WB demonstrates greater E values than others even though they had concrete release strength around 4,500 psi (Bodapati, 2018). WG2 and C5 have differences within 3%, and approximately 30% variance is observed in WG1.

Table 3.7 Young's modulus of elasticity test results

Specimen	Ec_1, ksi	Ec_2, ksi	Ec_3, ksi	Average, ksi
WB-1	8995.92	8053.74	8212.55	8420.74
WB-2	6612.85	7139.48	7421.90	7058.08
WD-1	3731.03	4717.06	4058.103	4168.73
WD-2	2815.27	3349.56	3670.82	3278.55
WG1-1		3344.55	3617.87	3481.21
WG1-2	4294.08	4832.99	4590.62	4572.56
WG2-1	3825.73	2622.34	3926.68	3458.25
WG2-2	3417.42	3491.39	3796.97	3568.59
C5-1	2537.69	2544.27	2379.74	2487.23
C5-2	2252.04	2485.481	2925.10	2554.21
F4-1	4606.43	4380.14	4721.488	4569.35
F4-2	3797.94	3221.35	3170.07	3396.45
F3-1				
F3-2	1673.16	1874.17	2123.672	1890.34

Flexural Test with Digital Image Correlation

One additional test was conducted to locate first crack. Same flexural test setup was employed, and a digital image correlation (DIC) system was used to capture tie deformation at constant moment region. DIC measures structure deformation based on an optically non-contact and non-interferometric method. Digital images were captured throughout the testing, and image analysis was performed by GOM ARAMIS Professional 2020 software. DIC measurement was based on the correlation between selected reference image and distorted images.

A CXT 505S [WJ] tie was selected. Center region of the tie was patterned since the tie has a smooth surface without natural texture. The pattern was applied on the front surface with a thin layer of white background. Then an average 0.08 inches ± 0.02 inches diameter black dots were applied, and patterning dot size should be slightly varied to efficiently minimize noise shown in Figure 3.18. A good pattern was recommended approximately ratio of 50 to 50 white and dark pixels. Per facet size contains 3 to 5 pattern features per facet size.

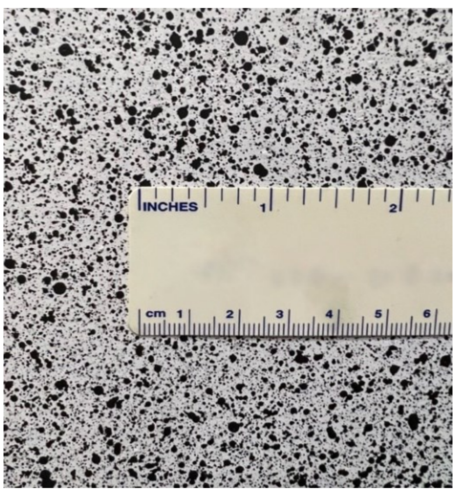

Figure 3.18 Typical DIC pattern

The selected DIC measuring system includes GOM ARAMIS Adjustable 2D/3D 12 megapixels (12M) camera system, and GOM testing controller. For this experiment, strain in horizontal direction was the quantity-of-interest (QOI), and region-of-interest (ROI) was between loading points. Stereo-DIC was used two cameras with a recommended camera angle 25 degrees and 16.93 inches camera distance. ARAMIS adjust based was placed approximately 41 inches away from specimen parallelly. Detail DIC parameters are listed in Table 3.8, and typical DIC setup shows in Figure 3.19.

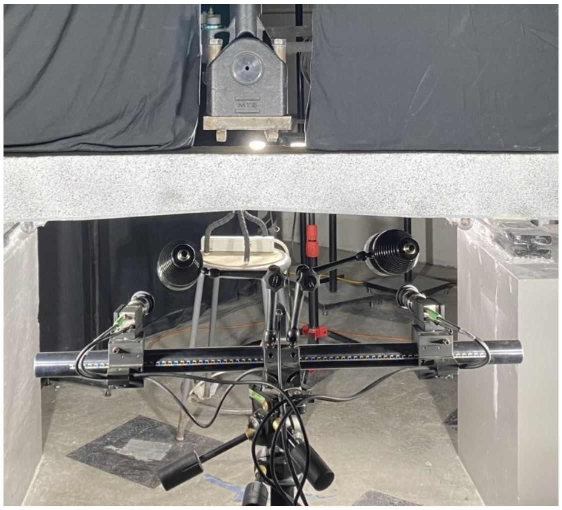

Figure 3.19 Typical DIC setup configuration

Table 3.8 Digital image correlation parameter (Jones & Iadicola, 2018)

DIC HARDWARE PARAMETERS	Description	
Camera Manufacturer, Model	GOM ARAMIS Adjustable 2D/3D	
Image Resolution	4096 x 3000	Total number of pixels contained in an image (width x height)
Image Size	4096 x 1000	Partial image 1/3 height
Lens Manufacturer, Model, Focal Length	Schneider Xenon Opal 2.8/12-0905 12 mm	
Length of FOV	1150.11mm (45.28 in.)	Region of space projected through lens system onto camera detector
Average Image Scale	3.56 pixel/mm	Number of pixels used to record an image of a region of physical length
Stereo-Angle	25 degrees	Angle between the optical axis of each camera system
Average SOD	1058 mm (41.65 in.)	Stand-Off Distance/Measuring/Working Distance: distance between aperture of lens and test specimen
Image Acquisition Rate	7 Hz, plus 4 frequency divider 160 additional images	Frame rate
Patterning Technique	Spray paint, black on white, 50% pattern density	Method of patterning on test specimen
Approximate Pattern Feature Size	White: solid coat; Black: 0.08 ± 0.02 inch	Approximate diameter of pattern features
Aperture	*f*/5.6 (range: *f*/2.8 - *f*/22)	Variable opening by which light enters camera
Calibration Object	CC20/1400/CG1277	

GOM calibration panel CC20/1400/CG1277 was used to calibrate sensors following instructions from ARAMIS software. The calibration deviation was 0.043 pixels which is within the deviation limit 0.05 pixels. To endure good contrast, a 7500-lumen LED panel light was shone on ROI. A surface component was created with facet size 21 pixels and point distance 20 pixels to ensure the system captured desired image. Adjusting lighting environment would help to improve quality of surface component and reducing noise.

The specimen was loaded following same testing procedure as mentioned. The DIC captured images at a fixed frame rate of 7 Hz, and an external trigger allowed for 4 clicks of 160 additional frequency divider images throughout the test. Two of these clicks were targeting at initial cracking occurred. The final two were spaced out during the displacement-controlled loading region, either when a crack was audibly heard or as the load approached expected failure.

The testing data was analyzed by GOM ARAMIS Professional 2020 software. Point-wise inspection was conducted at midspan of the tie. No image filtering or smoothing was applied. The analysis was focused on determined initial cracking so strain in x-direction was the quantities of interest. The noise was within acceptable range, thus no Spatial and Temporal filters applied to strain for a cleaner visual. Maximum strain was set at an average of 5000 µm/m, and minimum strain at an average of -750 µm/m. The crack developing displays as strain on the surface component shown in Figure 3.20. The testing result acquired from DIC system can be found in Figure 3.21 and Figure 3.22. The results were from the points (Point 13 and Point 14) in the constant moment region where the cracks occurred first.

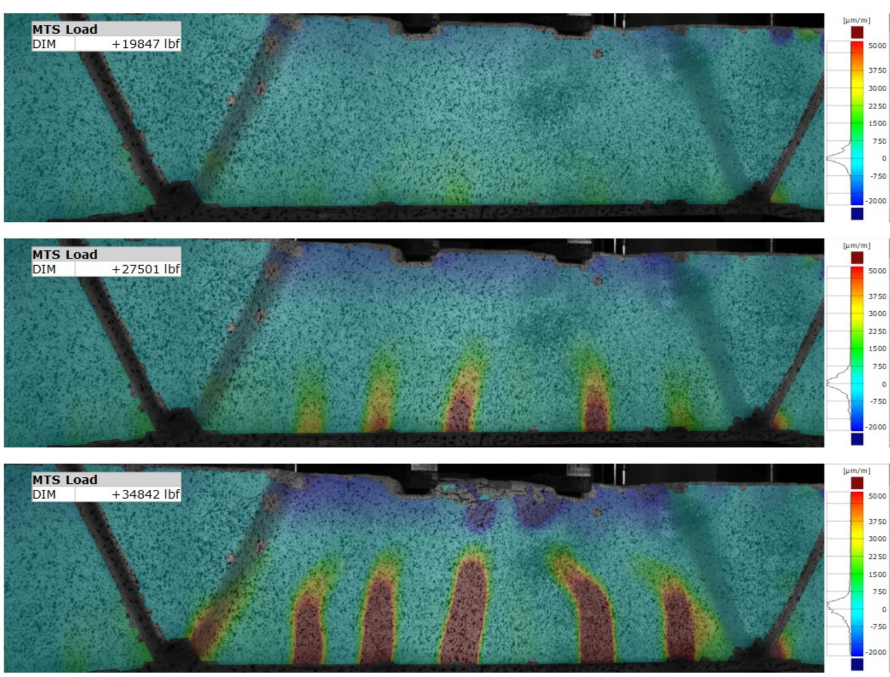

Figure 3.20 Typical DIC cracking development visualization

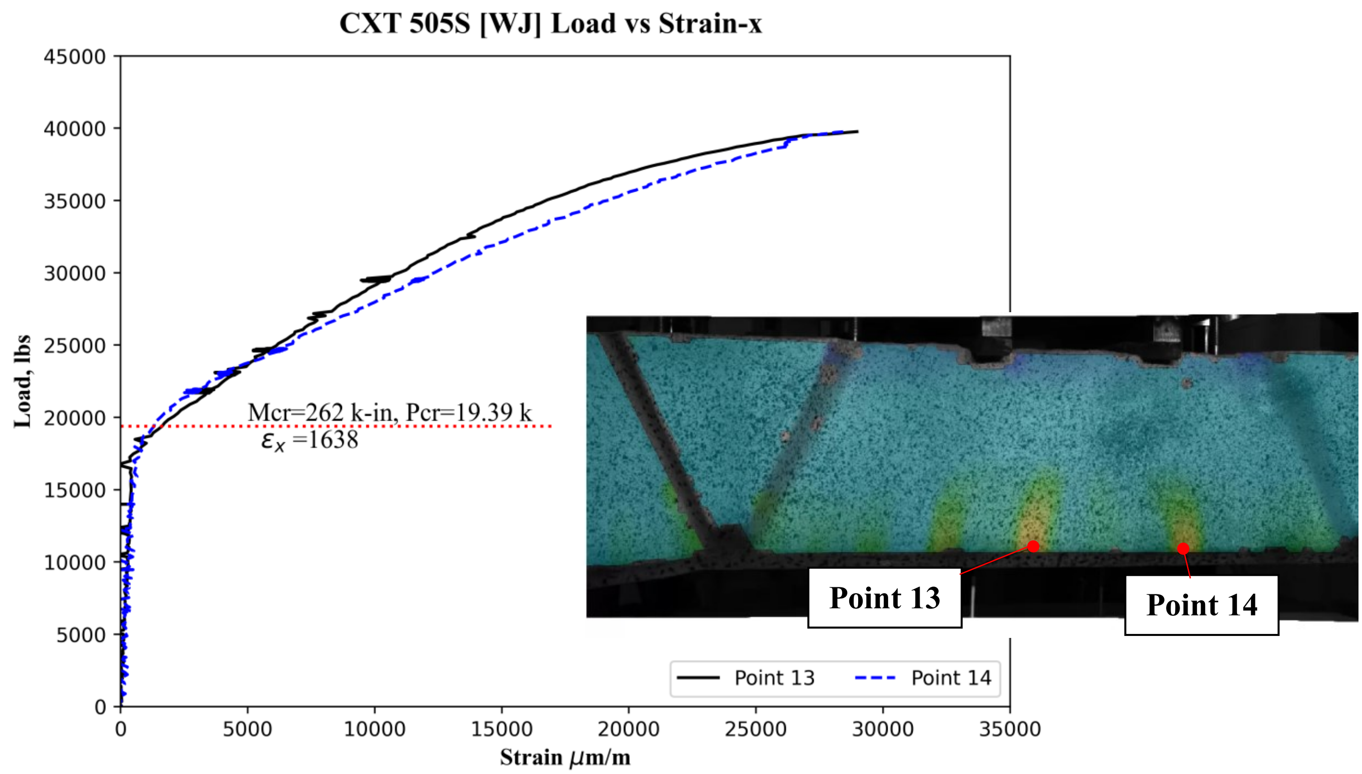

Figure 3.21 DIC result of load v.s. strain-x curve for CXT-[WJ] ties (DIC)

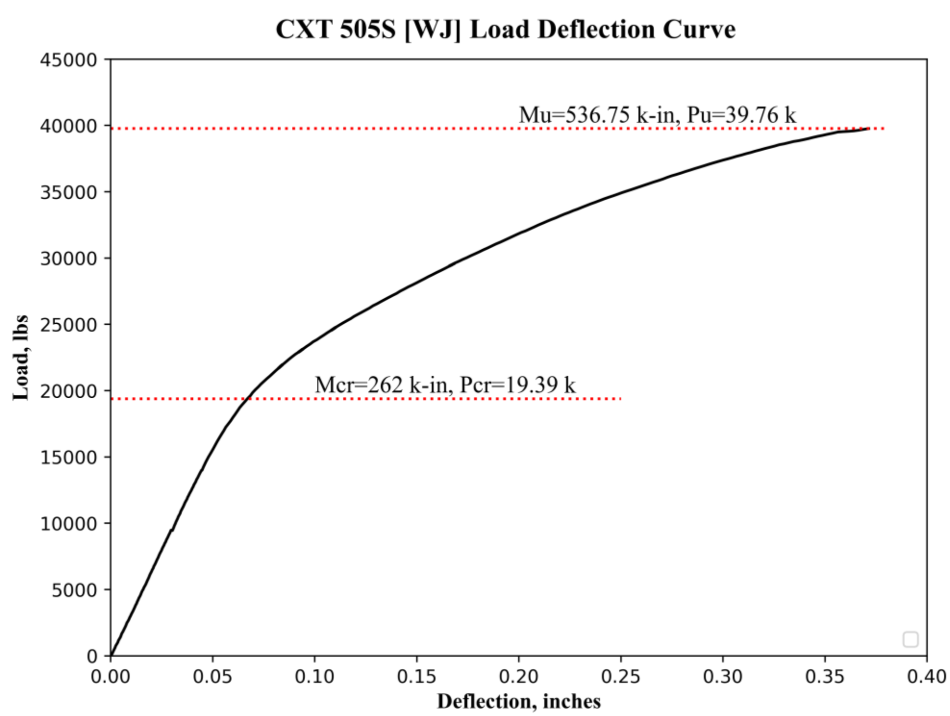

Figure 3.22 DIC result of load v.s. deflection curve for CXT-[WJ] ties

Chapter 4 - Monoblock Tie Analysis Program

Concrete ties in North America are recommended to follow the AREMA standard. Part 4 of AREMA discusses general aspects of the design (materials, dimensions, and loads). Additionally, structural strength and testing method are included for reinforcements pre-tensioned prior to concrete casting (AREMA, 2020). Track system assures a smooth and stable railway and provides support for combined forces (vertical, lateral, and longitudinal force). While trains travel along the track, concrete monoblock ties resist dynamic wheel load distributed by rail.

Considering the track as a beam on an elastic foundation, the load distribution is affected by tie spacing, supporting condition, rail rigidity, and axle distance (AREMA, 2020). This distributed load is transmitted to the rail-seat, and it induces the bending forces on monoblock tie. Subsequently, concrete monoblock ties deform and degrade in response to this load. It is desirable to capture tie response behavior so that the prediction of monoblock tie deformations can be made.

To predict tie performance, there are two criteria that should be properly pre-determined: track system (rail-seat load and ballast support) and prestressed concrete properties (cross-section, prestressing reinforcement, concrete, cracking, losses, etc.). Additionally, the tie cross-section may not be simple rectangle. To provide lateral force resistance, scallops are placed on the side of tie to increase lateral resistance which can be found in newer tie designs. The scallops result in a complex shape of tie cross-section. A common dimension of prestressed concrete railroad tie is minimum 8 ft. long to ensure adequate bond transfer (AREMA, 2020). However, tie geometry is not specified. In general cross-section is reduced at rail-center compared to rail-seat, and the cross-section shape is varied depending on tie manufacturer. To include the effects of changes in geometry, a numerical approach based on Moment-Curvature principle is employed for 1) design and 2) analysis of the flexural behavior of prestressed concrete monoblock ties.

The computational tool is computing M-C curve for each slice of tie where the tie can be divided into minimum half inch slice. At this stage, the crack propagation can be observed on concrete strain diagram. Then repeating the same process of computing M-C curve along the tie, and the rotation can be determined at a particular moment. Finally, deflection of tie is calculated by using moment-area method, additionally changes in rail-seat center-to-center spacing can be defined.

Moment Curvature

Moment-Curvature (M-C) relationship represents the actual performance of nonlinear material member subjected to combined forces, and it is commonly used to analyze the cross-sectional behavior of reinforced concrete members. Prestressed concrete members are subjected to axial stress from the prestressing force, external bi-axial load, and bending moment from the external load and from prestressing force eccentricity. It is desired that the member stays elastic but it is also important to predict member capacity beyond elastic behavior.

The material flexural rigidity is the product of moment of inertia, *I*, and Young's modulus of elasticity, *E.* Moment of Inertia depends on section geometry while *E* depends on the material properties of the member. For reinforced concrete the cross-section stiffness depends on the amount of reinforcement, level of cracking, and change in strain distribution in cross-section. Thus, instead of directly using *EI* as stiffness for the design, the reinforced concrete cross-section stiffness could be directly determined from the slope of the M-C curve which includes the effects of materials, cracking, stiffness due to tendon, effective cross-section reduction, and long term / short term effects of prestressed concrete (Anwar & Najam, 2016). EI is the moment, *M*, divided by rotation, $\emptyset$. Rotation is the ratio of the strain to the compressive depth when the member is subjected to flexure (Anwar & Najam, 2016).

To apply this method, it is common to apply condition of force equilibrium and compatibility, additionally, incorporating constitutive behavior of material. The general approach is to assume a value of concrete strain with iterating depth of neutral axis, and then iterate to find a force equilibrium condition. As shown in Figure 4.1, concrete strain distribution could be plotted based on the assumed concrete strain of compressive surface. Then the strains and stresses could be determined. Based on assumed strain value, the moment force can be calculated once the force equilibrium condition is achieved. Accordingly, the curvature value can be determined. Repeating procedures with varying concrete strain of compressive surface, the M-C curve can be completed for specific cross-section.

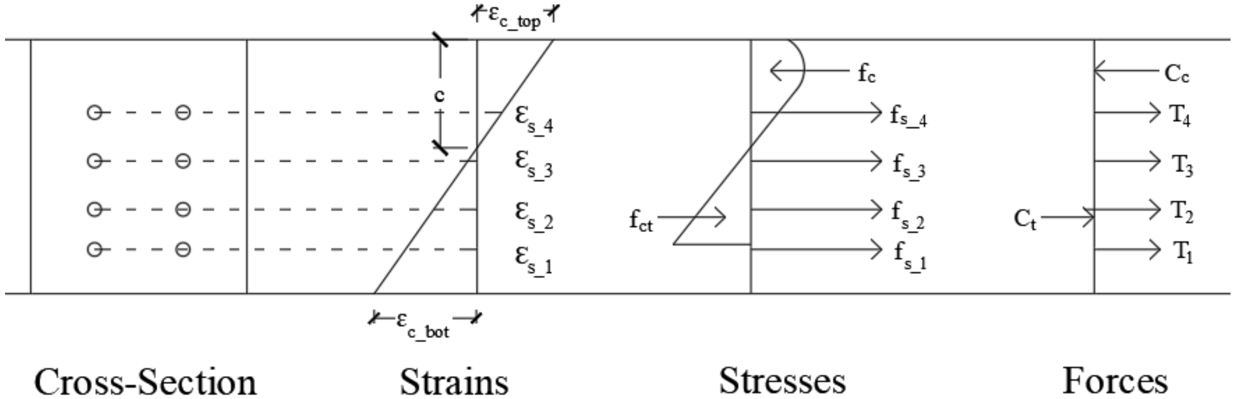

Figure 4.1 Concrete stress distribution

Material Constitutive Relation

Concrete

The Hognestad model is used to determine compressive stress in this research. It is from "Reinforced Concrete Structures" (Park & Paulay, 1975). The concrete stress-strain relationship is shown in Figure 4.2.

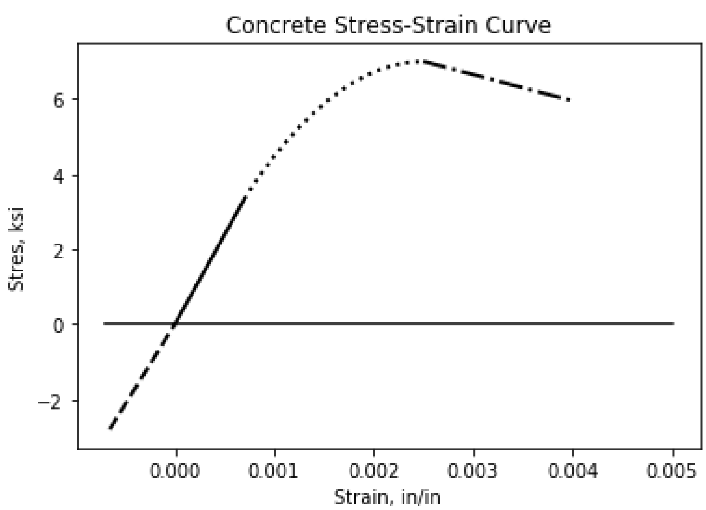

Figure 4.2 Compressive concrete stress strain relationship

The assumed concrete constitutive behavior demonstrates linear behavior (solid line in the Figure 4.2), until concrete stress reaches the elastic limit point which is commonly assumed 50% of maximum concrete strength. Then, plastic behavior starts after the elastic range (dotted line in the Figure 4.2), and the concrete stress begins to descend right after concrete stress passes peak stress (dash-dot line in the Figure 4.2). Completed curve is estimated by Equation 4.1 through Equation 4.3 (Park & Paulay, 1975; American Concrete Institute, 2019).

Elastic	$f_c = E_c \varepsilon_c$	**Equation 4.1**
Elastic - ε_0	$f_c = f_c' \left[\frac{2\varepsilon_c}{\varepsilon_o} - \left(\frac{\varepsilon_c}{\varepsilon_o} \right)^2 \right]$	**Equation 4.2**
ε_0-0.004 (Linear Decreasing)	$f_c = f_c' [1 - 100(\varepsilon_c - \varepsilon_o)]$	**Equation 4.3**

f'$_c$: maximum stress in concrete, ksi

E_c: concrete modulus, ksi

ε_o: Strain that corresponds to peak stress, in/in

ε_c : Concrete elastic limit stain at $0.5f_c'$, $\varepsilon_c = {}^{0.5f_c'}/_{E_c}$, in/in

The strain corresponding to peak stress can be determined by solving Equation 4.4 for $\varepsilon_o$when concrete stress is at elastic limit point.

$$0.5f_c = f_c' \left[\frac{2\varepsilon_c}{\varepsilon_o} - \left(\frac{\varepsilon_c}{\varepsilon_o} \right)^2 \right] \qquad \textbf{Equation 4.4}$$

Furthermore, tensile strength of concrete is assumed approximately 10 percent of concrete compressive strength (Park & Paulay, 1975), and behaviors linearly up to maximum tensile strength.

Prestressed Tendon

There are several equations used to estimate force in prestressed reinforcement. Precast/Prestressed Concrete Institute (PCI) Design Handbook 7th Edition provides the design stress-strain curve for Seven-Wire Low-Relaxation prestressing strand. The stress in prestressed strand can be determined by using Equation 4.5 and Equation 4.6, applying for tendon tensile strength at 250 ksi and 270 ksi respectively. For prestressing wire, a proposed wire strength formula can be used (Equation 4.7), this model is a modified Ramberg-Osgood function from research conducted at Kansas State University (Chen Y.-S. , 2016). By using this function, the corresponding coefficients are provided for general prestress wire, and the specific parameters (K, Q and R) are also given for specific wire types.

PCI Strand (250)

$$\varepsilon_{ps} \leq 0.0076 \qquad \mathrm{f_{ps}} = 28{,}800\varepsilon_{\mathrm{ps}}$$

$$\varepsilon_{ps} > 0.0076 \qquad \mathrm{f_{ps}} = 250 - \frac{0.04}{\varepsilon_{ps} - 0.0064}$$

Equation 4.5

PCI Strand (270)

$$\varepsilon_{ps} \leq 0.0085 \qquad \mathrm{f_{ps}} = 28{,}800\varepsilon_{\mathrm{ps}}$$

$$\varepsilon_{ps} > 0.0085 \qquad \mathrm{f_{ps}} = 270 - \frac{0.04}{\varepsilon_{ps} - 0.007}$$

Equation 4.6

Wire Strength Formula

$$f_{ps} = E\varepsilon_{ps}\left[Q + \frac{1 - Q}{\left(1 + \left(\frac{\varepsilon_{ps}E}{Kf_y}\right)^R\right)^{1/R}}\right]$$

Equation 4.7

K=1.0355, Q=0.0180, R=7.4386

Flexural Response

After material relationships are defined, the response of the flexure in beam can be presented. The Moment-Curvature is used, and the basic flexural theory are as following below:

Assumptions

M-C curve is the relationship of action with corresponding deformation.

There are three assumptions:

- Plane section remain plane: Navier's hypothesis
- Bond between concrete and reinforcement
- Stress-Strain relationship of concrete and tendon

There are three stages of flexural beam behavior. The initial stage involves the strain from effective prestress force. In the next stage, the beam undergoes elastic flexure with no cracking. Finally, the beam deforms after cracking and displays nonlinear material response. Therefore, there are certain stages occurring in beam behavior that are recommended to be defined for constructing a completed M-C curve.

1. Initial, $\emptyset_{init}$, due to effective prestress in tendon where $M_{external}=0$
2. Cracking, $\emptyset_{cr}$
3. Nominal Capacity, $\emptyset_{cu}$, where $\varepsilon_{cu} = 0.003$

Before loading, $M_{external}=0$

For non-prestressed members, there are no stresses and strain prior to external load being applied. Contradictorily, prestressed concrete members are designed to be pre-compressed via a group of high-tension reinforcement. This pre-compression enables the member to sustain higher load. Under force equilibrium condition, pre-compression relates to the strain in steel. Accordingly, the concrete undergoes stress and strain even though no external load is applied. To determine the strain in concrete at the level of steel, the concrete strain distribution should be computed first as shown in Figure 4.3. At the initial stage, the strain in the concrete on top and bottom of section is computed by using Equation 4.8 and Equation 4.9. The initial strain is varied depending on the cross-section and amount of tendon, since the loss and section properties are changed.

$$\sigma = -\frac{P}{A} \pm \frac{Pe}{S} \qquad \textbf{Equation 4.8}$$

$$\varepsilon = \frac{\sigma}{E} \qquad \textbf{Equation 4.9}$$

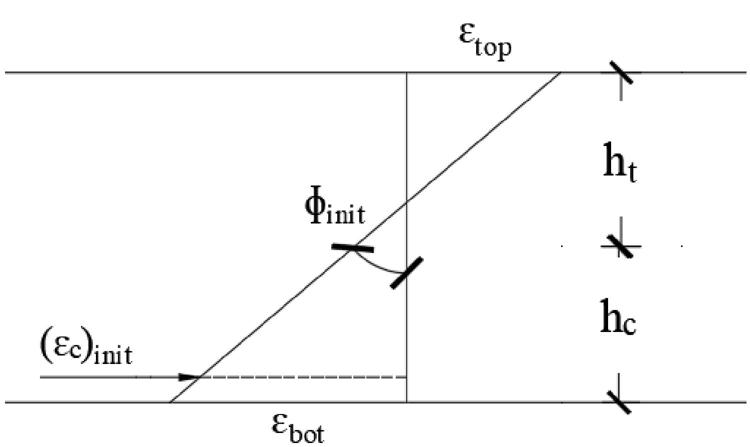

Figure 4.3 Concrete strain distribution at initial stage

Since the location of the tendons are known, the pre-compression is found by using concrete strain distribution and similar triangle approach. The same method is also used to calculate rotation at initial stage, $\emptyset_{init}$. $\emptyset_{init}$ is the ratio of distance from concrete surface to neutral axis to the corresponding strain at top/bottom surface. The distance to the neutral axis can be determined from triangle similarity of compressive and tensile strain zone or strain divided by rotation.

First Crack

Concrete resists the tensile force before cracking, and strength contribution from effective prestressing is included. According to ACI 318-19, modulus of rupture, f_r, is calculated using Equation 4.10 where prestressed concrete tie is designed as Class U uncracked member (American Concrete Institute, 2019). The theoretical cracking moment, M_{cr}, can be defined by solving Equation 4.11. The corresponding curvature, $\emptyset_{cr}$, is calculated according to Equation 4.12.

$$f_r = 7.5\sqrt{f_c'} \text{ , psi} \qquad \textbf{Equation 4.10}$$

$$f_r = -\frac{P}{A} \pm \frac{Pe}{S} \mp \frac{M_{cr}}{S} \qquad \textbf{Equation 4.11}$$

$$\emptyset_{cr} = \frac{M_{cr} - M_{init}}{E_c I} \qquad \textbf{Equation 4.12}$$

M_{init}: the moment force from effective prestress force times eccentricity of prestressing, kips-in

E_c: Young's modulus of elasticity, ksi

After Crack

After initial cracking, the actual concrete stresses are no longer linear through the cross-section, and the internal compressive force of concrete could be determined by concrete stress, f'_c, times compressive concrete area. The concrete area is varied on the compression depth which iteratively determines the force equilibrium. For the rectangular cross-section, width of cross-section is constant, the concrete force can be computed by Equation 4.13. Equation 4.13 is obtained by integrating the Hognestad model (Equation 4.2) times cross-section width with respect to variable x on interval zero to compressive depth. The distance from the centroid of compressive block to neutral axis is determined from Equation 4.14.

$$C_c = bf_c' \frac{\emptyset}{\varepsilon_0} x^2 \left[1 - \frac{\emptyset x}{3\varepsilon_0}\right]$$ **Equation 4.13**

$$\bar{x} = x \left[\frac{8\varepsilon_0 - 3\emptyset x}{12\varepsilon_0 - 4\emptyset x}\right]$$ **Equation 4.14**

x: compressive depth, in

$\emptyset$: ratio of strain at compression surface to compressive depth, ${}^{\varepsilon_c}/_{x}$, rad/in

If the cross-section is not simply rectangular or the "stress and strain are varied over the depth of the member" (Mitchell & Collins, 1991), the section force can be evaluated layer-by layer as shown in Figure 4.11.

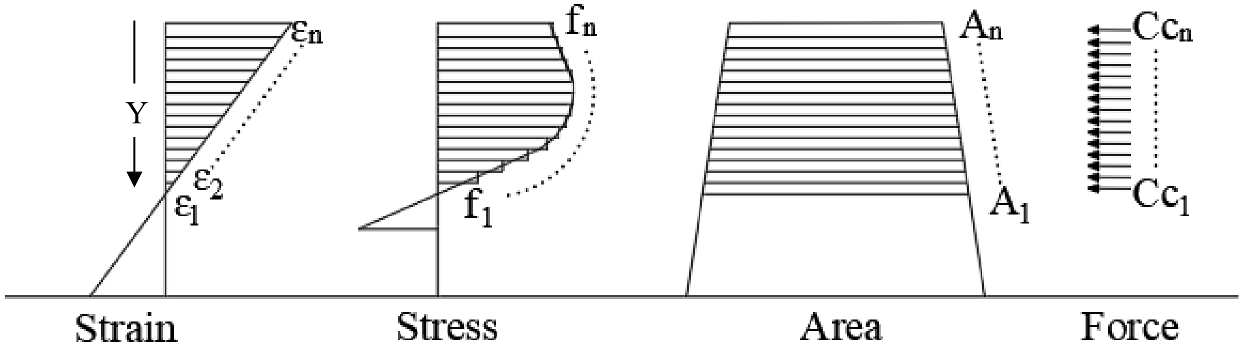

Figure 4.4 Concrete stress-strain relationship (Mitchell & Collins, 1991)

A numerical approximation approach is used to determine the concrete compression force, C_c. First, the compressive depth is divided into even layers, n. Then, the stress is computed by using Hognestad model at each layer, and the average stress is taken (Equation 4.15). The resultant concrete compressive force is equal to the stress, f_{cn}, multiplied by the corresponding area at each interval. Subsequently, total internal concrete compressive force is the summation of concrete compression force from each layer.

$$f_{cn} = \frac{f_{c(n-1)} + f_{cn}}{2}$$ **Equation 4.15**

To avoid double-counting the area of concrete and steel, the area of reinforcement at each layer is subtracted from the area of concrete. At each layer, area of reinforcement can be determined by computing area of a segment in a circle. If the reinforcement has been sliced into two segments (Figure 4.5), in this case, minor circular segment can be computed by using Equation 4.16. Remaining circular segment can be computed by total area of circle subtracting minor circular segment.

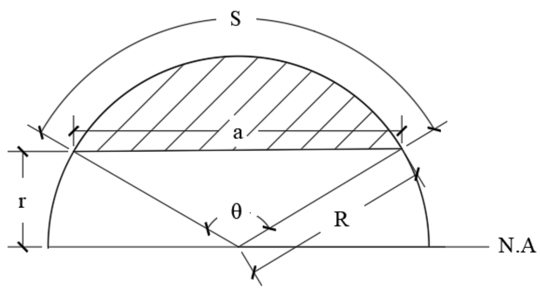

Figure 4.5 Minor circular segment

$$A = \frac{1}{2}[RS - ar] \qquad \textbf{Equation 4.16}$$

$$S = R\theta$$

$$a = \sqrt{R^2 - r^2}$$

R= radius of reinforcement, inch

a = chord length, inch

S = arch length, inch

Ɵ = central angle, rad.

r = height of the triangular portion, inch

If the reinforcement has two parallel chords on the same side of semicircle (Figure 4.6 (a)), the area of reinforcement is the difference of two minor segments. On the other hand, if the two parallel chords are on a different side of semicircle (Figure 4.6 (b)), the area of reinforcement is the total area subtracted by two minor segments.

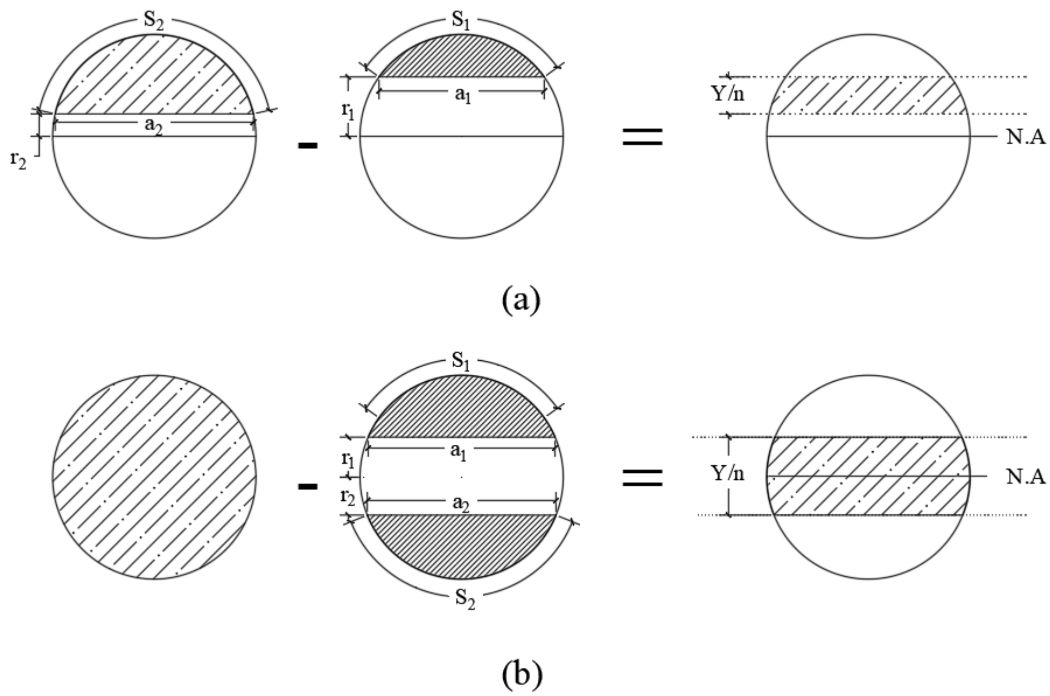

Figure 4.6 Reinforcement has two parallel chords.

The model for computing stress in prestressing steel depends on the level of strain. Strains include three components as below:

1. ε_{se}, strain in prestressing due to effective prestress after losses
2. ε_{ci}, initial concrete strain at each layer of prestressing steel without external load
3. ε_{c}, strain in the concrete at each layer of prestressing steel under specified moment

The strain distribution is presented in Figure 4.7, including the strain distribution before and after external load is applied. Total strain in prestressing steel is summation of the three components, and applied to the selected prestressing stress-strain model. Total tensile fore is summation of resultant tension force, T_n, at each layer of reinforcement. T_n can be computed by stress in prestress times the area of prestressing reinforcements.

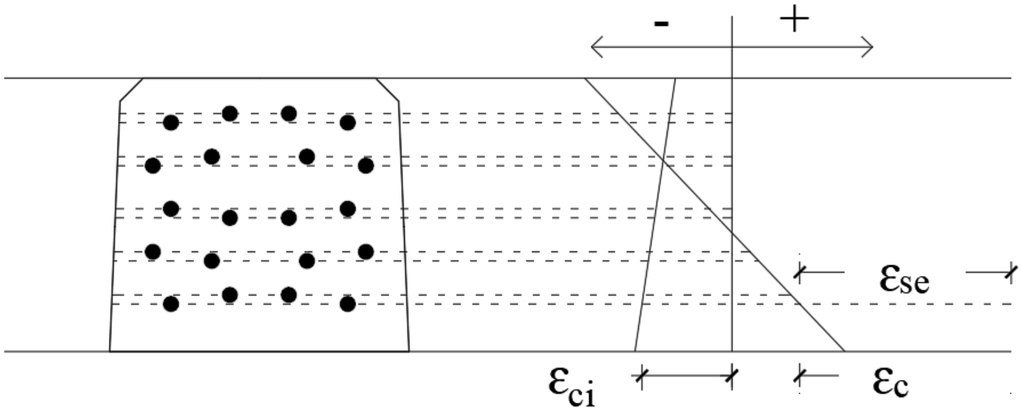

Figure 4.7 Prestress steel strain distribution in different stages (Lutch, 2009)

After the internal forces are defined, the compressive depth, *Y*, can be found when force equilibrium is satisfied where T = C. Subsequently, curvature and moment can be computed.

Code Development

The first part of the code handles design considerations (the user input information), and it includes tie geometry, concrete and steel material properties, prestress tendon pattern, and selection of ballast condition. There are four categories of design considerations as below:

1. Static Rail-Seat Load, *R*

   The design rail-seat load can be calculated by using Equation 2.3 when AL, DF and IF are determined. Then the ballast pressure is computed and checked (AREMA, 2020).

2. Ballast Support Condition

   The user selects pre-defined ballast support as shown in Figure 4.8, and defining desired distance.

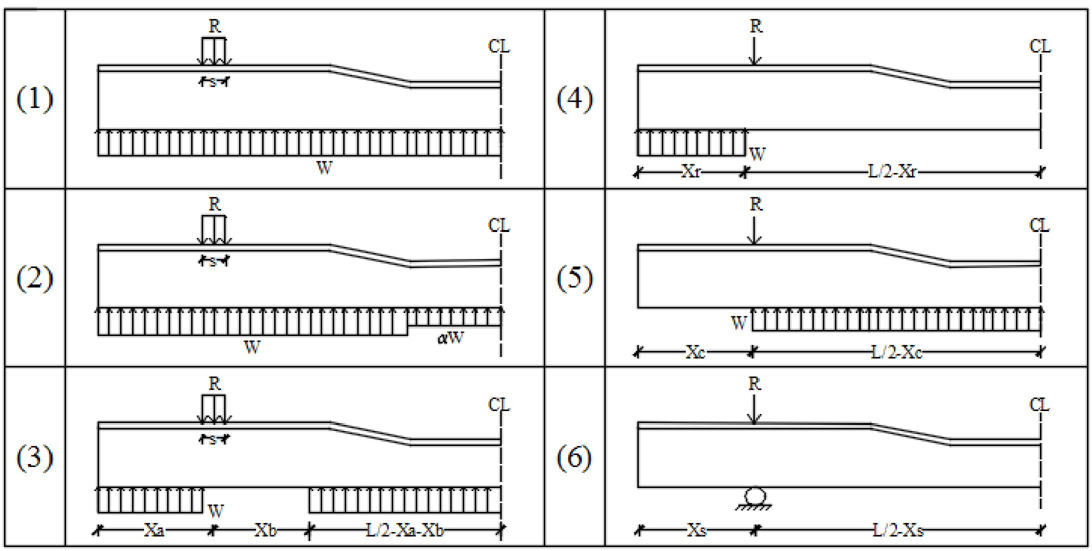

Figure 4.8 Program ballast options

3. Tie Geometry and Concrete Properties

   For tie geometry, the user is allowed to determine desired length of monoblock tie and gauge length. Then details of tie shape information are required to determined cross-section properties, such as cross-sections, distance between cross-sections, and number of cross-section before rail-seat and in between rail-seat and rail-center. The cross-section can be defined by x- z coordinate system (Figure 4.9). If scallops are preferred, the shape and location is defined by y-z coordinate system (Figure 4.10 (a)). Moreover, top and bottom width is the thickness of scallop in x-z coordinated system (Figure 4.10 (b)), and it is required to be determined by designer. The program is designed to input coordinates in a clockwise pattern starting from the bottom left. To be noted, it is important to not intersect points of polygon which will interrupt section properties computation.

For concrete properties, concrete Young's modulus of elasticity will be computed using initial (at time of de-tension) and long-term concrete compressive strength. The minimum 28-days design compressive strength will be checked with AREMA (2020) requirement which should be at least 7,000 psi. If the requirement has failed to be satisfied, the program can either be interrupted or allowed to continue based on user preference. Furthermore, modulus of rupture, f_r, is calculated using Equation 4.10.

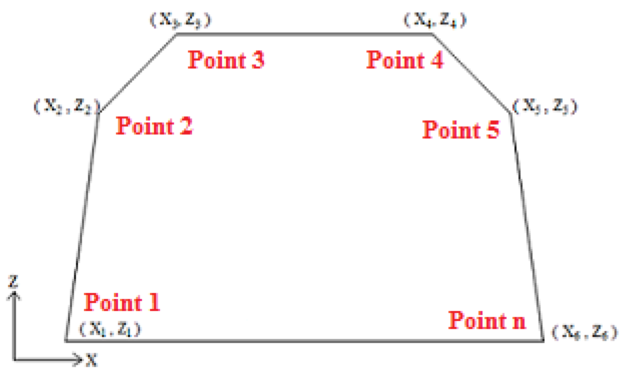

Figure 4.9 Cross-section defining diagram

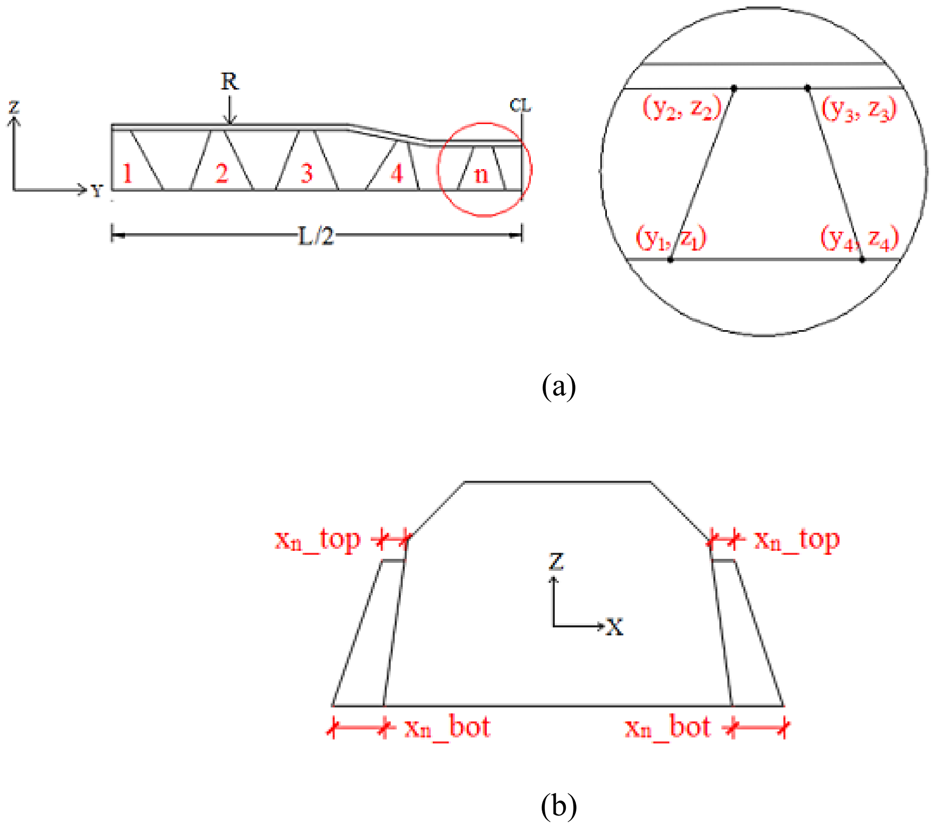

Figure 4.10 Scallops defining diagram

4. Prestressing

   There two types of prestressing tendon that can be used in the analysis program, low-relaxation prestressing wire and 3/8" -diameter low-relaxation 7-wire strand. The correlated properties can be user preferred, and prestressing wire has an option to use experimental data from (Chen Y.-S. , 2016). Next, the placement of prestressing reinforcement should be defined either by number of wires per row or individually defined. The prestressing losses will be computed based on user chosen method, including user defined losses, AASHTO Approximated Method, AASHTO Refined Method, and PCI Method.

   It is important to ensure that the prestressing force is fully developed in the distance between tie-end and rail-seat. Transfer length, L_{tr}, and developed length, L_d, will be computed by equation from (Momeni, 2016) and (Bodapati, 2018) corresponding in order after wire type is selected.

Once design parameters are determined, the program will check the design elements with correlated requirements. If it fails to satisfy code recommendation, the adjustment of design assumptions will be needed. Then the second part of the code will proceed, and the program processing flowchart is presented in Figure 4.11.

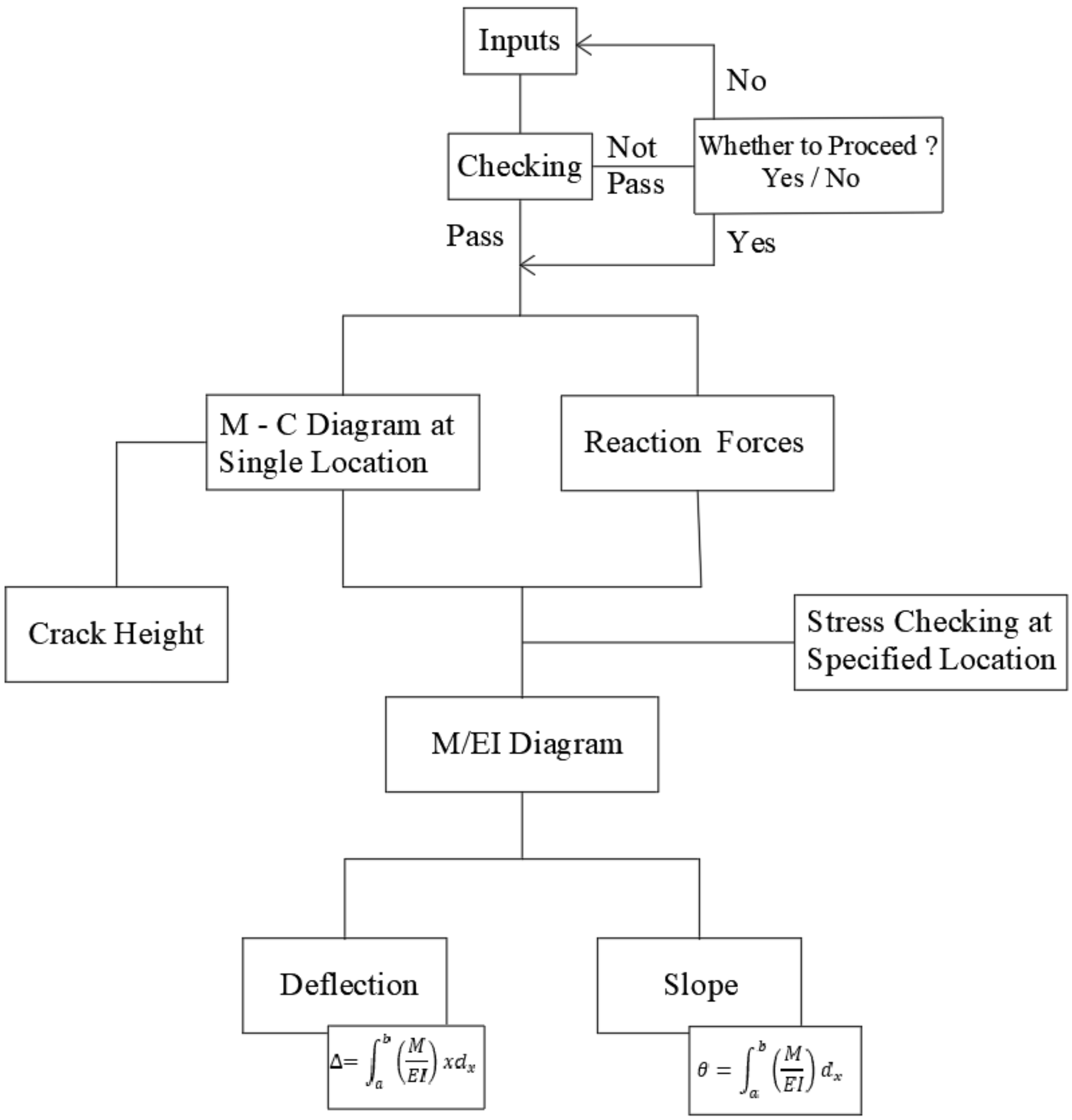

Figure 4.11 Analysis program process flowchart

Second part of code is computation, including

1. Computing moment and shear force based on user selected ballast condition and rail-seat load.
2. Moment-Curvature is different for beams subjected to positive or negative bending. The program default setting computes positive curvature at rail-seat and negative curvature at rail-center (Figure 4.12), and can be changed depending on user preference. The single cross-section analysis is performed, and the estimated crack height and ultimate moment capacity can be observed.
3. To compute deflection of the tie, the M-C curve will be generated at each slice following the procedure as described earlier in this chapter. The positive or negative curvature is based on the subjected bending force, relying on the tie ballast condition. The radius of curvature value corresponds to the computed moment force on the specified M-C curve.
4. The stress limits can be checked at specified point and the limits are listed in Table 4.1.

Table 4.1 Concrete stress limits (American Concrete Institute, 2019)

	Tension		Compression	
	End of Simply supported	Other Locations	End of Simply supported	Other Locations
At Transfer	$6\sqrt{f'_{ci}}$	$3\sqrt{f'_{ci}}$	$0.7f'_{ci}$	$0.6f'_{ci}$
At Service	$\leq 7.5\sqrt{f'_c}$ (Class U)		$0.60f'_c$	

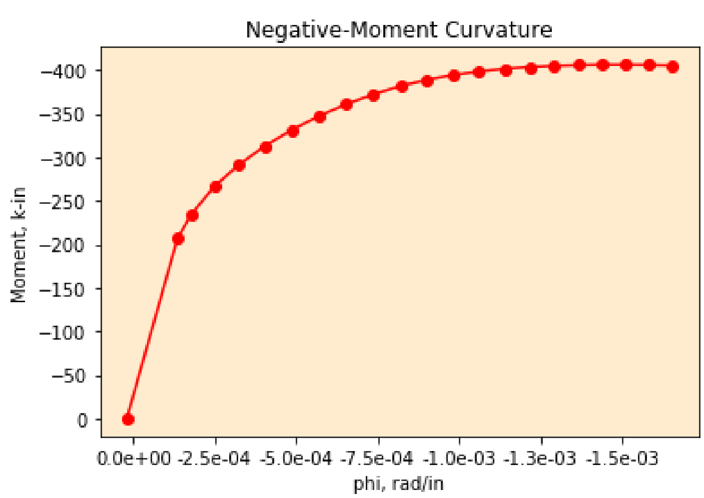

Figure 4.12 Typical M-C curve by program

The third part of code is using the radius of curvature values which have been defined in the previous part. A M/EI vs. tie length diagram is plotted (Figure 4.13), and deflection and slope are estimated at each increment. Figure 4.14 presents the output of computing slope and deflection curve. The typical deflection plot includes total deflection (blue dotted dashed curve), initial deflection due to prestressing reinforcement (yellow dashed curve), and deflection due to concrete (red solid curve).

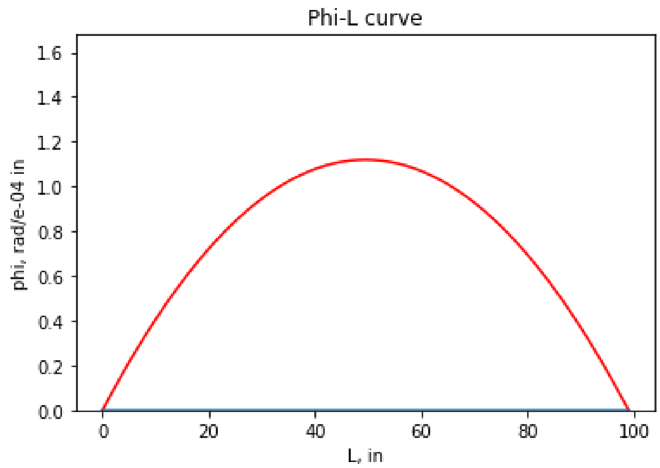

Figure 4.13 Typical M/EI diagram by program

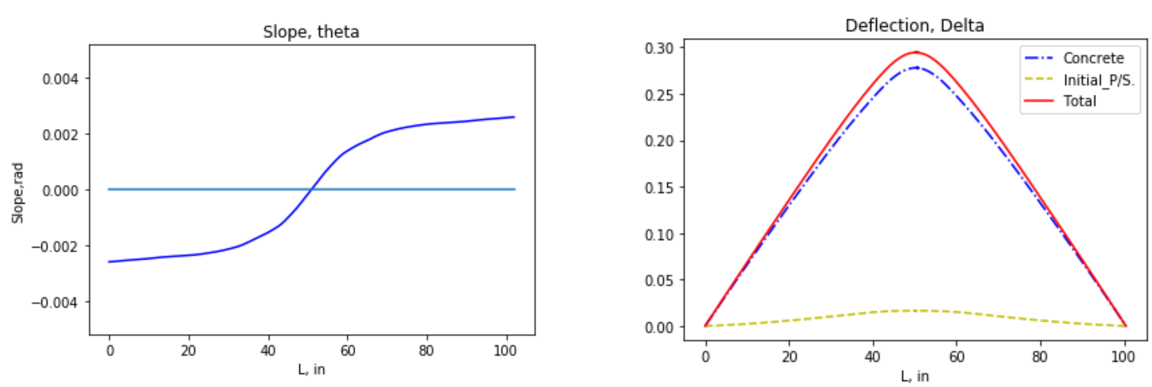

Figure 4.14 Typical slope and deflection diagram by program

Moreover, the crack propagation distance, d_{cr}, is computed. The crack strain can be an user defined value or $7.5\sqrt{f_c'}/E$ according to ACI specification. Under a point of interest in M-C curve, the crack height can be estimated using similar triangles in the strain distribution as shown in Figure 4.15.

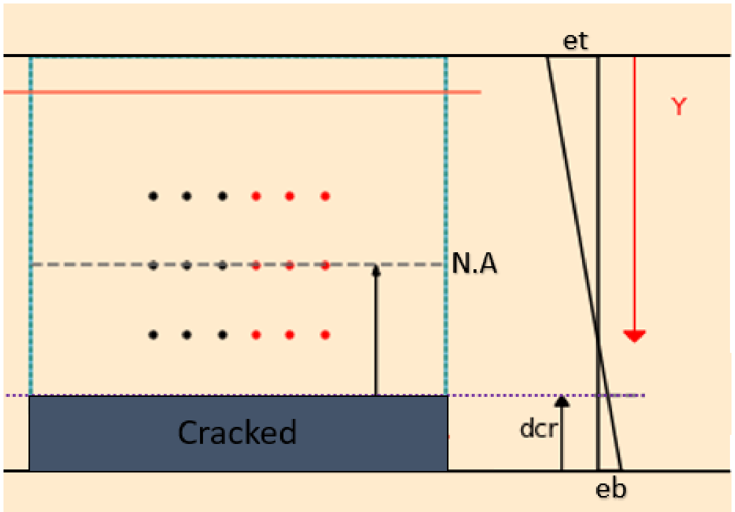

Figure 4.15 Determination of crack height at interest point by program

For the center bound condition, the rotation distance of rail can be estimated by slope, Θ, times height of the rail, h_{rail}, and change in rail gauge width, Δ_g, can be determined by rail height times Θ as shown in Figure 4.16. The total gage width is summation of gauge length and Δ_g at each side of rail-seat.

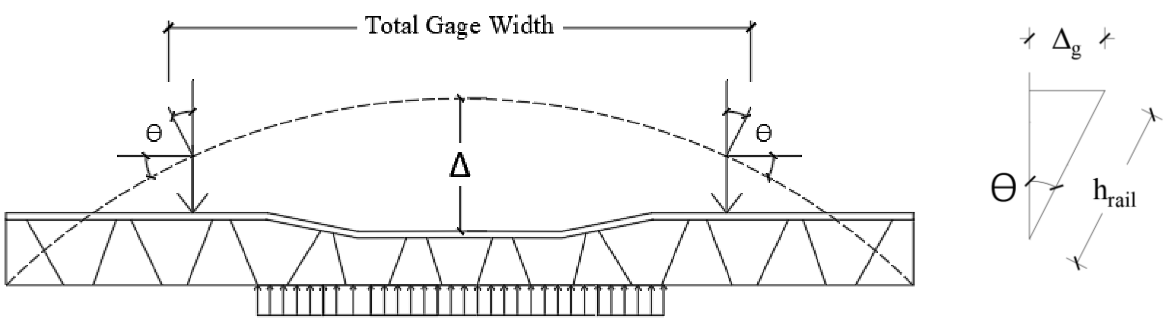

Figure 4.16 Tie-seat center-to-center measurement

Chapter 5 - Code Verification and Validation

To establish accuracy and reliability a verification and validation (V&V) approach can be employed after development of the numerical program. Verification is the process to evaluate program response accuracy in a controlled environment by comparing computational results to the anticipated values from the developer. Validation is the process of evaluating the program performance in a realistic environment, checking whether it fulfills the intended purpose or matches experimental measurement (Oberkampf & Trucano, 2008).

Verification

In this section, code was compared with the corresponding analytical solution or numerical solution at each intermediate step, where the answer should be the “correct answer”. The "correct answer" is an appropriate benchmark including highly accurate solutions. These benchmarks often are isolated examples where the uncertainties are minimized or eliminated. (Oberkampf & Trucano, 2008).

There are three benchmarks chosen to verify the code, including

Case 1- A rectangle cross-section beam with a row of prestressing wires, the benchmark type is numerical and analytical solutions given by self-built M-C approach Excel spreadsheet program.

Case 2- A simplified concrete beam with a simply supported condition, the benchmark type is numerical solution given by structural design software, RISA.

Case 3- A prestressed concrete monoblock tie analysis at critical points (Rail-Seat and Rail-Center), the benchmark type is analytical solution of an existing tie analysis case given by Michigan Technological University (Lutch, 2009).

Case 1 - Code to Hand Solution

An example chosen in verification is a uniform 8-inch x 4-inch rectangular prestressed concrete beam cross-section, and assumptions are listed below:

- Concrete compressive strength f'_c =7 ksi,
- Grade 287 [WC] wire, (6) 0.209”-diameter prestressing wires,
  E_{ps} = 28,747.51 ksi, f_{py} = 255.55 ksi
- Prestressing force (after all losses), f_{se} = 173.83 ksi
- Center of gravity of the wires is 1-inch from bottom of the beam

To ensure the code performed and functioned correctly, the numerical algorithm had been carefully evaluated throughout the process in determination of moment and curvature from initial stage ($M_{external}$ = 0 k-in) to the ultimate capacity (compressive concrete strain at 0.003). The codes were compared with hand solutions step by step, and detailed hand calculations can be found in Appendix B. The hand solution consists of section properties calculation, stress and strain calculation and checking with specification, and a single point of M-C relationship at top fiber strain, ε_{ct}, of 0.001. Once a single point of M-C response was confirmed, an Excel spreadsheet was developed to perform repetitive procedures to construct a completed M-C diagram. Appendix B presents the detailed calculations by Excel program and the results generated by computational program.

A good agreement is observed between hand/Excel solution and computational program. The Excel calculation and program computing results are shown in Table 5.1, and plotted M-C diagram are shown in Figure 5.1.

Table 5.1 Comparison of computing M-C response results

	Excel		**Program**		**Difference, %**	
ε_{ct}	Φ, rad/in	M, k-in	Φ, rad/in	M, k-in	Φ	M
At M=0	-1.32E-04	0.00	-1.32E-04	0.00	0.0%	0.0%
Crack	9.15E-05	181.80	9.15E-05	181.80	0.0%	0.0%
-0.0008	1.54E-04	214.70	1.54E-04	214.73	0.0%	0.0%
-0.001	2.27E-04	231.91	2.27E-04	231.93	0.0%	0.0%
-0.002	6.55E-04	293.40	6.55E-04	293.44	0.0%	0.0%
-0.003	1.12E-03	318.52	1.12E-03	318.70	0.1%	0.1%

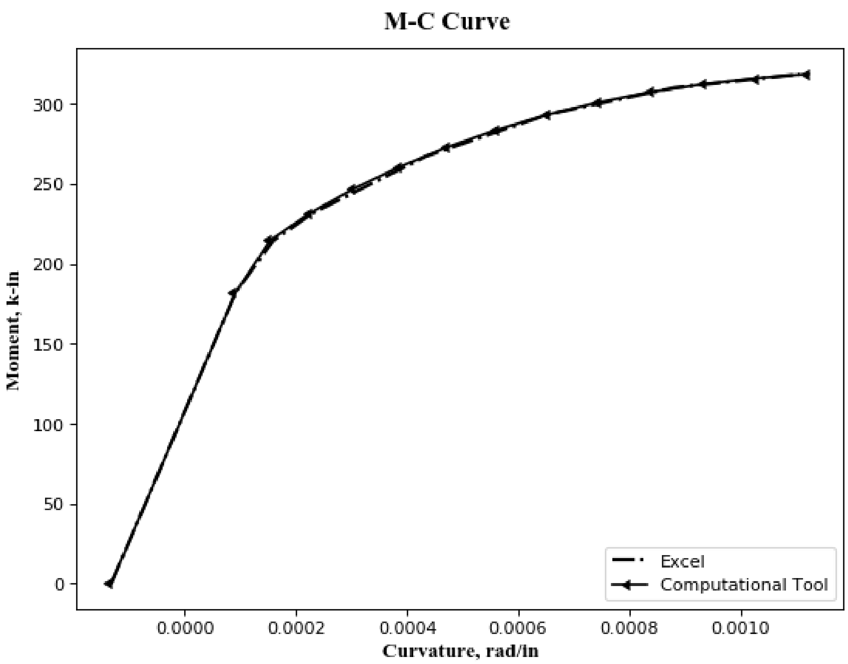

Figure 5.1 M-C curvature comparison

Case 2 - Code to Code Comparison

In this section, a commercial finite element software RISA was used. The comparison included moment, shear, and deflection at rail-seat and rail-center location. An 8’-3” long simply supported rectangular beam with uniformly distributed load was selected, and positive and negative loading situations were included. The prestressed tendons were included in the developed program, and transformed section properties were used. On the other hand, RISA model used concrete beam without reinforcement. Additionally, the behavior after elastic region of beam were not included in this comparison.

Figure 5.2 presents defined cross-section and calculated properties in the developed program, and Figure 5.3 shows the RISA model and defined properties.

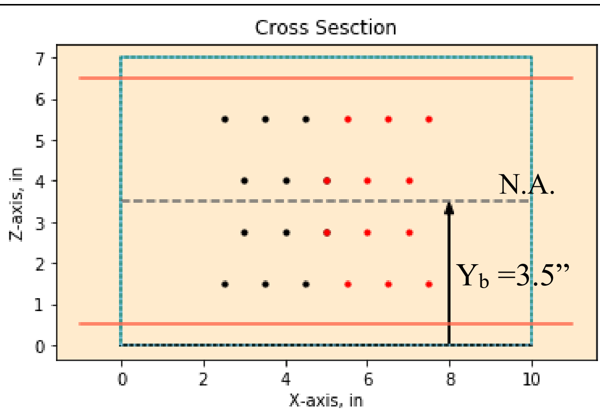

$L = 99$ in

Width $=10$ in

Height $= 7$ in

$f'_c = 6500$ psi

$E_c = 4595.5$ ksi

$I_{x\_tran} = 285.85$ in^4

$S_{t\_tran} = 81.6$ in^3

$S_{b\_tran} = 81.7$ in^3

$e = 0.0536$ in

$P = 118.05$ kips

$d_p = [5.5”, 4.25”, 3.0”, 1.5”]$

Figure 5.2 Cross-section and properties from Python code

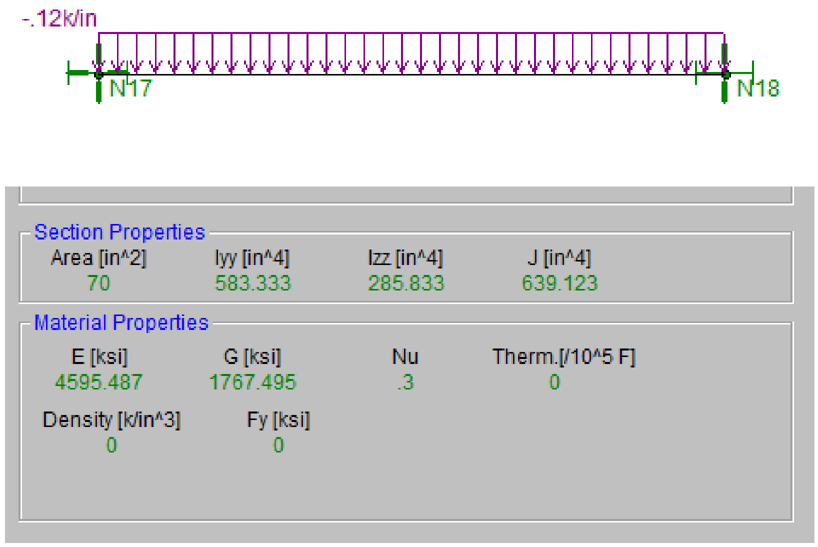

Figure 5.3 RISA model and properties

The 0.12 kips per inches uniform distributed load was applied, and the moment force at center is 147.05 kips-in which is below cracking moment force. The cracking moment and load could be found in Figure 5.4, and the moment-curvatures used to determine deflection in the code. The cracking load (w_{cr}) could be determined by solving Equation 5.1 for simply-supported beam.

$$M_{cr} = \mp S\left(f_r + \frac{P}{A} \pm \frac{Pe}{S}\right) = \frac{w_{cr}L^2}{4} - \frac{w_{cr}L^2}{8} \qquad \textbf{Equation 5.1}$$

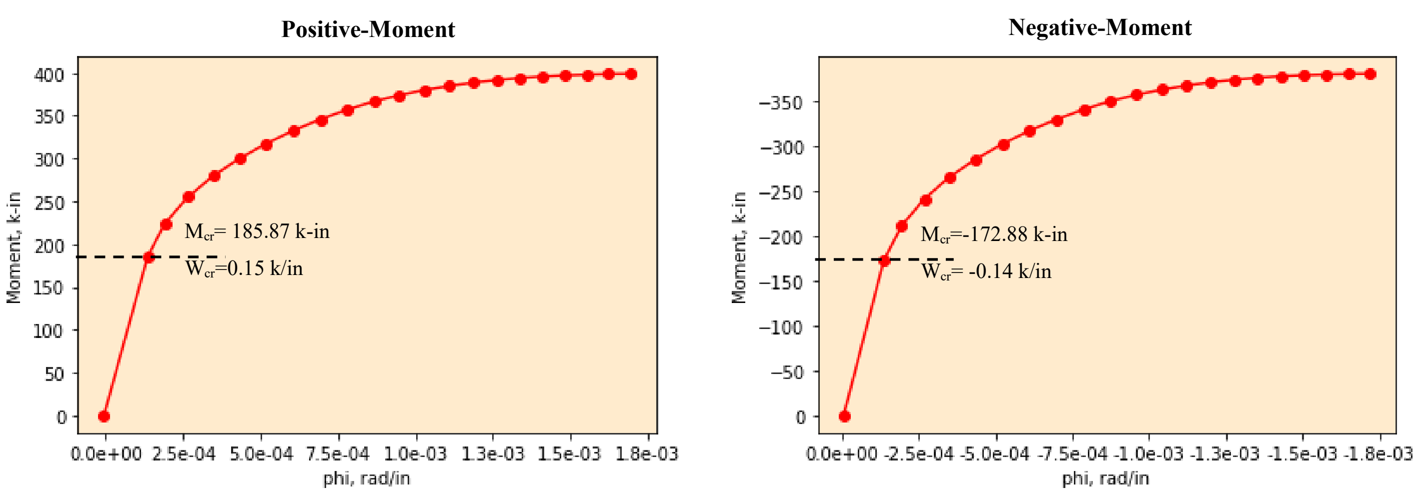

Figure 5.4 Moment-Curvatures of positive and negative loading

For analysis program, the beam is subjected to positive and negative moments, and vertical displacements were shown in Figure 5.5. Since the developed codes handled positive and negative bending individually, the purpose of generating two deflection curves was to verify outputs and eliminate error. The identical results were observed at rail-seat and rail-center. Figure 5.6 presents the deflection curve result from RISA. Furthermore, the calculated forces and deflections were shown in Table 5.2. The difference is 0.45% at rail-seat, and overall the code has good agreement with RISA in force and deflection.

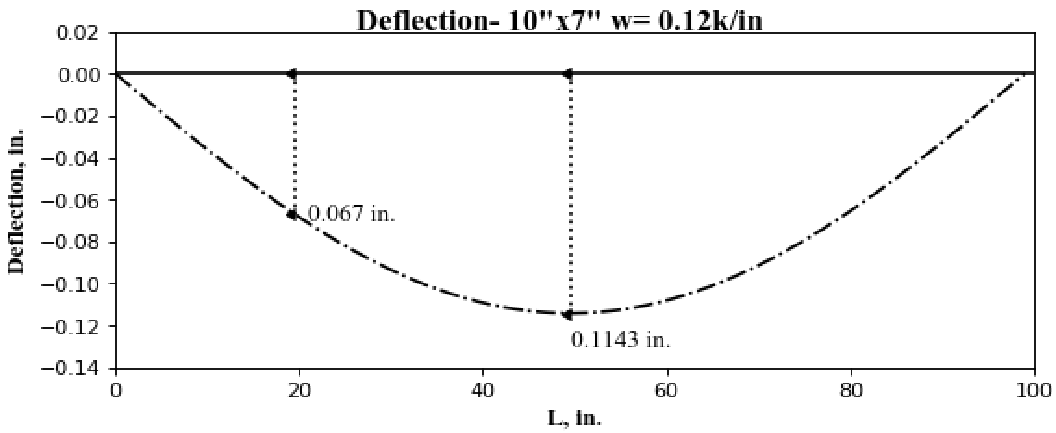

(a)

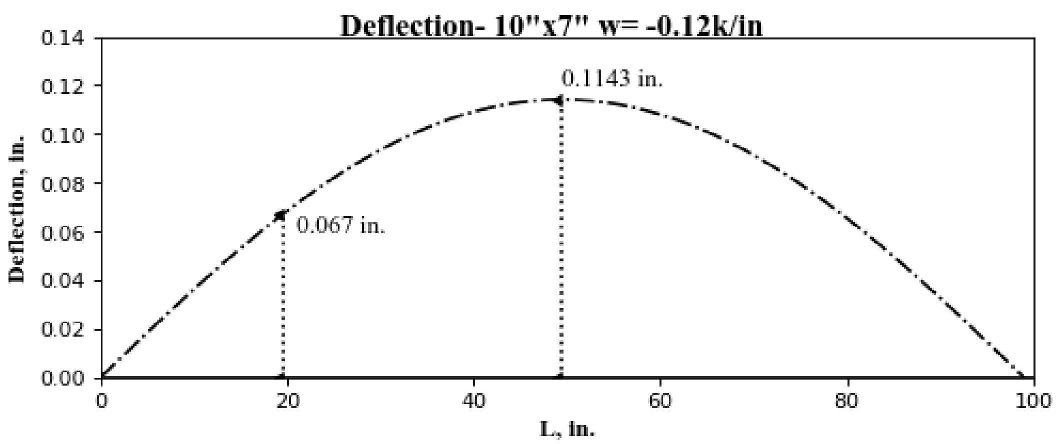

(b)

Figure 5.5 Deflection curve by code (a) positive bending (b) negative bending

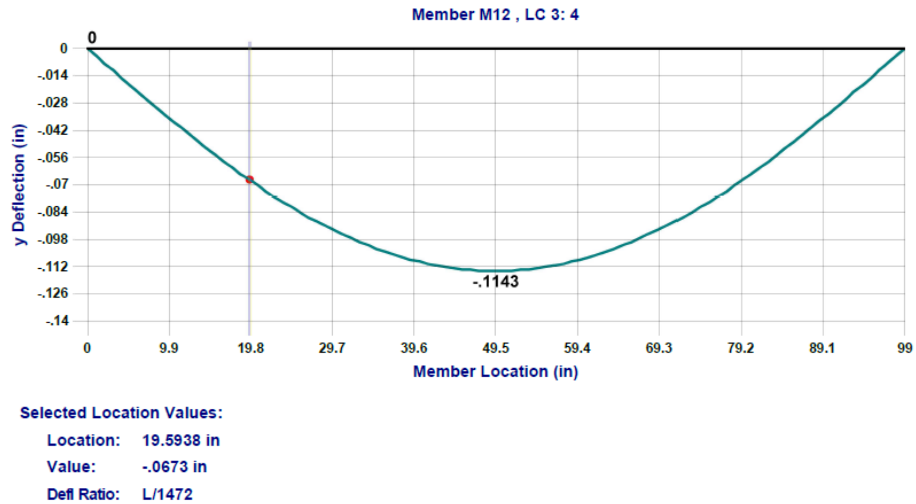

Figure 5.6 Deflection curve by RISA

Table 5.2 Code computation comparison

		Python			**RISA**			**Difference, %**		
	L, in	M, k-in	V, k	δ, in	M, k-in	V, k	δ, in	M	V	δ
Rail-Seat	19.5	93.02	3.6	-0.0670	93.01	3.6	-0.0673	0.01%	0.00%	0.45%
Rail-Center	49.5	147.02	0	-0.1143	147.02	0	-0.1143	0.00%	0.00%	0.00%

Case 3 - Code to Existing Tie Analysis Example

To prove the accuracy of moment-curvature, at concrete compressive stains of 0.003, the code computation results should match to the method of strain compatibility. This section intends to verify nominal flexural capacity, M_n, by comparing the tie design example by Russell H. Lutch from Michigan Technology University (Lutch, 2009). The comparison focused on critical sections (rail-seat and rail-center). The example followed 2003 AREMA, ACI 318-08 and 2004 PCI design specification for analysis and design, and also included detailed design properties. A CXT 505S-50 tie design from LBFoster was used and the cross-section at critical locations is shown in Figure 5.7.

In the example, the nominal positive and negative capacity were defined by the strain compatibility method. The design tie assumed 4.5 ksi concrete strength at transfer and 7 ksi 28-days design strength. A total of twenty 5.32-mm-diameter prestressed wires were used, and the wire positions were as listed in Table 5.3. The Python program utilized the same concrete properties but steel properties were not the same due to the unknown stress-strain model in the example. Thus, the stress in the prestress wire was calculated using Equation 4.7 with specific parameters (Q=0.016, K=1.037, and R=6.795) for WG wire which has the nearest f_{pu} to the example. The detailed inputs and calculated values are presented in Appendix C.

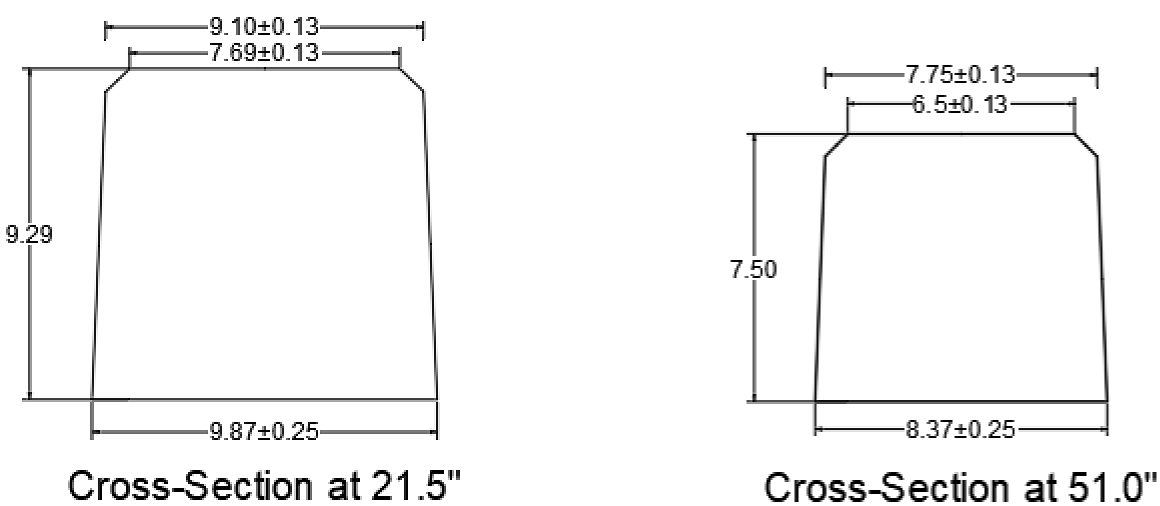

Figure 5.7 Michigan Tech design tie cross-section (Lutch, 2009)

Table 5.3 Michigan Tech prestressed tendon positions (Lutch, 2009)

Layer number	n	d_p_bot, in
1	2	1.3125
2	2	1.5625
3	2	2.5
4	2	2.75
5	2	3.6875
6	2	3.9375
7	2	5.125
8	2	5.375
9	2	6.3125
10	2	6.5625

d_p_bot: distance from bottom surface to layer of reinforcement, inch.
n: number of reinforcements.

Results

Code inputs followed the example as closely as possible, and CXT tie section properties incorporated the measurement data from (Bodapati, 2018). The properties and losses computation results can be found in Appendix C. As shown in Table C. 2, the cross-section property values at rail-center were up to 2.7% different and it results in a 12% variance in eccentricity. The nominal moment capacity results are listed in Table 5.4, and the M-C curve generated from the computational tool is presented in Figure 5.8. A good match was observed at rail-seat where the difference is within 0.5%. However, at rail-center subjected to negative bending, the computed result is 1.4% lower than Michigan Tech example. The close match in rail-seat result indicates minor affect by the difference in wire properties.

Table 5.4 Nominal capacity comparison (Lutch, 2009)

		Michigan Tech	Program	Difference, %
Mn, k-in	Rail-Seat / Positive Bending	610	612.94	0.49%
	Rail-Center / Negative Bending	385	379.62	1.40%

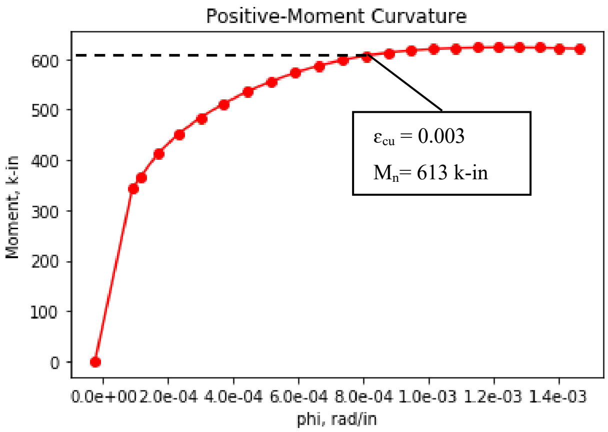

At Rail-seat

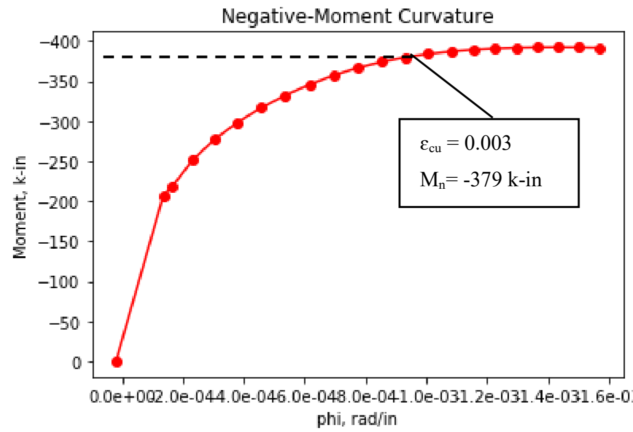

At Rail-center

Figure 5.8 M-C diagram at rail-seat and rail-center

Validation

This section is to validate the developed program by comparison with flexural testing results. The point of interest is the overall deflection at rail-center, and four-point loading configuration was modeled in the program. In order to have an accurate modeling result, the tie properties are key factors. The properties closely followed the original tie design input to the developed program. For the new design tie group, CXT tie, the properties of cross-section, wire type, and concrete were known. The experimental result of wire stress-strain relationship was used. For the existing tie group, the known properties were cross-section and concrete strength. This tie was cast with a steel bar on the bottom of tie to protect brass inserts which were previously used for laser speckle imaging reading. A groove was observed after the steel bar was removed, the groove area was slightly varied. An approximately 2”x 1” groove observed on the bottom of CXT-[WB] tie (Figure 5.9) on CXT-[WG] it was 1” x 1” except the center region.

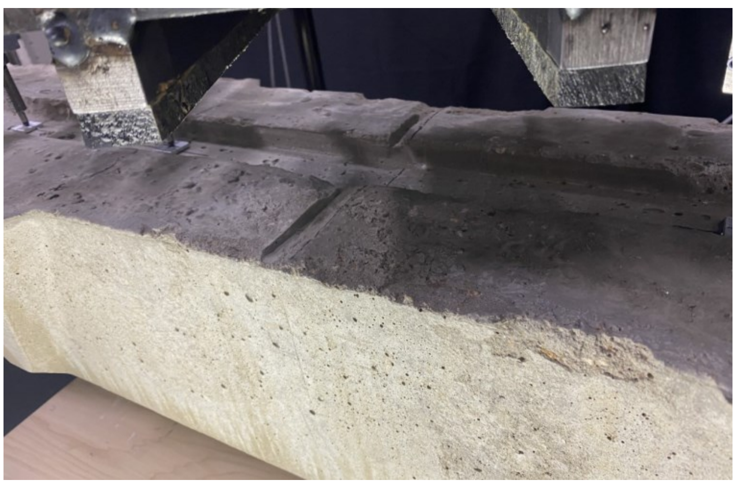

Figure 5.9 Bottom of CXT-[WB] tie

The actual reinforcement relationship was unknown for wire in Type-F tie, and the existing equations were used. The crucial factors were absent for type-C tie, consequently it was not included in code validation. The experimental result of Young’s modulus of elasticity presented a significant discrepancy from the equation by ACI (2019). Thus, iterative modeling was performed to estimate the proper Young’s modulus of elasticity.

The cross-section intended to be used in the analysis program was idealized as a trapezoid, shown in the Figure 5.10. In Figure 5.10 (a), the chamfer was ignored, and the top width was taken as the average values between chamfer. If the tie has scallops, the simplified shape was based on the top and bottom width as shown in Figure 5.10 (b). The idealized shape reduced analysis time but it may introduce error.

(a) (b)

Figure 5.10 Simplified cross-section

AREMA center negative moment was determined by using Equation 2.4 and Equation 2.5. The calculation used the recommended axle load (AL) 82 kips, and distribution factor (DF) of 0.505 used by assuming 24-inch tie spacing. Center reaction factor of 0.84 and 0.74 were used for CXT and Type-F tie respectively. Speed of 40 mph corresponded to 0.8 speed factor, and tonnage of 60 million gross tons corresponded to 1.0 tonnage factor. Table 5.5 lists the factored center negative moments, M_{c-}, and the corresponding load at rail-seat, P_{c-}.

Table 5.5 AREMA design center negative moment

Tie design	M_{c-}, k-in.	P_{c-}, kips
CXT	193.29	14.32
Type-F	204.34	15.14

The analysis results are presented in terms of load versus deflection, and can be found in Figure 5.11 to Figure 5.17. The comparison can be examined into two parts (elastic, and plastic region). The elastic zone is governed by Young's modulus of elasticity, and it shows good fit to the experimental results. The Young's modulus of elasticity is varied from 300 ksi to 1,000 ksi in CXT-[WB] tie (Table 5.6). Furthermore, the defined E_c are also compared by using ACI equation as shown in Table 5.6 and a maximum 29% of discrepancy detected in CXT tie group. For concrete strength below 8 ksi, Type-F tie in the testing group, an 8% variance is found.

Table 5.6 Comparison of Young’s modulus of elasticity and ACI equation

f'_c=10,740 psi	WB_Trial	WB1	WB2	ACI
Ec, ksi	4200	5200	4500	5910
Difference, %	29%	12%	24%	
f'_c =8,270 psi	WD	ACI		
Ec, ksi	4700	5190		
Difference, %	9.4%			
f'_c=10,670 psi	WG1	WG2	ACI	
Ec, ksi	4700	4500	5890	
Difference, %	20%	24%		
f'_c=7,090 psi	Type-F	ACI		
Ec, ksi	4430	4800		
Difference, %	7.7%			

At transition region, the good agreement is found in CXT-[WD] and CXT-[WB2], the difference is nearly 5%. A significant difference is detected in Type-F tie, and it results in lacking actual wire stress-strain relationship. The wire ultimate strength was around 255 ksi, it was determined by tensile test a wire extracted from the tie. The nearest model is PCI-250 strand equation. Subsequently, the analysis results did not have good match with experimental outcomes. For the CXT tie group, the estimated cracking forces are generally beyond the actual value, overestimate may be caused by insufficiently defined first cracking force.

As the force increases, the difference becomes increasingly variable. The governing factors are tendon stress-strain relationship and cross-section. The imprecise cross-section may consequently result in insufficient determination of concrete compressive force when computing M-C curve. Overall the analysis results are less conservative once cracking appears. The AREMA design bending moment occurs near the end of elastic range, excluding Type-F tie. The tie fails to meet AREMA requirement but these ties served on track over 2 decades without failure.

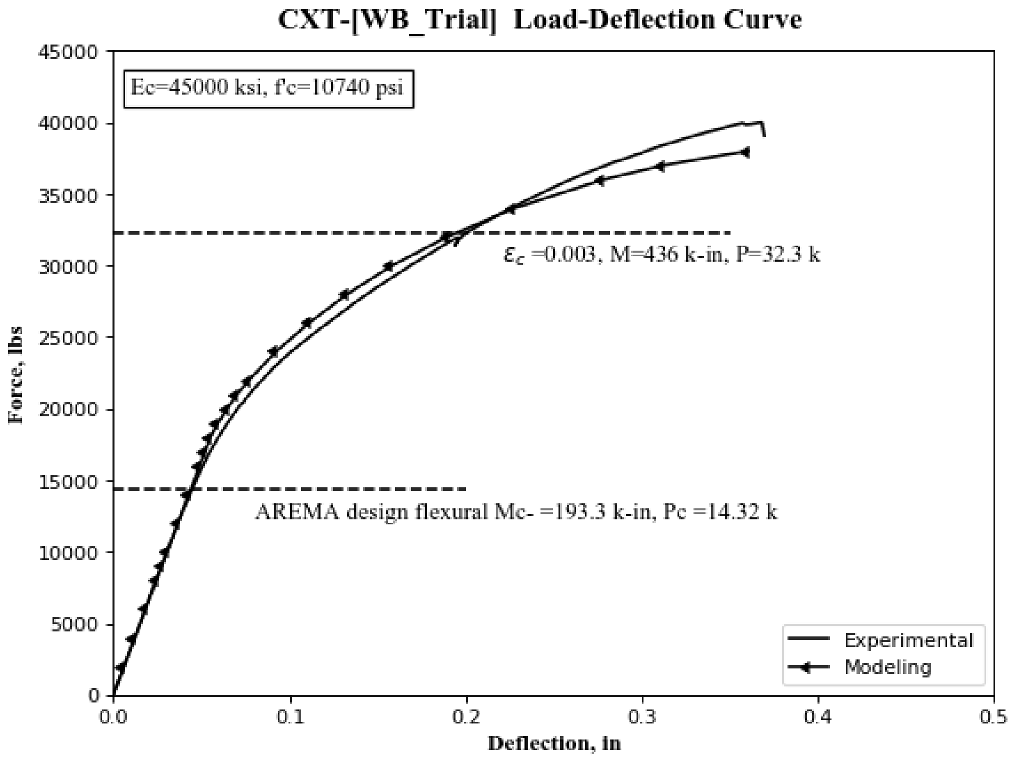

Figure 5.11 CXT-[WB_Trial] Load versus Deflection

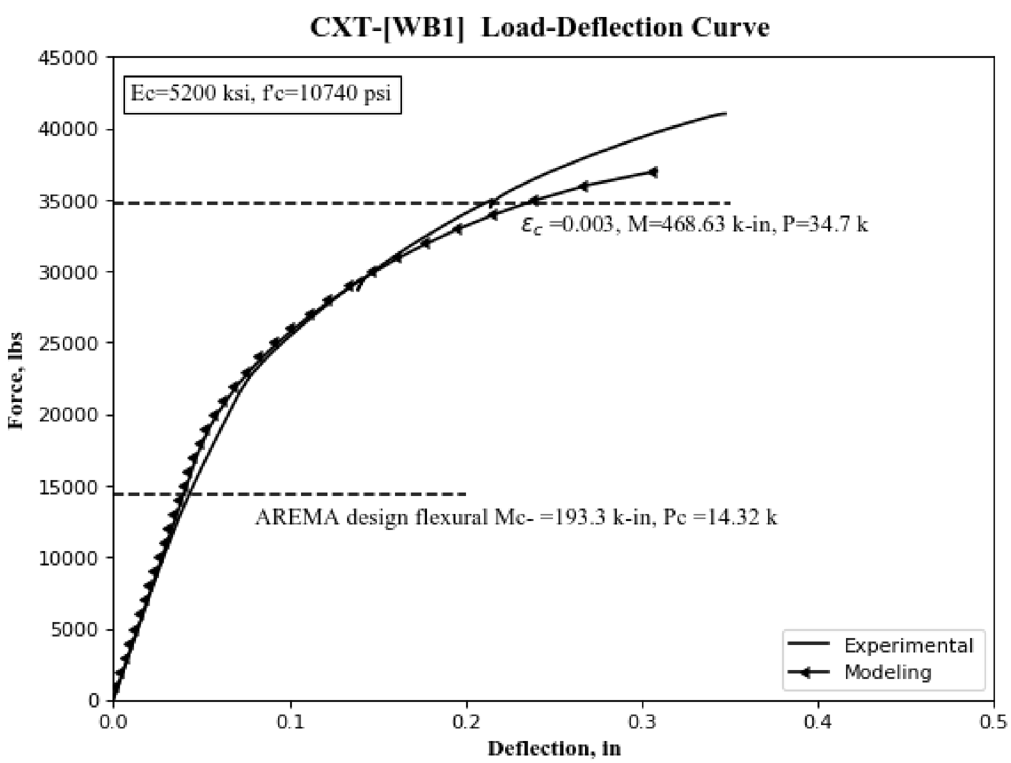

Figure 5.12 CXT-[WB1] Load versus Deflection

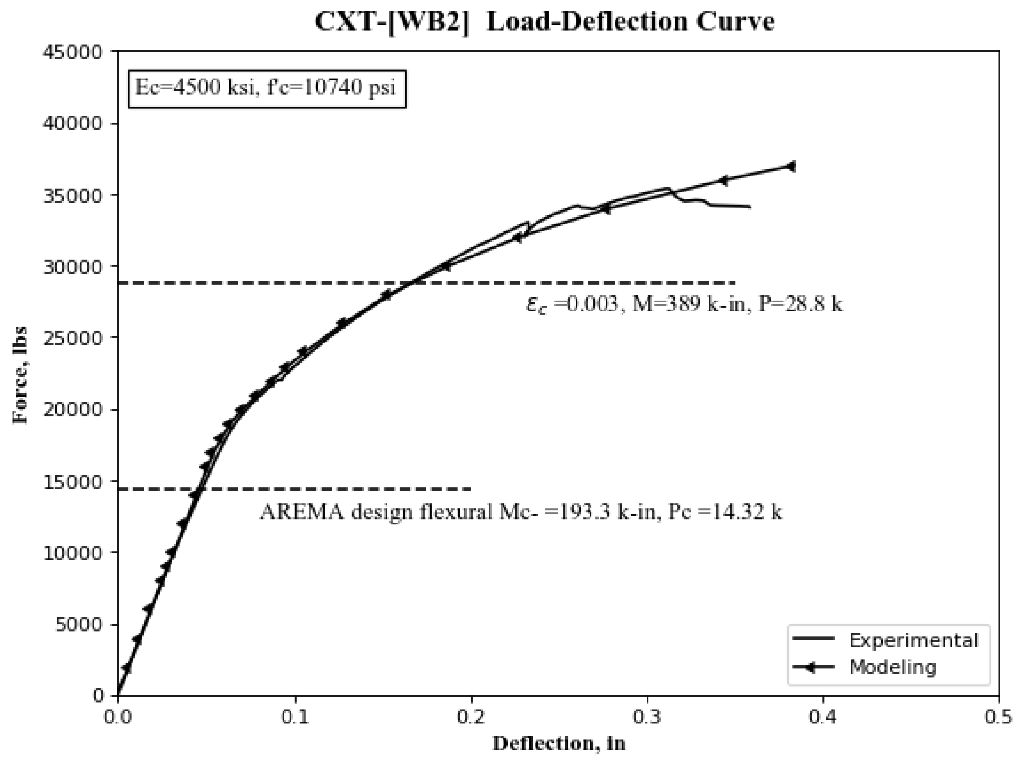

Figure 5.13 CXT-[WB2] Load versus Deflection

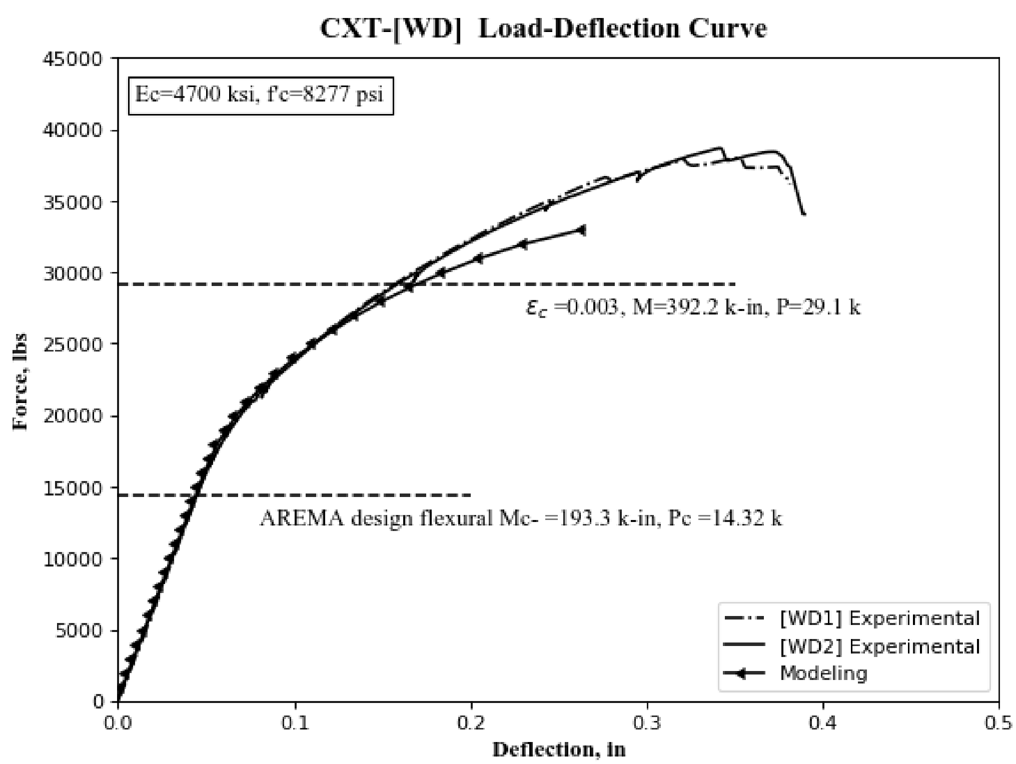

Figure 5.14 CXT-[WD] Load versus Deflection

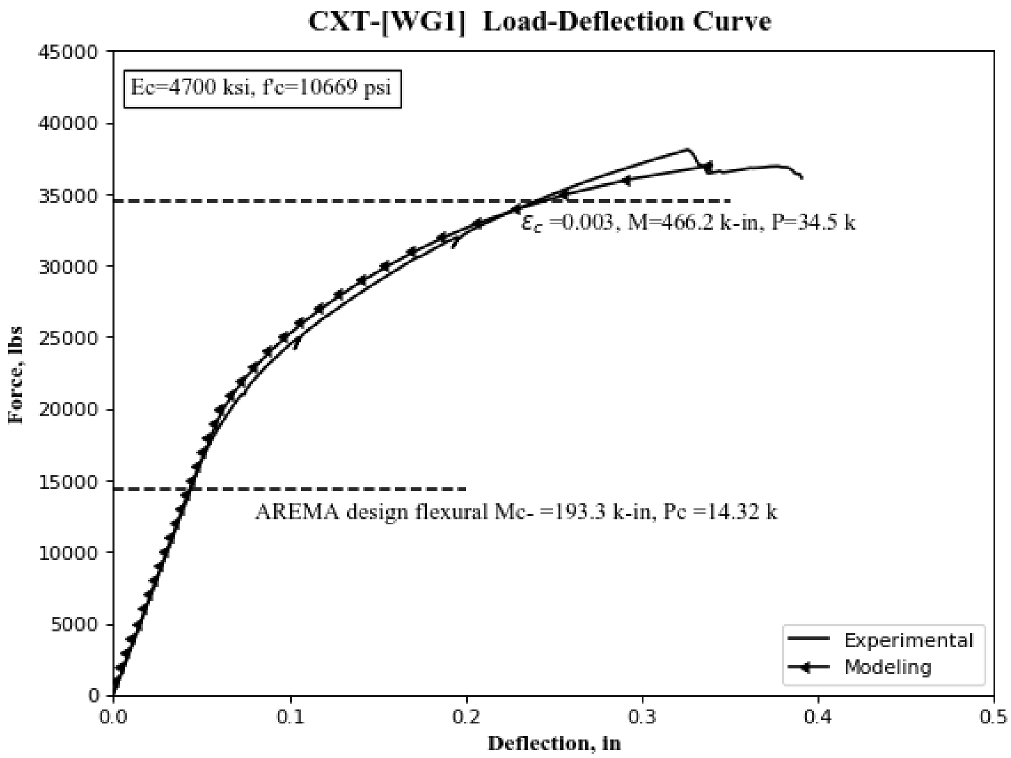

Figure 5.15 CXT-[WG1] Load versus Deflection

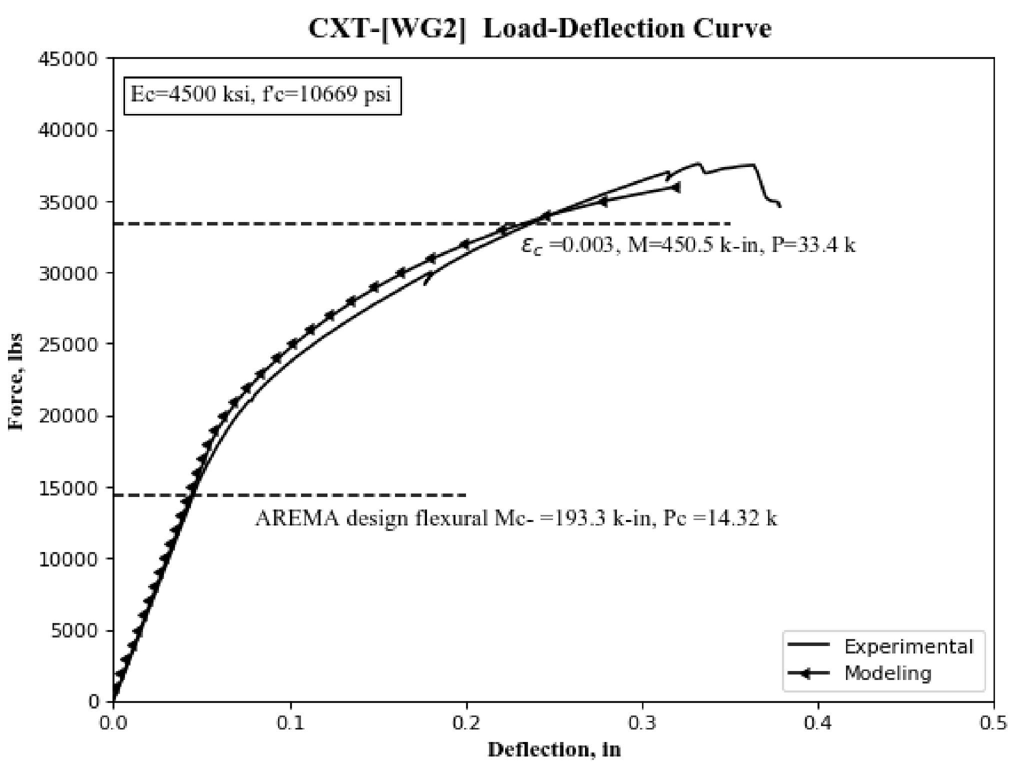

Figure 5.16 CXT-[WG2] Load versus Deflection

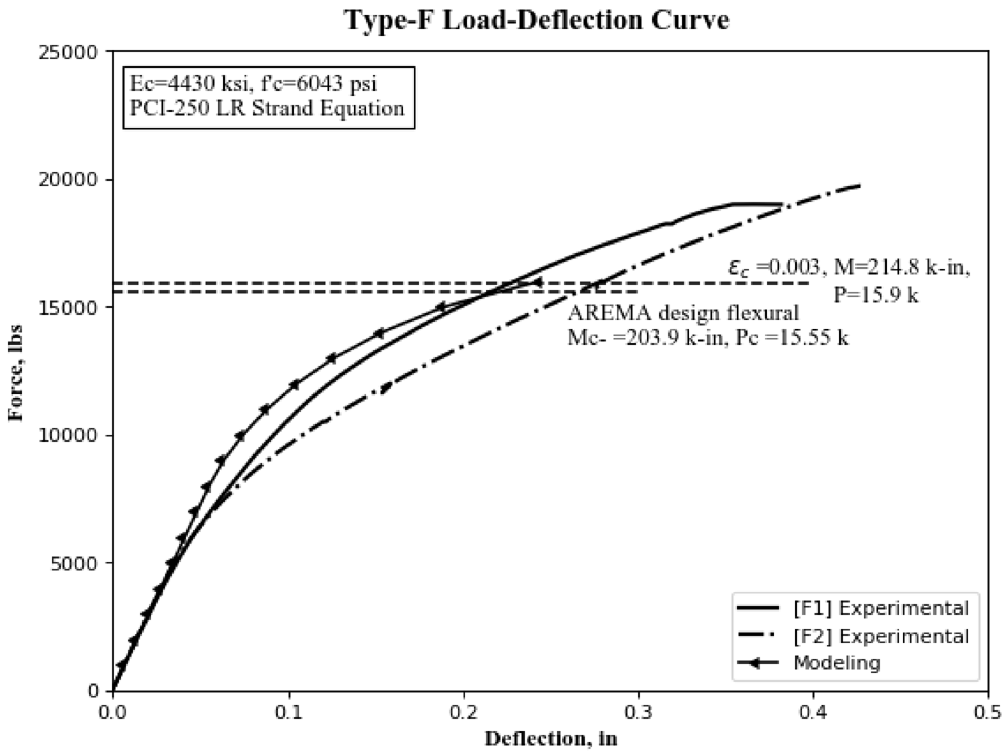

Figure 5.17 Type-F Load versus Deflection

Chapter 6 - Monte-Carlo Simulation

This chapter discusses the Monte-Carlo Simulation that was conducted to quantify correlation of key design parameters. The prediction results could be used to improve or check preliminary design decision and optimize design before conducting design approval experimental test. Furthermore, the probabilistic estimation could be used for risk analysis for existing in track crosstie performance. The quantities of interest (QOIs) are cracking force at rail-seat and rail-center. At each location, three QOIs were predicated by a moment-curvature based numerical program, including

1) initial cracking moment, M_{cr},
2) moment at cracking reach to outer layer of reinforcement, M_{1st},
3) ultimate moment, M_{ult}.

The simulation involves multiple tie geometry, wire positions, wire type and random variation of key tie deign parameters. Three types of tie were selected, including Type-F, Type-M and CXT 505S. These ties have variance in cross-section height at rail-center and rail-seat. All the cross-sections were modeled as trapezoidal except CXT 505S tie which cross-section properties were accurately determined by previous research at Kansas State University from (Bodapati, 2018). The tie section properties were varied in Monte-Carlo simulation consistent with random sampled wire type and wire location. The prestressing wire locations were varied up or down 1/8 inches vertically. Horizontal variation was not considered due to no significant affect in flexural behavior indicated. Table 6.1 lists the tie dimensions in height and width on the top and bottom surface which were generally not varied in the simulation. Table 6.2 lists nominal wire positions and amount of wires corresponding to specific tie type. The distance of wires, $d_{\#}$, were measured from bottom surface to center of the wire.

Table 6.1 Tie Geometry

Type of Tie	Length, in	Rail-Seat			Rail-Center		
		h, in	W_{Bot}, in	W_{Top}, in	h, in	W_{Bot}, in	W_{Top}, in
Type-F	99	7.9	10.1	8.5	5.6	10.1	8.5
Type-M	99	7.8	10.1	8.5	6.3	8.5	10.1
CXT-505S	102	9.3	11.3	7.0	7.5	8.4	7.0

Table 6.2 Tie Wire Positions

Tie Type	Row 1, wires	d_1, in	Row 2, wires	d_2, in	Row 3, wires	d_3, in	Row 4, wires	d_4, in	Total number of Wire
Type F	8	1.5	4	2.69	8	3.81	-	-	**20**
Type M	6	1.5	4	2.63	4	3.69	6	4.88	**20**
CXT 505S	4	2	5	3.25	5	4.5	4	5.75	**18**

All prestressing wire are 5.32mm diameter, and there were three type of wire chosen WA, WB and WH with wire indentation smooth and chevrons, respectively. Detailed wire properties are listed in Table 6.3. In Table 6.3, wire transfer length was computed with 4.5 ksi concrete release strength and specified ASTM A1096 values. The transfer length was determined through the transfer length prediction model developed by Bodapati (2018) as

$$L_{tr} = 3.42 - \frac{f'_{ci}}{300} - \frac{(A1096\,Value)}{\left[f'_{ci}\left(0.4 - \frac{f'_{ci}}{16{,}000} - 1250\right)\right]}, inch \qquad \textbf{Equation 6.1}$$

The wire pullout force, ASTM A1096 value, was adopted from the research, un-tensioned pullout tests, results from Arnold (2013).

Table 6.3 Prestressing Wire Properties

Wire Type	L_{tr} , in	ds, in	E, ksi	f_{pu}, kis	f_{py}, ksi
WA (Smooth)	16.33	0.21	29476.16	288.34	262.05
WB (Chevron)	11.6	0.205	29418.78	296.01	269.24
WH (Chevron)	7.5	0.302	30882.33	290.39	264.81

Another primary parameter of tie design is concrete properties. The 28 days concrete compressive, f'_{c},, was assumed from 6,000 psi to 10,000 psi with 5,00 psi increment. The concrete compressive strength at de-tension, f'_{ci}, and modulus of rupture, f_r, were calculated as (Mindess, Young, & Darwin, 2003),

$$f'_{ci} = (0.7 - 0.8)f'_c + (100 - 600), ksi \qquad \textbf{Equation 6.2}$$

$$f_r = (6 - 9){f'_c}^{(0.4-0.55)}, psi \qquad \textbf{Equation 6.3}$$

The prestressing jacking force, f_j, is a specific percent of wire ultimate strength which is defined as 70 percent to 80 percent with 5 percent increment. Consequently, the input parameters contained six normal distributed variables, three type of wires, vertically shifting in wire position. The input parameters were random sampled with specific tie type and wire position through a Python based preprocessing script. Then, individual input files were generated. Each input file was processed by the aforementioned moment-curvature scripts, and three quantity of interests were collected and tabulated at each location. The QOIs were acquired from generated moment verse rotation curve diagrams as shown in Figure 6.1. Figure 6.1 is a typical moment curvature for center-negative bending situation.

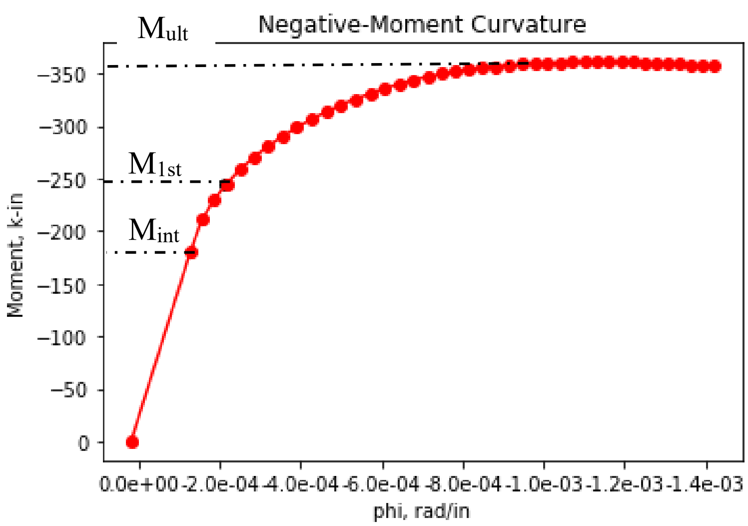

Figure 6.1 Typical moment-curvature curve

A parameter sweep application was developed to run modified moment-curvature based computational program. In order to minimize overall processing time, the numerical program was revised to capture QOIs. A python-based parameter sweep tool was developed by Grant Willford, a former computer science student at Kansas State University. The tool was developed to operate the parameter sweep on the supercomputer at Kansas State University, including function of

1. Generate individual input file
2. Setup virtual Python environment
3. Run and manage parameter sweep

4. Sorting outputs

The supercomputer Beocat was used to perform all the simulations which is the high-performance computing cluster at Kansas State University. Beocat is running by the computer science department at K-State, and it is available to any educational researcher in State of Kansas. Beocat can be accessed via secure shell on Linux and the basic Linux commands is provided in the Beocat website. The jobs were scheduled and submitted to slurm by developed sbatch submit scripts. The sbatch script was the sbatch command to define the resources to run the jobs. After all required scripts were created, each script was tested on local computer before upload to the supercomputer. Then a small batch of jobs were submitted on Beocat, and the results were verified.

To run a parameter sweep on Beocat, the first step was to upload all Python and sbatch files then setup virtual Python environment by executing “set_up_beocat.sh” file. The sbatch file (.sh file) could be executable by using “chmod” command. The virtual environment setup is required for the first-time access only. Next, the parameter sweep could be scheduled by either assigning the number of jobs or by performing the whole sweep. The limited amount of jobs could be scheduled at one time, the remaining jobs were recorded in “remaining_jobs” file. The next batch of jobs could be submitted once the current batch completed. Repeating same procedure until no jobs remained, and the parameter sweeps were accomplished. The result was tabulated in individual file and it could be organized through “sort output” function. The results could be filtered by user specified parameter name and value, and multiple sorting criteria could be applied. The detail parameter sweep operation procedure is shown in Figure 6.2.

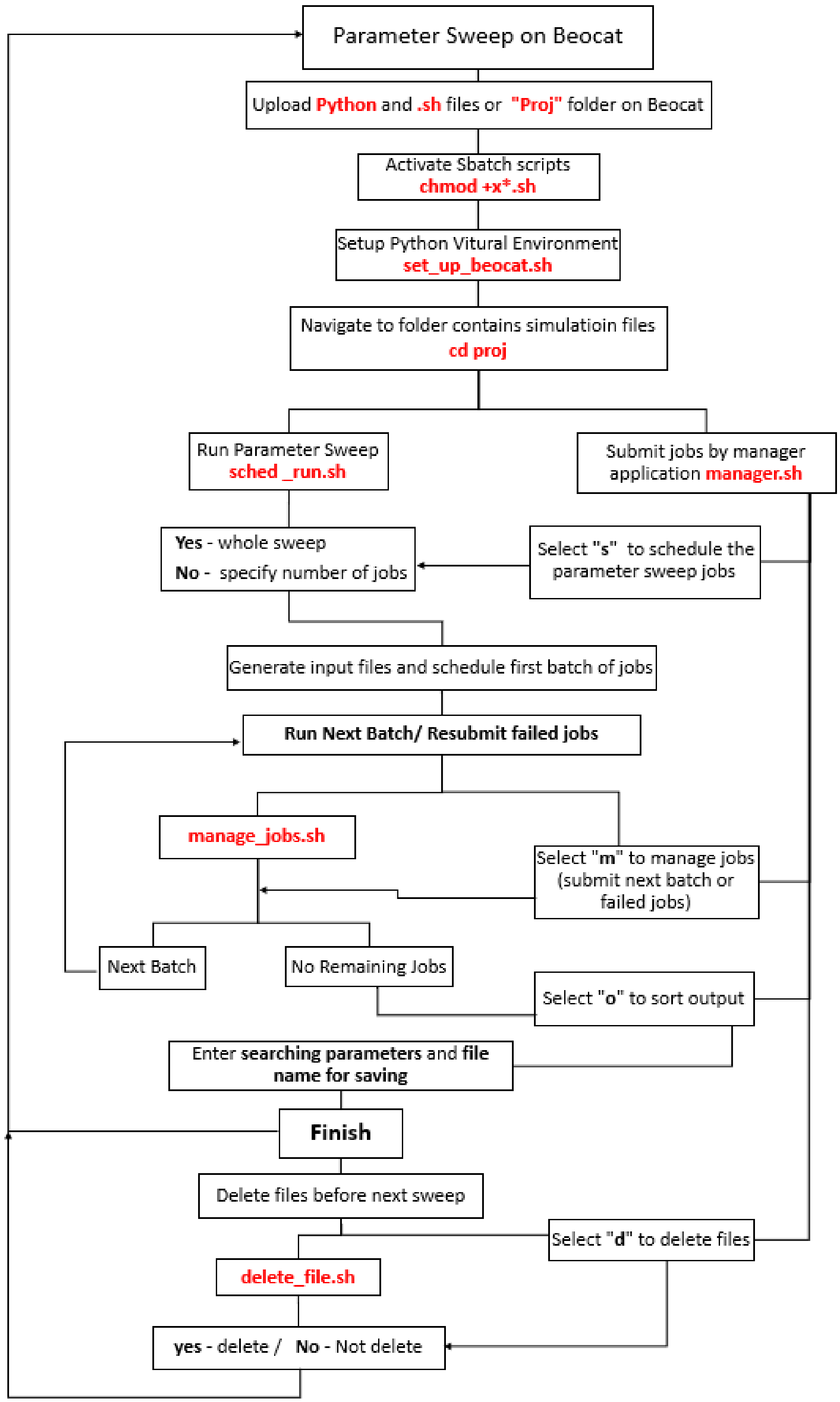

Figure 6.2 Parameter sweep on Beocat implementation flowchart

Results

Totally 1,928,934 realizations were simulated, and each QOI had 321,489 realizations. The simulation results were further utilized to create a cumulative distribution function (CDF) of the standard normal distribution for the QOIs. The CDF distribution is representing a fitted probability density function (PDF) distribution. The PDF were assumed normally distributed by fitting the frequency distribution of Monte-Carlo simulation results, and the PDF distribution could be computed by applying Equation 6.4. In Equation 6.4, parameters were calculated from particular QOI moment simulated by Monte-Carlo method where parameter μ is mean, σ is standard deviation, x is the generated bending moment. Furthermore, the corresponded CDF could be created after best fitted PDF was defined. The CDF could be calculated by using Equation 6.5. Figure 6.3 presents a histogram of simulation results, a fitted PDF distribution, and the corresponding CDF curve. At each location, individual best-fit PDF and the corresponding CDF is provided in Appendix D. In each figure the vertical axis is the probability density for PDF and cumulate probability for CDF, also the horizontal axis is the particular QOI of Monte-Carlo moment.

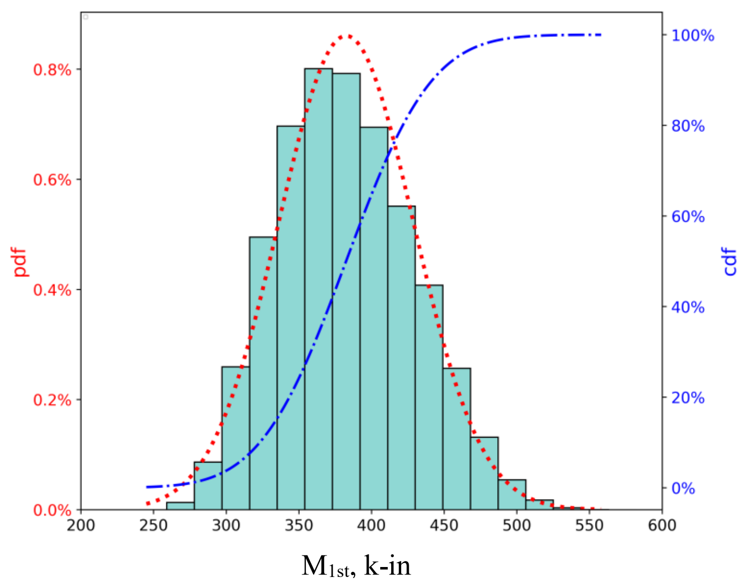

Figure 6.3 Typical fitted probability density function distribution (PDF) and cumulative distribution function (CDF) plot

$$PDF = f(x) = \frac{1}{\sigma\sqrt{2\pi}} e^{-\frac{1}{2}\left(\frac{x-\mu}{\sigma}\right)^2} \qquad \textbf{Equation 6.4}$$

$$\mathrm{CDF} = \Phi(x) = \int_{-\infty}^{x} f(x) d\mu \qquad \textbf{Equation 6.5}$$

The boundary of numerical value is listed in Table 6.4., including the value of minimum, maximum, and average from Monte-Carlo simulation results at each location. Three key scenarios were looked into (tie type, wire type and concrete compressive strength) in order to identify the correlation between key design parameters and cracking moment at QOIs. Subsequently, the results were further compared with recommended design load, and is discussed in the following section. Figure 6.4 - Figure 6.6 show the CDF for all QOIs at each location for all tie type, all wire type and concrete compressive strength, respectively. In each scenario, individual CDFs were represented in non-solid line and average result was presented in red solid line. The plotted values represent a cumulated probability estimation corresponding to predict cracking moment at specific QOI. Additionally, mean and standard deviation for each of simulated QOIs are presented in Table 6.5 through Table 6.7 for all tie type, all wire type and concrete compressive strength, respectively.

Table 6.4 Monte-Carlo simulated QOIs

	Rail-Seat			**Rail-Center**		
	Min.	Max.	Average	Min.	Max.	Average
M_{cr}, k-in	205.89	489.91	333.70	78.33	294.57	166.44
M_{1st}, k-in	259.07	545.32	382.34	130.18	324.46	210.57
M_{ult}, k-in	447.46	774.92	611.45	198.05	480.85	338.73

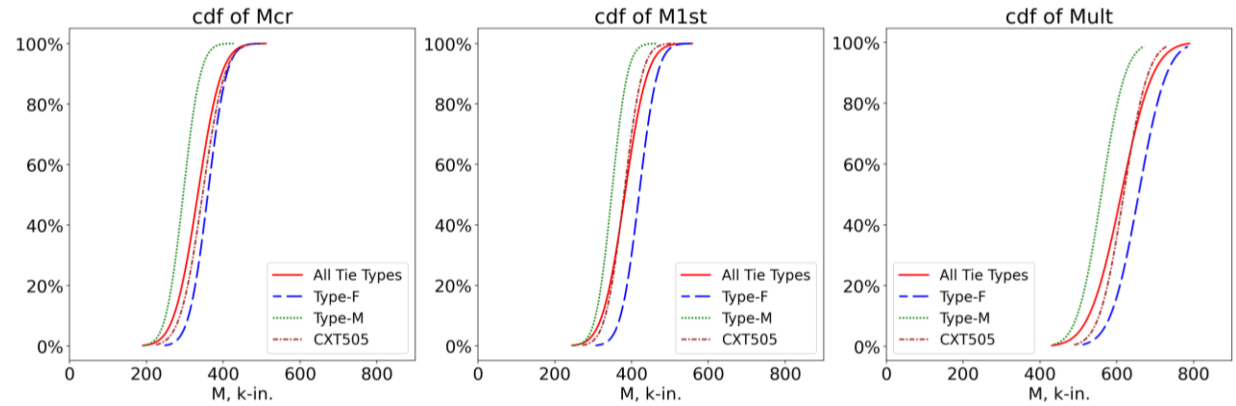

(a) Rail-seat positive moment

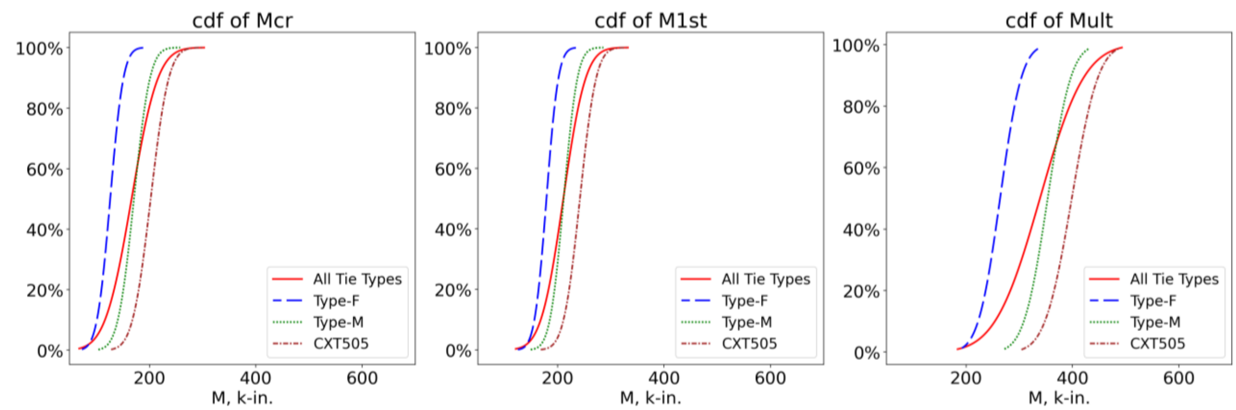

(b) Rail-center negative moment

Figure 6.4 CDF of Monte-Carlo simulated moment at first crack (M_{cr}), when crack reach to outer layer of reinforcement (M_{1st}), and at ultimate (M_{ult}) for all tie type.

Table 6.5 Monte Carlo Simulated QOIs presented in Tie type

		μ (k-in)			σ (k-in)		
		Type-F	**Type-M**	**CXT 505S**	**Type-F**	**Type-M**	**CXT 505S**
Rail-Seat	First Crack, M_{cr}	359.44	295.79	345.67	38.8	35.52	45.98
	Crack at Outer layer of Reinforcement, M_{1st}	419.27	347.65	379.92	37.54	32.53	37.78
	Ultimate, M_{ult}	656.68	559.45	617.99	57.96	49.45	50.53
Rail-Center	First Crack, M_{cr}	126.31	170.82	202.29	19.59	23.69	26.68
	Crack at Outer layer of Reinforcement, M_{1st}	178.82	211.15	241.72	17.7	20.39	24.02
	Ultimate, M_{ult}	264.19	353.45	398.66	32.14	35.18	39.48

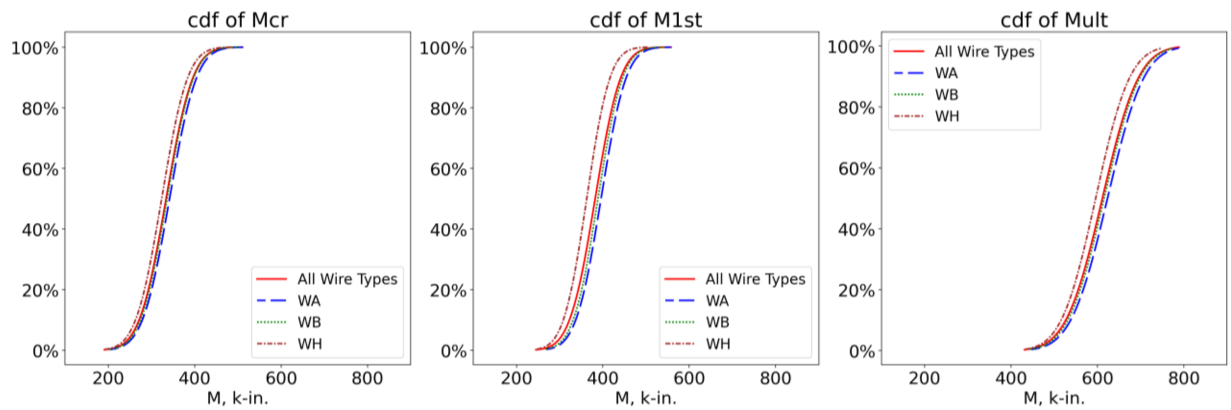

(a) Rail-seat positive moment

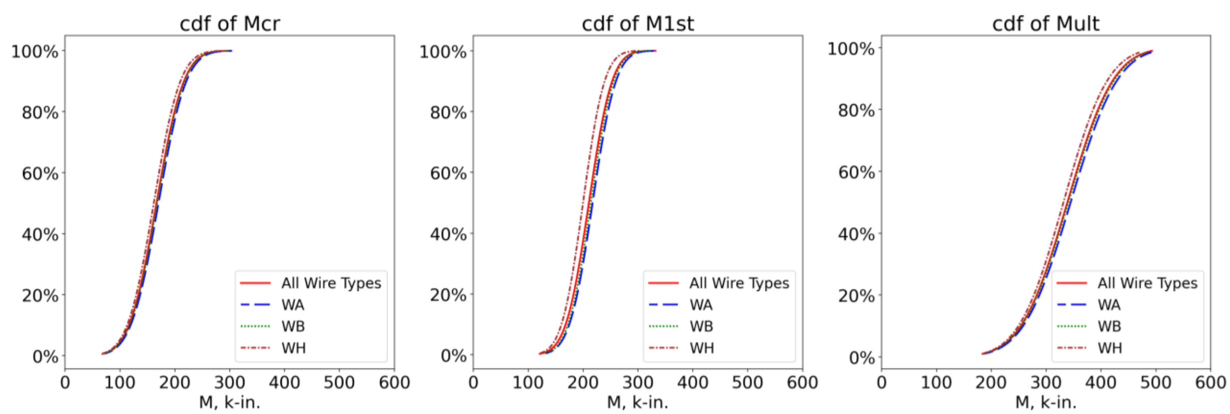

(b) Rail-center negative moment

Figure 6.5 CDF of Monte-Carlo simulated moment at first crack (M_{cr}), when crack reach to outer layer of reinforcement (M_{1st}), and at ultimate (M_{ult}) for all wire type

Table 6.6 Monte Carlo Simulated QOIs presented in wire type

		μ (k-in)			σ (k-in)		
		WA	**WB**	**WH**	**WA**	**WB**	**WH**
Rail-Seat	First Crack, $\mathbf{M_{cr}}$	341.60	336.14	323.08	49.07	48.16	47.1
	Crack at Outer layer of Reinforcement, $\mathbf{M_{1st}}$	395.56	388.68	362.7	45.66	44.54	42.15
	Ultimate, $\mathbf{M_{ult}}$	623.4	615.6	595.85	67.17	65.58	62.68
Rail-Center	First Crack, $\mathbf{M_{cr}}$	170.18	167.91	161.6	39.77	39.19	37.86
	Crack at Outer layer of Reinforcement, $\mathbf{M_{1st}}$	217.52	214.4	199.91	33.16	32.63	30.78
	Ultimate, $\mathbf{M_{ult}}$	343.92	340.32	331.86	67.62	66.84	63.48

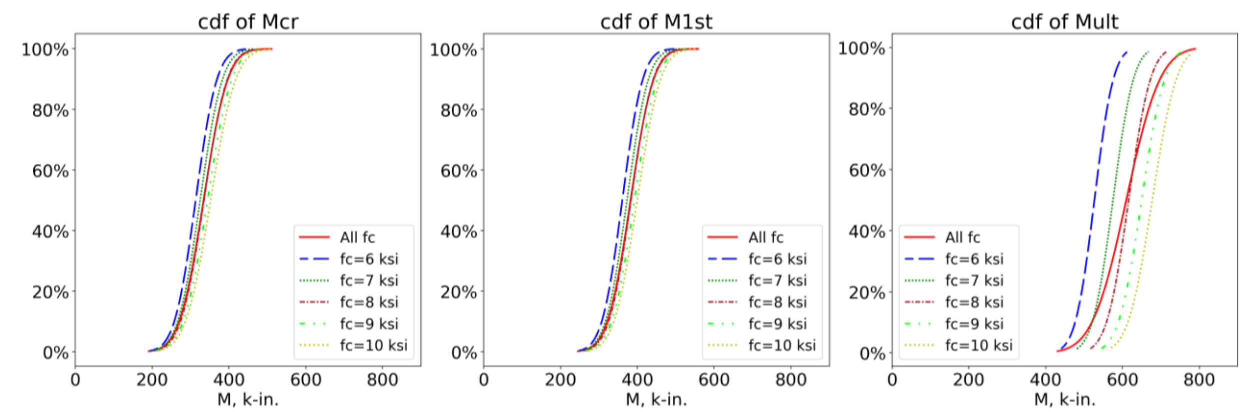

(a) Rail-seat positive moment

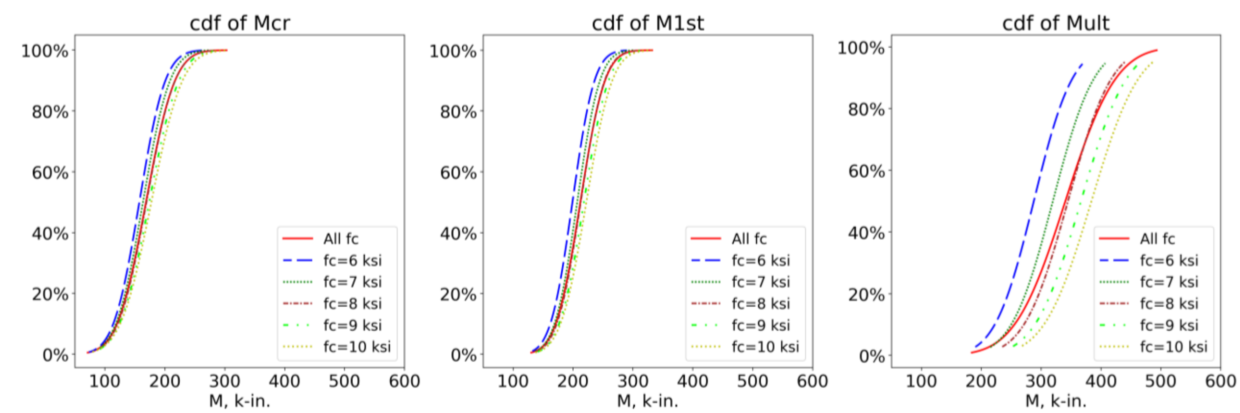

(b) Rail-center negative moment

Figure 6.6 CDF of Monte-Carlo simulated moment at first crack (M_{cr}), when crack reach to outer layer of reinforcement (M_{1st}), and at ultimate (M_{ult}) for concrete compressive strength (f'_c)

Table 6.7 Monte Carlo Simulated QOIs presented in concrete compressive strength (f'_c)

		Rail-Seat			**Rail-Center**		
	f'_c	First Crack, **M_{cr}**	Crack at Outer layer of Reinforcement, **M_{1st}**	Ultimate, **M_{ult}**	First Crack, **M_{cr}**	Crack at Outer layer of Reinforcement, **M_{1st}**	Ultimate, **M_{ult}**
μ (k-in)	6 ksi	313.03	360.72	526.45	157.11	199.10	287.67
	7 ksi	324.58	373.19	575.06	163.66	207.23	318.91
	8 ksi	335.04	383.2	616.01	168.94	213.15	344.91
	9 ksi	344.36	393.02	649.69	173.31	218.08	366.62
	10 ksi	352.22	400.18	677.02	177.33	221.91	383.95
σ (k-in)	6 ksi	43.63	42.1	39.12	34.05	28.78	50.71
	7 ksi	45.7	43.91	42.17	35.31	29.71	54.28
	8 ksi	47.51	45.09	45.28	37.24	30.88	57.62
	9 ksi	49.54	46.53	47.53	38.78	32.32	59.71
	10 ksi	50.76	47.63	49.81	40.45	33.81	62.63

Discussions

Overall good fitting was observed with 1,928,934 individual realizations. The Monte-Carlo realization results imply the sensitivity of moment at each QOI as changing in design parameters. The sensitivity of key design factors could be observed through the dispersion of central tendency. In the preliminary comparisons, three major scenarios were investigated. The CDFs of wire type (Figure 6.5) shows similar shape of S-curves with minor variance at 50th percentile in all QOIs. The insignificant variance of mean between wire types suggest it is inconsequential in optimizing tie design.

On the other hand, for CDFs of concrete compressive strength (Figure 6.6), overall CDF curves have similar length and shape which infer similar level of risk. The Moment at first crack and reach to 1st layer of reinforcement has up to 4% of central tendency apart. However, there are more clear discrepancy in central tendencies at ultimate moment stage in both locations where the mean of S-curves has maximum 11% divergency. Thus, this observation infers increasing design concrete compressive strength benefits in developing ultimate capacity. Moreover, CDFs of tie type (Figure 6.4) shows the CXT 5050S tie has lower cracking resistance than Type F tie at rail-seat even though it has a larger cross section. The opposite scenario was observed at rail-center, the CDF of CXT 5050S tie has higher cracking moment at each QOIs. Changes in wire eccentricity may explain this. The wire eccentricity is respected to the tie neutral axis, and the cross section tends to reduce in height from seat to center location. Three types of ties were selected in this practice had varied in height as shown in Figure 6.7.

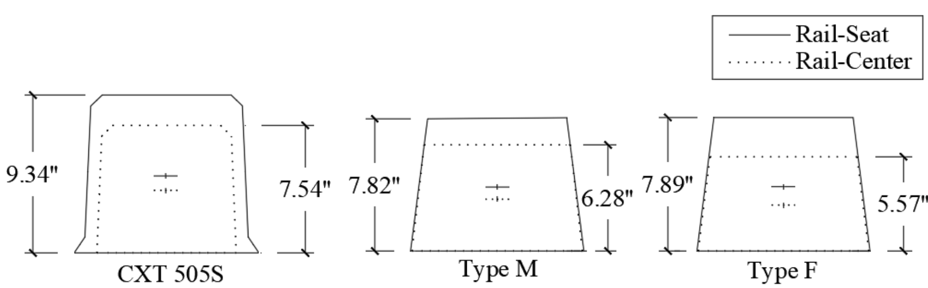

Figure 6.7 Graphical comparison of three tie geometry at rail-seat and rail-center

Consequently, the centroid is increased following with reducing in cross session height as shown in Figure 6.8. At rail-seat, Type F tie has larger eccentricity than CXT 505S tie, in contrast, the CXT 505S is the governing case at rail-center location. The CDF curves tend to deviate more at ultimate moment stage at both locations. At other stages, the central tendency has clearly differed in center region of the tie. CDF of tie geometry demonstrates more sensitive in all QOI moment at rail-center than rail-seat. Consequently, the CDFs of the tie type and concrete compressive strength shows more directly the influence of structural crack resistance at each QOIs.

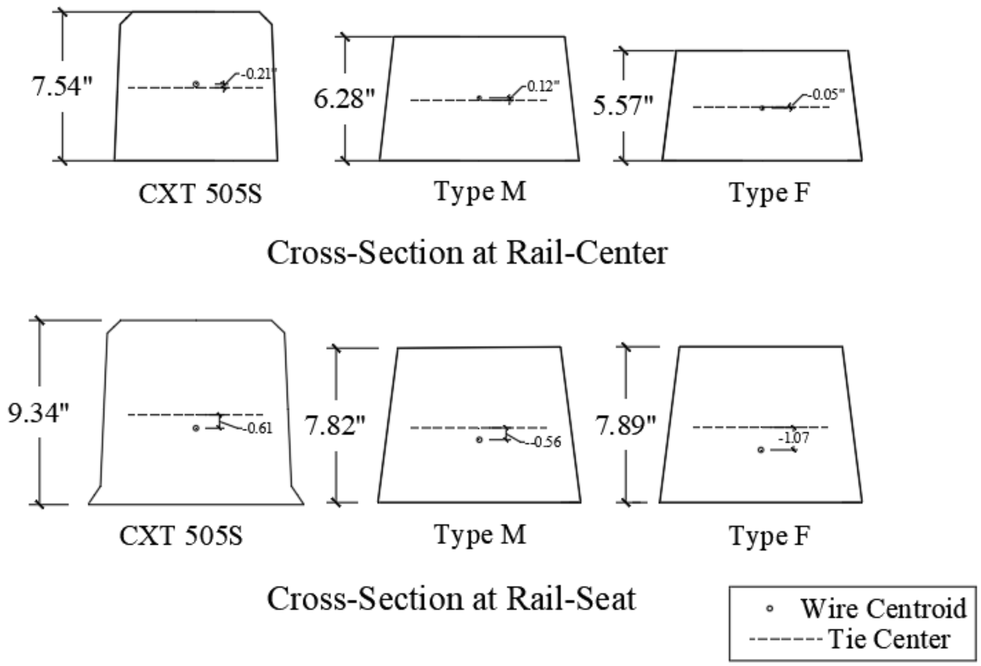

Figure 6.8 Wire eccentricity at rail-seat and rail-center

Wire location is commonly shifted while casting the tie, and 1/8 inches varied vertically was considered. Also, the structural capacity shows sensitive to concrete compressive strength based on the simulation results. Thus, the correlation of moment capacity with varying eccentricity was conducted at both locations, the quantity of interest in this comparison was moment at crack reaches to outer layer of reinforcement and ultimate moment. The comparisons are presented in Figure 6.9 - Figure 6.10 and Figure 6.11 - Figure 6.12 for rail-center and rail-seat, respectively. Table D. 1 lists the average estimated tie moment capacity with eccentricity variance where "e" is original eccentricity of wire, "e+" is eccentricity increased 1/8", and "e-" is 1/8" lower. Overall all, at rail-center, the flexural resistance is deviated from 4% to 6.6%, and the difference is compared moment force with wire eccentricity without vertical shifting. Center negative bending moment has up to 4.6%, 6.5%, and 5% drop when wire eccentricity reduced, corresponding to CXT 505S, Type-F, and Type-M. Contradictory, a growth in moment force was detected in increasing wire eccentricity, the difference is within 5.4%, 6.6%, and 5.1% for CXT 505S, Type-F and Type-M tie. Increment in design concrete strength with varying wire eccentricity has more benefit in determining ultimate bending capacity compared to moment at crack reaches to outermost reinforcement.

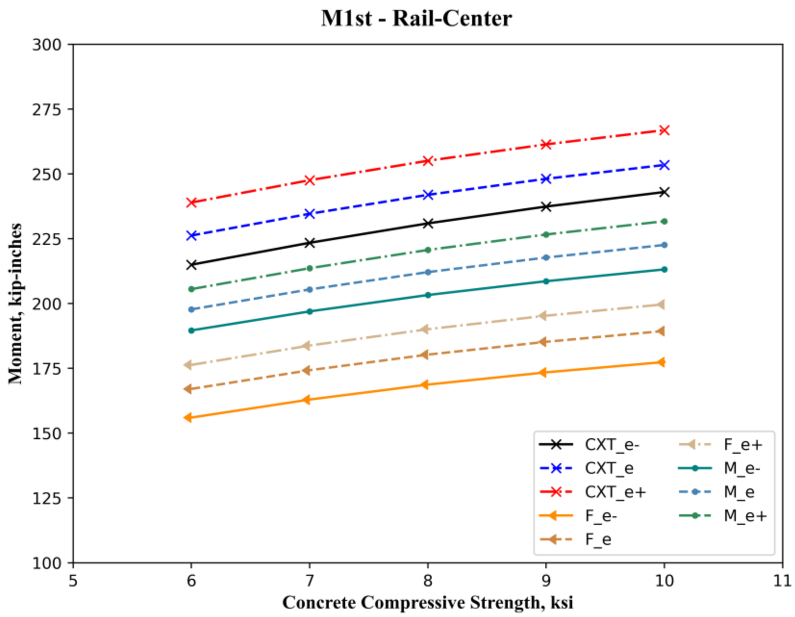

Figure 6.9 Graphical comparison of eccentricity variance in Monte-Carlo simulated moment at crack reaches to first level of reinforcement at rail-center

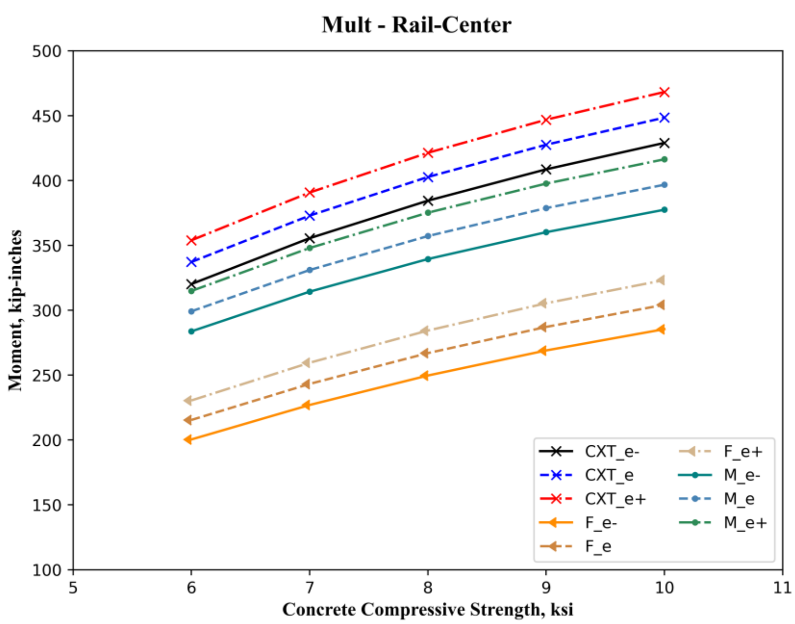

Figure 6.10 Graphical comparison of eccentricity variance in Monte-Carlo simulated ultimate moment at rail-center

At rail-seat, average difference of moment at M_{1st} (moment at which the crack reach to first level reinforcement) and M_{ult} (ultimate moment) is within 4% except M_{1st} for CXT 505S tie. Overall a 3% improvement of M_{1st} is observed for wire location shift below, however less than 1% reduction in flexural capacity while wire location move upward.

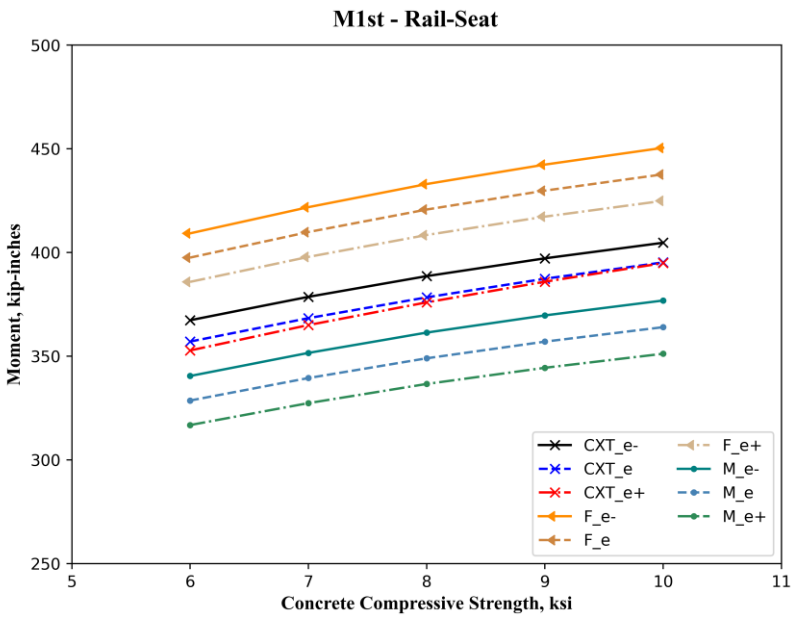

Figure 6.11 Graphical comparison of eccentricity variance in Monte-Carlo simulated moment at crack reaches to first level of reinforcement at rail-seat

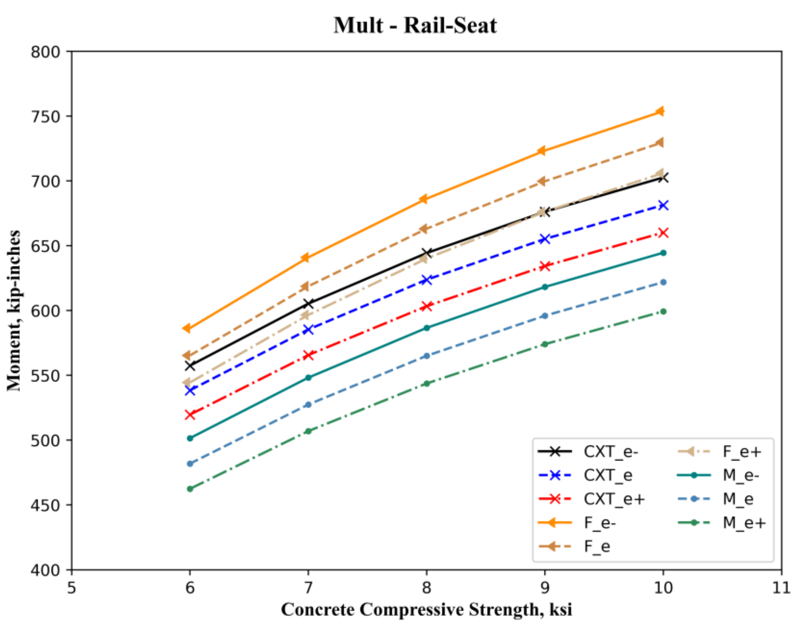

Figure 6.12 Graphical comparison of eccentricity variance in Monte-Carlo simulated ultimate moment at rail-seat

AREAM Specification Comparison

As mentioned in previous chapter, the current tie design specification recommends that ties show resistance to the design load without crack after minimum 3 minutes hold (AREMA, 2020). Besides, the tie flexural capacity is defined as the tensile crack reaching first level of reinforcement. The concrete monoblock tie design strength requirement was calculated based on the assumed and recommended values. The rail-seat positive and rail-center negative unfactored moment were computed by using Equation 2.2 and Equation 2.3 with the recommended axle load 82 kips, and 24 inches tie center-to-center spacing. The center reaction factor (α) was recommended zero at rail-seat, the value of 0.8 and 0.74 were used at rail-center for tie length 102 inches and 99 inches, respectively. The factored center negative moment was 193.29 kips-in. and 204.32 kips-in. for CXT 505S and Type F/M tie, correspondingly. The factored rail seat positive moment was 213.43 kips-in., 193.05 kips-in., and 191.00 kips-in. for CXT 505S, Type M, and Type F tie, respectively.

The CDFs of the tie type and concrete compressive strength were further compared with AREMA design strength independently, and for CXT 505S and Type F tie, the comparison was also made with visually observed first cracking force experimentally.

At rail-seat, the design positive strength recommendation was satisfied for all tie types as shown in Figure 6.16. In Figure 6.16, the design force falls before and at end of left tail which imply the section remains uncracked. The tie at rail-seat tends to have a lager cross-section, and it gives more material and increase in centroid which improves the positive moment resistance. Thus, the design recommended force is most likely to be fulfilled, and at rail-seat, the comparison of design strength and CDFs of concrete compressive strength with individual tie can be found in Figure D. 43 - Figure D. 51.

At rail-center, the design center negative bending moment fall within the first crack moment distribution and distribution of moment at crack reach to outer layer of reinforcement which was observed through Figure 6.17 to Figure 6.20. Based on the Figure 6.17, the probability of design load occurs when crack reach to first layer of reinforcement is approximately 92%, 38%, and 2% corresponding to Type-F, Type-M, and CXT 505S tie. The result indicates, for tie length of 99 inches, the 13% of increase in cross-section height could increase roughly 50% of change passing the design load at crack reach to outer layer of reinforcement stage. Of note the Type-F tie has nearly 5% of probability that the design load reaches the structural ultimate capacity. Furthermore, the CDF of CXT 505S tie imply approximately 64% of probability the section remains uncracked.

The Figure 6.18 to Figure 6.20 presents CDF of increment concrete compressive strength at rail-center for Type-F, Type-M, and CXT 505S tie respectively. For Type-F tie, majority of design load fall into the distribution corresponding to structural cracking reaching the outer layer of reinforcement (Figure 6.18), and small amount fall into ultimate moment distribution while 6 ksi concrete compressive strength chosen. The distribution results indicate the probability of crack remaining at 1st layer of reinforcement is approximately 3% and 20% corresponding to 7ksi and 10 ksi concrete compressive strength. There are 15% of probability the tie may not able to resist design load while 6ksi concrete compressive strength selected.

For Type-M tie, the result indicates the design load falls within left tail of first moment distribution and positive side of reaching to 1st layer of reinforcement moment distribution (Figure 6.19). An approximately 20% of probability the type-M tie remaining uncracked while 10 ksi concrete designed. Probability of remaining uncracked is decreasing while the concrete strength reducing. The probability of crack reaching to outermost layer of reinforcement is around 35% to 80% corresponding to 6ksi and 10 ksi concrete compressive strength. A roughly 10% decreasing in probability of meeting design criteria was observed following with 1 ksi increment in concrete compressive strength.

For CXT 505S tie, the results imply approximately 44 % of ties remain uncracked for f'c=6ksi and 21% of 10 ksi concrete compressive strength could increase approximately 35% of probability (Figure 6.20). There are 5% of probability that the crack reach to first layer of reinforcement when 6 ksi concrete compressive strength was selected.

Crack Detection

A 5-power magnifying is recommended to locate crack during the experiment testing (AREMA, 2020). The load of first crack occurred was identified for CXT 505S and Type-F tie, and the average cracking force was 285 k-in and 145 k-in respectively. The initial crack load was 262 k-in observed from flexural test with DIC system, the specimen had same tie type but different wire type. The DIC observed region did not include chamfer which the first crack load should be less than determined crack load. Thus, the purpose of comparison is to point out the timing of determining initial crack occurred. The CDFs of first crack moment was compared with experimental force shown in Figure 6.18 and Figure 6.20 corresponding to Type-F and CXT

505S tie. For Type-F tie, the experimental cracking loads fall in between negative of first crack moment distribution and left tail of distribution corresponding to cracking penetrating to outer layer of reinforcement. The probability of structural cracking is approximately 95%. Contrastively, the cracking load fall in right tail of moment while crack at first level of reinforcement distribution for CXT 505S which infer approximately 90% of probability structural cracked beyond first level of reinforcement. Based on observation, it implies the first crack occurred earlier than the determined cracking load which following the current design specification.

Ultimate Moment, M_u

The concrete compressive strength was increased from 6 ksi to 10 ksi, and the difference between each 1 ksi increment was from 11% to 4% in ultimate moment as shown in Figure 6.13.

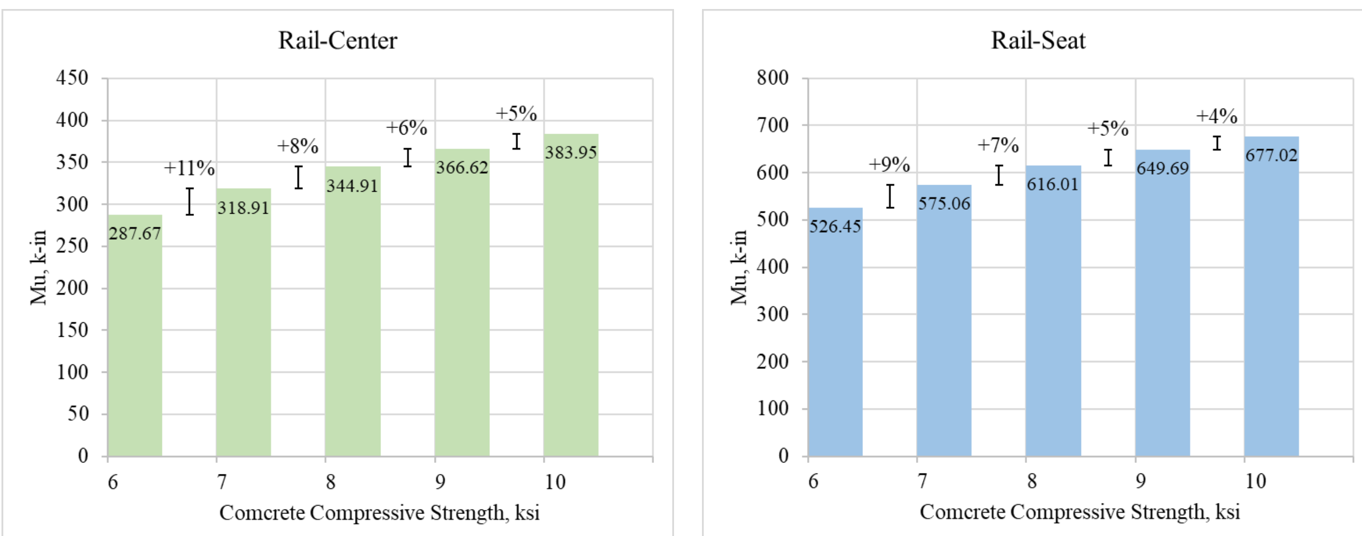

Figure 6.13 Average ultimate moment strength with concrete compressive strength

On the other hand, the averaged 30% of increment in the ultimate moment strength was observed, when concrete compressive strength increased from 6 ksi to 10 ksi. In prestressed concrete design, approximately 6% of raise in ultimate moment is expected which is relatively small comparing to the finding. This phenomenon may be explained by the following:

1. Compact shallow cross-section
2. Prestressing reinforcement location
3. Compressive response of prestressing

4. Compression failure

The tie is designed to resist positive and negative bending at rail-seat and rail-center. The typical tie design has non-uniform compacted cross-section and straight prestressing reinforcement. To meet flexure strength requirement at both locations simultaneously, the amount of wire and wire location are the one of the parameters to adjust in order to reach design load requirement. The combination of prestressing and compact cross-section, resulting in the tie failing in compression. The flexure compression is failed in crushing concrete at compression surface and tendons are yielded. The prestressing is commonly located at the bottom section of the beam known as tension zone, however the tie has prestressing in compression and tension zone. In the compression zone, the stress in prestressing is reduced and the prestressing reinforcement did not yield. The prestressing in compression can lead to reduced capacity and increased deformation. The strain in concrete compression reduces total strain in the prestressing, resulting in the prestressing reinforcement response in the elastic region.

To visualize the noticeable increment of stress in prestressing, f_{ps}, a comparison was made. A tie cross-section 7” x 7.54” and hypothetical cross-section 7” x 24” with four layers and single layer of prestressing reinforcement respectively. The total area of prestressing reinforcement 0.62 in^2 was assumed in both hypothetical and tie cross-section. The stress-strain relationship for a grade 280 ksi prestressing wire with yield stress 255.56 ksi was assumed which can be computed by using Equation 4.7. The concrete compressive strength was 6 ksi and 10 ksi, and other design parameters were identical. The computed f_{ps} for each example was presented in Figure 6.14 and Figure 6.15.

In Figure 6.14, a section deep 24 inches, the total stain in prestressing steel is correspond to stress 270 ksi for f’c = 6 ksi and 271 ksi for f’c=10 ksi where the steels were yielded. An approximately 6% difference in ultimate moment was observed. While the cross-section depth reduced for 24” to 7.53”, and the reinforcements were distributed into four layers. When the concrete compressive strength was going from 6 ksi to 10 ksi, the ultimate moment was increased from 271 k-in to 369 k-in which was a roughly 37% difference. For lower design concrete strength, upper two layers of prestressing wires are in the compression zone, and the stress in prestressing is 142 ksi and 170 ksi with correspond strain 0.0051 and 0.0061 as shown in Figure 6.15(a). For 10 ksi concrete compressive strength, the top layer of reinforcement is still in compression zone as shown in Figure 4.15(b). Additionally, an approximately 10% increasing was observed in f_{ps}, and the difference in strain is 0.0005. The prestressing in tension zone, the overall increasing in f_{ps} is between 13% to 15% approximately. Overall the prestressing steels have elastic behavior. In the elastic region, the small changing in strain results in large differences in stress. Consequently, when the concrete compressive strength increased, the ultimate capacity of the tie has noticeable increment compared to typical prestressing concrete beams.

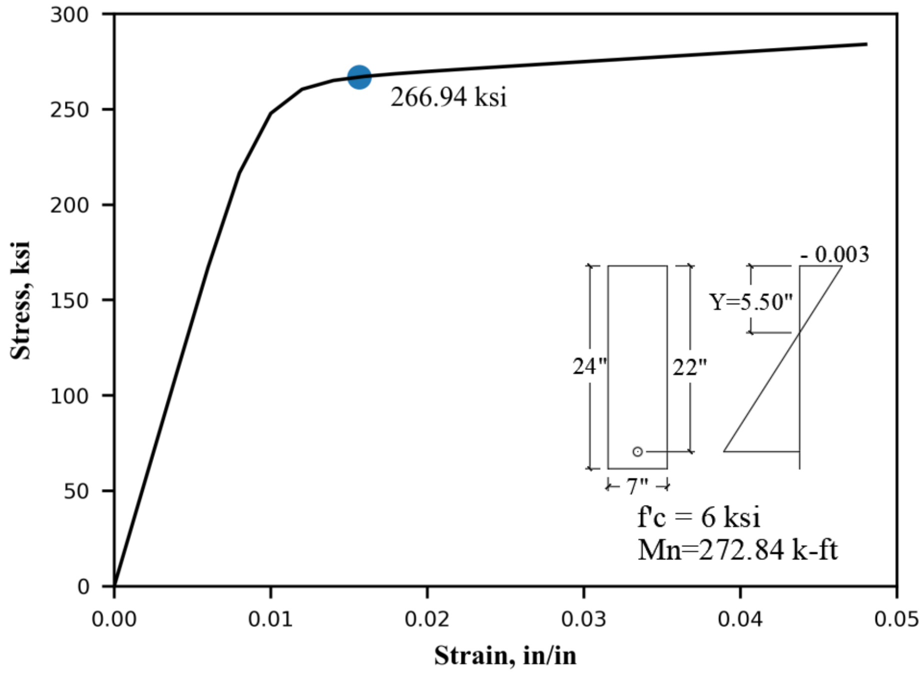

(a) Conccrete compressive strength 6 ksi

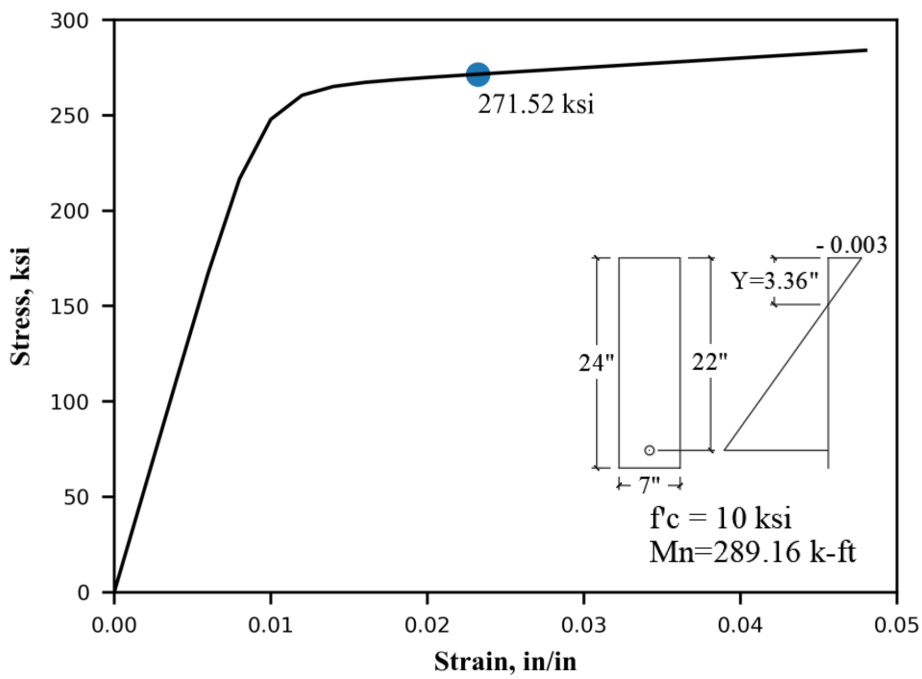

(b) Concrete compressive strength 10 ksi

Figure 6.14 Stress in prestressing reinforcement presented on stress-stain curve with a specific design concrete compressive strength and one-layer reinforcement in a 24" deep cross-section

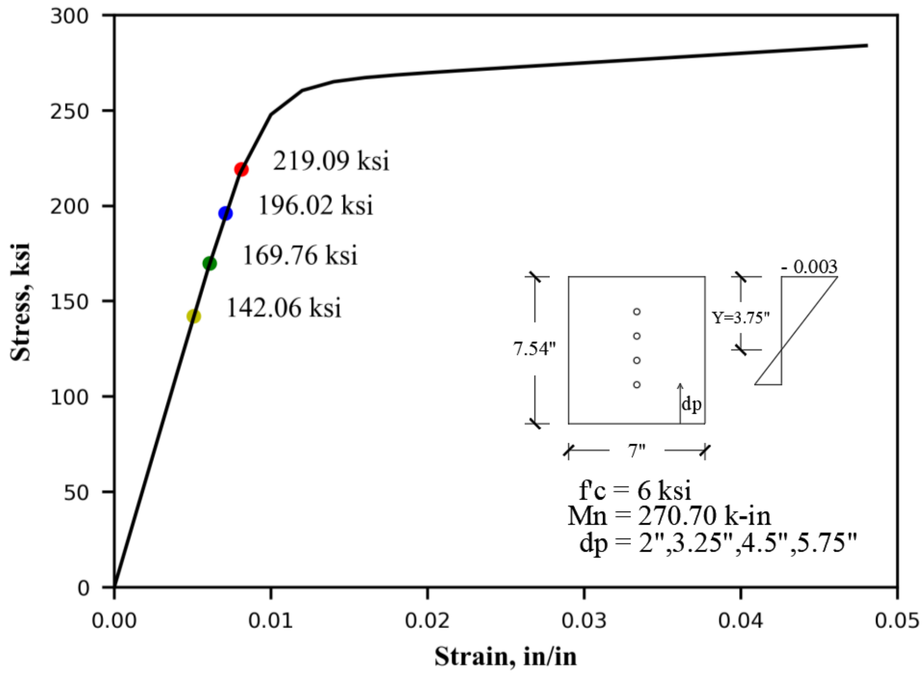

(a) Concrete compressive strength 6 ksi

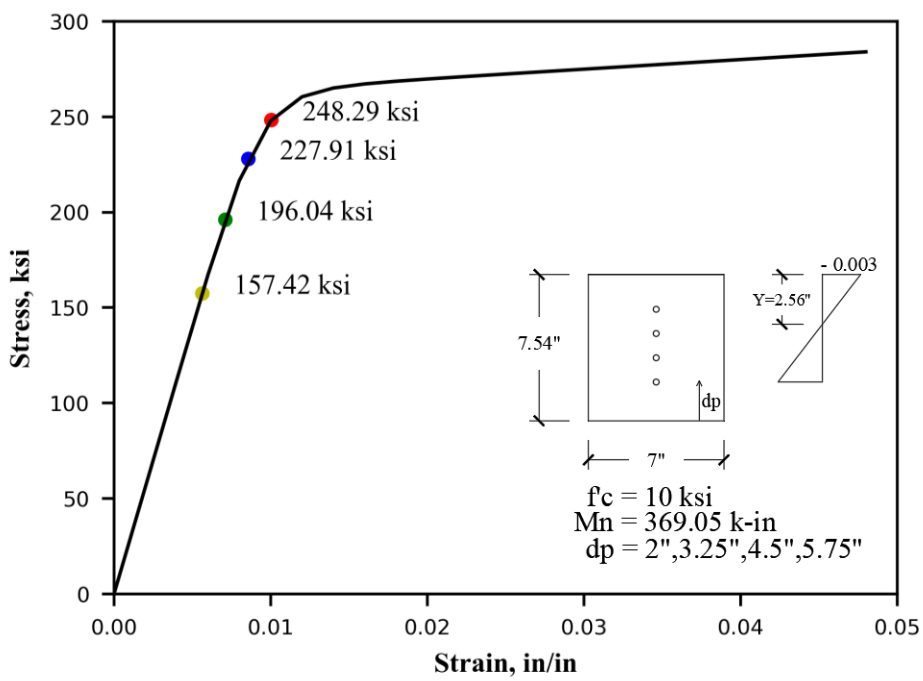

(b) Concrete compressive strength 10 ksi

Figure 6.15 Stress in prestressing reinforcement presented on stress-stain curve with a specific design concrete compressive strength and four-layers reinforcement in a 7.54" deep tie cross-section

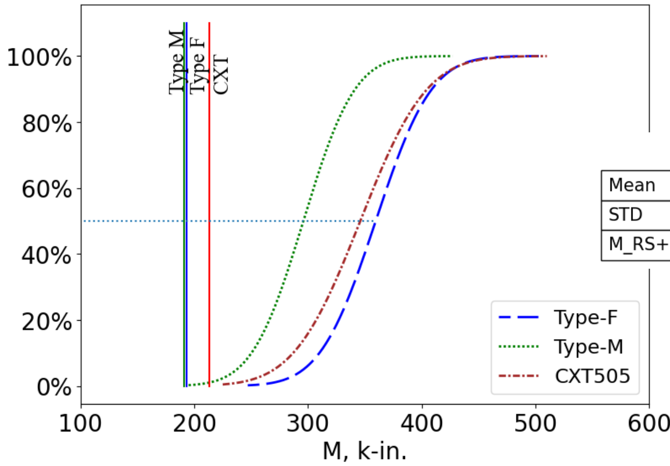

	Type-F	Type-M	CXT 505S
Mean	359	295	345
STD	38	35	46
M_RS+	193	191	213

(a) First crack moment, M_{cr}

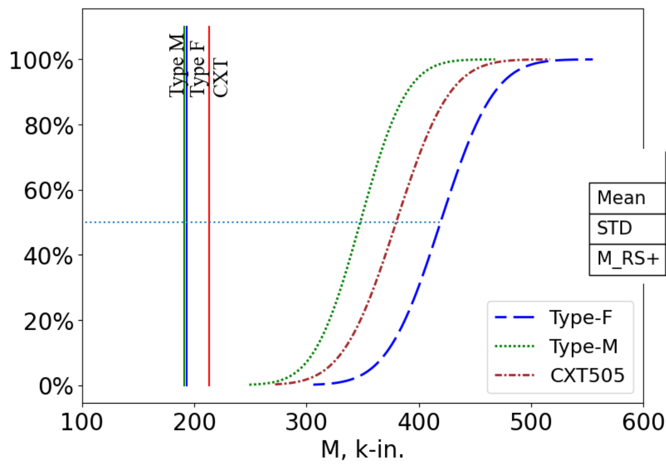

	Type-F	Type-M	CXT 505S
Mean	419	347	379
STD	37	32	37
M_RS+	193	191	213

(b) Crack reach to outer layer of reinforcement moment, M_{1st}

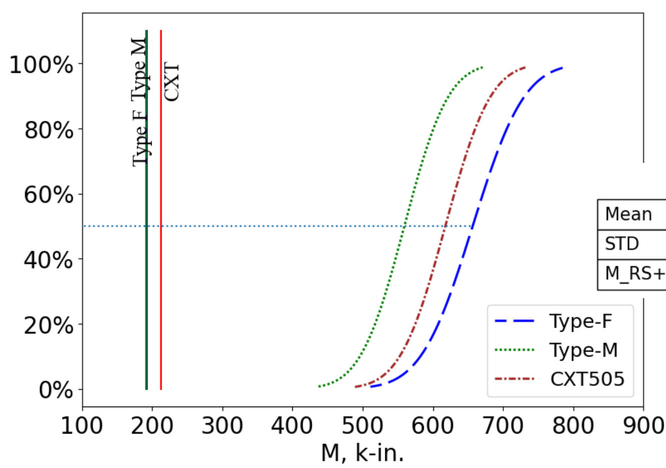

	Type-F	Type-M	CXT 505S
Mean	656	559	617
STD	58	49	50
M_RS+	193	191	213

(c) Ultimate moment, M_{ult}

Figure 6.16 Comparison of CDFs with AREMA design strength of each tie type at rail-seat

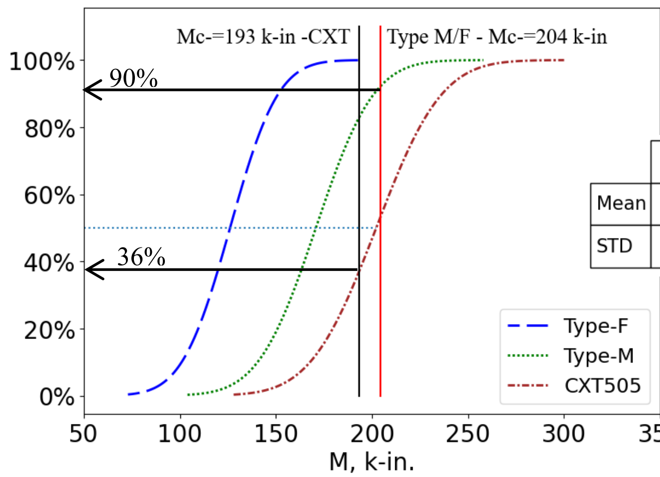

	Type-F	Type-M	CXT 505S
Mean	126	170	202
STD	19	23	26

(a) First crack moment, M_{cr}

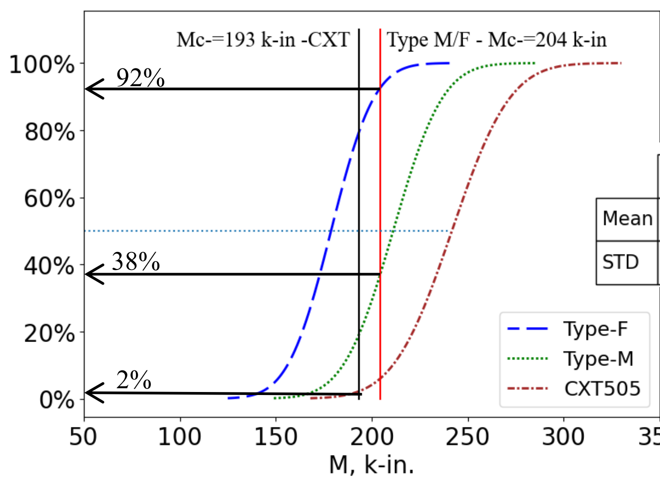

	Type-F	Type-M	CXT 505S
Mean	178	211	241
STD	17	20	23

(b) Crack reach to outer layer of reinforcement moment, M_{1st}

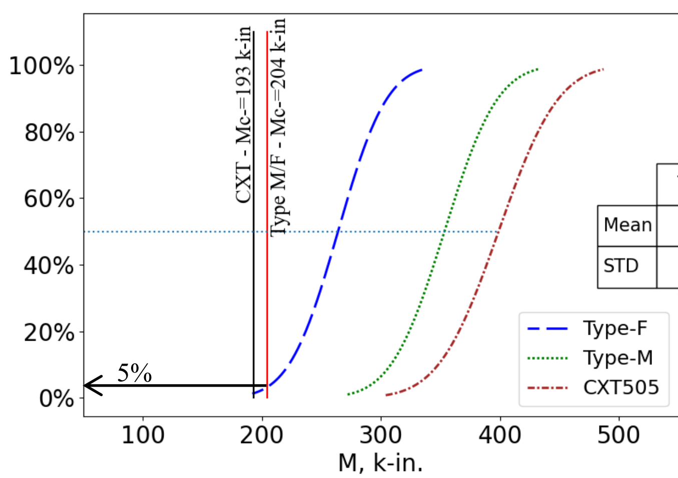

	Type-F	Type-M	CXT 505S
Mean	263	353	398
STD	32	35	39

(c) Ultimate moment, M_{ult}

Figure 6.17 Comparison of CDFs with AREMA design strength for different tie types at rail-center

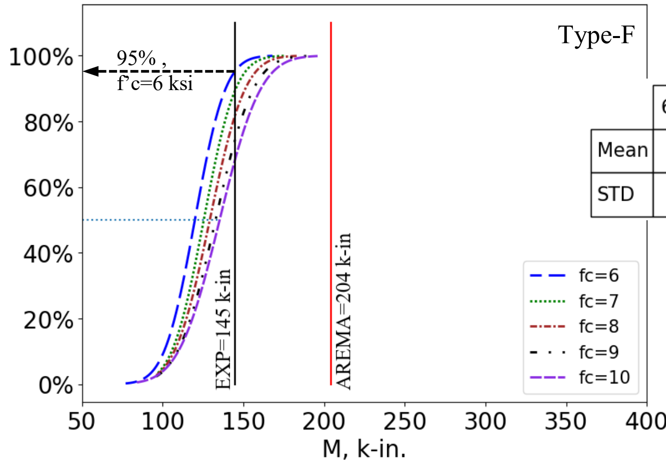

	6 ksi	7 ksi	8 ksi	9 ksi	10 ksi
Mean	119	125	129	132	135
STD	14	15	17	18	19

(a) First crack moment, M_{cr}

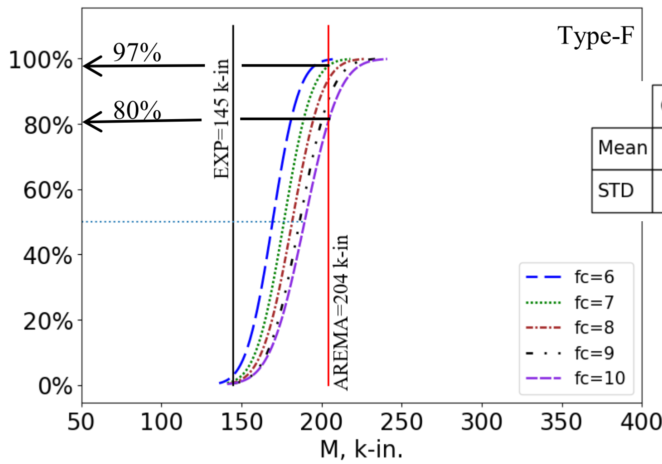

	6 ksi	7 ksi	8 ksi	9 ksi	10 ksi
Mean	169	176	181	186	189
STD	12	13	14	15	17

(b) Crack reach to outer layer of reinforcement moment, M_{1st}

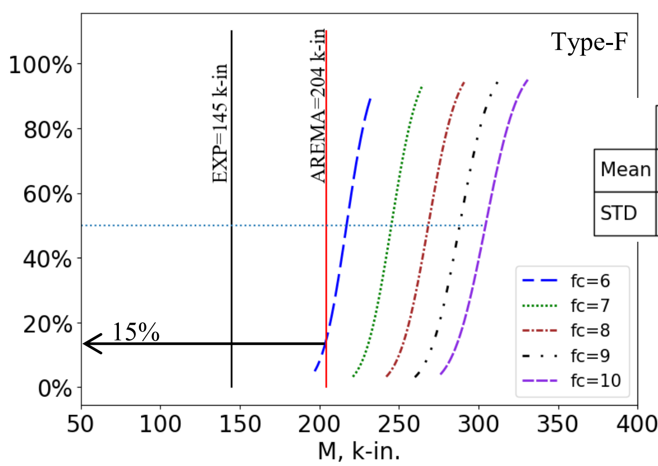

	6 ksi	7 ksi	8 ksi	9 ksi	10 ksi
Mean	217	245	268	288	304
STD	12	13	14	15	16

(c) Ultimate moment, M_{ult}

Figure 6.18 Rail-Center comparison of AREMA design strength, Experimental result, and CDFs of Type F tie concrete compressive strength

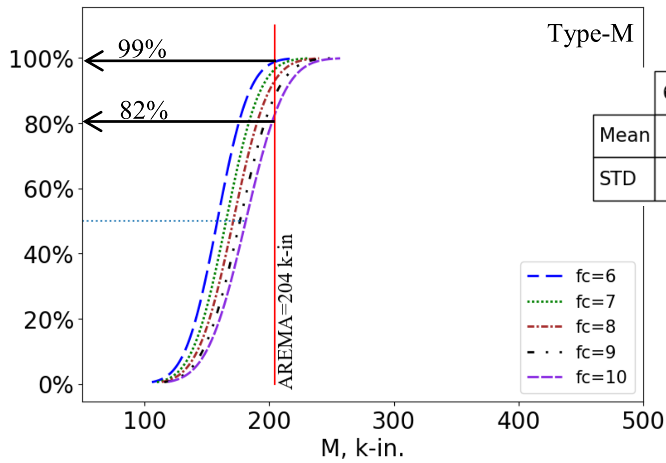

	6 ksi	7 ksi	8 ksi	9 ksi	10 ksi
Mean	158	165	171	176	181
STD	20	21	22	23	24

(a) First crack moment, M_{cr}

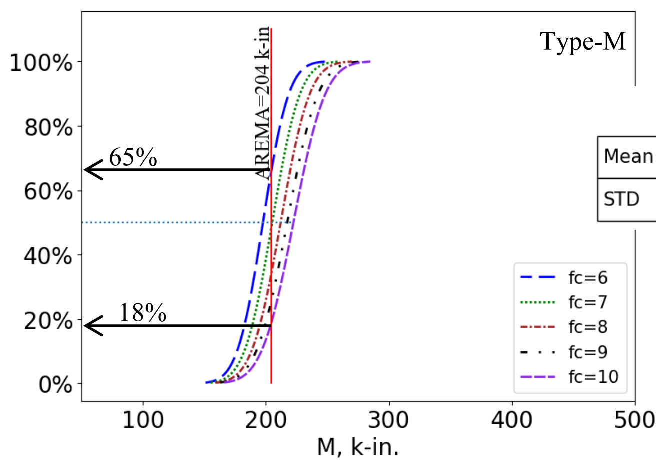

	6 ksi	7 ksi	8 ksi	9 ksi	10 ksi
Mean	197	205	212	217	222
STD	16	17	18	19	20

(b) Crack reach to outer layer of reinforcement moment, M_{1st}

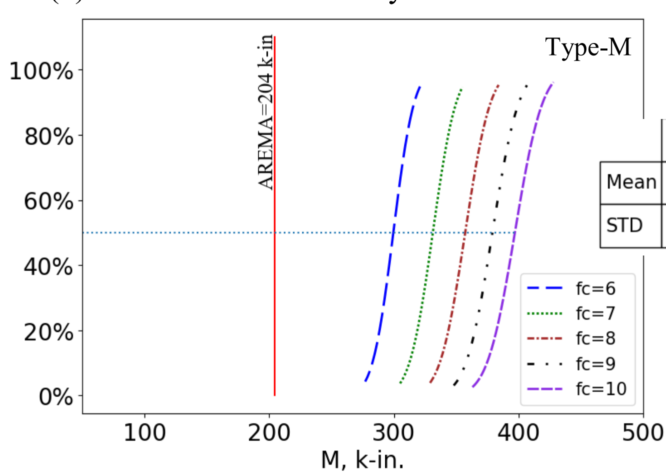

	6 ksi	7 ksi	8 ksi	9 ksi	10 ksi
Mean	299	331	357	379	397
STD	13	14	15	16	17

(c) Ultimate moment, M_{ult}

Figure 6.19 Rail-center comparison of AREMA design strength and CDFs of Type M tie concrete compressive strength

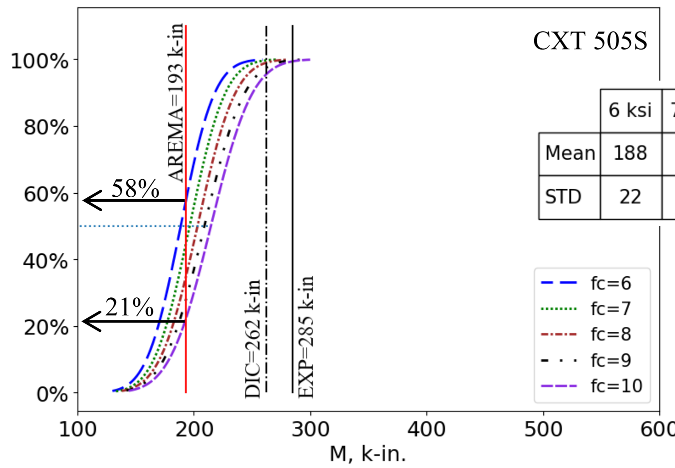

	6 ksi	7 ksi	8 ksi	9 ksi	10 ksi
Mean	188	196	202	208	214
STD	22	24	25	26	27

(a) First crack moment, M_{cr}

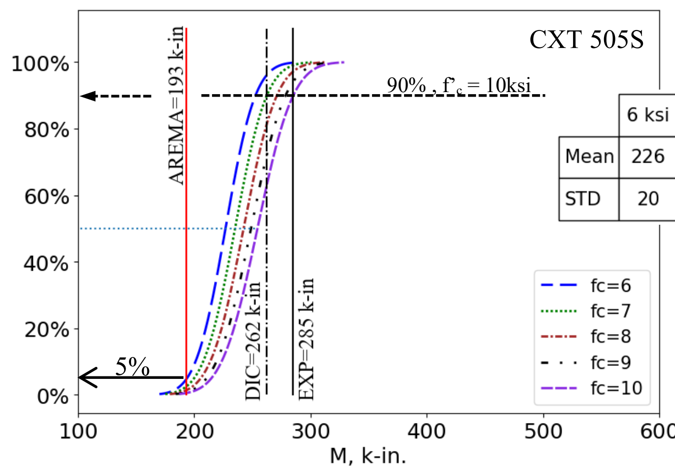

	6 ksi	7 ksi	8 ksi	9 ksi	10 ksi
Mean	226	235	242	248	254
STD	20	21	22	23	24

(b) Crack reach to outer layer of reinforcement moment, M_{1st}

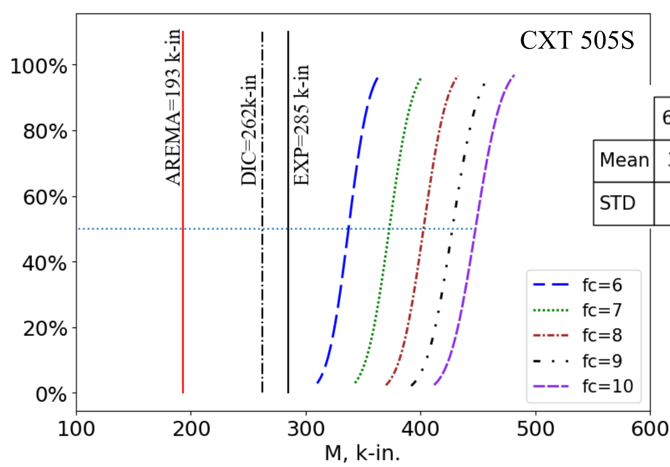

	6 ksi	7 ksi	8 ksi	9 ksi	10 ksi
Mean	337	373	402	427	448
STD	14	15	16	17	18

(c) Ultimate moment, M_{ult}

Figure 6.20 Rail-center comparison of AREMA design strength and CDFs of CXT 505S tie concrete compressive strength

Chapter 7 - Conclusion

A Python based computational tool was developed to estimate the flexural behavior of prestressed concrete monoblock ties. A risk analysis was conducted through Monte-Carlo Simulation and key design parameters were identified. The following insights were gained in this research.

Code Development and Experimental Testing

1. The flexural test was conducted on existing (Type-F and Type-C) in addition new design tie (CXT). The new tie was designed with a larger cross-section, high strength concrete and low eccentricity. As a result, the newly designed tie has approximately 40% more in flexure load capacity than the existing ties.
2. At code verification, the program performed as expected and the outputs fit with the benchmarks. The first two cases had good agreement but a small discrepancy was found in case 3. When verified case 3, a 1 % discrepancy in the nominal capacity was noted between rail-seat and rail-center location. These discrepancies were attributed by computing area and wire eccentricity.
3. The code was validated experimentally, and overall good agreement was observed. The flexural performance of prestressed concrete monoblock ties can be accurately predicted while the design parameters were well defined. A precise estimation could be achieved while the modeling parameters and material constitutive relationship were matched with the testing specimen. Unmatched material properties and idealized cross-section geometry induced errors that negatively affected end results which was indicated in non-linear region.

Monte- Carlo Simulation Compared to AREMA Recommendation

Monte-Carlo simulation was used to forecast flexural behavior of prestressed concrete monoblock ties, and the results were further analyzed to correlate key design parameters.

1. At Rail-Seat

   The results indicated the ties had sufficient capacity to meet design positive bending moment. Based on the CDF curves, the ultimate bending resistance was more controlled by concrete compressive strength than tie geometry which the opposite situation was observed at other two QOIs. Overall the wire type had less affect in increasing tie bending capacity. Since the tie design, at rail-seat location, is conservative for flexural demand, the result may not be very beneficial for design optimization.

2. At Rail-Center

   More difference was observed in CDFs of tie geometry at first crack moment and crack reaching to first level of reinforcement moment. The size of cross-section governs the amount of concrete area and eccentricity of prestressing reinforcement which the negative bending capacity is sensitive to. Also, the larger cross-section (CXT 505S tie) has more benefit in designing with higher concrete compressive strength which could increase approximately 37% the probability of ties remaining uncracked.

Method of Crack Detection

The method of crack detection was followed the current design standard in AREMA Chapter 40. The initial crack load determined experimentally was further compared with Monte-Carlo simulation results for CXT 505S and Type-F tie. Additionally, CXT 505S simulation results were also compared with DIC analysis result. The comparison results indicated the cracking occurred before any visual indication. Overall, the inaccuracy in locating the first crack was recognized. Other method of crack detection should be looked into to improve the accuracy of cracking load determination.

Current Tie Design Requirement

This research involved virgin tie (CXT 505S) and existing tie (Type-F). Based on the experimental and modeling results, the existing tie did not satisfy current design requirement but performed well in track for over 25 years. The virgin tie has higher flexural capacity also met the design needed but never served in track. Based on experimental result, CXT 505S tie was capable to withstand average 38 kips load but the design load only used 37% of its capacity. However, type-F tie could resist average 20 kips applied load but the design load use 78% of its capacity. The conservative designed was observed on the newly designed tie which tie capacity hasn't been effectively used. The allowable design stress principle may be over conservatively for designing railroad tie. The different procedure of determining design load should be considered as the tie is one of the components in the track system. The role of the tie should be should be transmitting the force to subgrade system instead of to resist it.

Ultimate Moment

The simulation results indicated the noticeable growth in ultimate moment following with increasing in concrete compressive strength. The ratio of cross-section height and compression zone is relatively large comparing to typical prestressed concrete beam. Larger compressive depth is bringing up the possibility that prestressing is located in compression zone. In compression zone, the concrete strain is increased resulting in reducing total strain in prestressing reinforcement. Then, the stress in prestressing has noticeable change because the prestressing is staying in elastic region. Consequently, the ultimate capacity of tie has significant increment while the concrete compressive strength increased from 6 ksi to 10 ksi. Thus, the wire location and cross-section size show direct impact in determining ultimate moment of tie. The capability of prestressing reinforcement is limited by compressive response.

Consequently, the prestressed concrete monoblock ties could be modeled accurately by the developed computational tool. The existing and new tie could be designed and analyzed effectively, and the targeted design load could be achieved at stage of approval tie design testing. This insight will help industry in designing an economical tie meanwhile all design requirements will be satisfied. Additionally, this tool also shows potential for supporting risk-based analysis of the tie flexural performance.

References

American Concrete Institute. (2019). *Building Code Requirements for Structural Concrete (ACI 318-19): Commentary on Building Code Requirements for Structural Concrete (ACI 318R-19).* American Concrete Institute. ACI.

Anwar, N., & Najam, F. A. (2016). *Structural Cross Sections: Analysis and Design.* Cambridge: Butterworth-Heinemann. Retrieved from https://ebookcentral-proquest-com.er.lib.k-state.edu/lib/ksu/reader.action?docID=4737243

AREMA (American Railway Engineering and Maintenance-of-Way Associatation). *Manual for Railway Engineering.* Landover, Maryland: AREMA. (2020).

Arnold , M. L. (2013). *Un-tensioned Pull-Out Tests to Predict the Bond Quality of Different Prestressing Reinforcements Used in Concrete Railroad Ties.* Manhattan: Kansas State university.

ASTM Standard C39/C39M. (2020). Standard Test Method for Compressive Strength of CylindricalCincrete Specimens. West Conshohocken, PA: ASTM International.

ASTM Standard C42/C42M. (2020). Standard Test Method for obtaining and Testing Drilled Cores and Sawed Beams of Concrete. West Conshohocken, PA: ASTM International.

ASTM Standard C469/C469M. (2014). Standard Test Method for Static Modulud of Elasticity and Poisson's Ratio of Concrete in Compression. West Conshohocken, PA: ASTM International.

Bastos, J. C. (2016). *Analysis of the Preformance and Failure of Railroad Concrete Crossties with Various Track Support Conditions.* Urbana-Champaign: University of Illinois at Urbana-Champaign.

Bodapati, N. N. (2018). *A Comprehensive Study of Prestressing Steel and Concrete Variables Affecting Transfer Length in Pre-tensioned Concrete Crossties.* Manhattan: Kansas State University.

Chen, Y.-S. (2016). *Testing and Modeling Tensile Stress-Strain Curve for Prestressing Wires in Railroad Ties.* Manhattan, KS: Kansas State University.

Chen, Y.-S., Rasheed, H. A., & Peterman, R. J. (2018). Stress-Strain Curves for Modeling Prestressing Wires. *ACI Materials Journal, 115*, 773-782.

Chen, Z., Shin, M., Andrawes, B., & Edwards, J. R. (2014). Parametric Study on Damage and Load Demand of Prestressed Concrete Crosstie and Fastening Systems. *ELSEVIER*, 49-61.

Edwards , R. J., Dersch, M. S., & Oliveira, A. d. (2019, Feburary 25). Concrete Crossties: A New Paradigm for Design. Railway Track and Structures. Retrieved from https://railtec.illinois.edu/wp/wp-content/uploads/2019_02_25_magazine_RTS-ConcreteCrosstie.pdf

Edwards, R. J. (2019). *Quantification of Prestressed Concrete Railroad Crosstie Flexural Response: Implications for Mechanistic Design.* Urbana: University of Illinois at Urbana Champaign.

Edwards, R. J., & Dersch, M. S. (2017). *Mechanistic Design of Concrete Crossties and Fastening Systems – Phase 1.* Urbana-Champaign: National University Rail Center-NURail.

Hanna, A. N. (1979, September - October). Prestressed Concrete Ties for North American Railroads. *PCI*, 32-61.

Harris, D. K., Lutch , R. H., Ahlborn, T. M., & Duong , P. (2011). Optimization of A Prestressed Concrete Railroad Crosstie for Heavy-Haul Applications. *TRANSPORTATION ENGINEERING © ASCE*, 815-822.

Hasan, N. (2014). Railroad Tie Spacing Related to Wheel-Load Distribution and ballast Pressure. *American Society of Civil Engineers*.

Hay, W. W. (1982). *Railroad Engineering.* A Wiley-Interscience Publication.

International Union of Railways. (2004). *UIC Code 731: Design of Monblock Concrete Sleepers.* International Union of Railways.

Jones, E., & Iadicola, M. (. (2018). *A Good Practices Guide for Digital Image Correlation.* International Digital Image Correlation Society. doi:https://idics.org/guide/

Kerr, A. D. (2003). *Fundamentals of Railway Track Engineering.* Simmons Boardman Pub Co.

Liu, X., Barkan, C. P., & Rapik Saat, M. (2011). Analysis of Derailments by Accident Cause: Evaluting Railroad Track Upgrades to Reduce Transportation Risk. *Journal of the Transportation Research Board*, 17-185.

Liu, X., Saat, M., & Barkan , C. (2013). Analysis of Major Derailment Causes on Heavy Haul Railways in the United States. *Proceedings of the 10th International Heavy Haul Association Conference.* New Delhi, India. Retrieved from https://railtec.illinois.edu/wp/wp-content/uploads/2019/01/Liu%20et%20al%202013.pdf

Lutch, R. H. (2009). *Capacity Optimization of A Prestressed Concrete Railroad Tie.* Michigan Technological University. Retrieved from https://digitalcommons.mtu.edu/etds/254/

Marquis, B., LeBlanc, J., Yu, H., & Jeong, D. (2014). *Vlop Report on CSX Derailment on Metro-North Tracks in Bronx, NY.* National Transportation Safety Board, United States.

McQueen, J. P. (2010). *Flexural Performance Requirements for Prestressed Concrete Ties by Factoring.* San Rafael, California.

Mindess, S., Young, F. J., & Darwin, D. (2003). *Concrete Second Edition.* Upper Saddle River, NJ: Pearson Education, Inc.

Mitchell, D., & Collins, M. P. (1991). *Prestressed Concrete Structures.* Englewood Cliffs: Prentice-Hall.

Momeni, A. F. (2016). *Effect of Concrete Properties and Prestressing Steel Indentation Types on The Developement Length and Flexural Capacity of Prestressed Concrete Member.* Manhattan, KS: Kansas State University.

Oberkampf, W. L., & Barone, M. F. (2006). Measures of Agreement Between Computation and Experiment: Validation Metrics. *ELSEVIER*, 5-36.

Oberkampf, W. L., & Trucano, T. G. (2008). Verification and Validation Benchmarks. *ELSEVIER*, 716-743.

Park, R., & Paulay, T. (1975). *Reinforced Concrete Structures.* Canada: John Wiley & Sons.

PCI. (2010). *PCI Design Handbook: Precast and Prestressed Concrete (7th ed.).* Chicage, Illionis: Precast/Prestressed Concrete Institute.

Scott, J. D. (2019). *Experimental Evaluation of Remaining Prestress Force and Center Negative Bending-Moment in Railroad Ties Removed From Track After 25 years of Service.* Manhattan: Kansas State University.

Timoshenko, S. (1930). *Strength of Materials.* New York: D. Van Nostrand Company, Inc.

Van Dyk, B. K. (2014). *Characterization of The Loading Environment For Shared-Use Railway Superstructure in North America.* Urbana, Illinois: University of Illinois at Urbana-Champaign.

Wolf, H. E. (2015). *Flexural Behavior of Prestressed Concrete Monoblock Crossties.* Urbana, Illinois: University of Illinois at Urbana-Champaign.

Yu, H., Jeong , D., Marquis, B., & Coltman, M. (2015). Railroad Concrete Tie Failure Modes and Research Needs. *Transportation Research Board 94th Annual Meeting.* Washington, DC : Transportation Research Board .

Yu, H., Jeong, D., Choros, J., & Sussmann, T. (2011). Finite Element Modeling of Prestressed Concrete Crossties with ballast and subgrade Support. *ASME 2011 International Design Engineering Technical Conferences & Computers and Information in Engineering Conference.* Washington, DC: IDETC/CIE.

Zeman, J. C. (2010). *Hydraulic Mechanisms of Concrete-Tie Rail Seat Deterioration.* Urbana, Illinois: University of Illinois at Urbana-Champaign.

Appendix A - Flexural Test Results

Figure title shows type of tie design and the distance measured from center of tie. For CXT tie, the wire type is included.

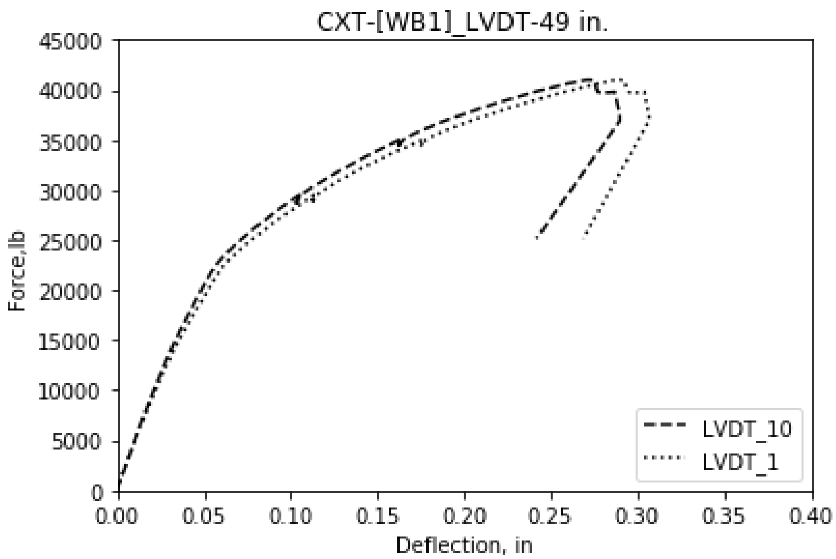

Figure A. 1 CXT-[WB1] Load versus LVDT #1 and #10 reading

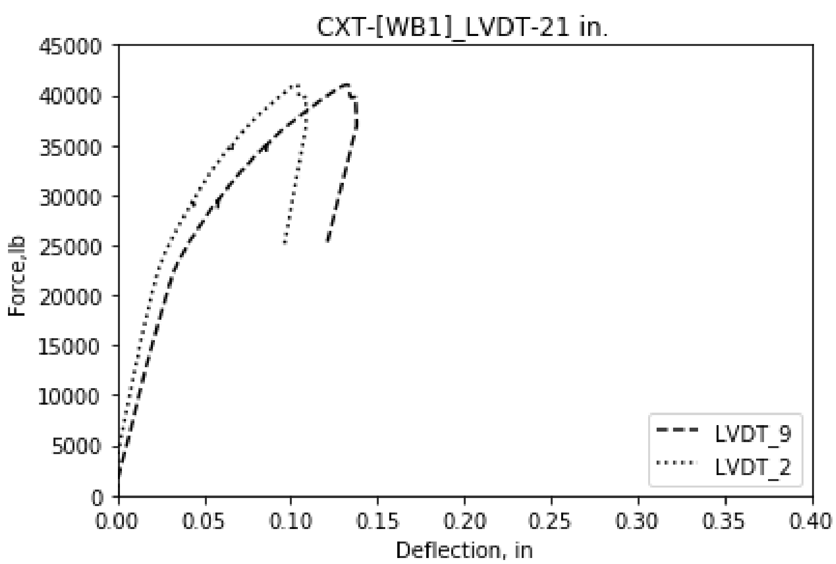

Figure A. 2 CXT-[WB1] Load versus LVDT #2 and #9 reading

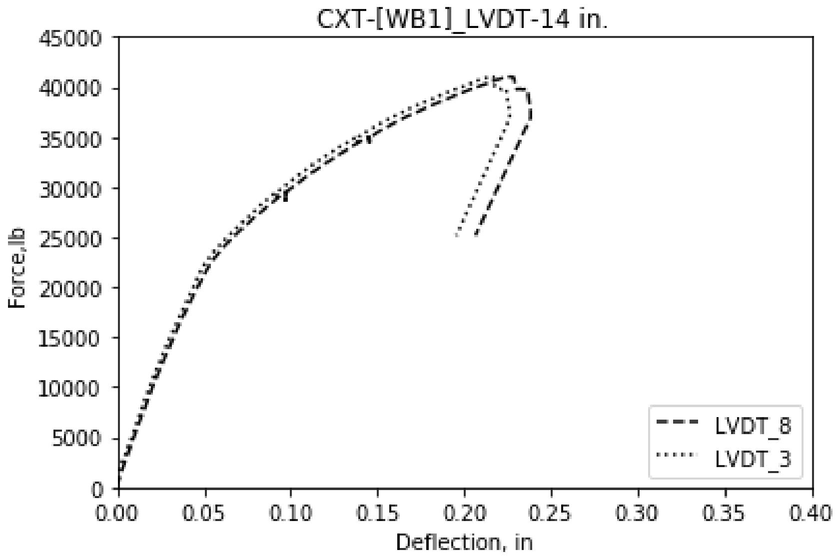

Figure A. 3 CXT-[WB1] Load versus LVDT #3 and #8 reading

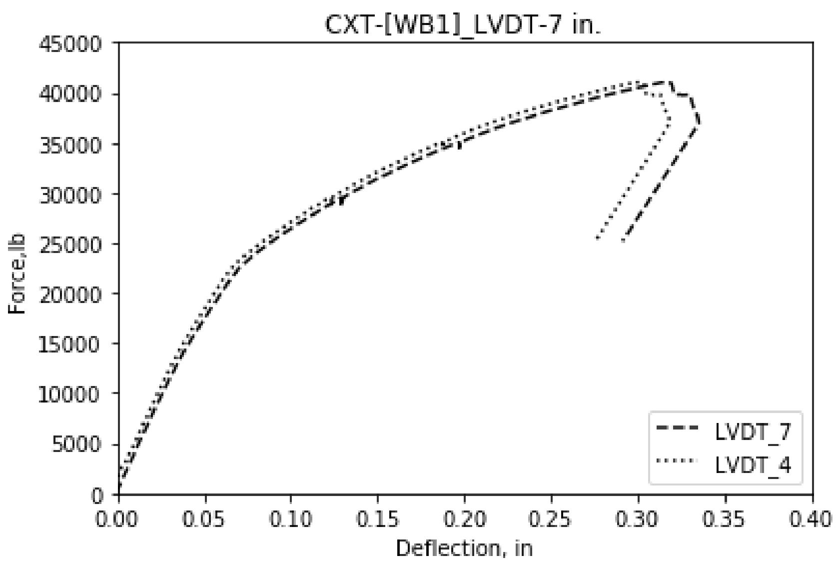

Figure A. 4 CXT-[WB1] Load versus LVDT #4 and #7 reading

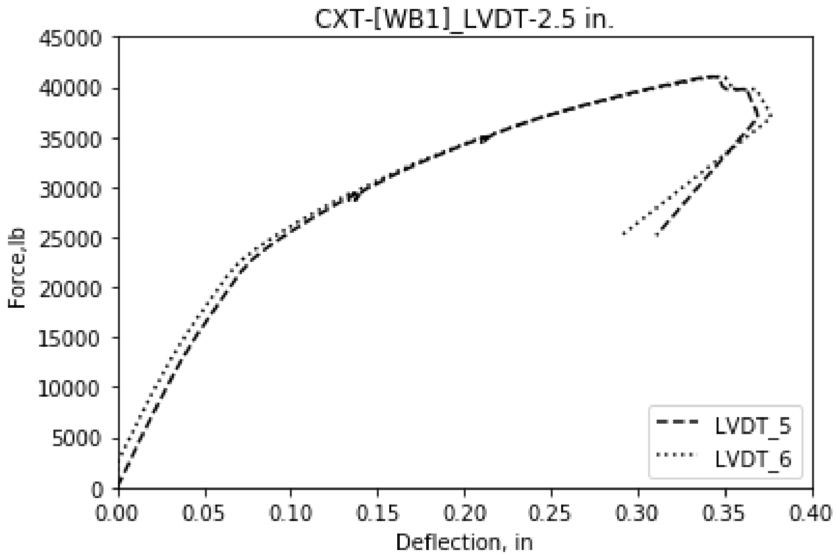

Figure A. 5 CXT-[WB1] Load versus LVDT #5 and #6 reading

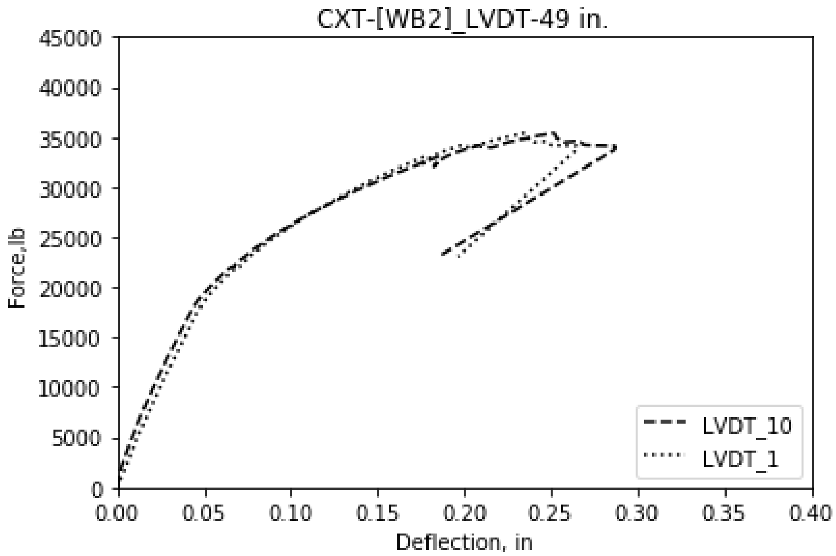

Figure A. 6 CXT-[WB2] Load versus LVDT #1 and #10 reading

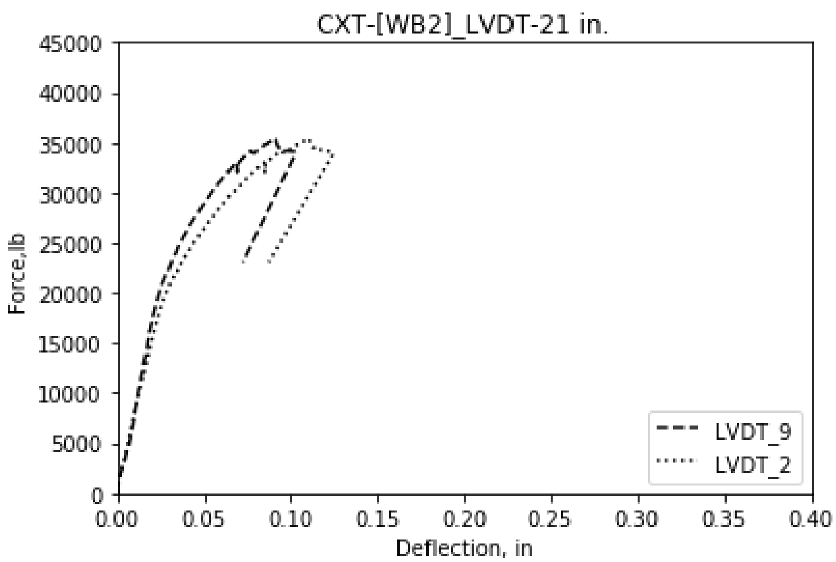

Figure A. 7 CXT-[WB2] Load versus LVDT #2 and #9 reading

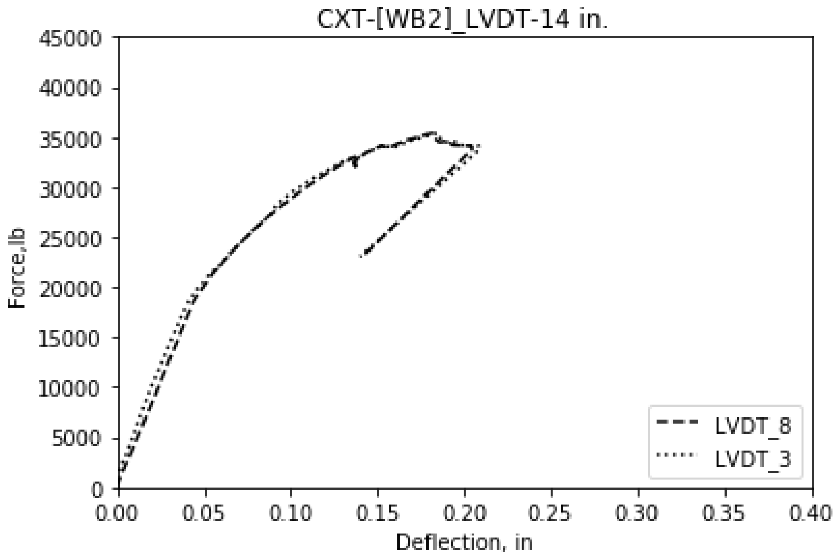

Figure A. 8 CXT-[WB2] Load versus LVDT #3 and #8 reading

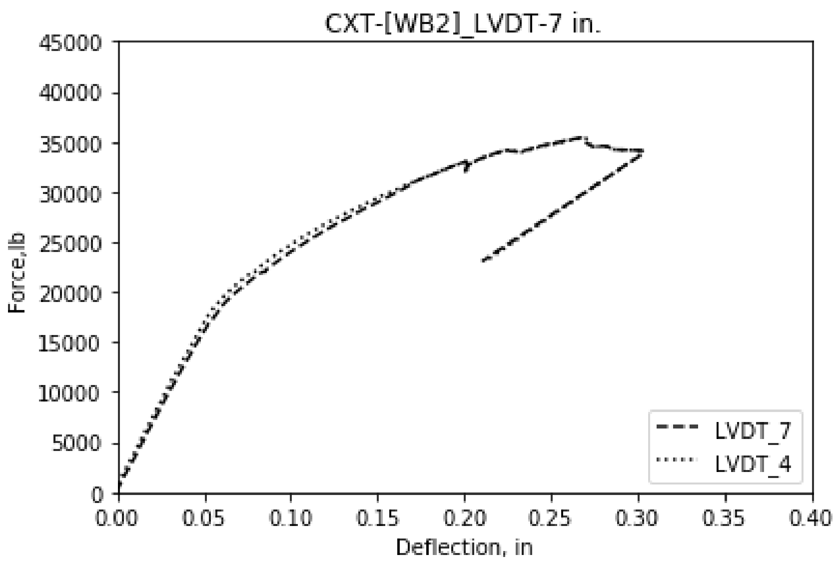

Figure A. 9 CXT-[WB2] Load versus LVDT #4 and #7 reading

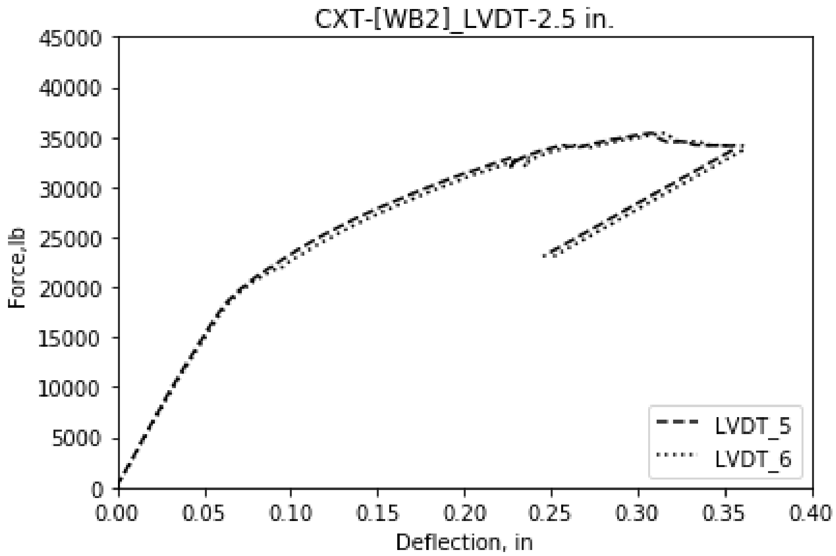

Figure A. 10 CXT-[WB2] Load versus LVDT #5 and #6 reading

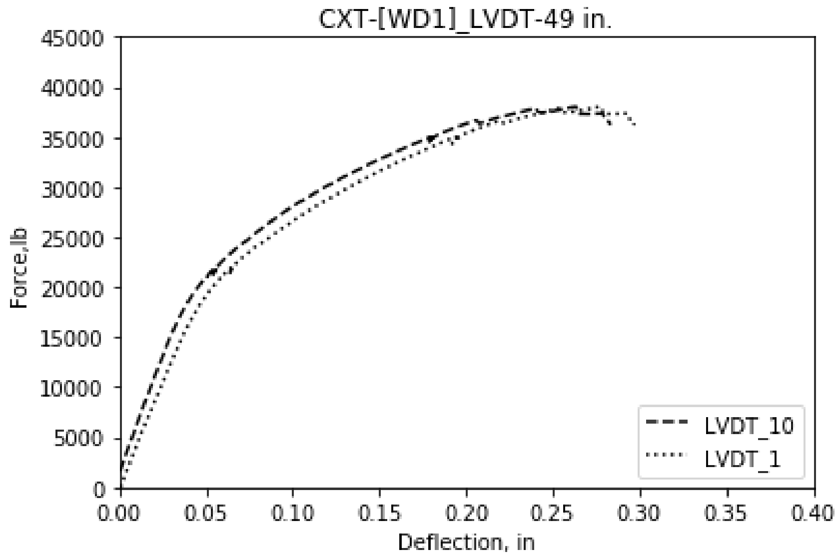

Figure A. 11 CXT-[WD1] Load versus LVDT #1 and #10 reading

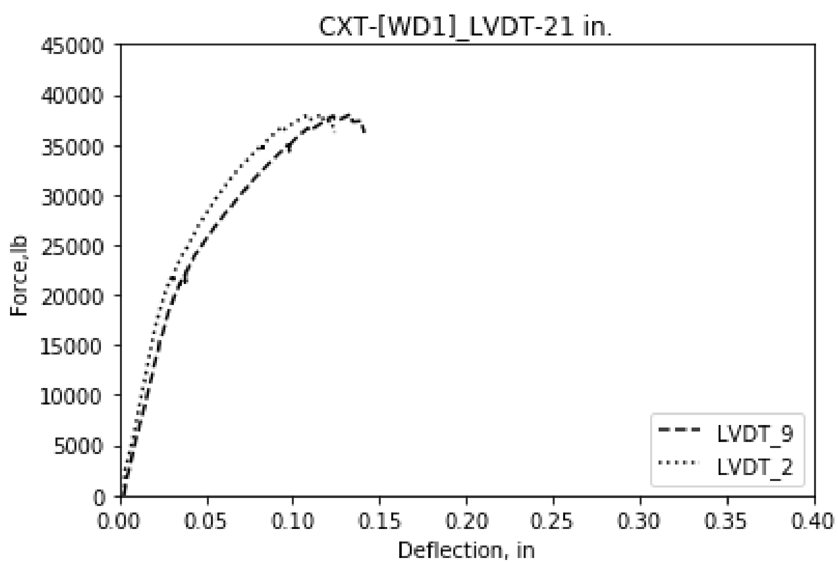

Figure A. 12 CXT-[WD1] Load versus LVDT #2 and #9 reading

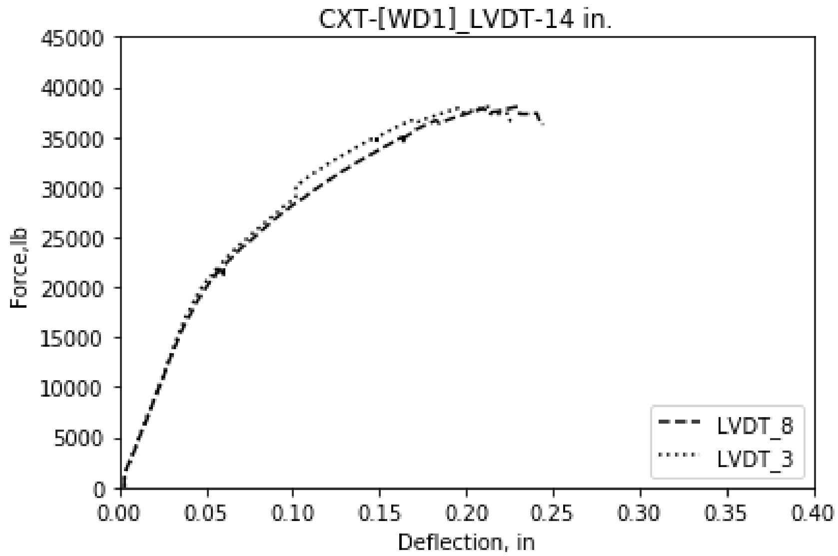

Figure A. 13 CXT-[WD1] Load versus LVDT #3 and #8 reading

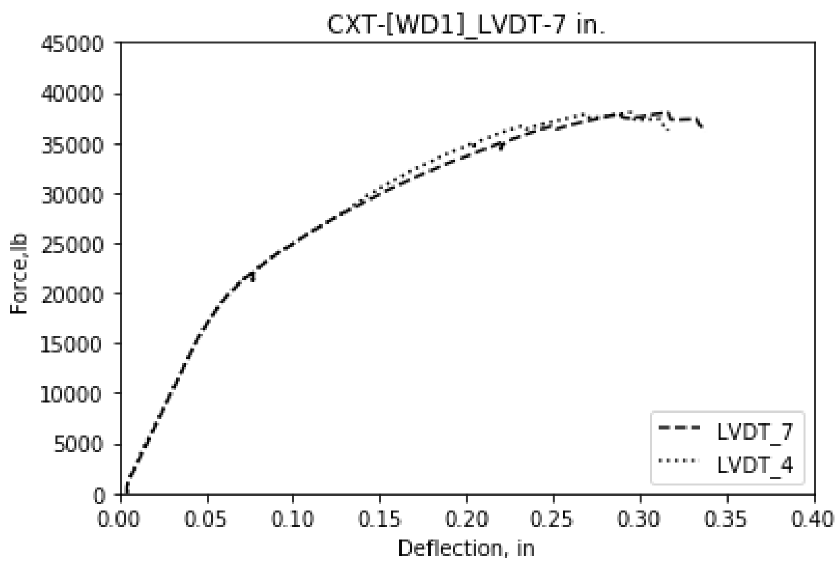

Figure A. 14 CXT-[WD1] Load versus LVDT #4 and #7 reading

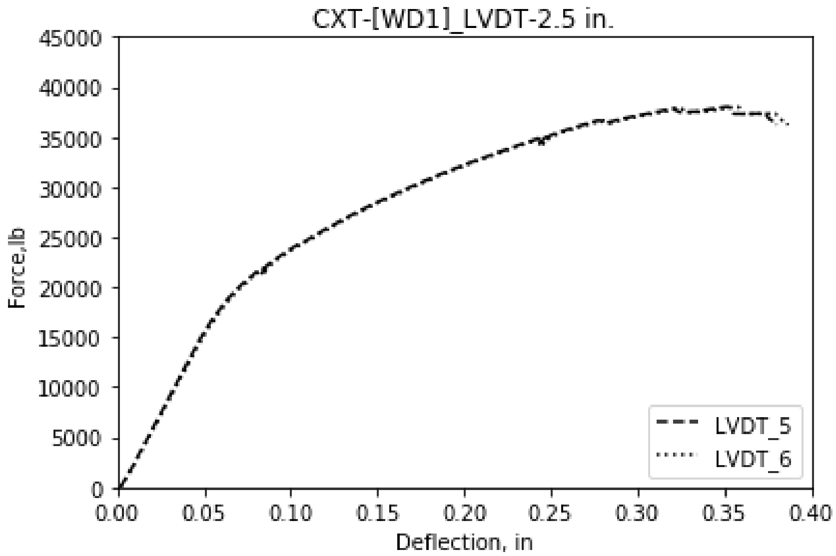

Figure A. 15 CXT-[WD1] Load versus LVDT #5 and #6 reading

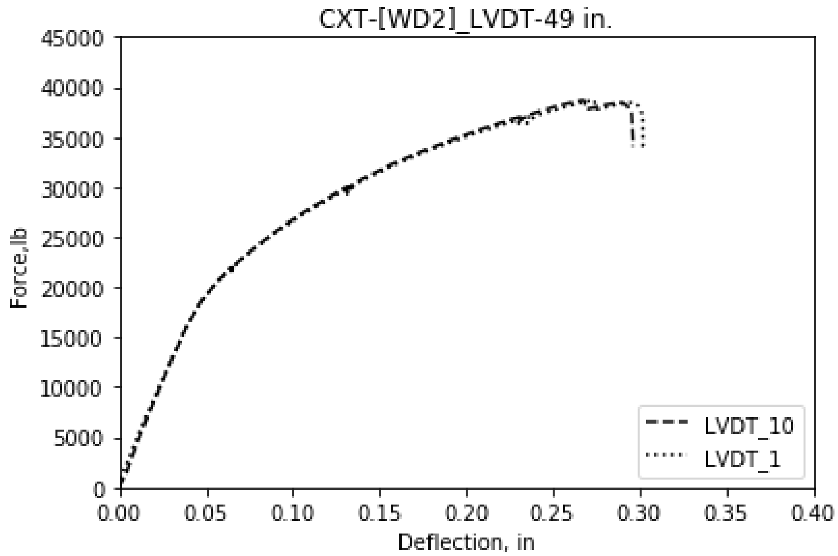

Figure A. 16 CXT-[WD2] Load versus LVDT #1 and #10 reading

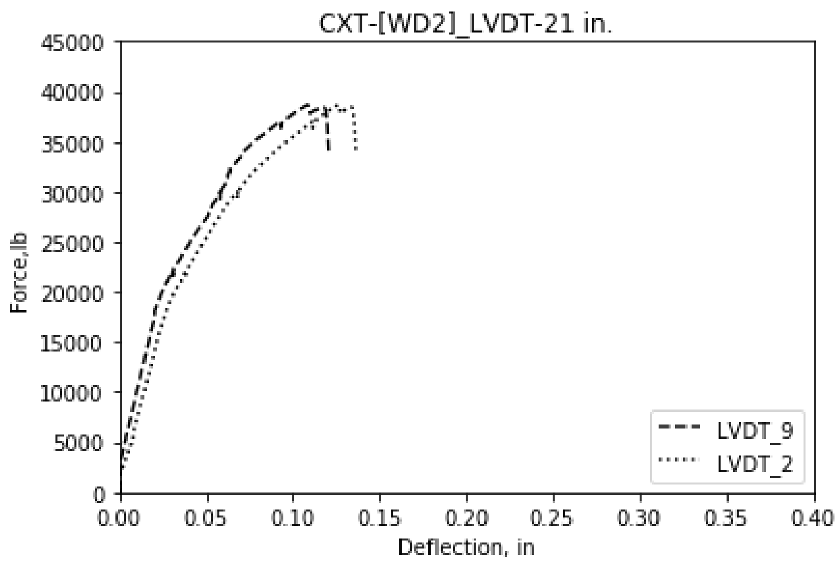

Figure A. 17 CXT-[WD2] Load versus LVDT #2 and #9 reading

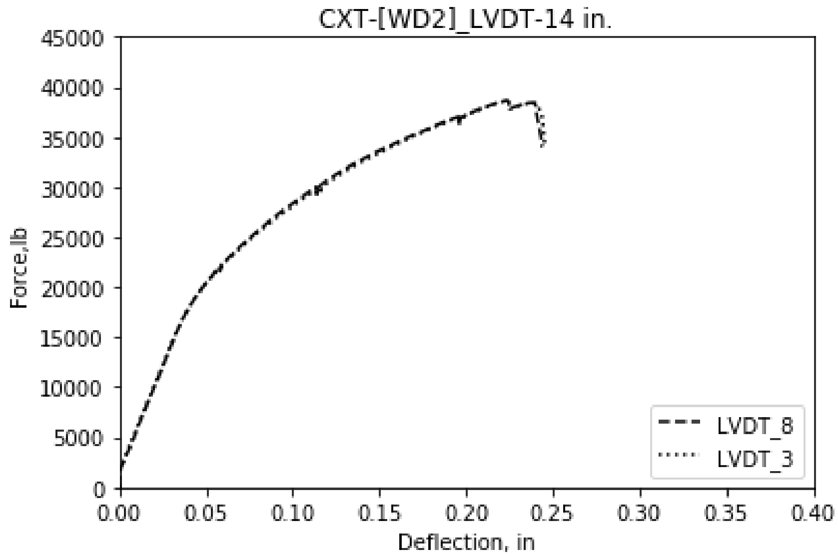

Figure A. 18 CXT-[WD2] Load versus LVDT #3 and #8 reading

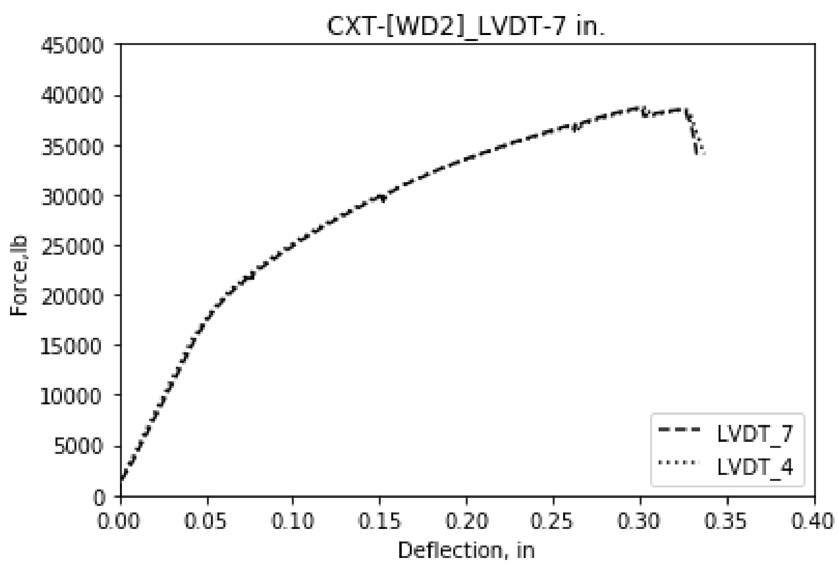

Figure A. 19 CXT-[WD2] Load versus LVDT #4 and #7 reading

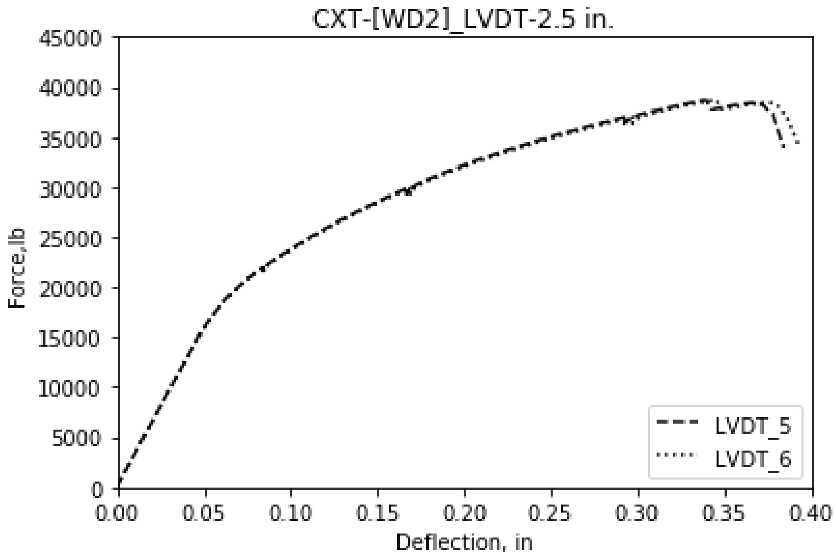

Figure A. 20 CXT-[WD2] Load versus LVDT #5 and #6 reading

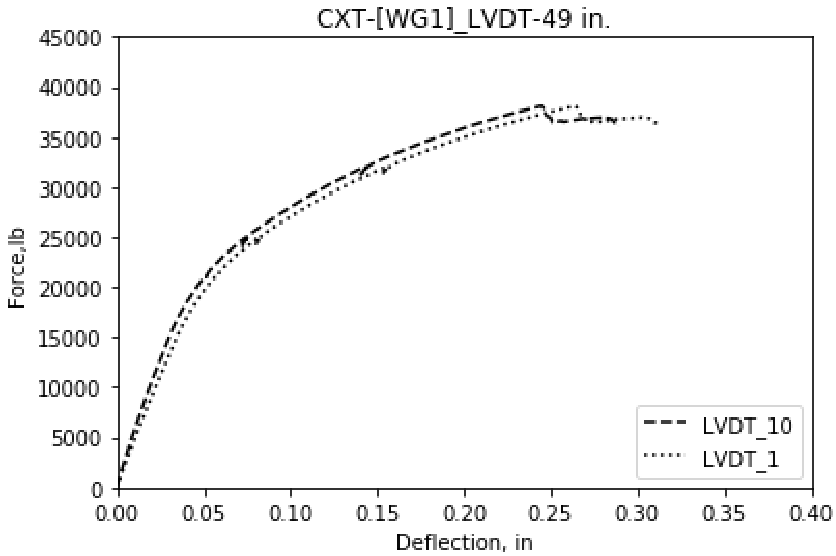

Figure A. 21 CXT-[WG1] Load versus LVDT #1 and #10 reading

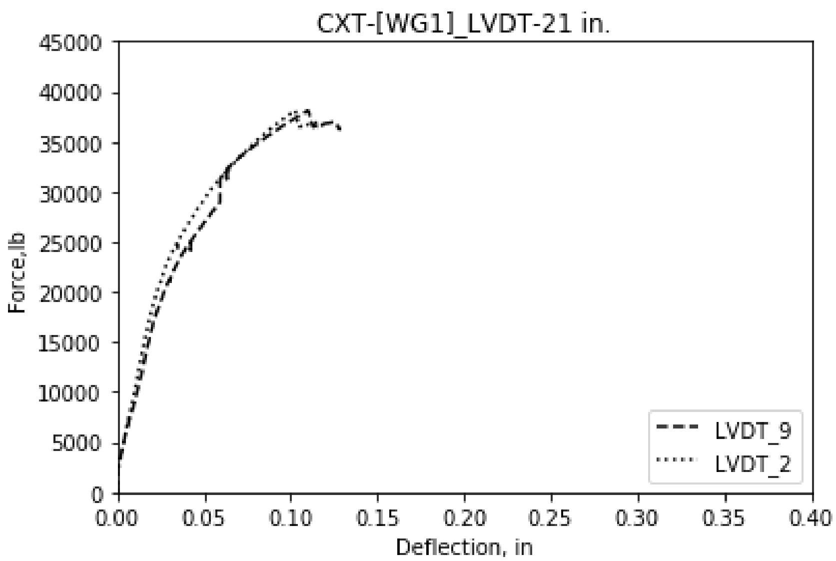

Figure A. 22 CXT-[WG1] Load versus LVDT #2 and #9 reading

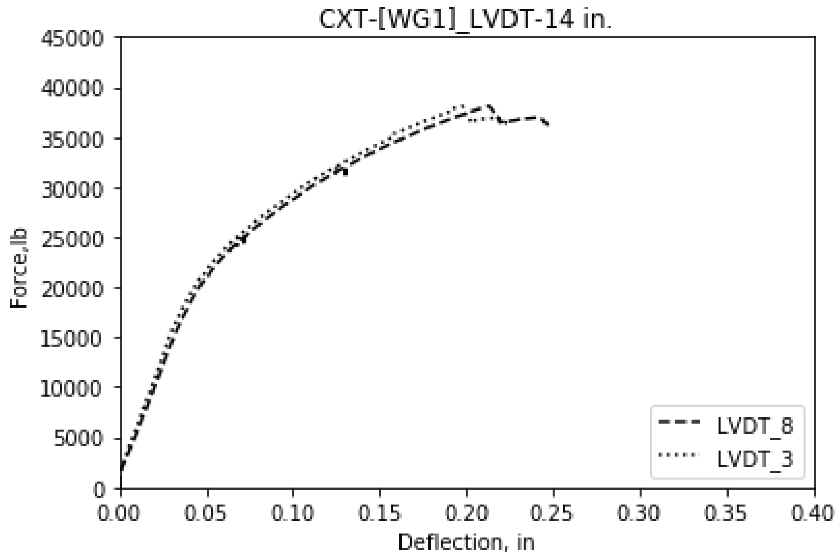

Figure A. 23 CXT-[WG1] Load versus LVDT #3 and #8 reading

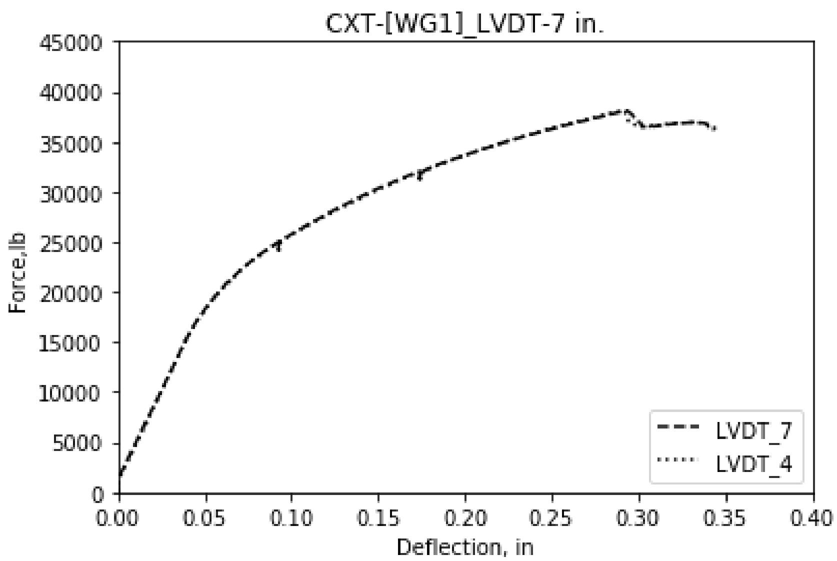

3

Figure A. 24 CXT-[WG1] Load versus LVDT #4 and #7 reading

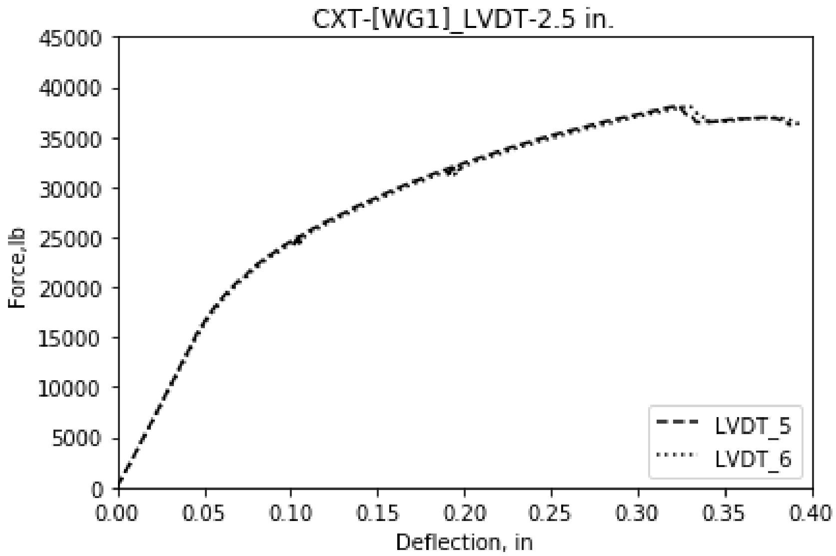

Figure A. 25 CXT-[WG1] Load versus LVDT #5 and #6 reading

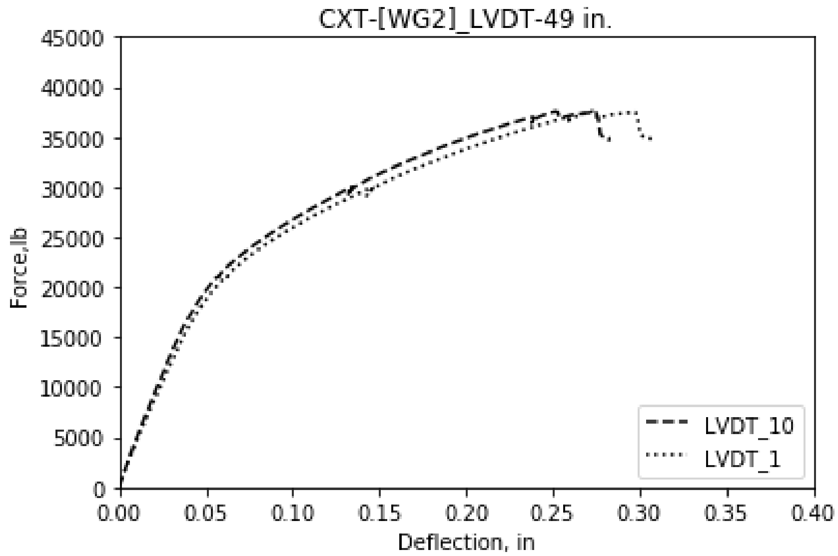

Figure A. 26 CXT-[WG2] Load versus LVDT #1 and #10 reading

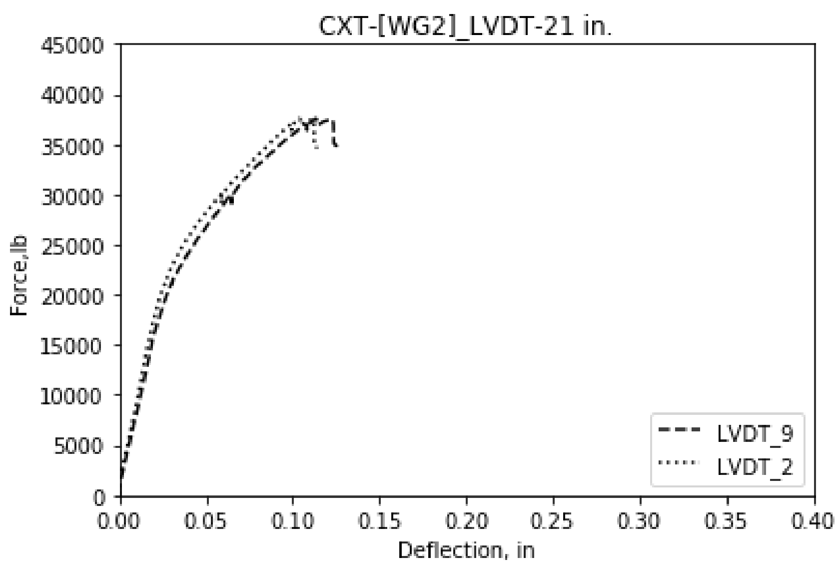

Figure A. 27 CXT-[WG2] Load versus LVDT #2 and #9 reading

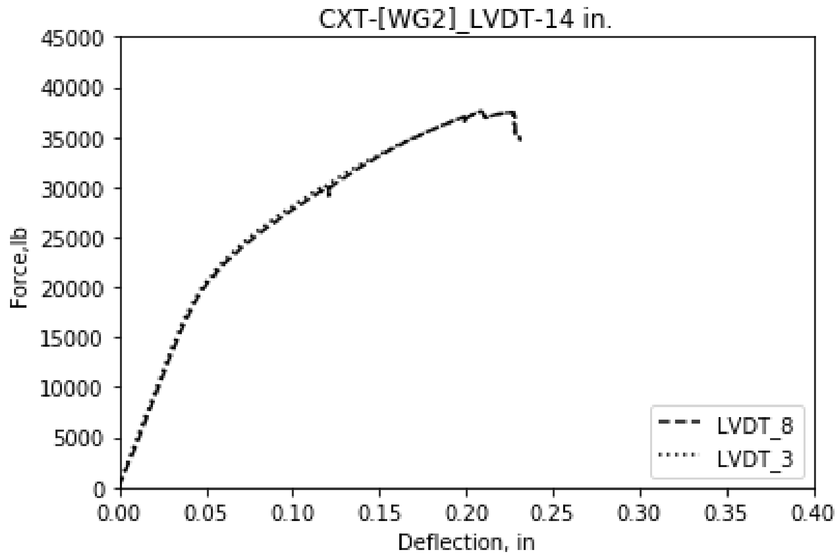

Figure A. 28 CXT-[WG2] Load versus LVDT #3 and #8 reading

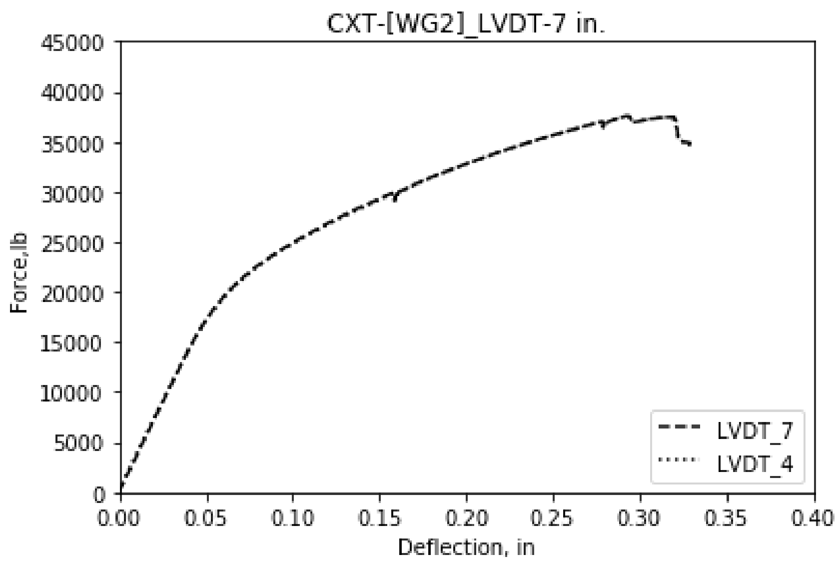

Figure A. 29 CXT-[WG2] Load versus LVDT #4 and #7 reading

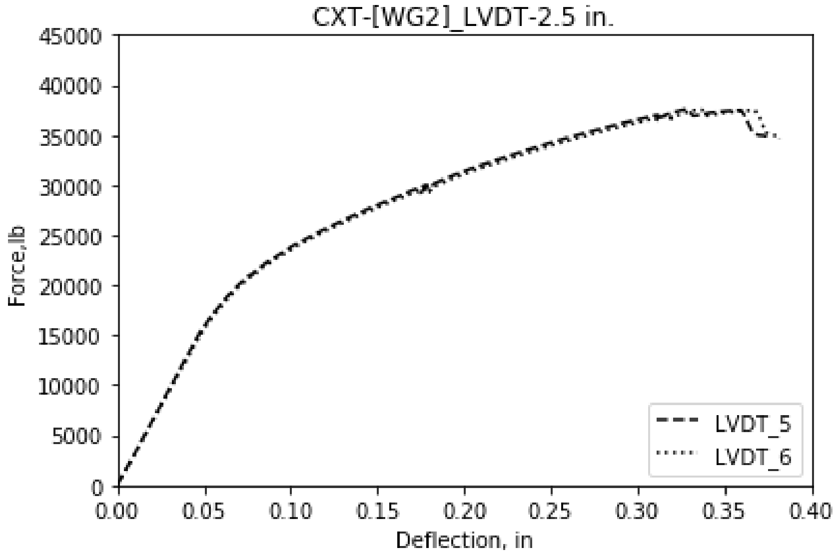

Figure A. 30 CXT-[WG2] Load versus LVDT #5 and #6 reading

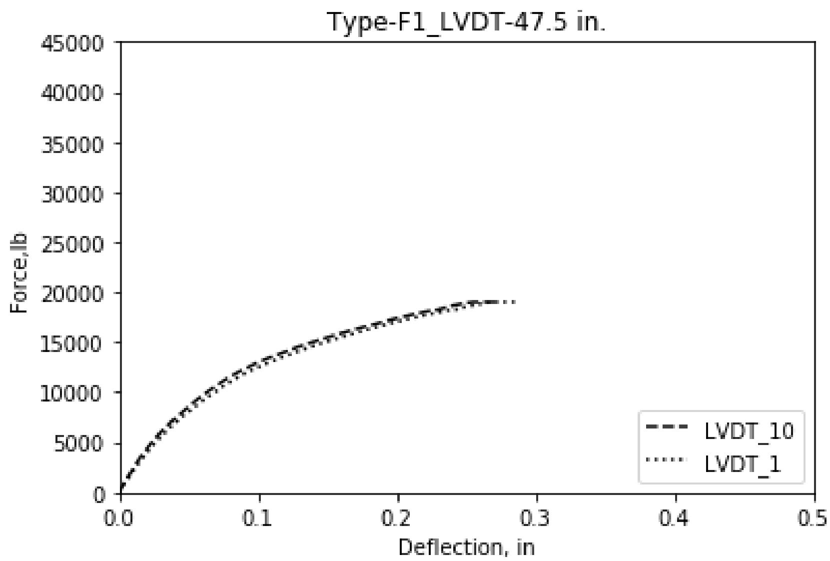

Figure A. 31 Type-F1 Load versus LVDT #1 and #10 reading

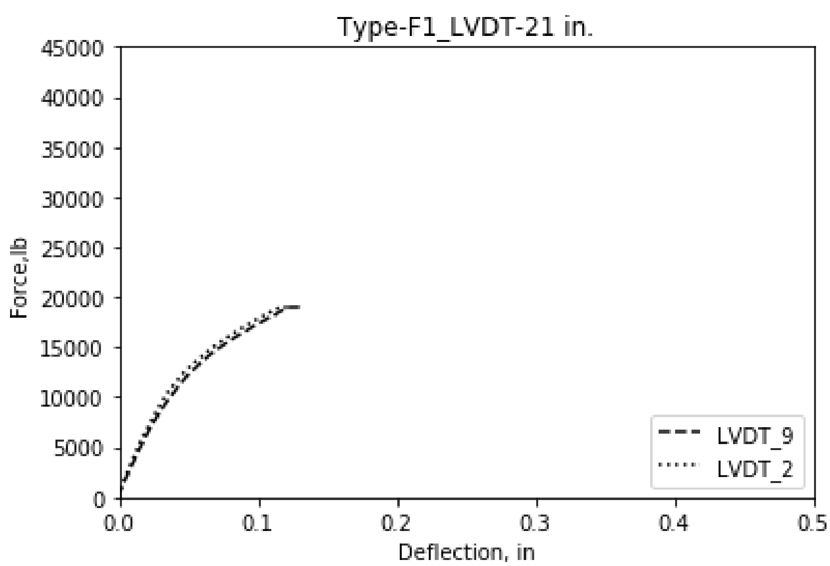

Figure A. 32 Type-F1 Load versus LVDT #2 and #9 reading

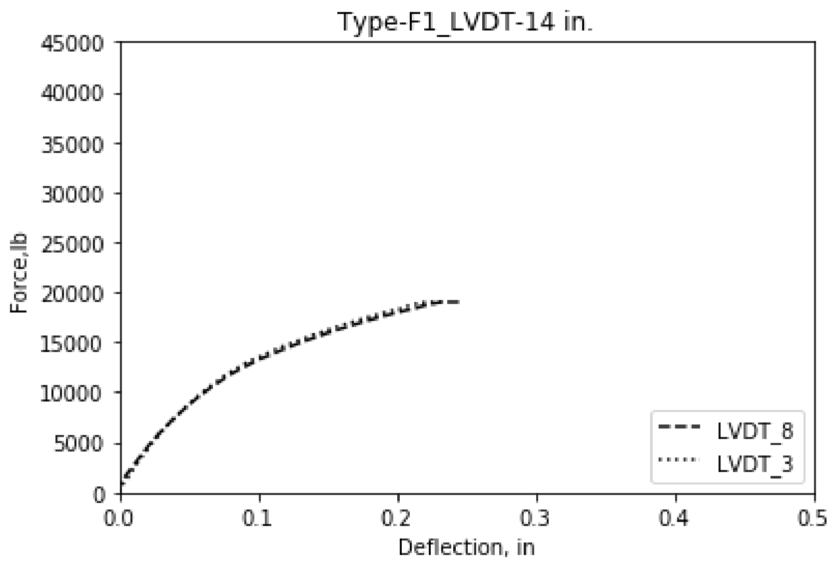

Figure A. 33 Type-F1 Load versus LVDT #3 and #8 reading

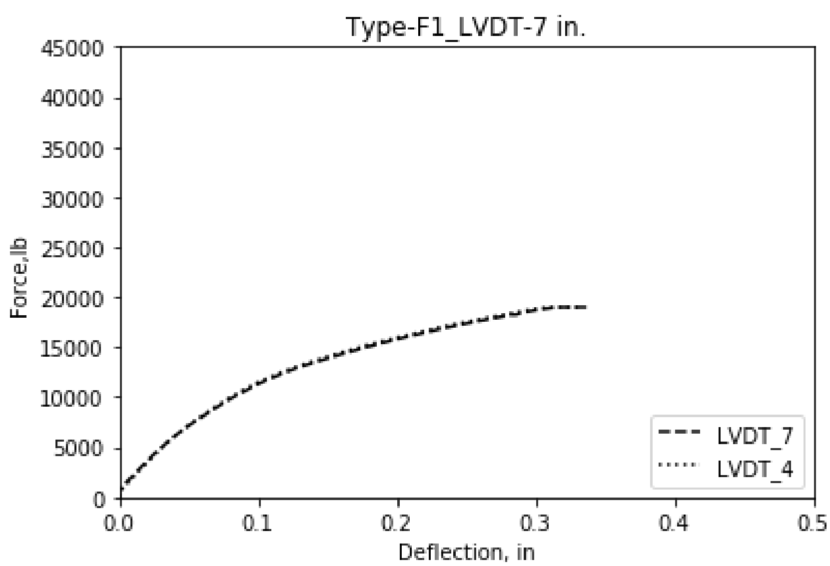

Figure A. 34 Type-F1 Load versus LVDT #4 and #7 reading

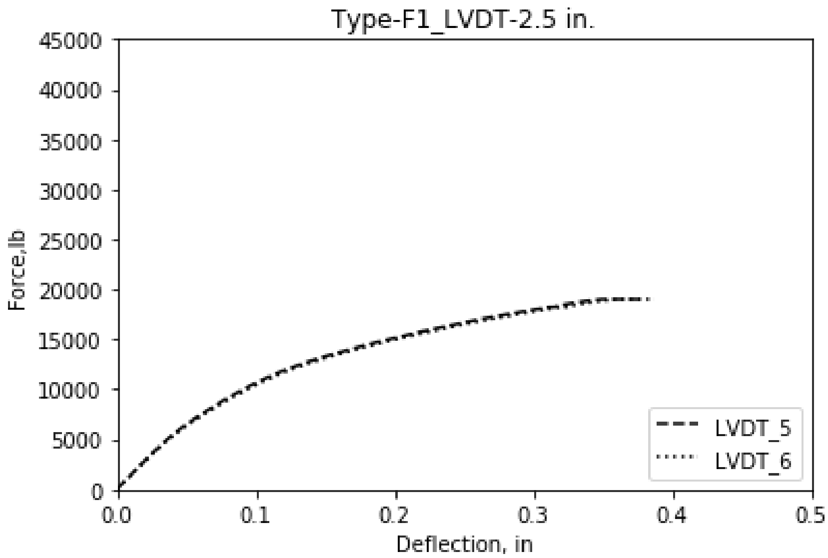

Figure A. 35 Type-F1 Load versus LVDT #5 and #6 reading

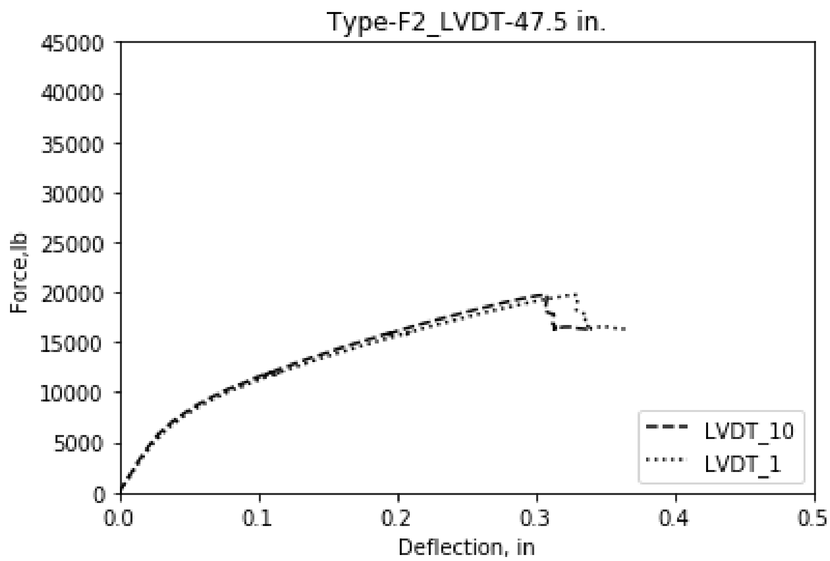

Figure A. 36 Type-F2 Load versus LVDT #1 and #10 reading

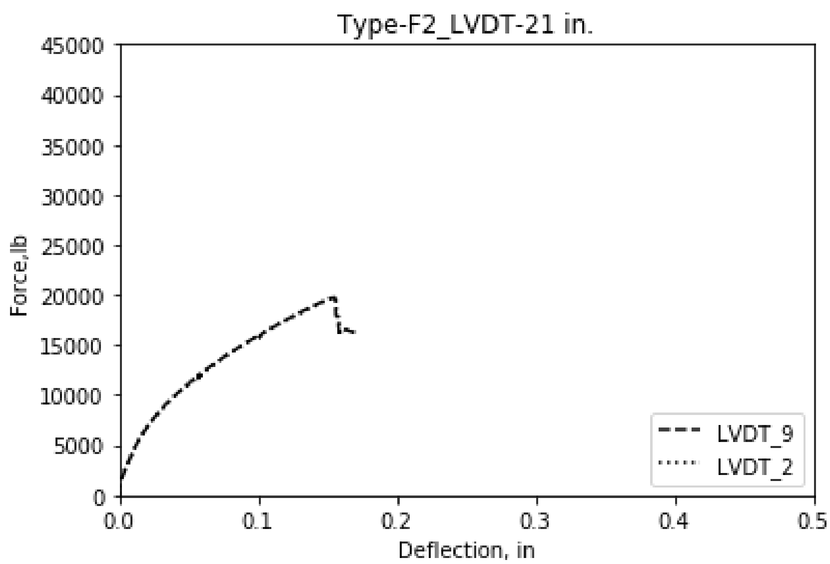

Figure A. 37 Type-F2 Load versus LVDT #2 and #9 reading

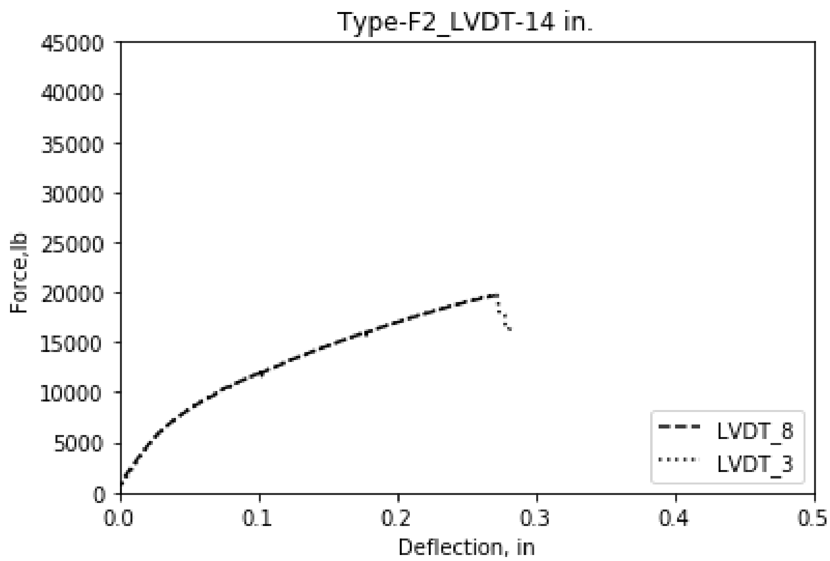

Figure A. 38 Type-F2 Load versus LVDT #3 and #8 reading

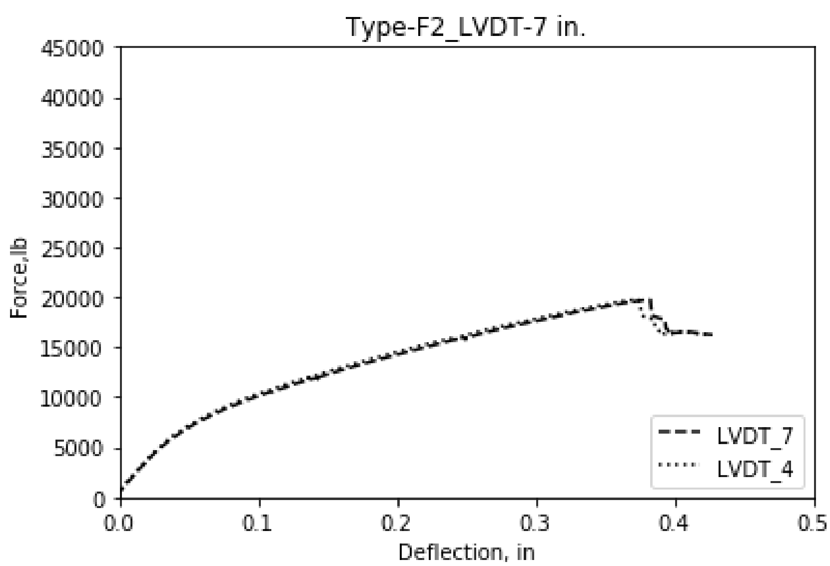

Figure A. 39 Type-F2 Load versus LVDT #4 and #7 reading

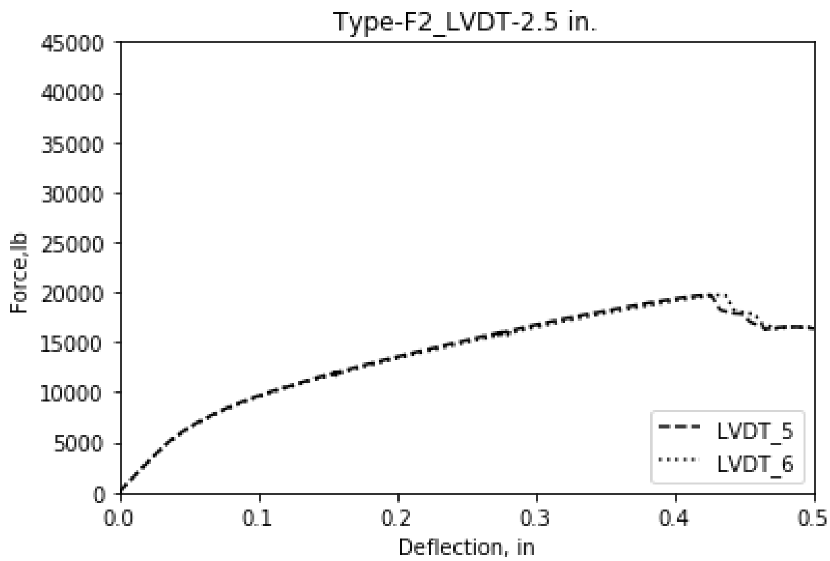

Figure A. 40 Type-F2 Load versus LVDT #5 and #6 reading

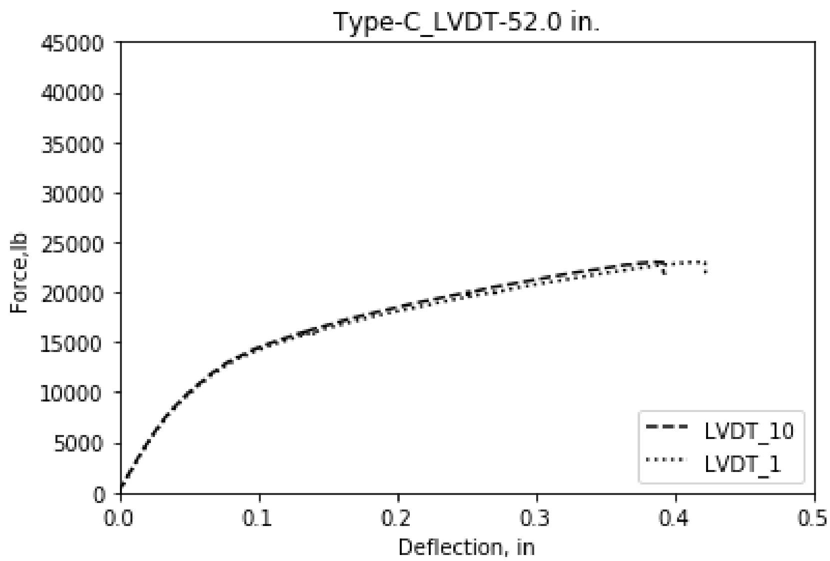

Figure A. 41 Type-C Load versus LVDT #1 and #10 reading

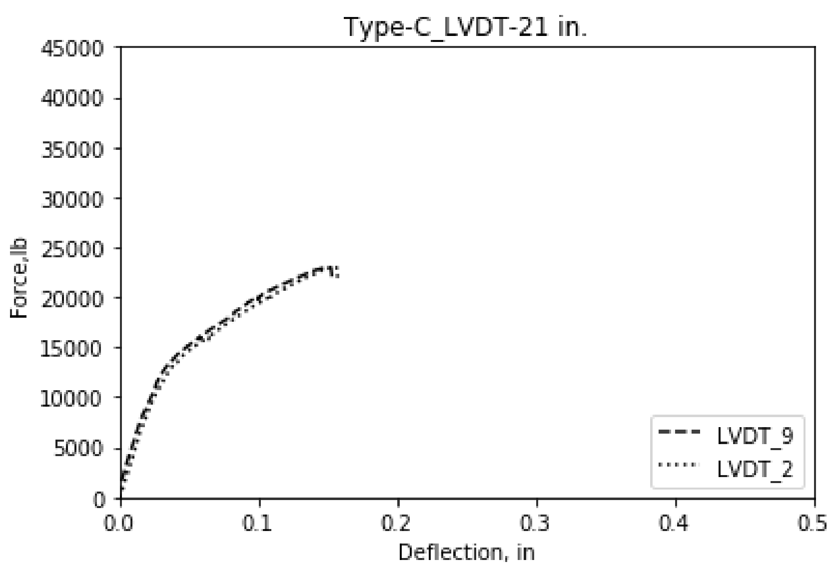

Figure A. 42 Type-C Load versus LVDT #2 and #9 reading

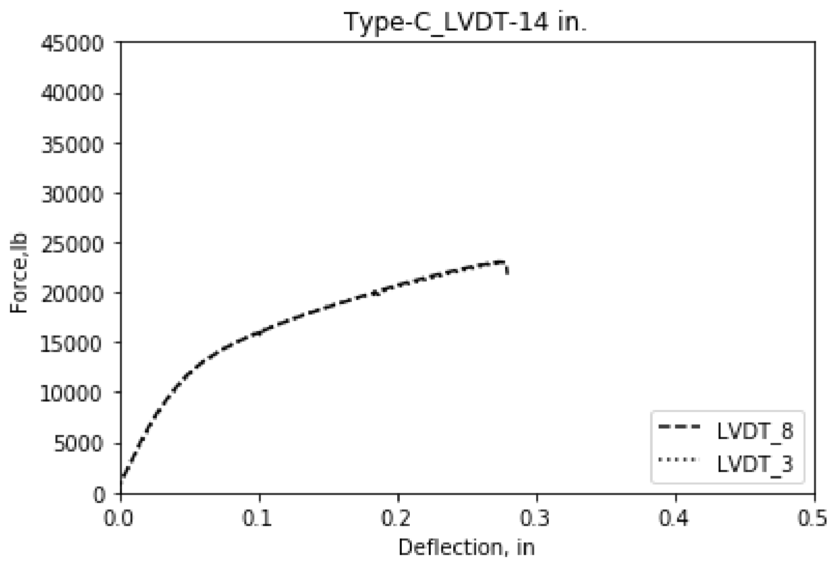

Figure A. 43 Type-C Load versus LVDT #3 and #8 reading

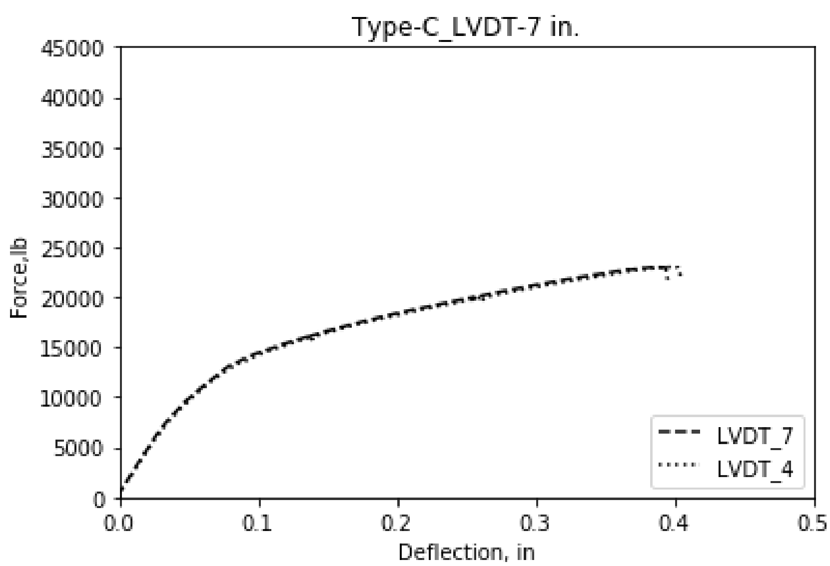

Figure A. 44 Type-C Load versus LVDT #4 and #7 reading

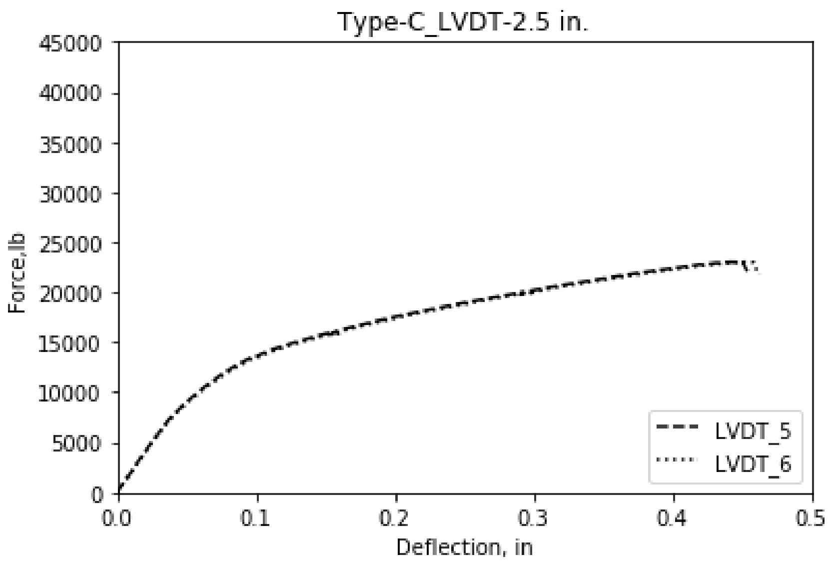

Figure A. 45 Type-C Load versus LVDT #5 and #6 reading

Appendix B - Moment-Curvature Analysis Example

This section presents a set of calculations using in the analysis program, and an Excel program built to compute repeating process for constructing complete moment-curvature curve. The M-C response was determined up to concrete compressive strain at 0.003. The example was a rectangular cross-section shown below:

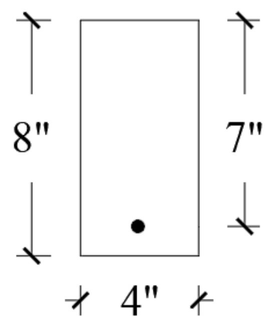

Cross-section Properties:

$A_c = 32\ in^2$

$I = \frac{bh^3}{12} = 170.67\ in^4$

$y = y_t = y_b = 4$ in

$S = S_t = S_b = 42.67\ in^3$

e = 3 in

Concrete Properties:

$f'_c = 7000$ psi

$E_c = 57\sqrt{f_c'} = 4768.96$ ksi

Steel Properties:

Number of wires, n = 6

$E_{ps} = 28414.51$ ksi

$f_{py} = 255.55$ ksi

$f_{se} = 173.803$ ksi (After all losses)

$d_s = 0.209$ in

$A_{ps} = 0.2058\ in^2$

1. Determine Peak Strain, ε_o

   Substituting values into Equation 4.4.

   $\varepsilon_c = \frac{0.5 f'_c}{E_c} = \frac{0.5 \ x \ 7}{4768.96} = 7.34 \times 10^{-4}$

   $0.5 f_c = f'_c \left[\frac{2\varepsilon_c}{\varepsilon_0} - \left(\frac{\varepsilon_c}{\varepsilon_0} \right)^2 \right] \quad \rightarrow 3.5 = 7 \left[\frac{2 \times 7.34 \times 10^{-4}}{\varepsilon_o} - \left(\frac{7.34 \times 10^{-4}}{\varepsilon_o} \right)^2 \right]$

   Solving the equation

   $\varepsilon_o = 0.002056$

2. Initial Stage, M = 0

   Effective stress, $P_e = A_{ps} f_{se} = 35.78$ kips

   Calculating Stress and strain at top and bottom:

   $$f_{top} = -\frac{P_e}{A_c} + \frac{P_e e}{S} = -\frac{35.78}{32} + \frac{35.78 \times 3}{42.67} = +1.4 \ ksi > 0.5 \ ksi$$

   $$f_{bot} = -\frac{P_e}{A_c} - \frac{P_e e}{S} = -\frac{35.78}{32} - \frac{35.78 \times 3}{42.67} = -3.6 \ ksi > 0.5 \ ksi$$

   AREMA Sec. 4.4.2 minimum pre-compressive stress is 0.5 ksi after all losses without external load applied.

   $$\varepsilon_t = \frac{f_t}{E_c} = 2.93 \times 10^{-4}$$

   $$\varepsilon_b = \frac{f_b}{E_c} = -7.62 \times 10^{-4}$$

   Calculating initial curvature, φ

   $$\varphi = \frac{\varepsilon_b - \varepsilon_t}{h} = -1.32 \times 10^{-4} \ \text{CW}$$

   Initial Stress and strain distribution:

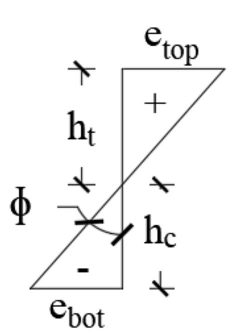

3. Pre-compression of Concrete

   Calculating h_c and h_t

   $h_c = \frac{\varepsilon_o}{\varphi} = 5.77\ in$

   $h_t = 2.23\ in$

   Determining initial concrete strain (ε_{ci}) at level of prestressing wire

   $\varepsilon_{ci} = \frac{\varepsilon_b}{h_c}\left(d_p - h_t\right) = 6.24 \times 10^{-4}$ in compression

   $f_{ci} = \varepsilon_{ci} E_c = 2.98\ ksi$

   Checking AREMA maximum pre-compression limit

   $f_{ci} = 2.98\ ksi\ > AREMA\ Limit = 2.5\ ksi$

   The pre-compression limit surpassed AREMA section 4.4.2 recommendation, the design assumptions need to be adjusted. This is ignored in this example, and the moment-curvature determination is continued.

   Determine strain in prestressing steel due to effective prestress after losses, ε_{pse}

   $\varepsilon_{pse} = \frac{f_{se}}{E_p} = 6.12 \times 10^{-3}$

   Then total strain in prestressing wire, ε_{ps}

   $\varepsilon_{ps} = \varepsilon_{ci} + \varepsilon_{pse} + \varphi\left(d_p - Y\right)$

4. Calculate $M - \varphi$ for $\varepsilon_{ct} = 0.001$

   Assumed compressive depth, Y = 4 in.

   Calculating concrete compression force, C_c by using Equation 4.13

   $\varphi_{0.001} = \frac{\varepsilon_{ct}}{Y} = 2.5 \times 10^{-4}$

   $$C_c = 4 \times 7 \times \frac{2.5 \times 10^{-4}}{0.002056} 4^2 \left[1 - \frac{0.001}{3 \times 0.002056}\right] = 45.64\ \ kips$$

   Calculating tensile force, T

   $\varepsilon_{ps} = 6.744 \times 10^{-3} + 2.5 \times 10^{-4}(7 - 4) = 7.494 \times 10^{-3}$

   Determine stress in prestressing wire (f_{ps}) by using Equation 4.7

$$f_{ps} = 28414.51 \times 7.494 \times 10^{-3}\left[0.018 + \frac{1-0.018}{\left(1+\left(\frac{7.494\times 10^{-3}\times 28414.51}{1.0355\times 255.55}\right)^{7.4386}\right)^{1/7.4386}}\right]$$

$f_{ps} = 207.91$ ksi

$T = A_{ps}f_{ps} = 42.79$ kips

Calculating concrete tension force, Ct

Determine the distance from neutral axis to crack

$$d_{cr} = \varepsilon_{cr} \times \frac{h-Y}{e_b} = 0.53\ in$$

$$f_{ct} = E_{ct} \times \varepsilon_{cr} = 0.281\ ksi$$

$$C_t = f_{ct} \times A_t = 0.59\ kips$$

$T_{Total} = 43.38$ kips

Checking $C_c = T_{Total}$

$C_c \neq T_{Total}$

Compression force is larger than tension force, reducing Y.

Reducing compressive depth, and repeating same procedures until tension and compression force converged. Excel program was used to compute repeating process.

Then found T = C when Y = 4.41 inch

$C_c = 42.68$kips

$T = 42.02$ kips

$C_t = 0.65$ kips

$$\varepsilon_b = 8.15 \times 10^{-4}$$

5. Determine $M_n = M_c - M_{ct}$

Calculating the distance from center of compression to bottom level of prestressing wire, d_c

$$d_c = \bar{x} + (d_p - Y)$$

Computing $\bar{x}$ by using Equation 4.14

$$\bar{x} = 4.41\left[\frac{8\times 0.002056 - 3\times 0.001}{12\times 0.002056 - 4\times 0.001}\right] = 2.87\ in$$

Then

$$d_c = 2.87 + (7 - 4.41) = 5.46\ in$$

$M_c = C_c \times d_c = 2233.03$ k-in.

Calculating the distance from center of tension to bottom level of prestressing wire, d_{ct}

$$d_{ct} = h - \left(Y + \frac{d_{cr}\times 2}{3}\right) = 2.205\ in$$

Then

$$M_{ct} = C_t \times d_{ct} = 1.44 \text{ k-in}$$

Computing M_n

$M_n = 231.59$ k-in

6. Determine M_{cr} and Φ_{cr}

Equation 4.11 used, and solving M_{cr}

$$\frac{7.5\sqrt{7}}{1{,}000} = -\frac{35.76}{32} - \frac{35.76 \times 3}{42.67} + \frac{M_{cr}}{42.67}$$

$M_{cr} = 181.74$ k-in.

Equation 4.12 used to determine Φ_{cr}

$$\emptyset_{cr} = \frac{181.74 - 35.76 \times 3}{4768.96 \times 170.67} = 9.15 \times 10^{-5}$$

7. Moment Capacity based on ACI stress limit (Table 4.1)

$$f_{Tension} = 7.5\sqrt{f_c'} = 0.627\ ksi$$

$$f_{Compression} = 0.6 f_c' = 4.2\ ksi$$

$$f_{top} = -\frac{P_e}{A_c} + \frac{P_e e}{S_t} - \frac{M_L}{S_t} = -\frac{35.76}{32} + \frac{35.76 \times 3}{42.67} - \frac{M_L}{42.67}$$

$$f_{bot} = -\frac{P_e}{A_c} - \frac{P_e e}{S_b} + \frac{M_L}{S_b} = -\frac{35.76}{32} - \frac{35.76 \times 3}{42.67} + \frac{M_L}{42.67}$$

Positive Moment, k-in				Negative Moment, k-in			
Rail-Seat		Rail-Center		Rail-Seat		Rail-Center	
Top	Bottom	Top	Bottom	Top	Bottom	Top	Bottom
238.81	181.72	238.81	181.72	-32.84	-24.25	-32.84	-24.25

Positive Moment Capacity:

$M_{R+} = 181.72$ k-in

Negative Moment Capacity:

M_{R-} = -24.25 k-in

The moment capacity can be compared with AREMA experimental flexural limit once the rail-seat load was defined. The minimum value should be taken as capacity limit.

Repeating step 5 and 6 with increased strain at compression surface until it reached 0.003. Excel program used to perform this process as shown below:

Inputs

Concrete Properties			Steel Properties		
h	8.00	in	Eps	28414.51	ksi
b	4.00	in	Aps	0.034	in2
fc	7000.00	ksi	fpy	255.55	ksi
Ec	4768.96	ksi	fse	173.80	ksi
A	32.00	in2	Q	0.018	
I	170.67	in2	K	1.0355	
yb	4.00	in	R	7.4386	
yt	4.00	in			
eo	2.51E-03				

Initial Stage, M=0

	layer 1	layer 2	layer 3	layer 4
n	6	0	0	0
dp, in	7	0	0	0
Aps, in2	0.206	0	0	0
P, k	35.78	0	0	0
e, in	3	-4	-4	-4
f_top, ksi	1.40	0	0	0
f_bot, ksi	-3.63	0	0	0

Summary at M=0

ft	1.40	ksi
fb	-3.63	ksi
et	2.93E-04	
eb	-7.62E-04	
phi	-1.32E-04	rad/in
Y	2.222	in

Assumption

ec_limit	7.34E-04	
ect	-0.0010000	
Y	4.41	in
eb	8.15E-04	in/in
phi	2.27E-04	rad/in

Concrete in Compression Force

	(1) Linear Eq.	(2) Rectangular Eq.	(3) layer analysis
x1	3.83	3.8	
b1	4	4	
fc	5.20		
Cc1	39.80	43.68	42.68
x_bar1	2.55	2.49	
dc	5.72	5.66	
Mc	227.84	247.28	233.34

Concrete in Tension

Ect_limit	2132.7	ksi
ect_limit	0.000328	
dcr	0.58006	in
dt	4.80	in
fct	1.32E-04	ksi
Ct	0.281	kips
dct	0.65111	in

Tensile Force

	e_{ci}	e_{pse}	e_c	e_{ps}	f_{ps}, ksi	P, kips
layer 1	6.30E-04	6.12E-03	5.88E-04	7.34E-03	204.16	42.02
layer 2	-2.93E-04	6.12E-03	-1.00E-03	5.12E-03	145.17	0.00
layer 3	-2.93E-04	6.12E-03	-1.00E-03	5.12E-03	145.17	0.00
layer 4	-2.93E-04	6.12E-03	-1.00E-03	5.12E-03	145.17	0.00

Force Equilibrium

T	42.02	kips
Cc	-42.68	kips
Ct	0.65	kips
C=T	0.000524	kips

Moment Force

Mc	233.34	k-in
Mct	-1.44	k-in
Mt	0.00	k-in
Mn	**231.91**	k-in

Cracking

fb=fr	0.627	ksi
fc_t	-2.863	ksi
ect	-6.00E-04	
ecb	1.32E-04	
Mcr	**181.802**	k-in
phi	**9.15E-05**	rad/in

3

The computing results and M-Φ curve are shown below:

	e_{ct}	e_b	Y, in	Φ , rad/in	M, k-in
Initial Stage, M=0				-1.32E-04	0.0
Crack				9.15E-05	181.8
	-0.0008	6.49E-04	4.417	1.54E-04	214.7
	-0.001	1.09E-03	3.827	2.27E-04	231.9
	-0.0015	2.35E-03	3.115	4.32E-04	267.2
	-0.002	3.70E-03	2.806	6.55E-04	293.4
	-0.0025	5.03E-03	2.656	8.89E-04	310.2
	-0.003	6.18E-03	2.613	1.12E-03	318.5

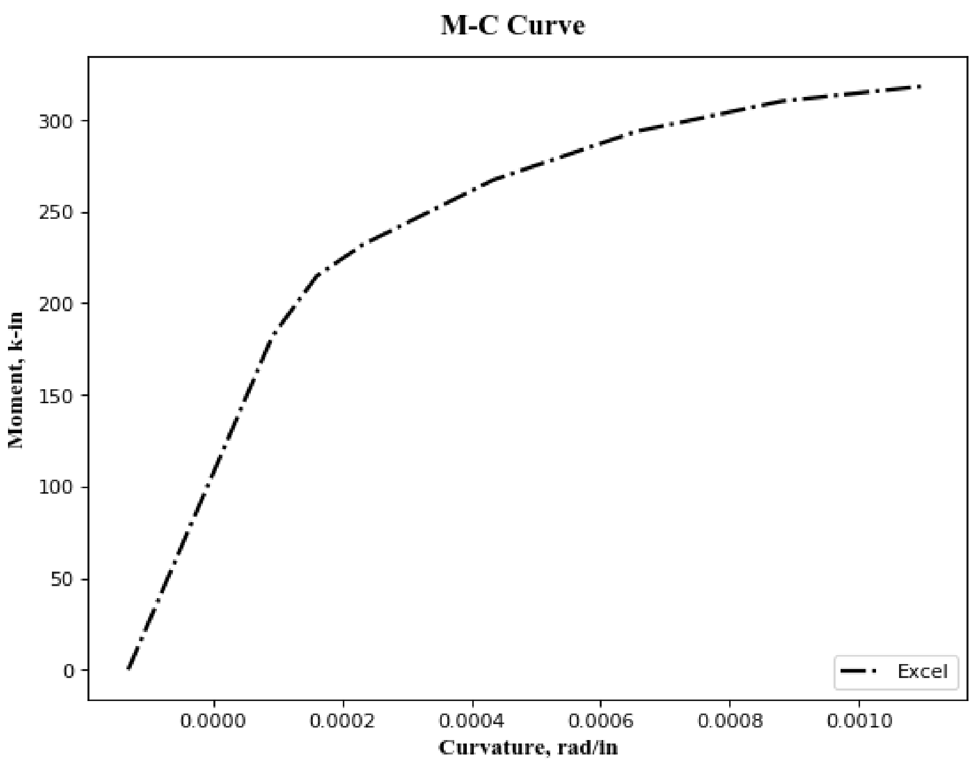

This example also analysis by using developed program, and the results and plot are presented below:

	ect	eb	Y	Φ , rad/in	M
Initial Stage, M=0				-1.32E-04	0.0
Crack				9.15E-05	181.8
	-0.0008	4.42E-04	5.15	1.55E-04	213.7
	-0.001	8.29E-04	4.37	2.29E-04	230.6
	-0.0012	1.27E-03	3.89	3.09E-04	245.5
	-0.0014	1.74E-03	3.56	3.93E-04	258.8
	-0.0016	2.25E-03	3.33	4.81E-04	270.8
	-0.0018	2.77E-03	3.15	5.71E-04	281.3
	-0.002	3.31E-03	3.01	6.64E-04	290.3
	-0.0022	3.86E-03	2.90	7.58E-04	297.9
	-0.0024	4.43E-03	2.81	8.53E-04	304.1
	-0.0026	4.99E-03	2.74	9.49E-04	309.1
	-0.0028	5.55E-03	2.68	1.04E-03	312.8
	-0.003	6.09E-03	2.64	1.14E-03	315.5

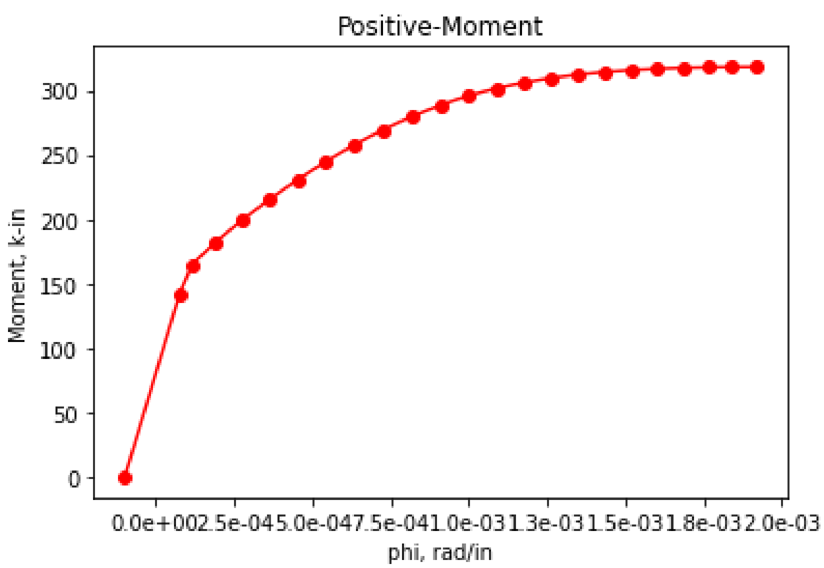

Appendix C - Code to Michigan Tech Example

The detail inputs and calculation results were presented in this section.

Table C. 1 Coordinate cross-section inputs in the Python program

X1	0	0.39	1.1	8.79	9.5	9.88
X2	0	0.39	1.1	8.79	9.5	9.88
X3	0	0.39	1.1	8.79	9.5	9.88
X4	0.75	1.06	1.69	8.19	8.82	9.13
X5	0.75	1.06	1.69	8.19	8.82	9.13
Z1	0	8.59	9.3	9.3	8.59	0
Z2	0	8.59	9.3	9.3	8.59	0
Z3	0	8.59	9.3	9.3	8.59	0
Z4	0	6.88	7.51	7.51	6.88	0
Z5	0	6.88	7.51	7.51	6.88	0

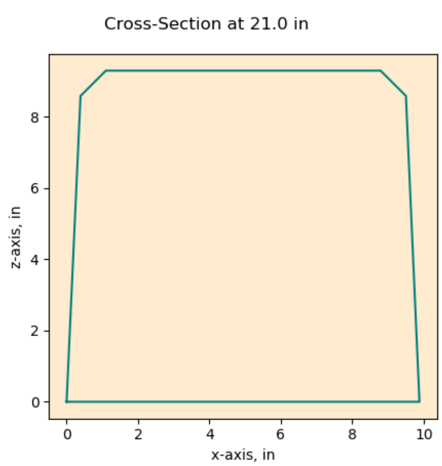

(a) Rail-seat

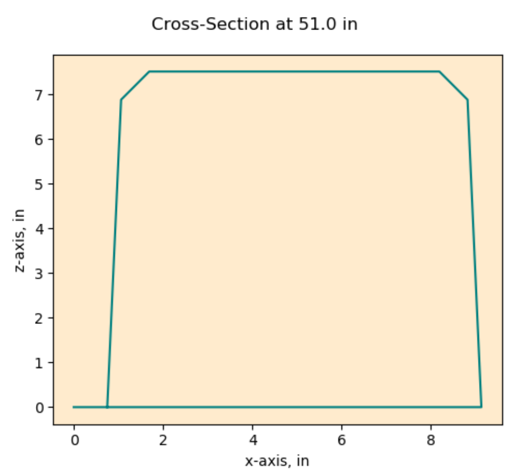

(b) Rail-center

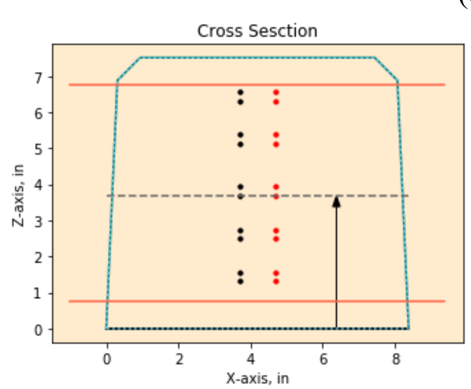

(c) Rail-center with reinforcements

Figure C. 1 Coded cross-section plots and reinforcement pattern

Table C. 2 Cross-section properties

	Rail-Seat			Rail-Center		
	Michigan Tech	Program	Difference, %	Michigan Tech	Program	Difference, %
Ac, in^2	87.35	87.53	0.2%	57.95	59.50	2.7%
y_t, in	4.74	4.76	0.4%	3.78	3.80	0.5%
y_b, in	4.55	4.55	0.0%	3.72	3.70	0.5%
I_x, in^4	621.76	634.72	2.1%	273.55	278.44	1.8%
e, in	0.6375	0.638	0.1%	-0.1925	-0.216	-12.2%

Table C. 3 Concrete properties

	Michigan Tech	Program
f'c, psi	7000	7000
Ec, ksi	4768.96 (ACI)	4768.96 (ACI)
f'ci, psi	4500	4500
Eci, ksi	3823.67 (ACI)	3823.67 (ACI)

Table C. 4 Prestressing wire properties

	Michigan Tech	Program	Difference, %
A_{ps}, in^2	0.689	0.686	0.4%
f_{py}, ksi	229.898	240.47	4.6%
f_{pu}, ksi	255.443	267.47	4.7%
E_{ps}, psi	28500	28889.56	1.4%
$f_{jacking}$, ksi	203.19	0.75fpu=200.6	1.3%

Table C. 5 Loss at 40 days

		Michigan Tech	Program (AASHTO Refine Method)	Difference, %
Rail Set	fsi, ksi	188.42	191.09	1.4%
	fse, ksi	173.07	171.32	1.0%
Rail Center	fsi, ksi	182.96	187.87	2.7%
	fse, ksi	163.71	164.04	0.2%

Appendix D - PDFs and CDFs of Monte-Carlo Simulation Moment

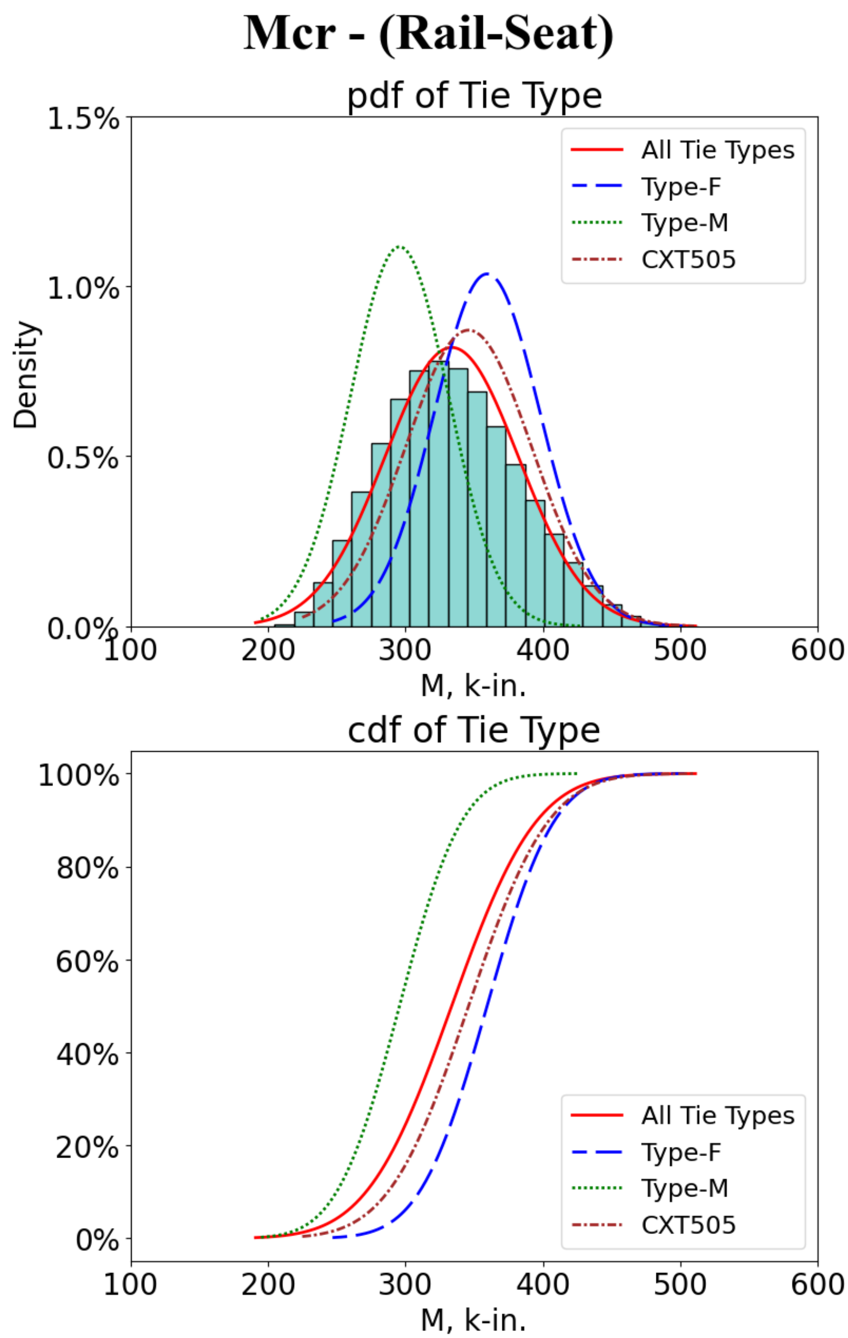

Figure D. 1 CDF and PDF plots of tie type - rail-seat positive at first crack moment (M_{cr}).

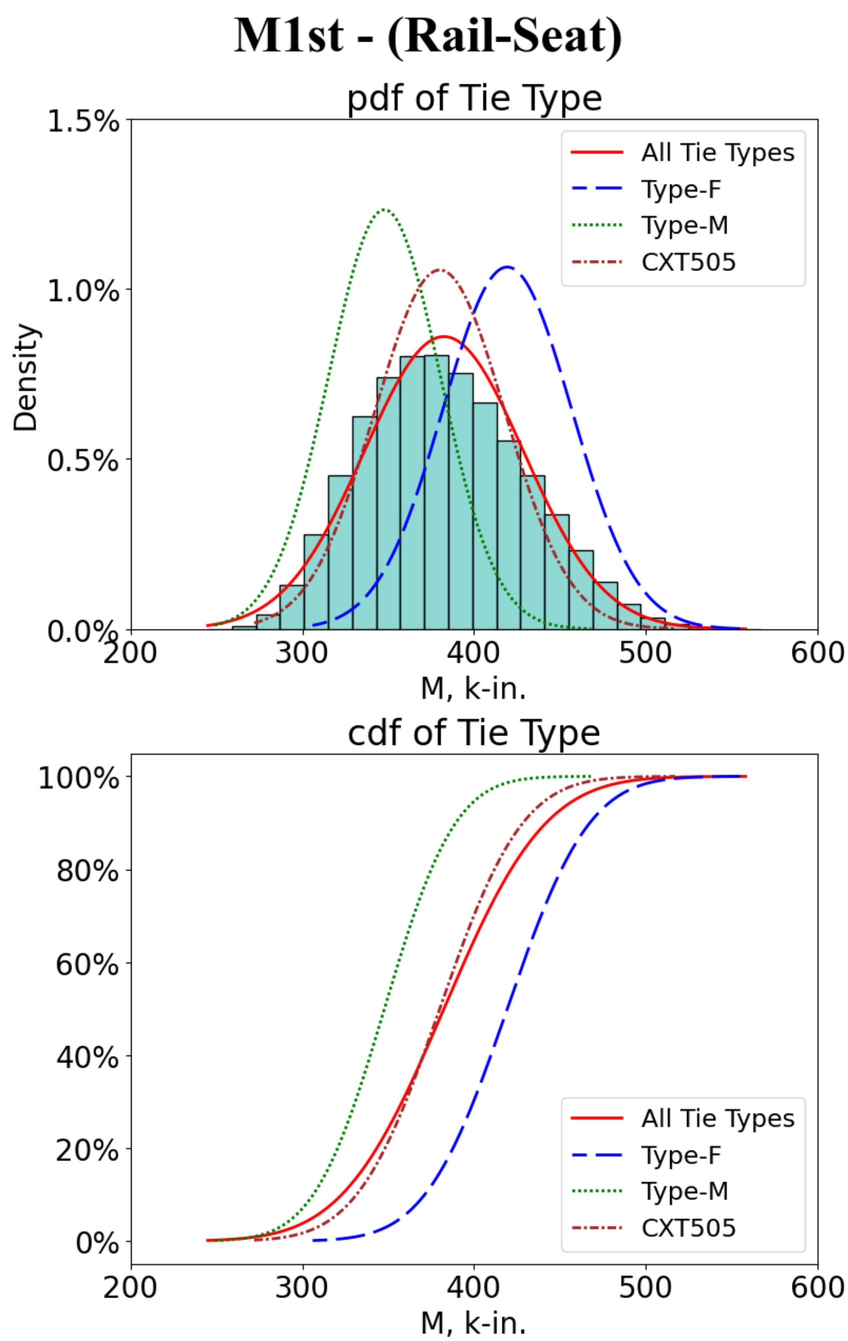

Figure D. 2 CDF and PDF plots of tie type - rail-seat positive at crack reached to outer layer of reinforcement moment (M_{1st}).

Mult - (Rail-Seat)

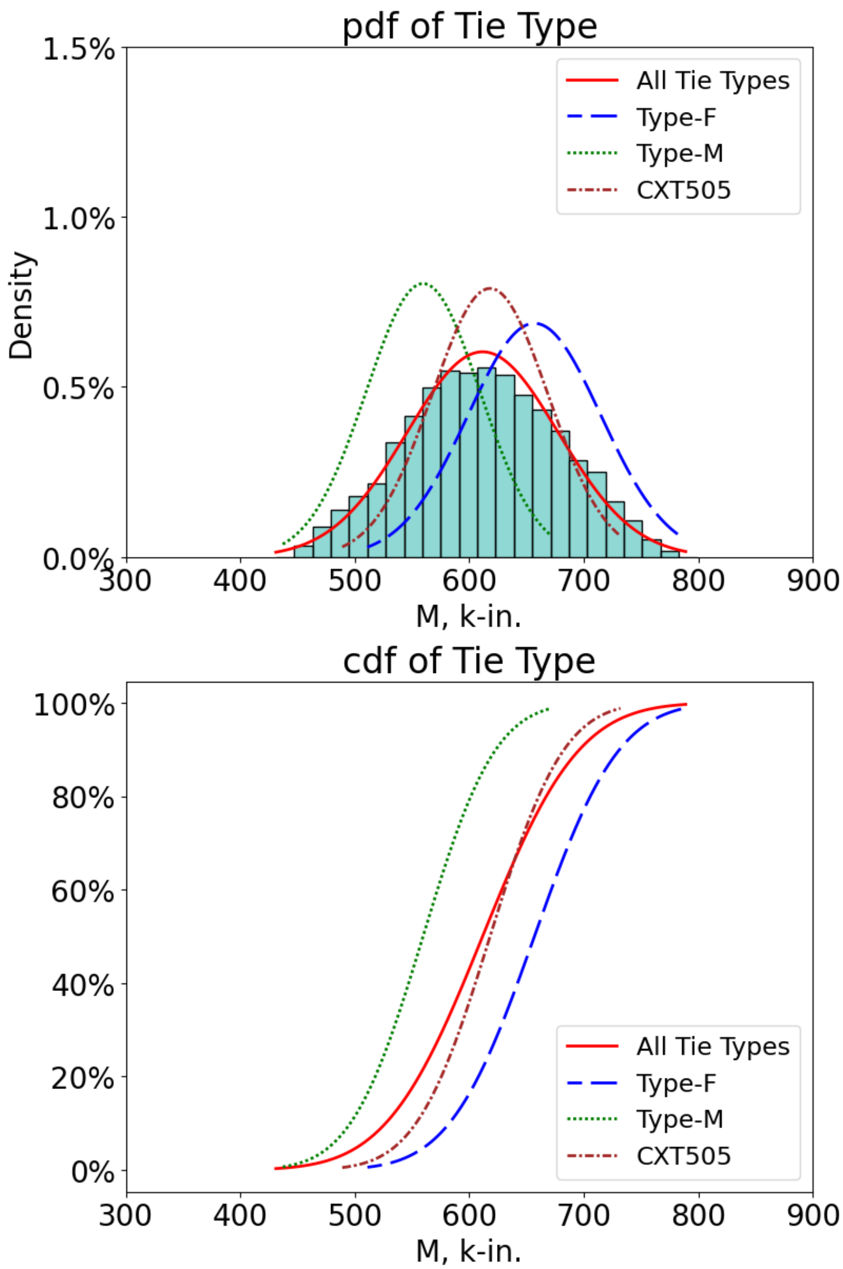

Figure D. 3 CDF and PDF plots of tie type - rail-seat positive at ultimate crack moment (M_{ult}).

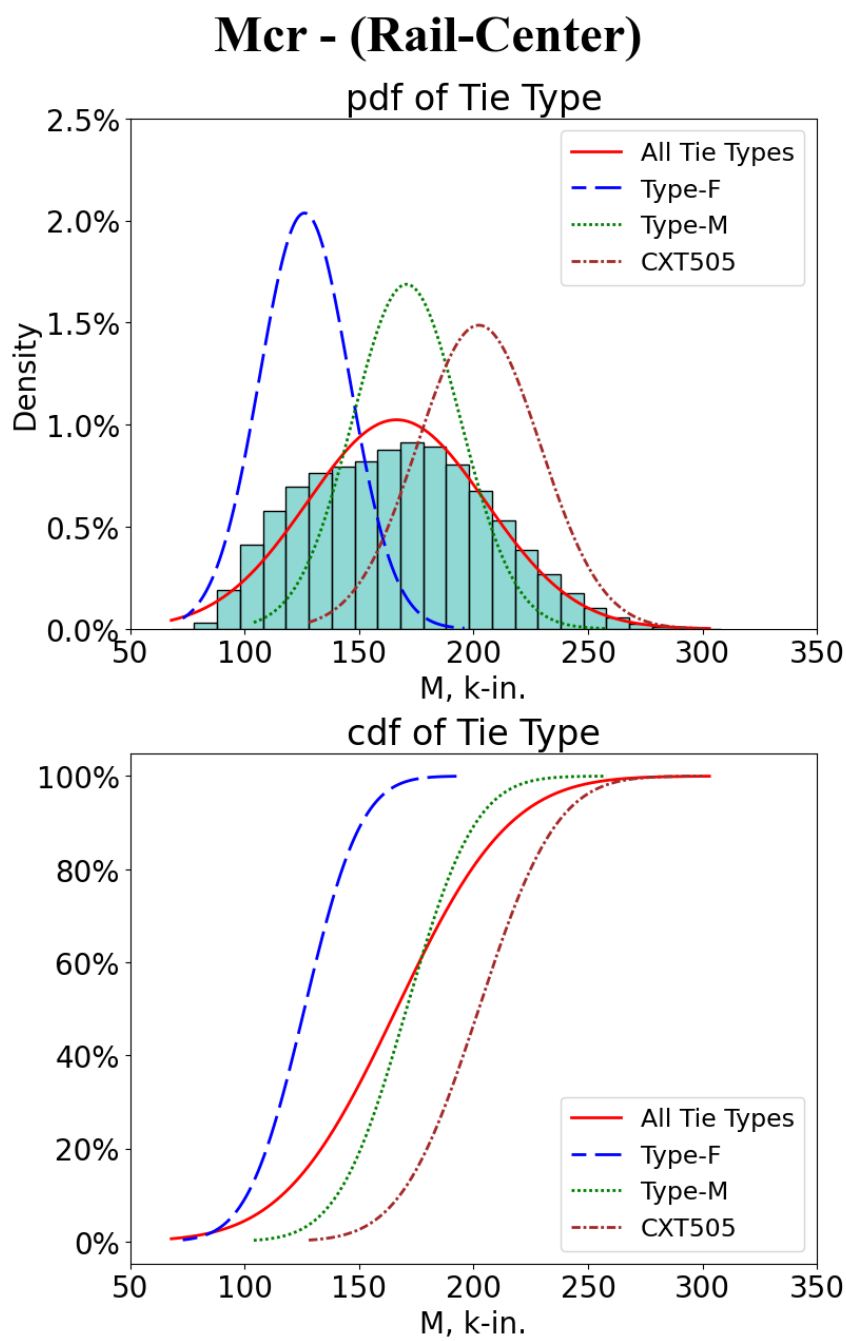

Figure D. 4 CDF and PDF plots of tie type - rail-center negative at first crack moment (M_{cr}).

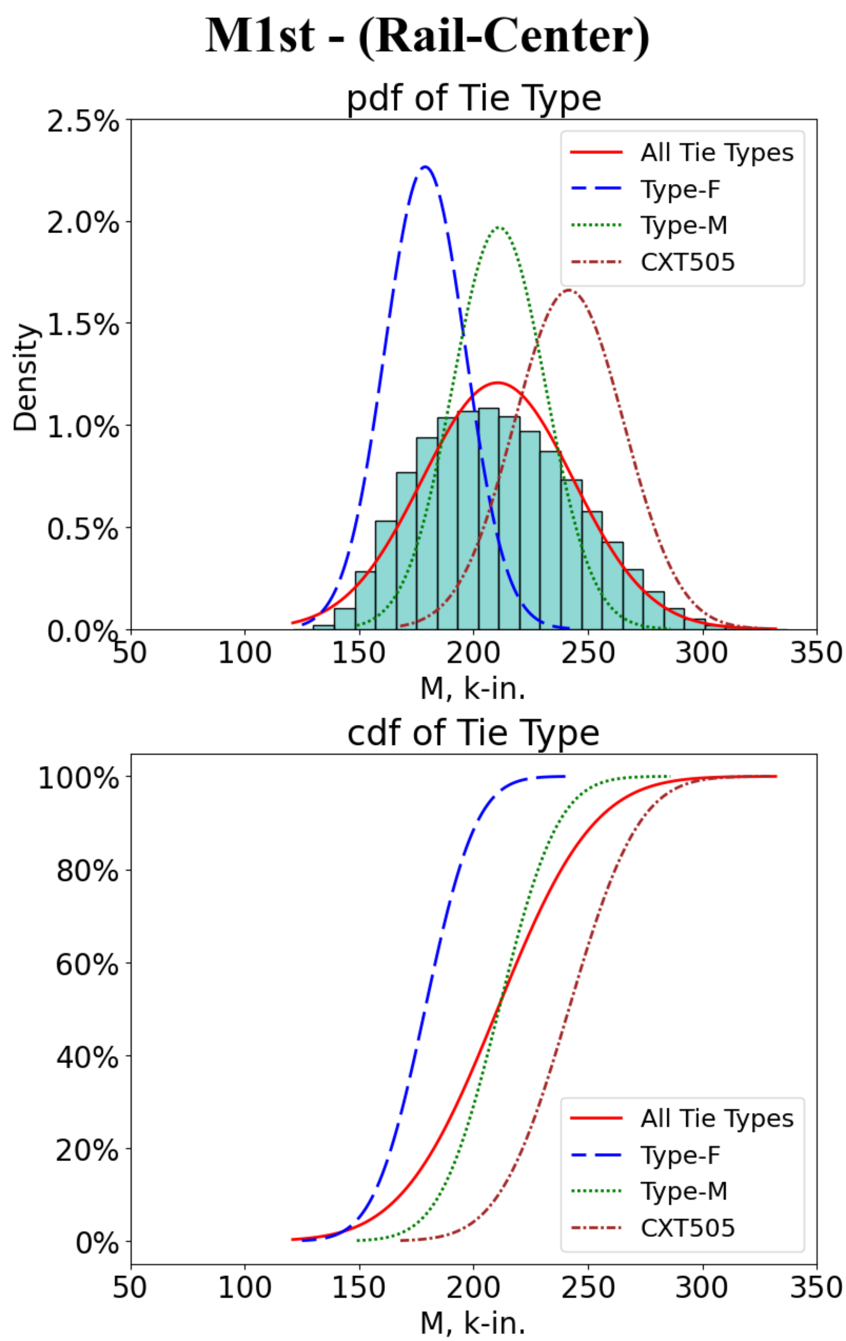

Figure D. 5 CDF and PDF plots of tie type - rail-center negative at crack reached to outer layer of reinforcement moment (M_{1st}).

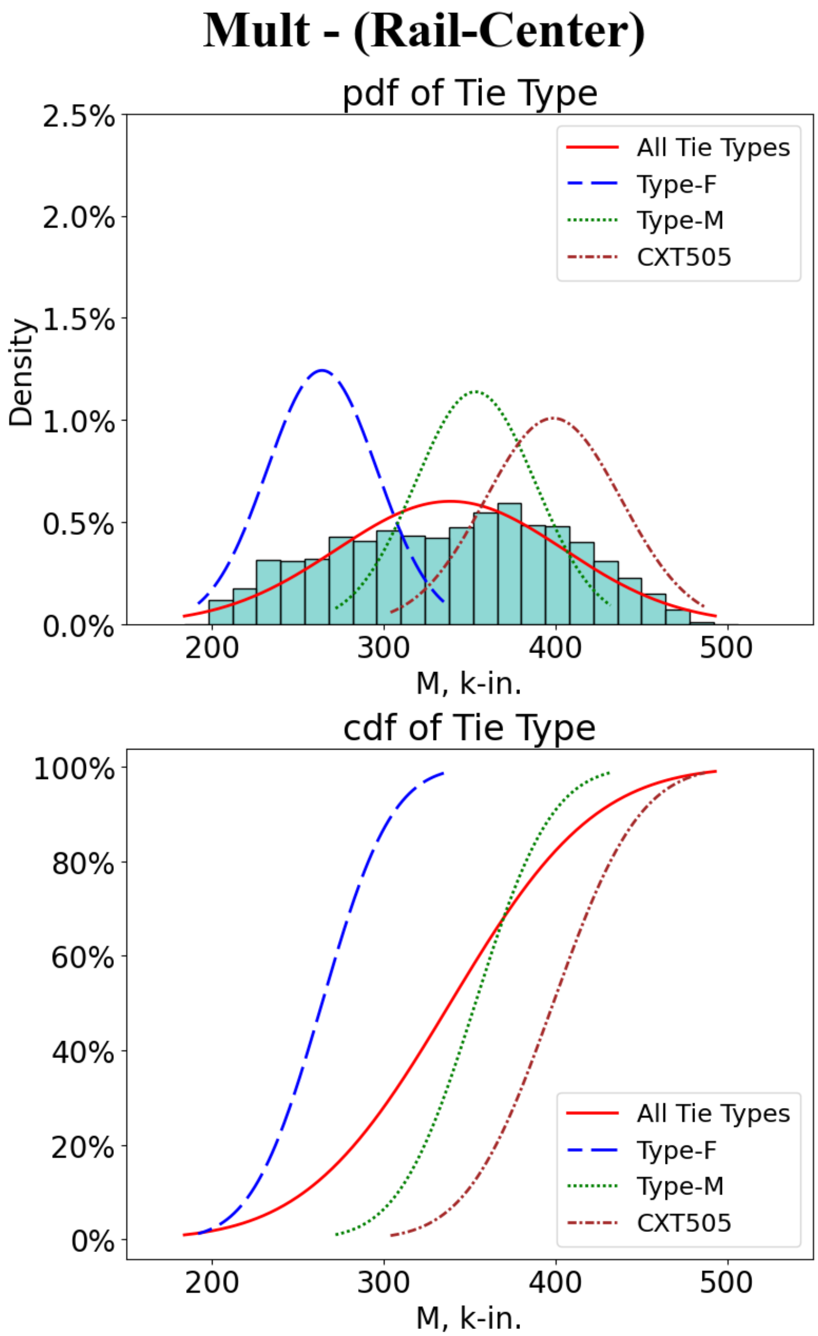

Figure D. 6 CDF and PDF plots of tie type rail - center negative at ultimate crack moment (M_{ult}).

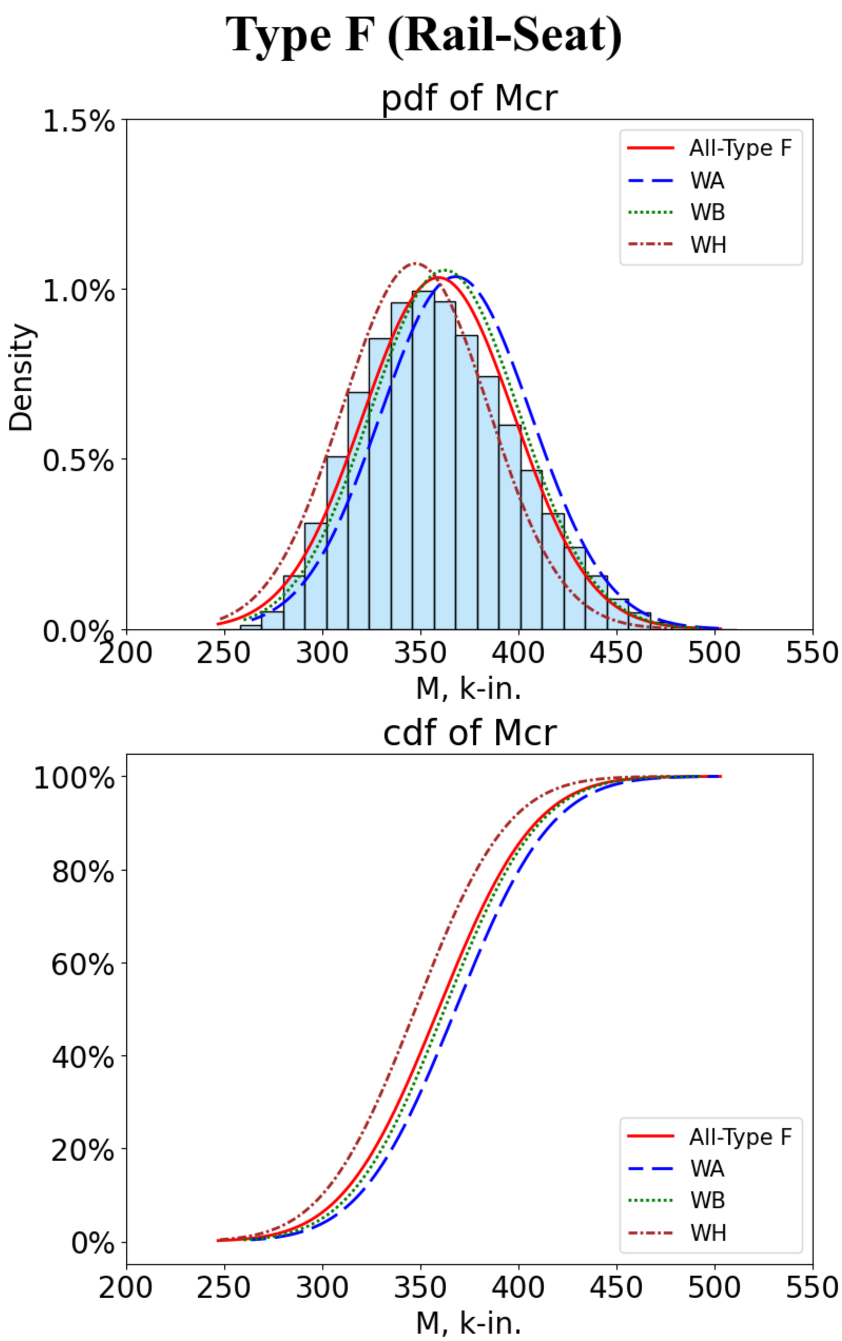

Figure D. 7 CDF and PDF plots of wire type for Type F tie rail-seat positive at first crack moment (M_{cr}).

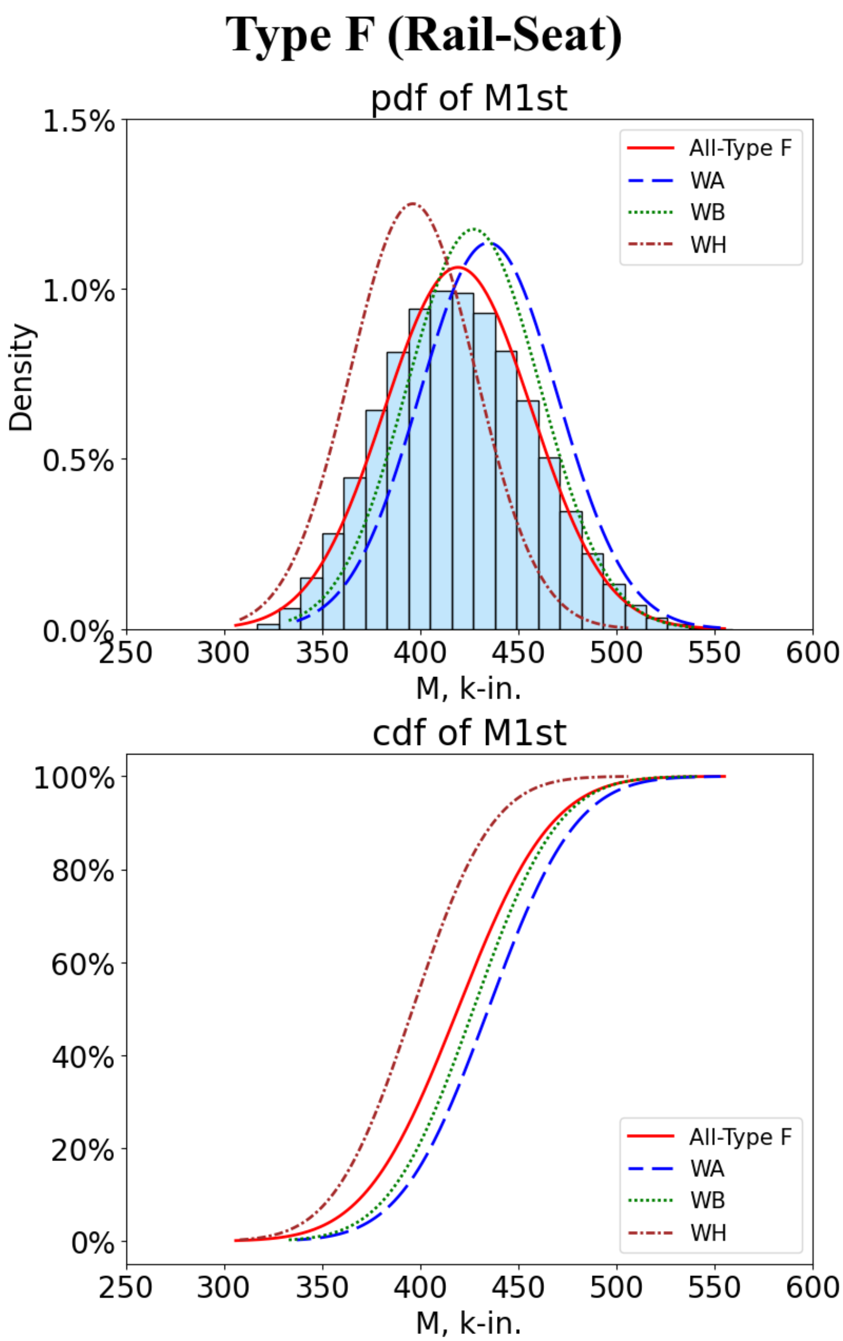

Figure D. 8 CDF and PDF plots of wire type for Type F tie rail-seat positive at crack reached to outer layer of reinforcement moment (M_{1st}).

Type F (Rail-Seat)

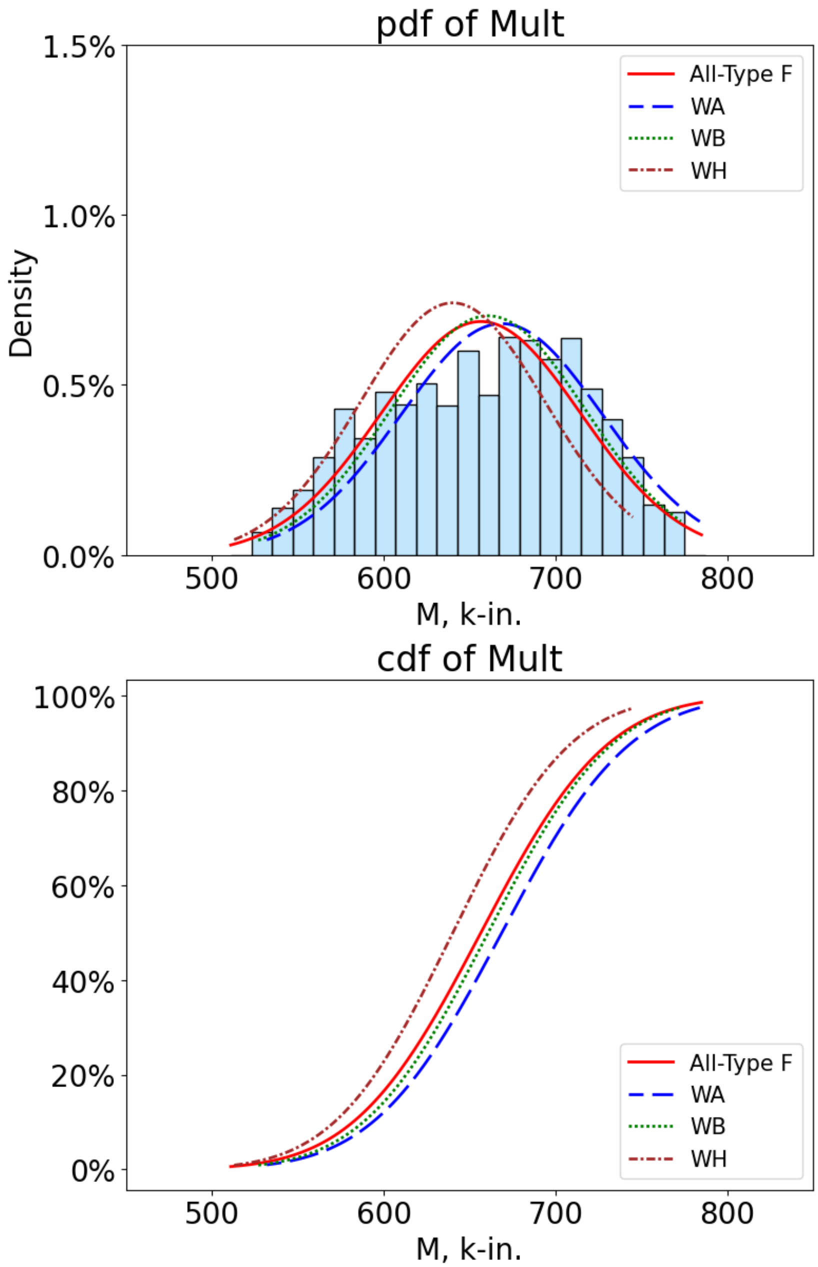

Figure D. 9 CDF and PDF plots of wire type for Type F tie rail-seat positive at ultimate crack moment (M_{ult}).

Type F (Rail-Center)

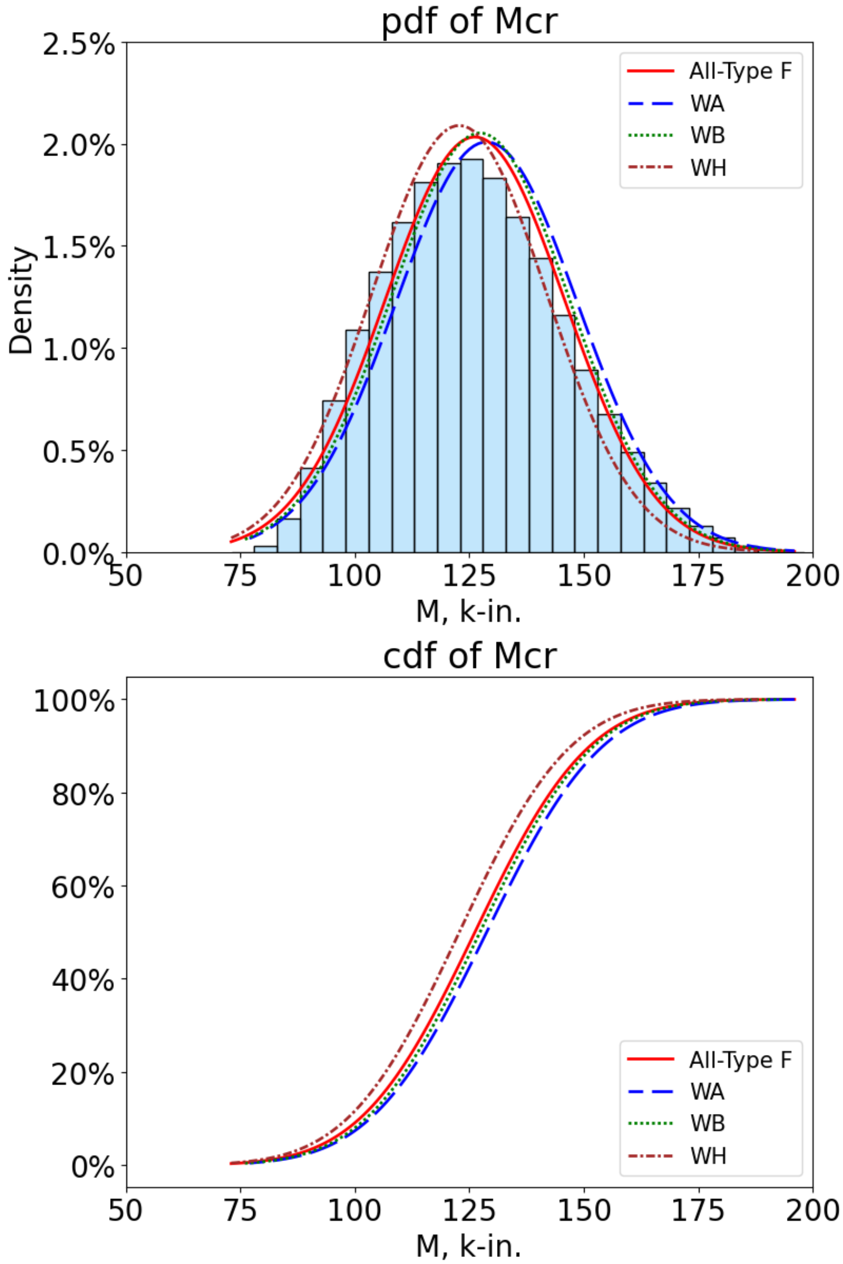

Figure D. 10 CDF and PDF plots of wire type for Type F tie rail-center negative at first crack moment (M_{cr}).

Type F (Rail-Center)

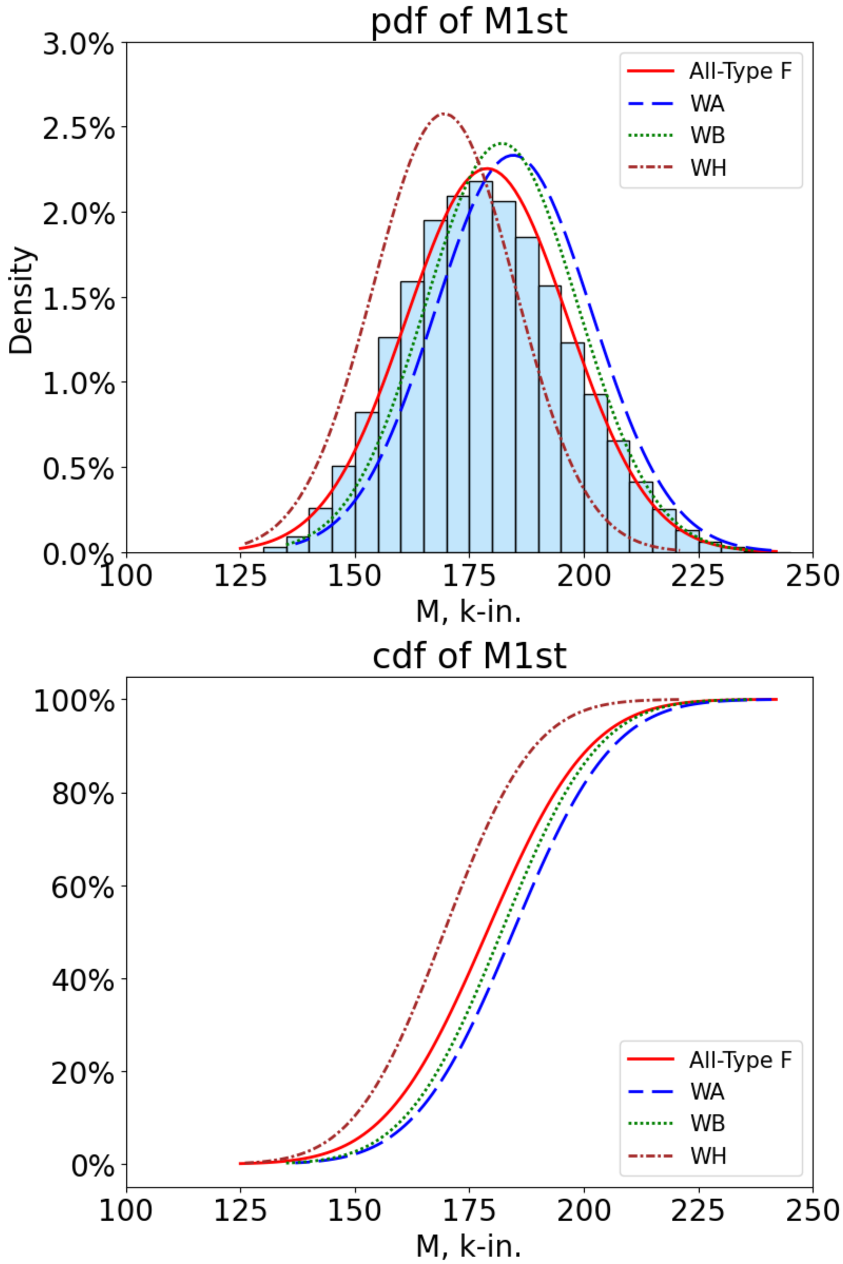

Figure D. 11 CDF and PDF plots of wire type for Type F tie - rail-center negative at crack reached to outer layer of reinforcement moment (M_{1st}).

Type F (Rail-Center)

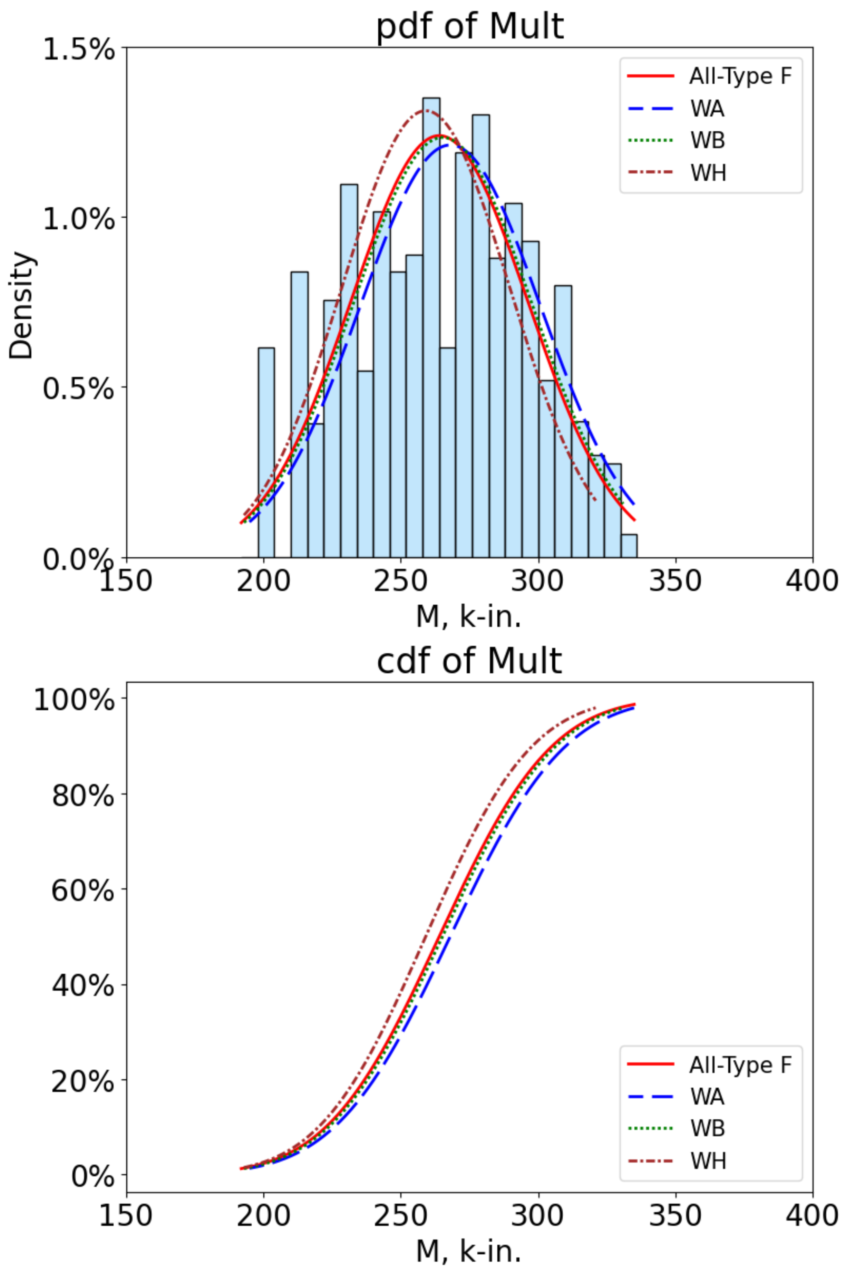

Figure D. 12 CDF and PDF plots of wire type for Type F tie rail-center negative at ultimate crack moment (M_{ult}).

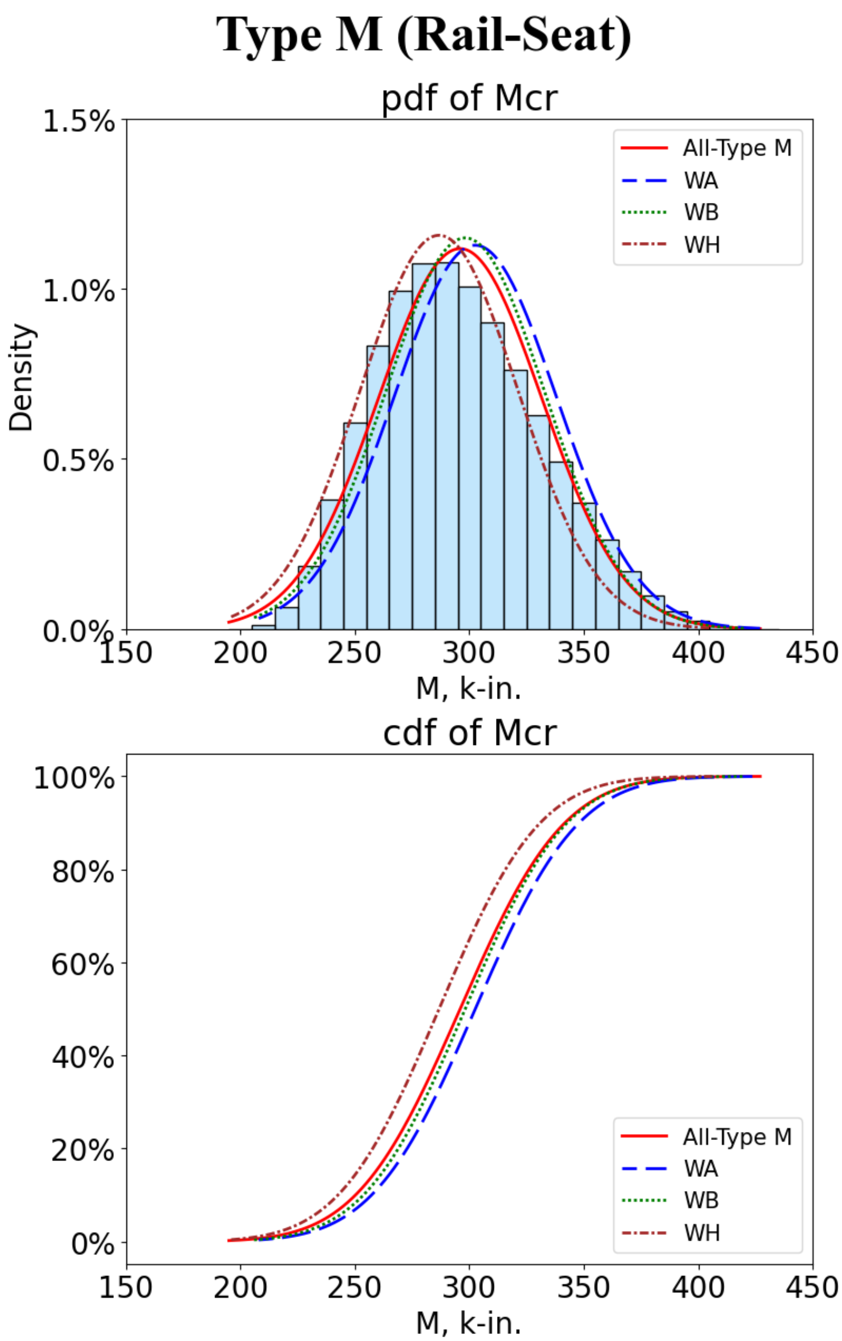

Figure D. 13 CDF and PDF plots of wire type for Type M tie rail-seat positive at first crack moment (M_{cr}).

Type M (Rail-Seat)

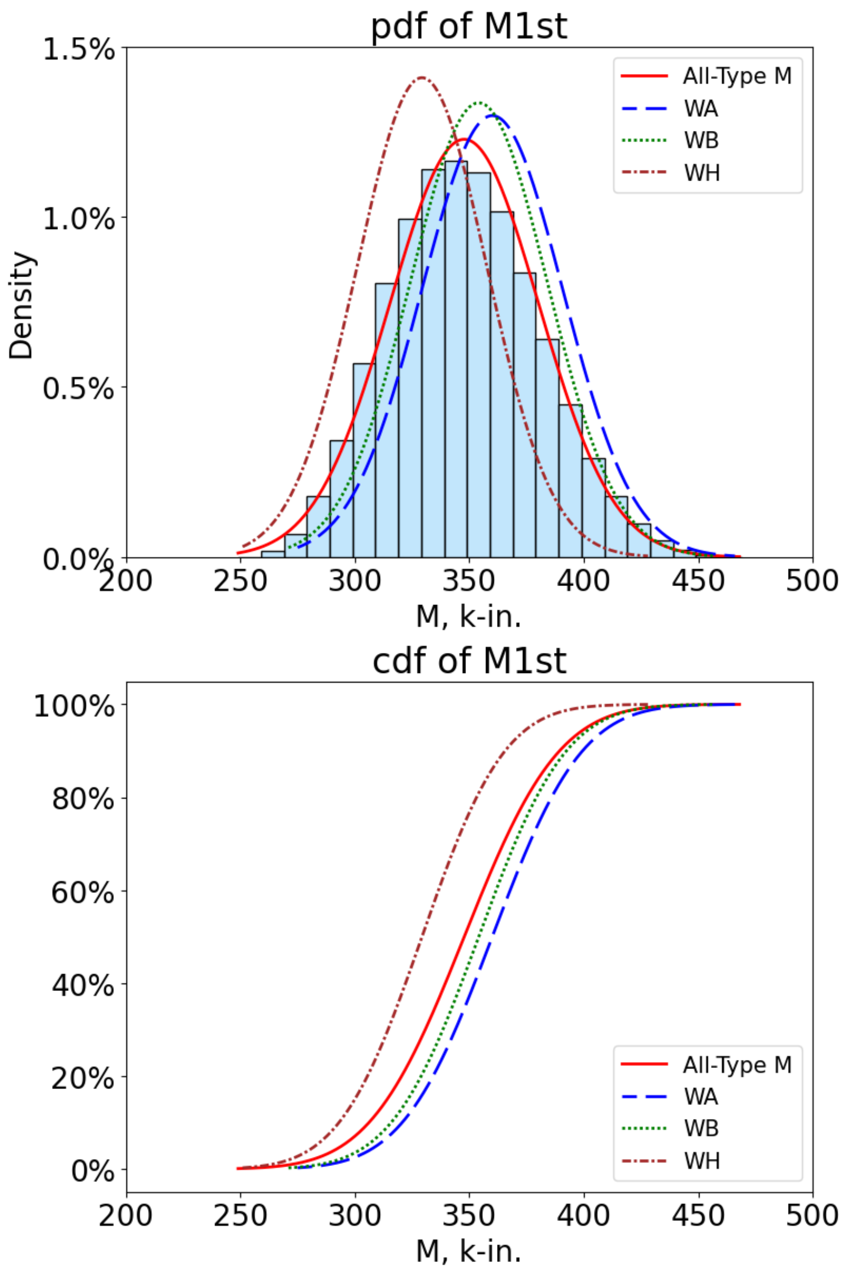

Figure D. 14 CDF and PDF plots of wire type for Type M tie rail-seat positive at crack reached to outer layer of reinforcement moment (M_{1st}).

Type M (Rail-Seat)

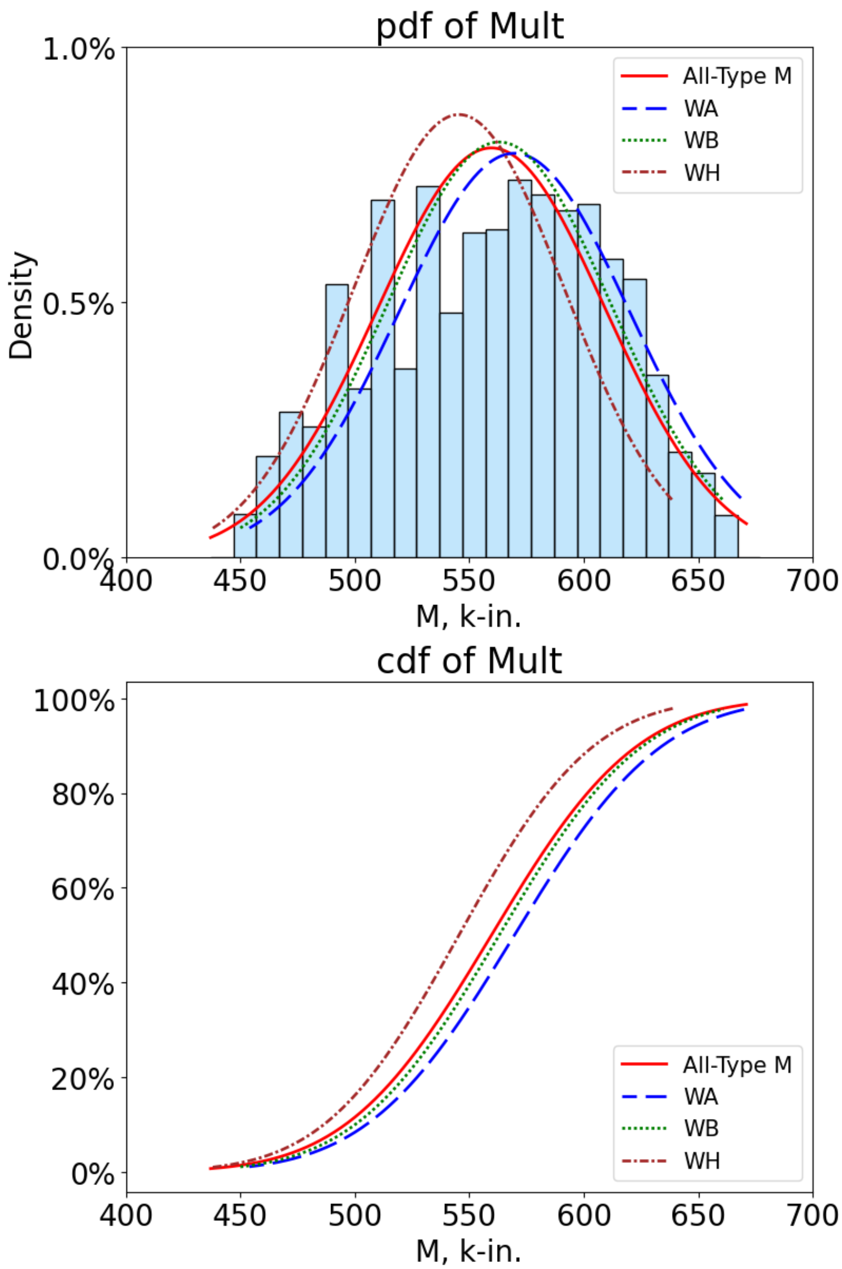

Figure D. 15 CDF and PDF plots of wire type for Type M tie rail-seat positive at ultimate crack moment (M_{ult}).

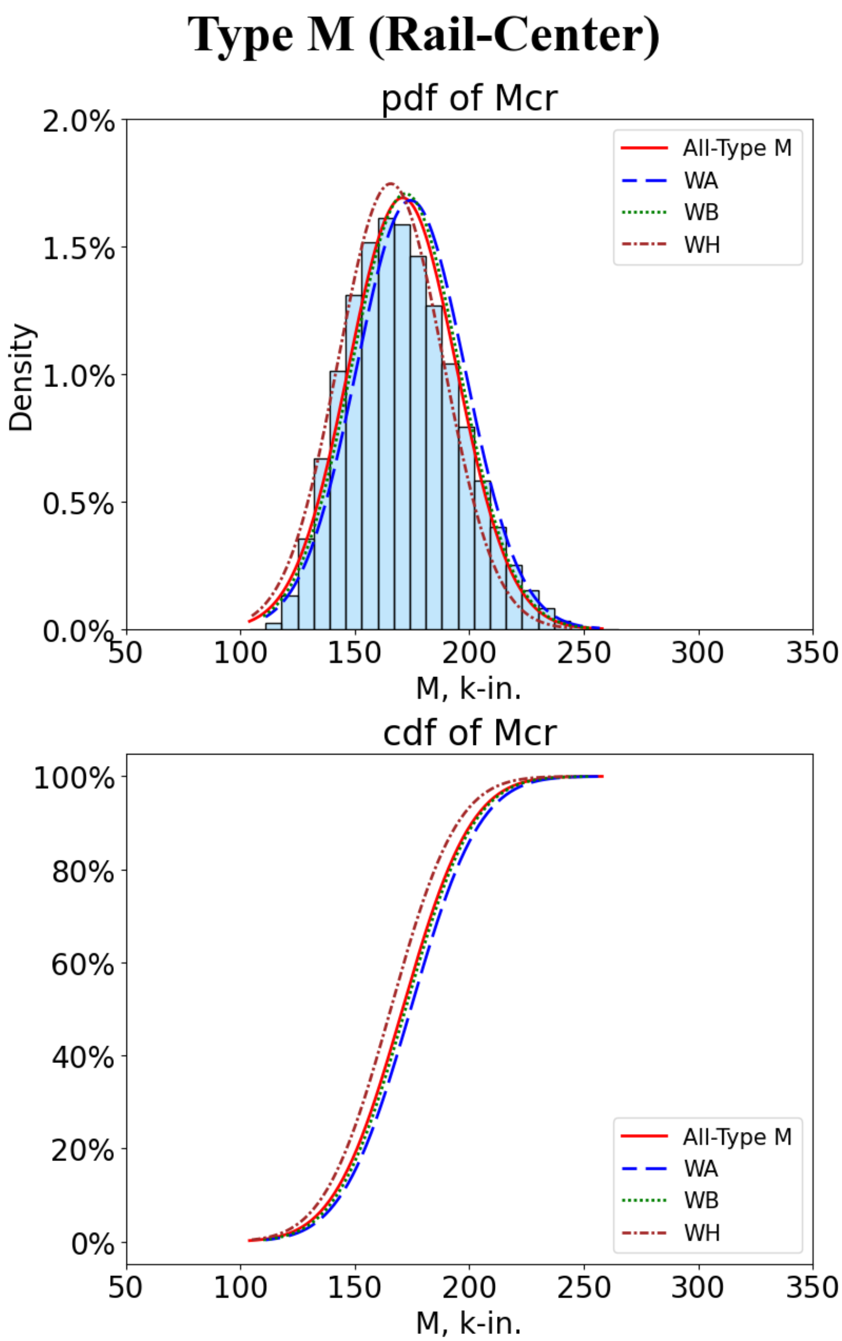

Figure D. 16 CDF and PDF plots of wire type for Type M tie rail-center negative at first crack moment (M_{cr}).

Type M (Rail-Center)

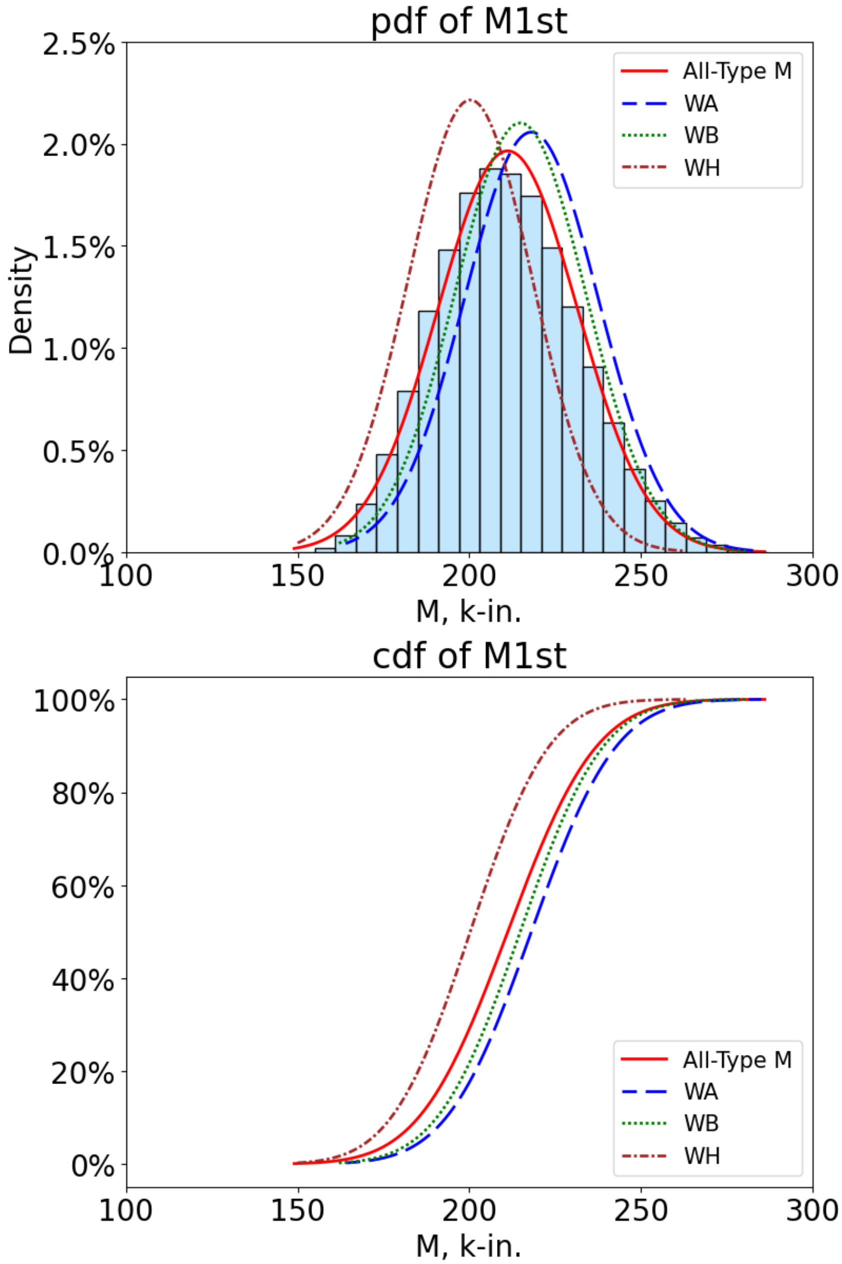

Figure D. 17 CDF and PDF plots of wire type for Type M tie rail-center negative at crack reached to outer layer of reinforcement moment (M_{1st}).

Type M (Rail-Center)

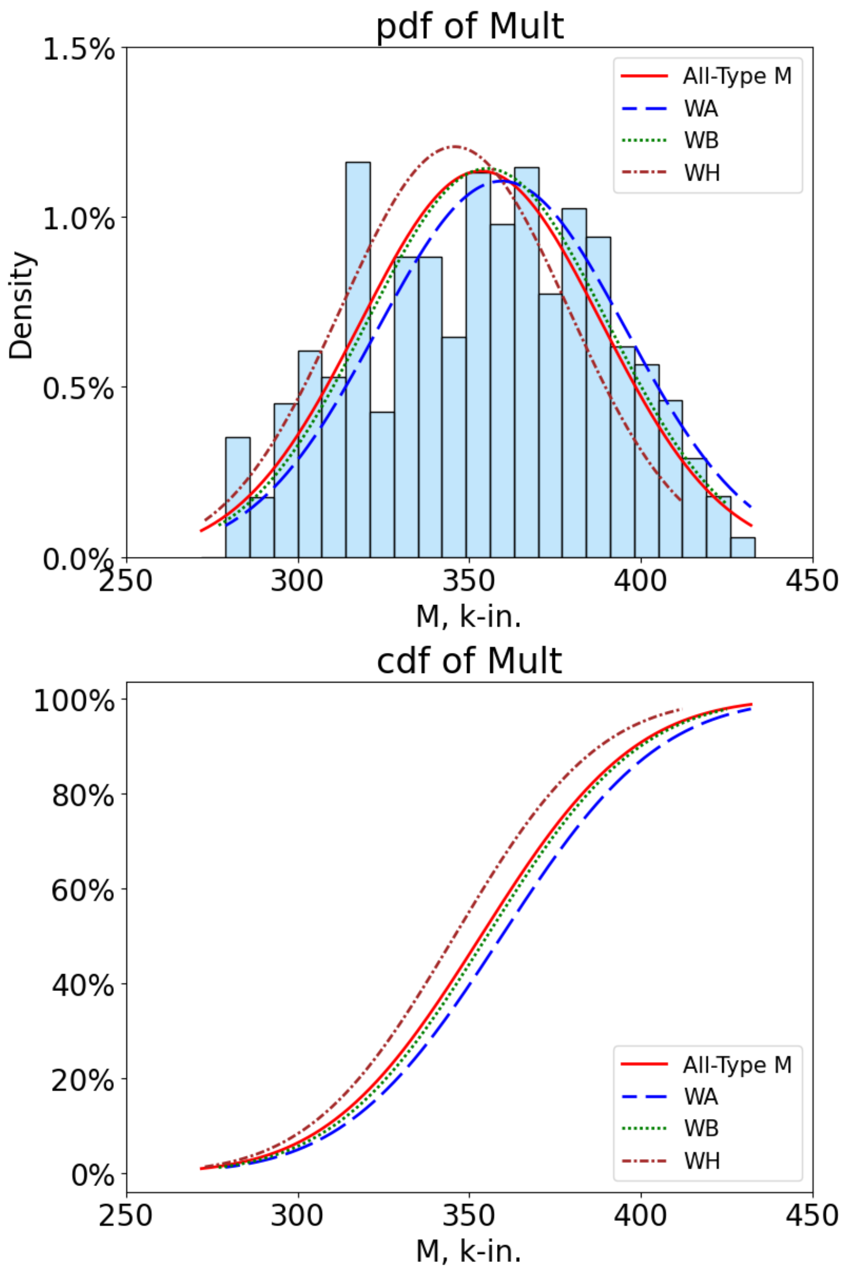

Figure D. 18 CDF and PDF plots of wire type for Type M tie rail-center negative at ultimate crack moment (M_{ult}).

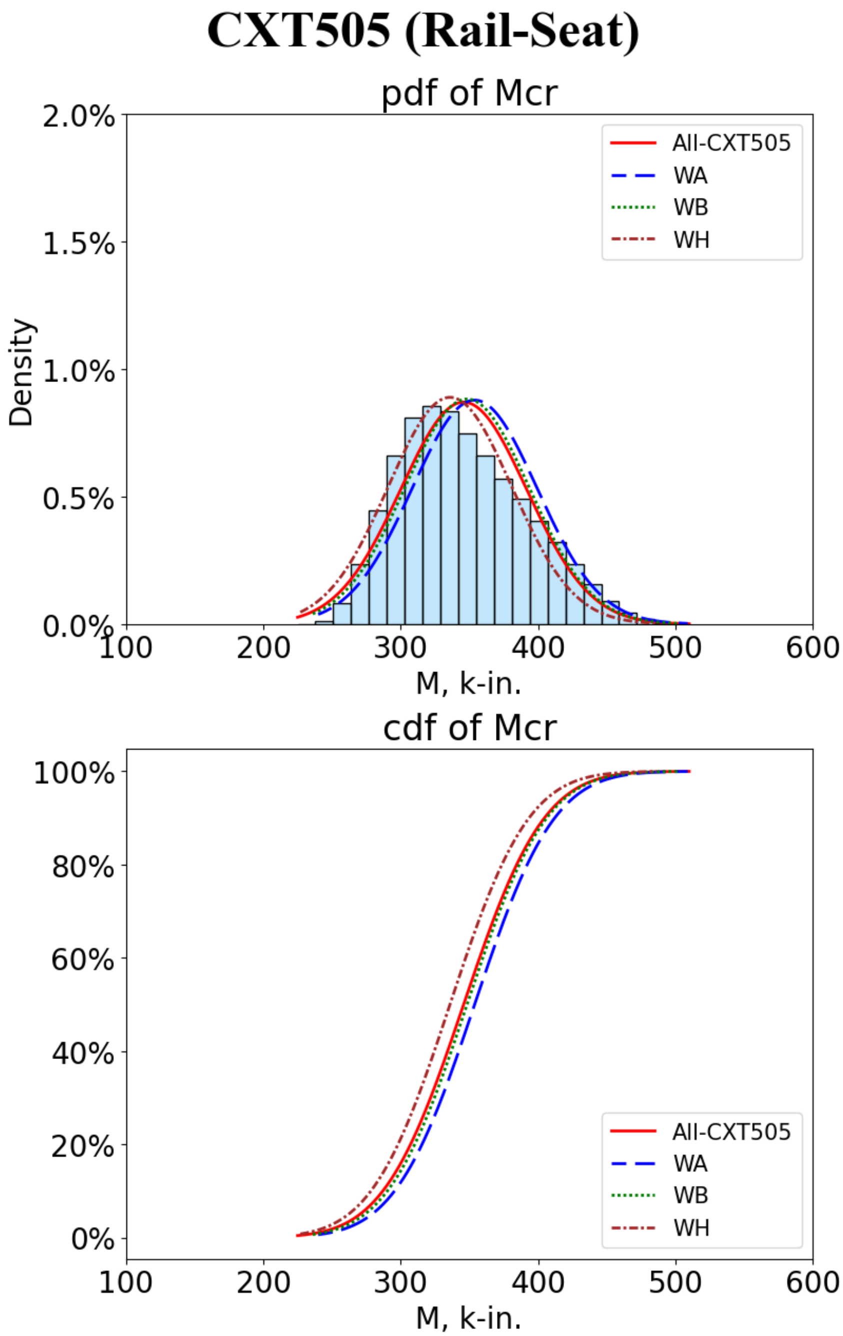

Figure D. 19 CDF and PDF plots of wire type for CXT 505S tie rail-seat positive at first crack moment (M_{cr}).

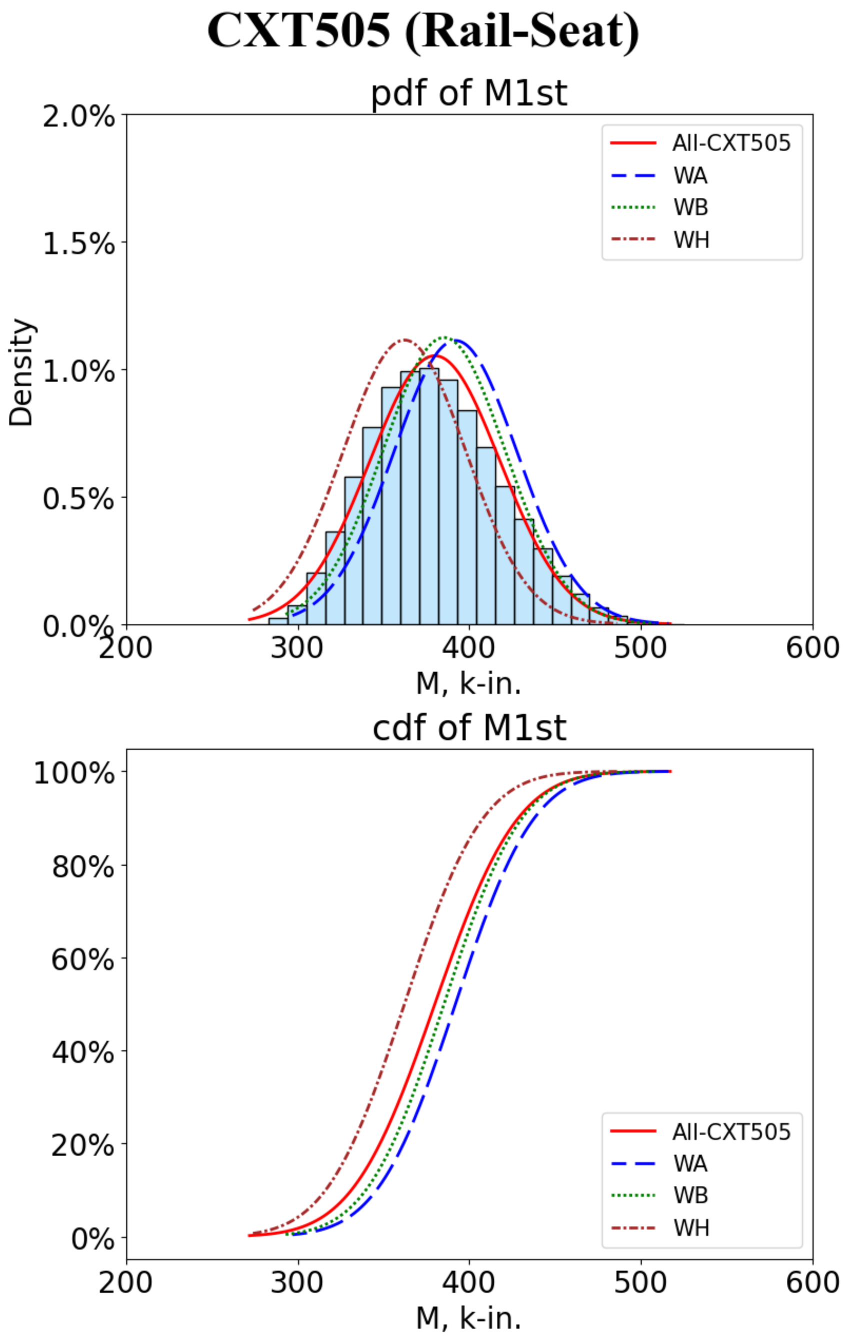

Figure D. 20 CDF and PDF plots of wire type for CXT 505S tie rail-seat positive at crack reached to outer layer of reinforcement moment (M_{1st}).

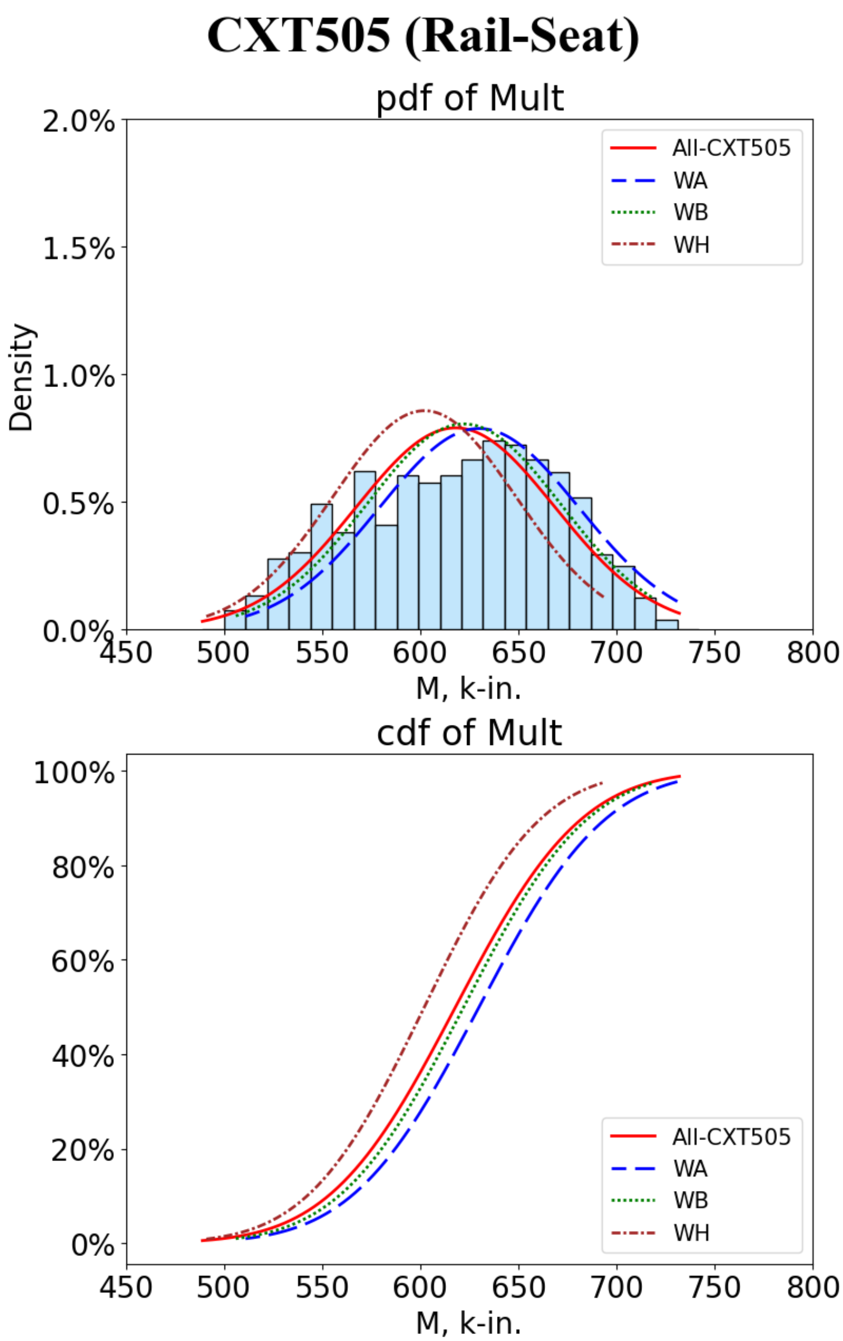

Figure D. 21 CDF and PDF plots of wire type for CXT 505S tie rail-seat positive at ultimate crack moment (M_{ult}).

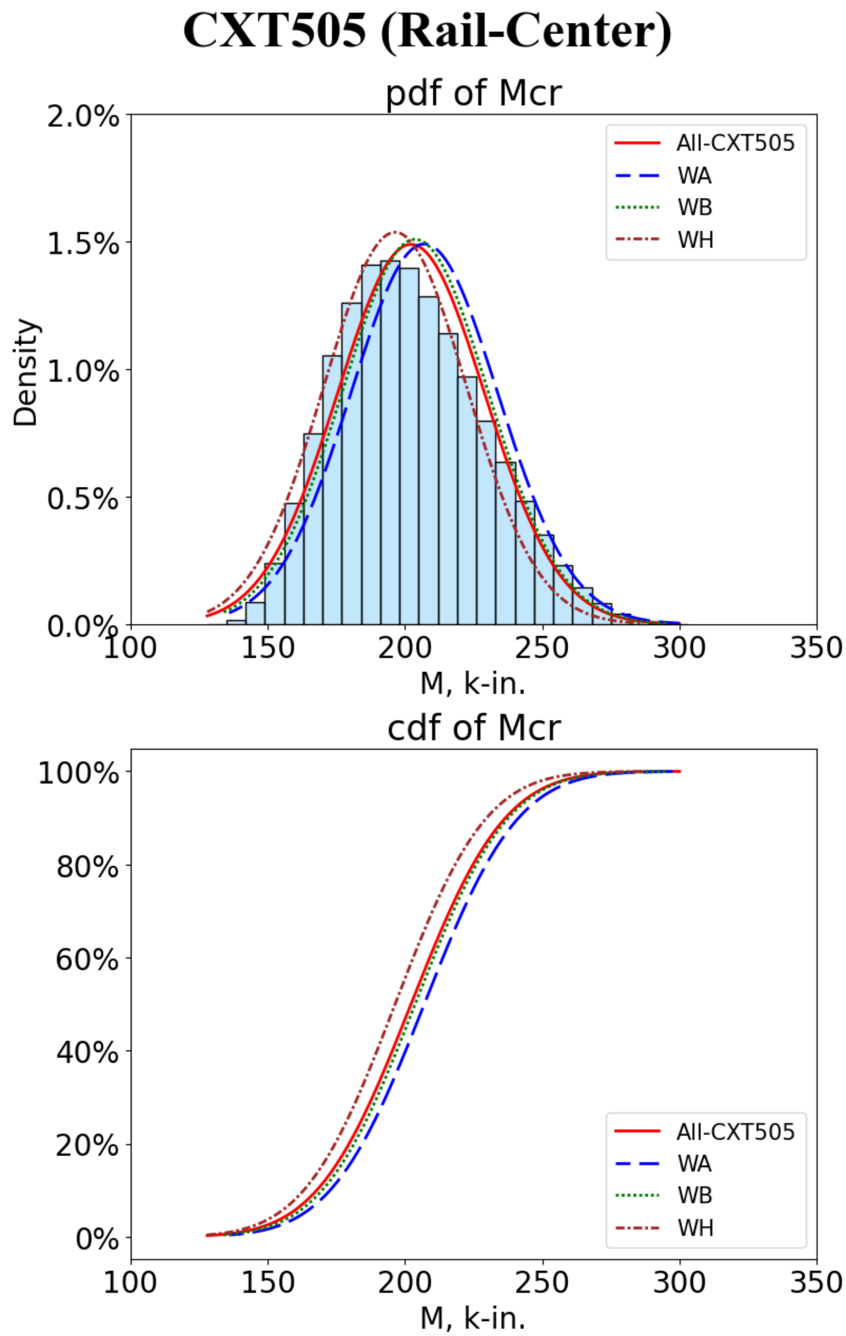

Figure D. 22 CDF and PDF plots of wire type for CXT 505S tie rail-center negative at first crack moment (M_{cr}).

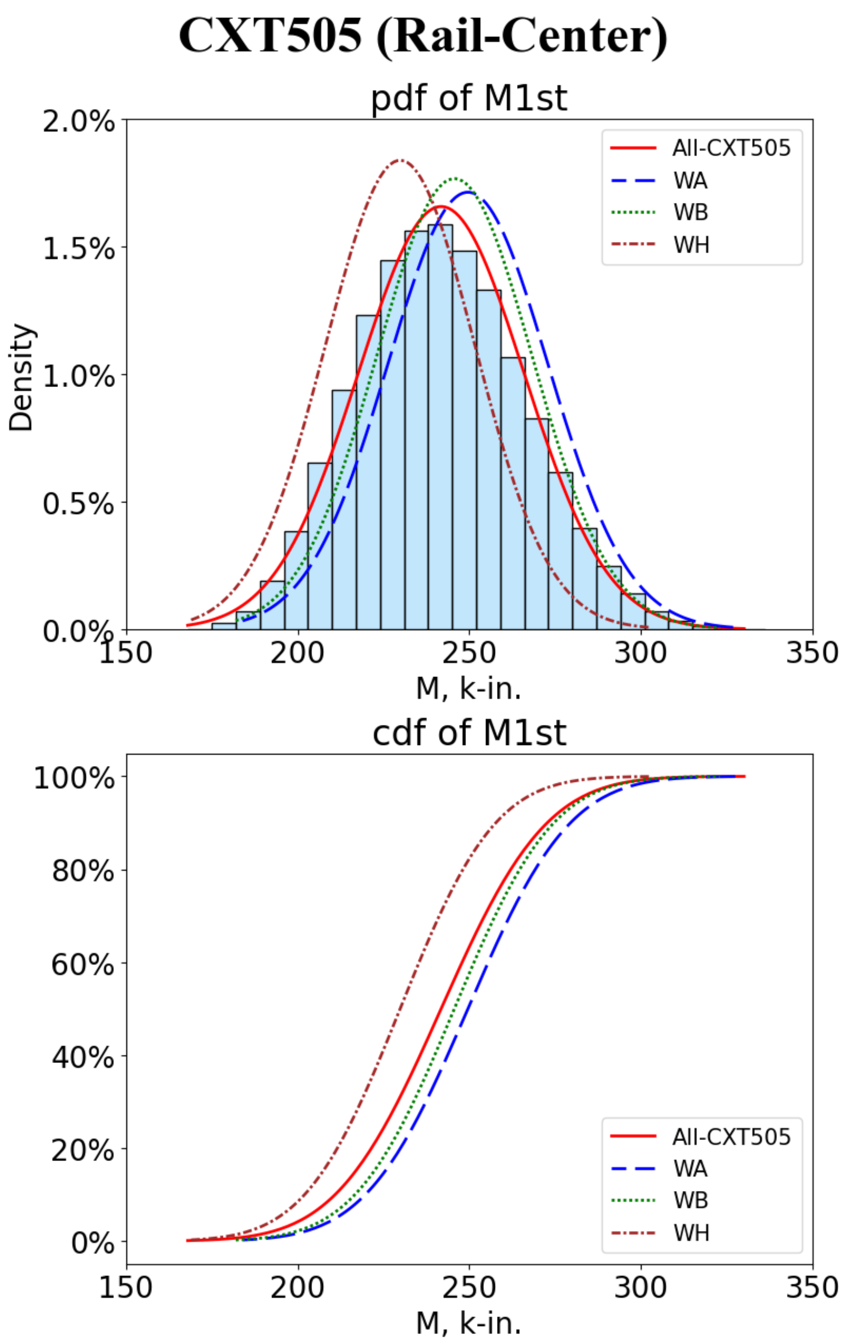

Figure D. 23 CDF and PDF plots of wire type for CXT 505S tie - rail-center negative at crack reached to outer layer of reinforcement moment (M_{1st}).

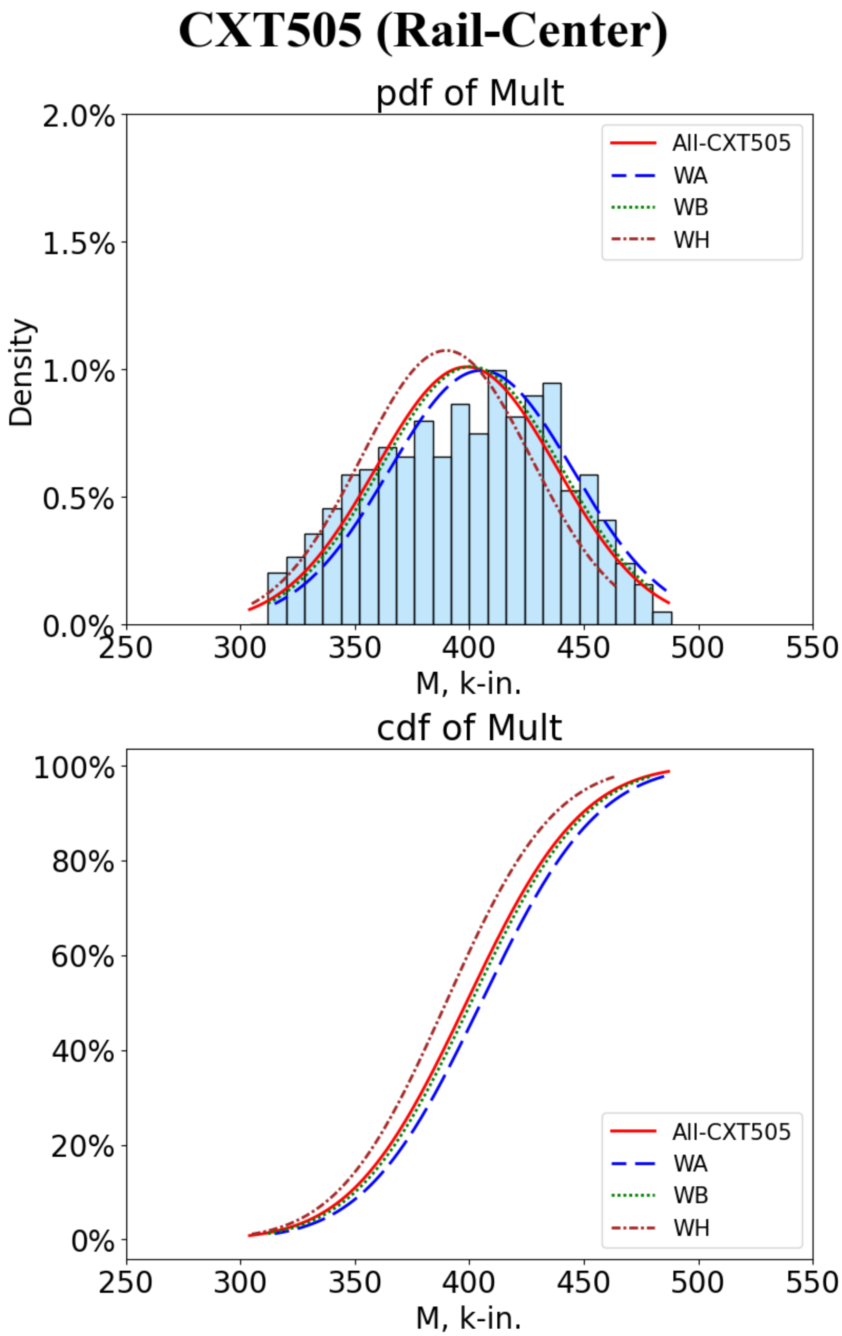

Figure D. 24 CDF and PDF plots of wire type for CXT 505S tie rail-center negative at ultimate crack moment (M_{ult}).

Type F (Rail-Seat)

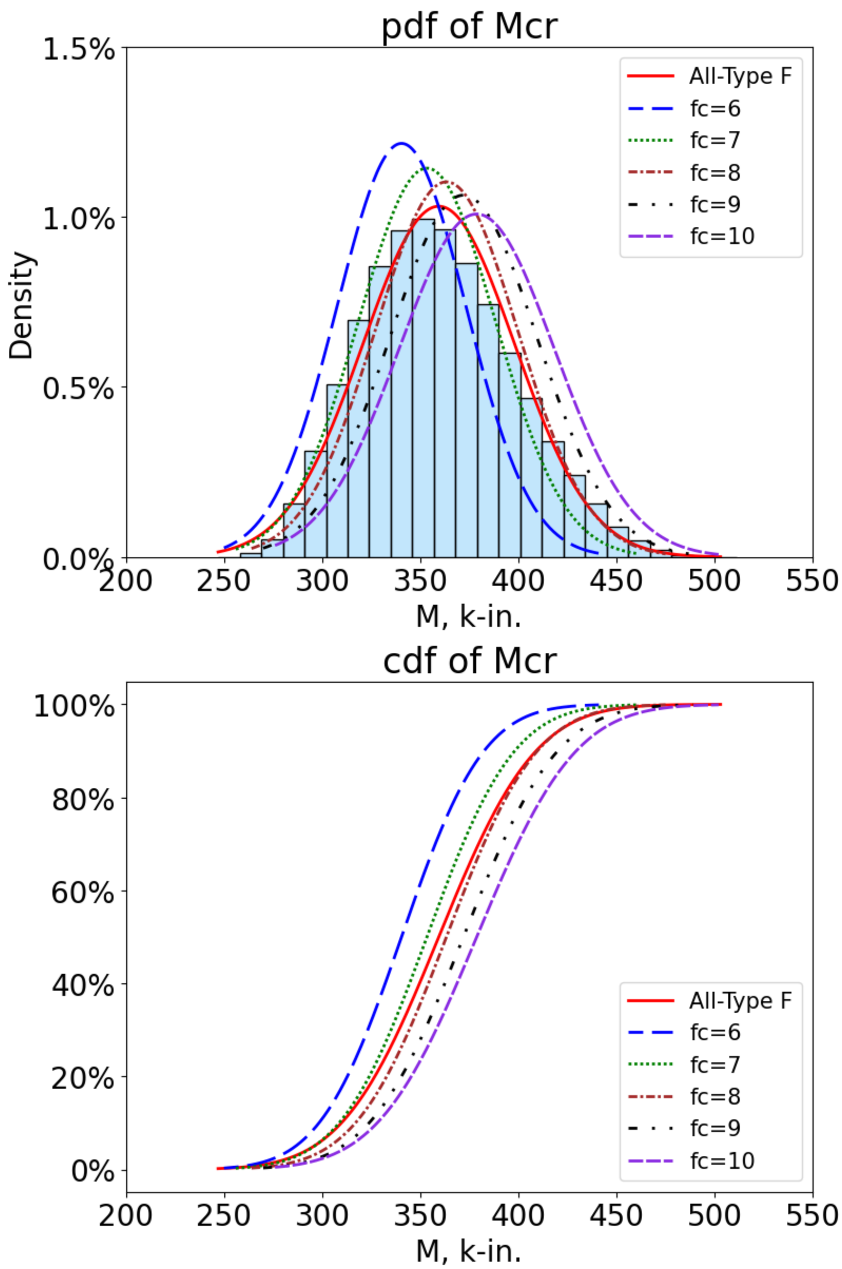

Figure D. 25 CDF and PDF plots of Concrete compressive strength (f'_c) for Type F tie rail-seat positive at first crack moment (M_{cr}).

Type F (Rail-Seat)

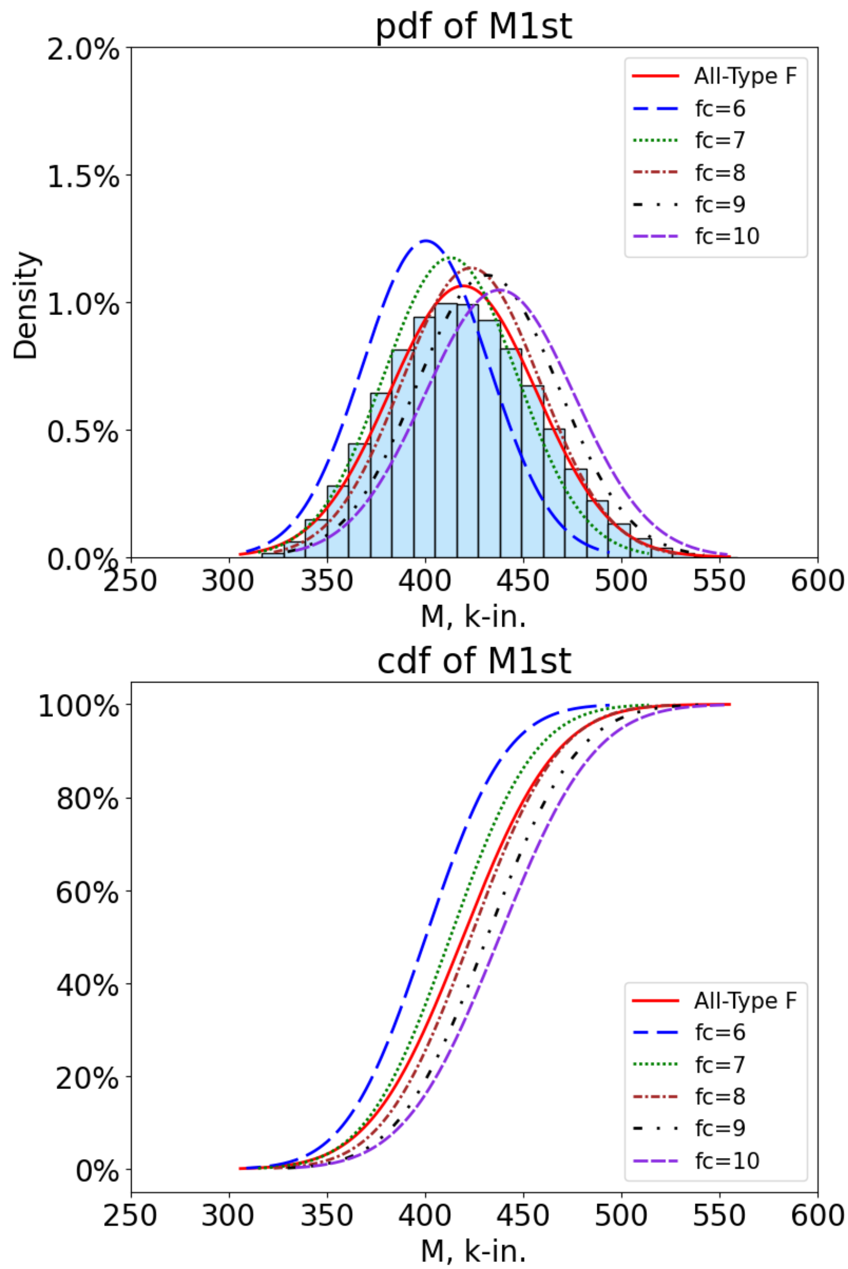

Figure D. 26 CDF and PDF plots of Concrete compressive strength (f'_c) for Type F tie - rail-seat positive at crack reached to outer layer of reinforcement moment (M_{1st}).

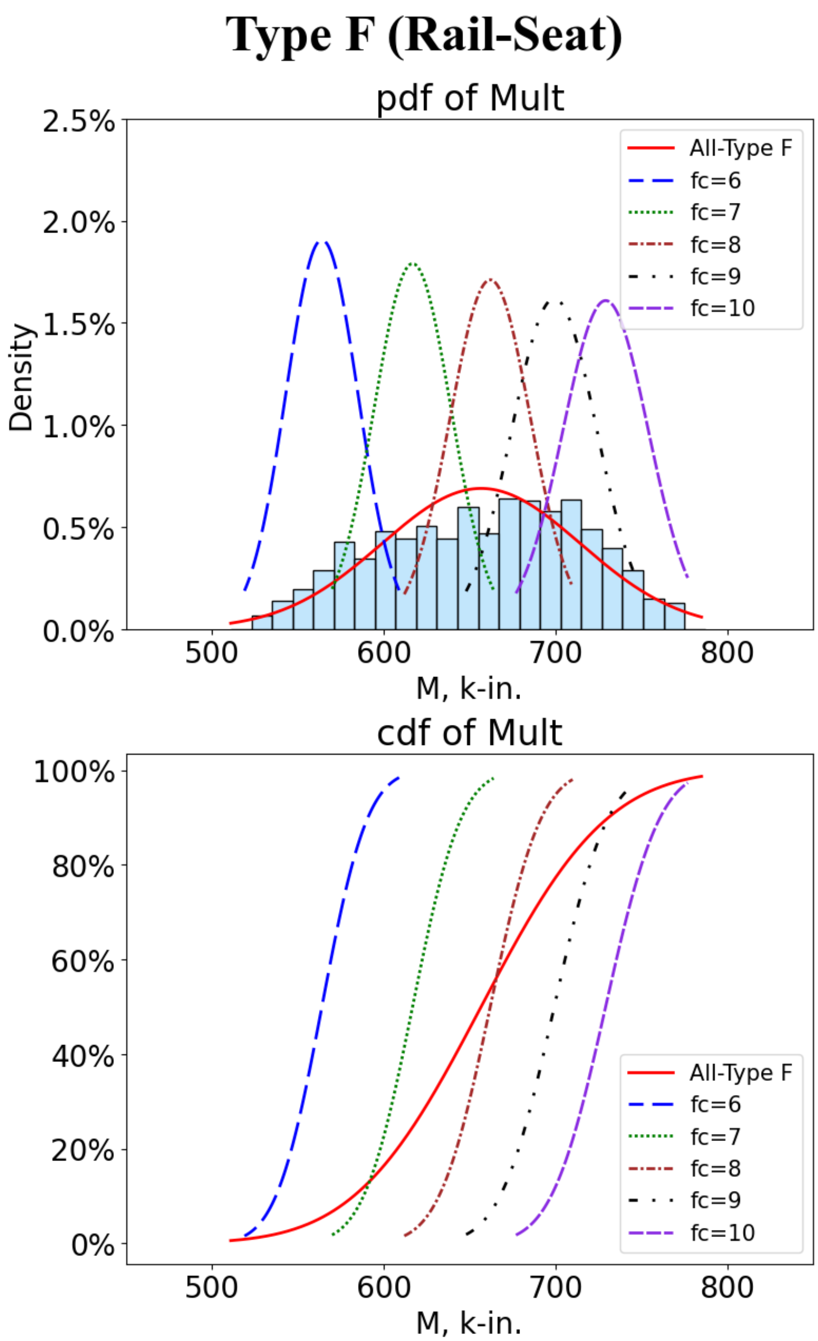

Figure D. 27 CDF and PDF plots of Concrete compressive strength (f'_c) for Type F tie rail-seat positive at ultimate crack moment (M_{ult}).

Type F (Rail-Center)

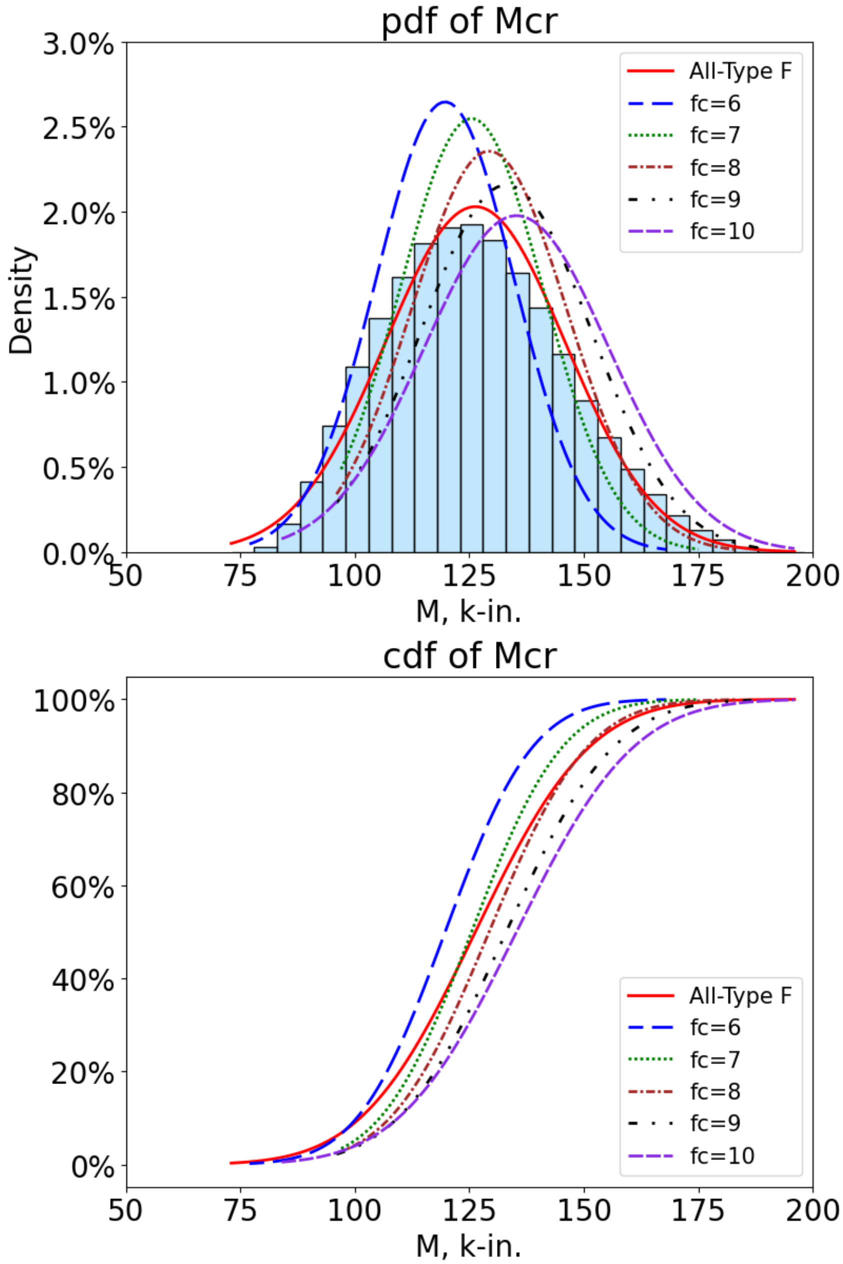

Figure D. 28 CDF and PDF plots of Concrete compressive strength (f'_c) for Type F tie rail-center negative at first crack moment (M_{cr}).

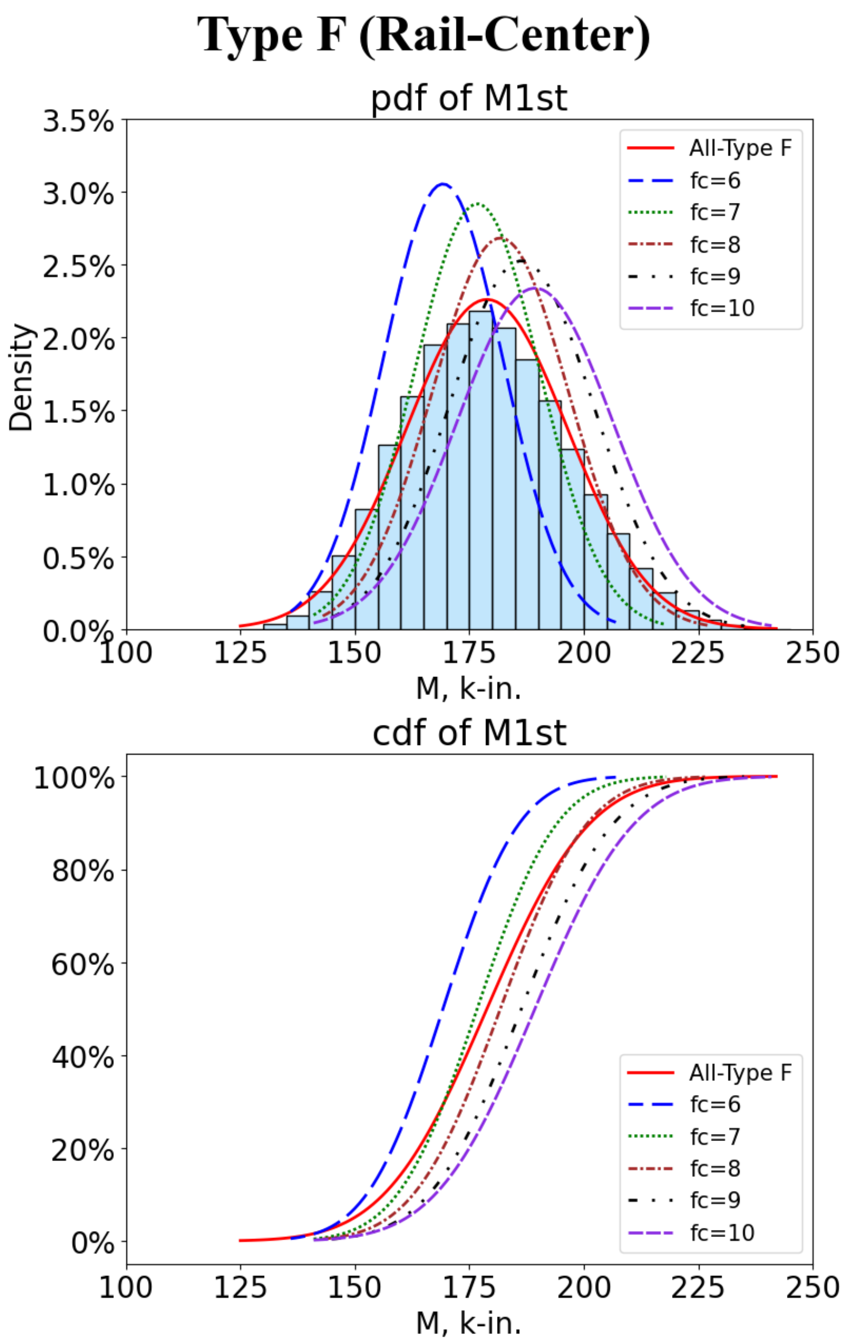

Figure D. 29 CDF and PDF plots of Concrete compressive strength (f'$_c$) for Type F tie rail-center negative at crack reached to outer layer of reinforcement moment (M_{1st}).

Type F (Rail-Center)

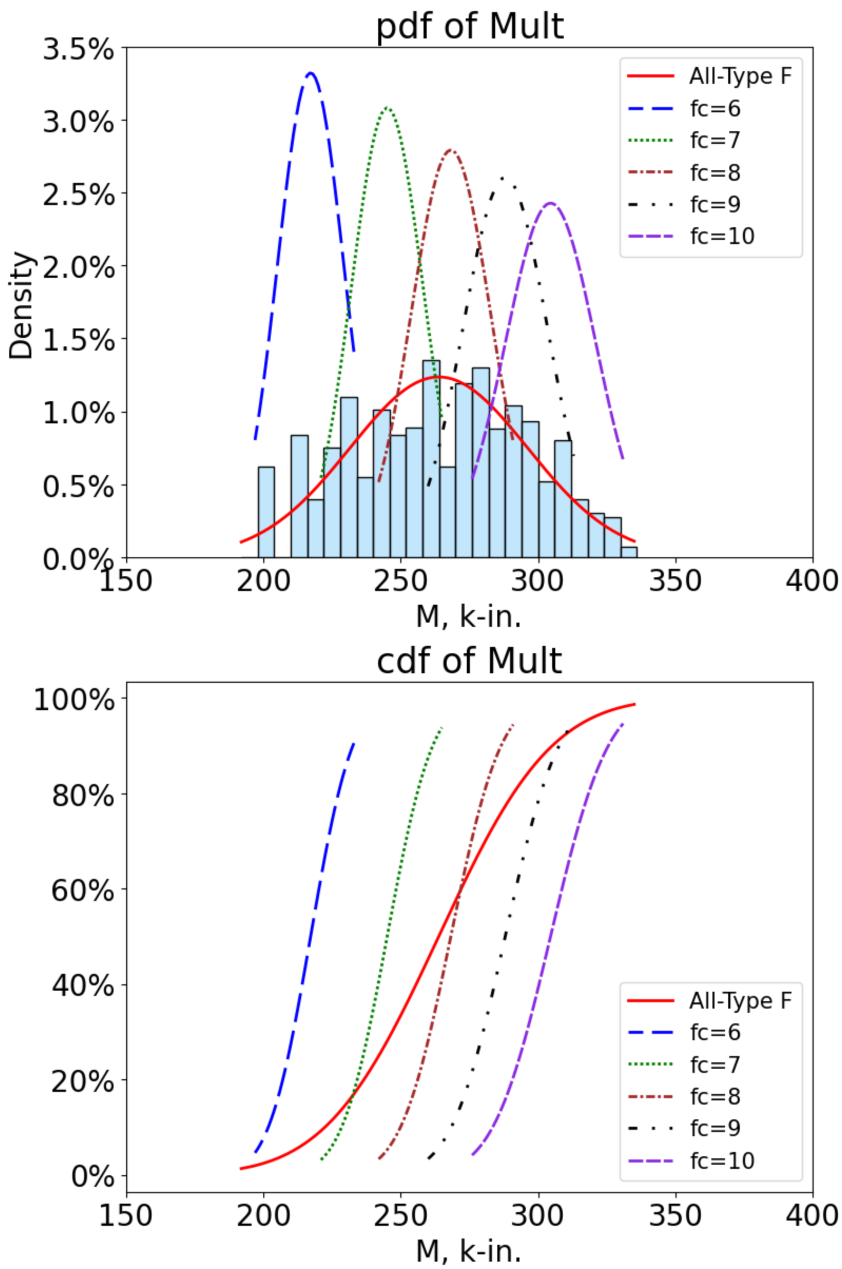

Figure D. 30 CDF and PDF plots of Concrete compressive strength (f'_c) for Type F tie rail-center negative at ultimate crack moment (M_{ult}).

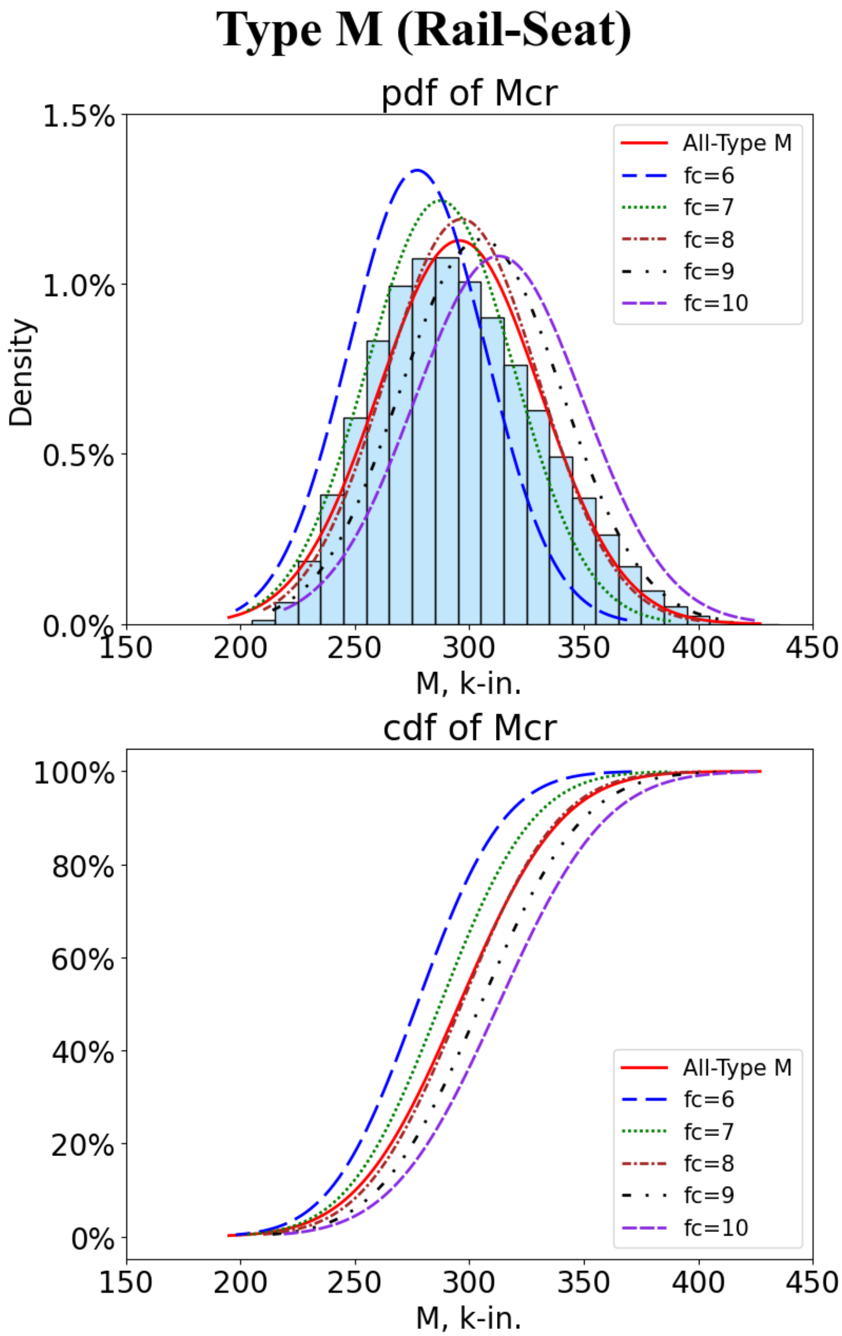

Figure D. 31 CDF and PDF plots of Concrete compressive strength (f'_c) for Type M tie - rail-seat positive at first crack moment (M_{cr}).

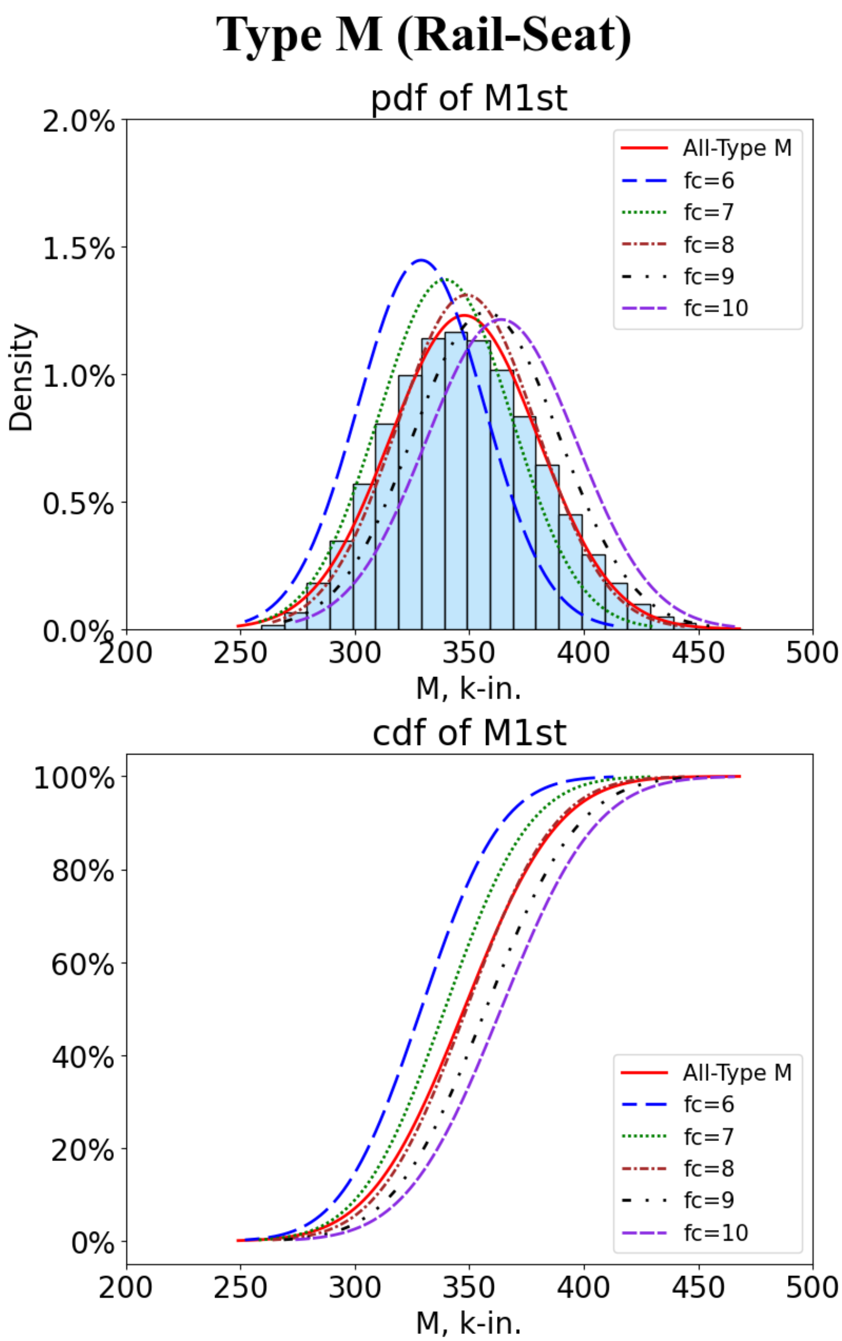

Figure D. 32 CDF and PDF plots of Concrete compressive strength (f'_c) for Type M tie rail-seat positive at crack reached to outer layer of reinforcement moment (M_{1st}).

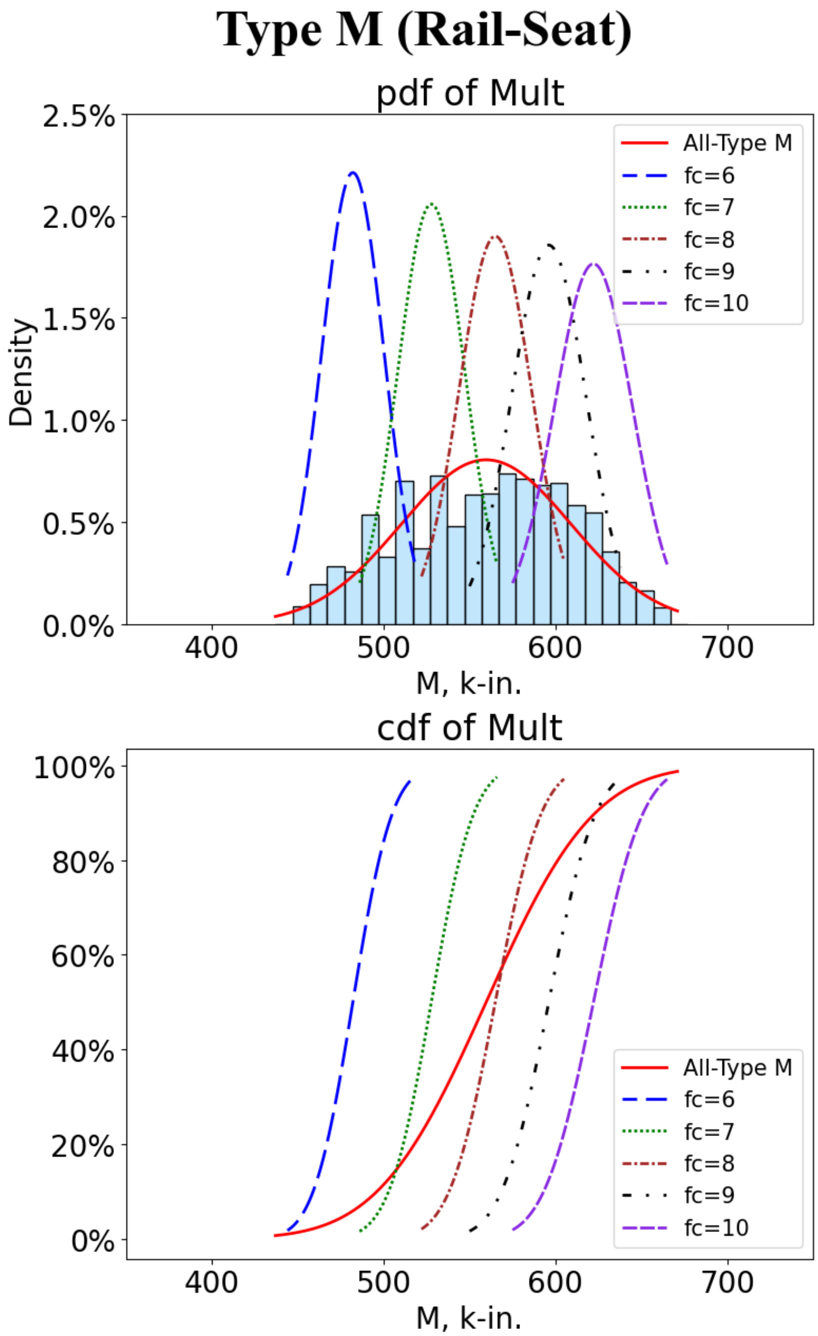

Figure D. 33 CDF and PDF plots of Concrete compressive strength (f'_c) for Type M tie rail-seat positive at ultimate crack moment (M_{ult}).

Type M (Rail-Center)

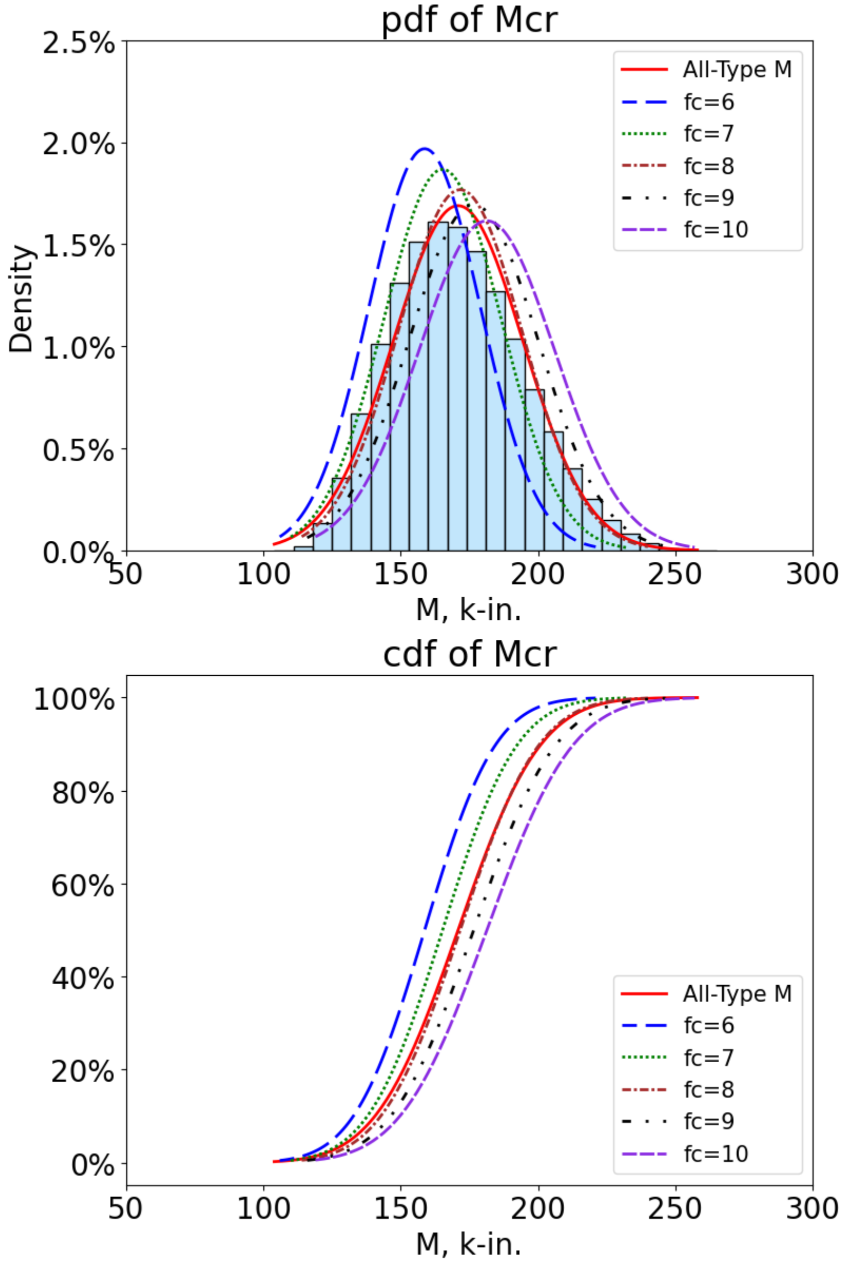

Figure D. 34 CDF and PDF plots of Concrete compressive strength (f'_c) for Type M tie rail-center negative at first crack moment (M_{cr}).

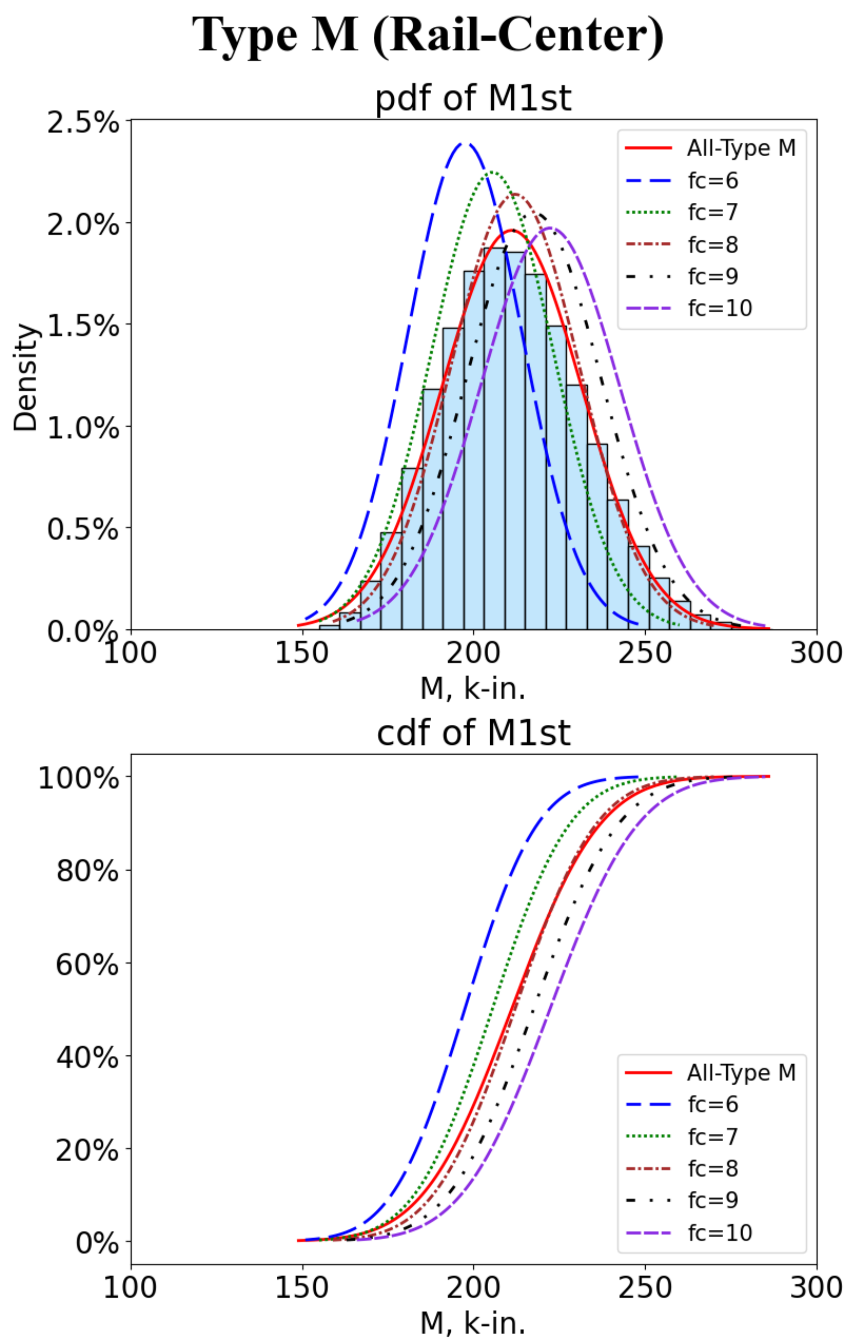

Figure D. 35 CDF and PDF plots of Concrete compressive strength (f'_c) for Type M tie rail-center negative at crack reached to outer layer of reinforcement moment (M_{1st}).

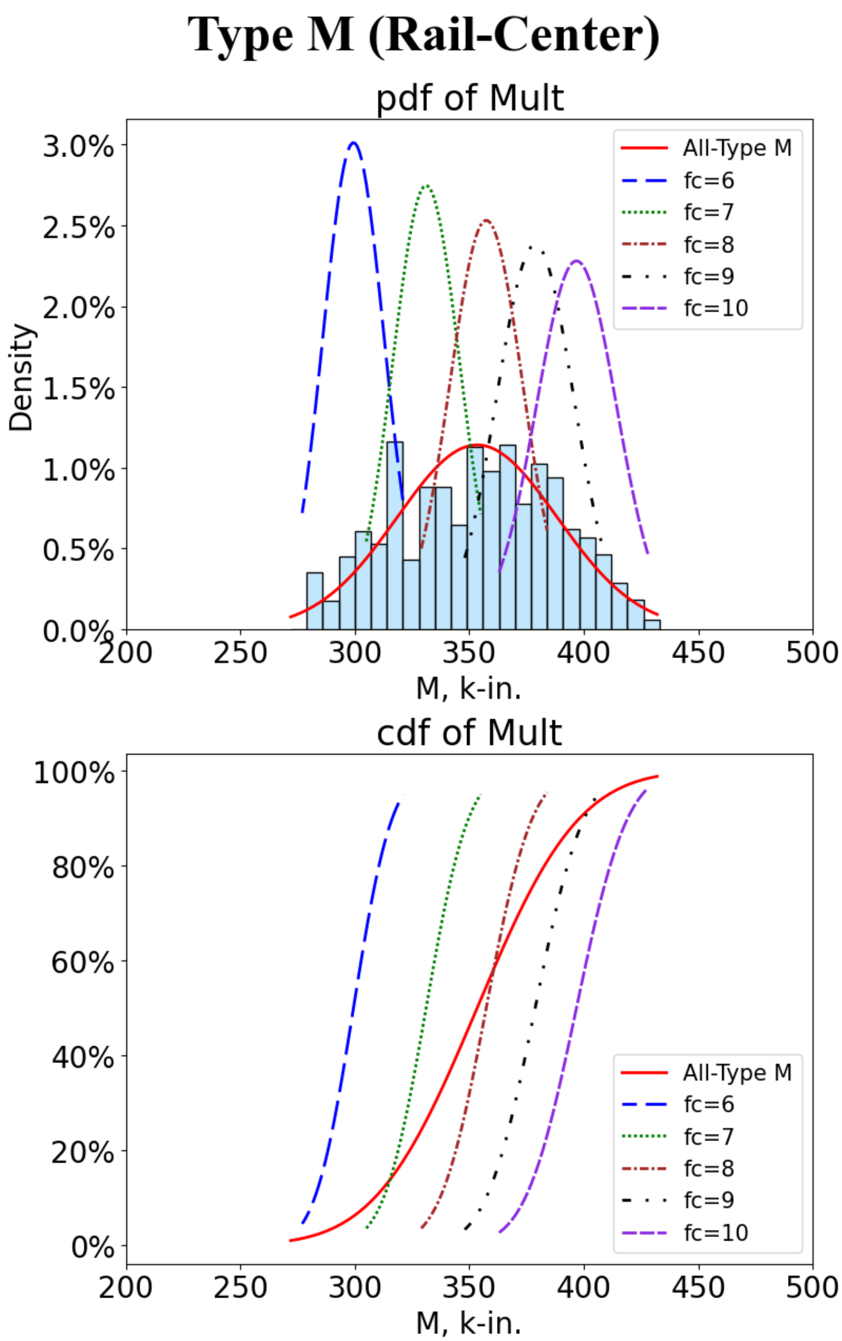

Figure D. 36 CDF and PDF plots of Concrete compressive strength (f'_c) for Type M tie rail-center negative at ultimate crack moment (M_{ult}).

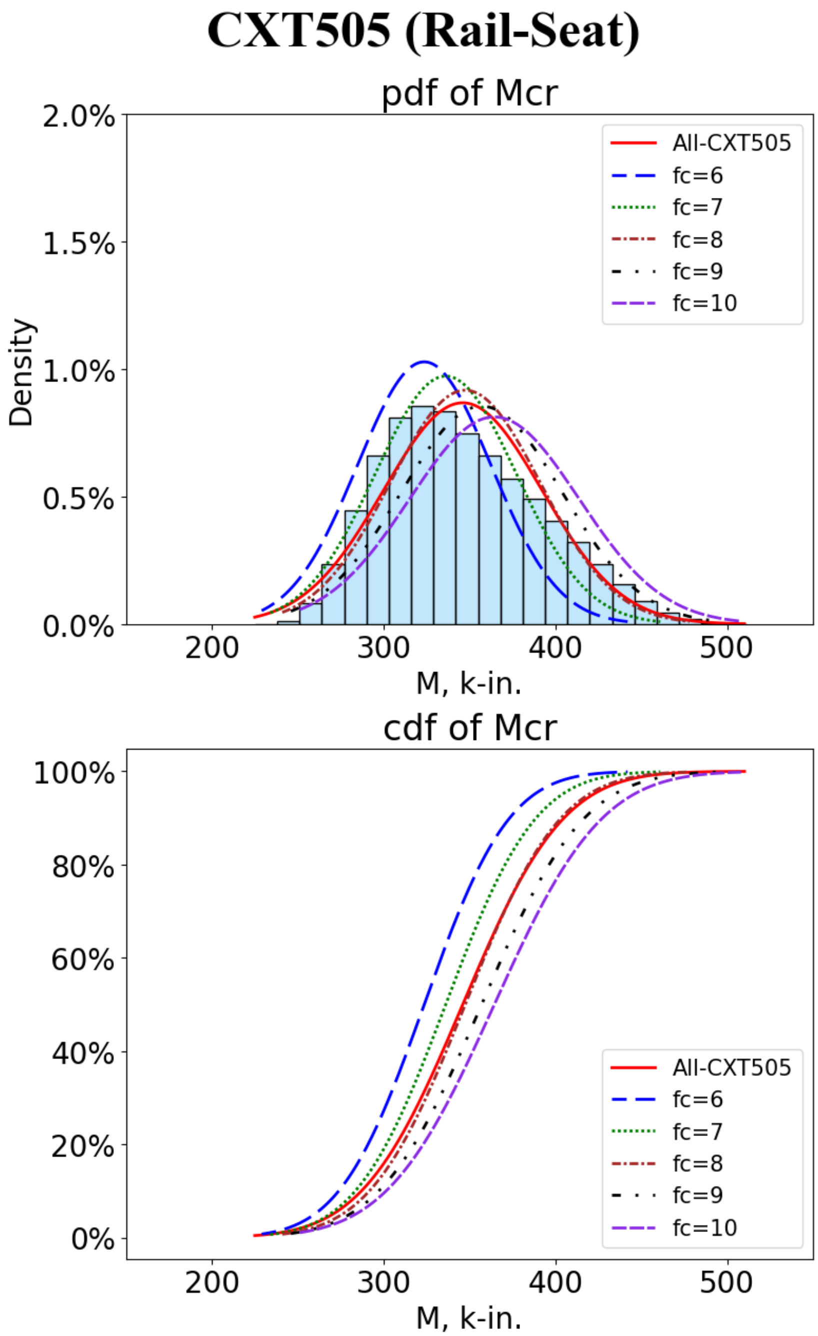

Figure D. 37 CDF and PDF plots of Concrete compressive strength (f'c) for CXT 505S tie - rail-seat positive at first crack moment (M_{cr}).

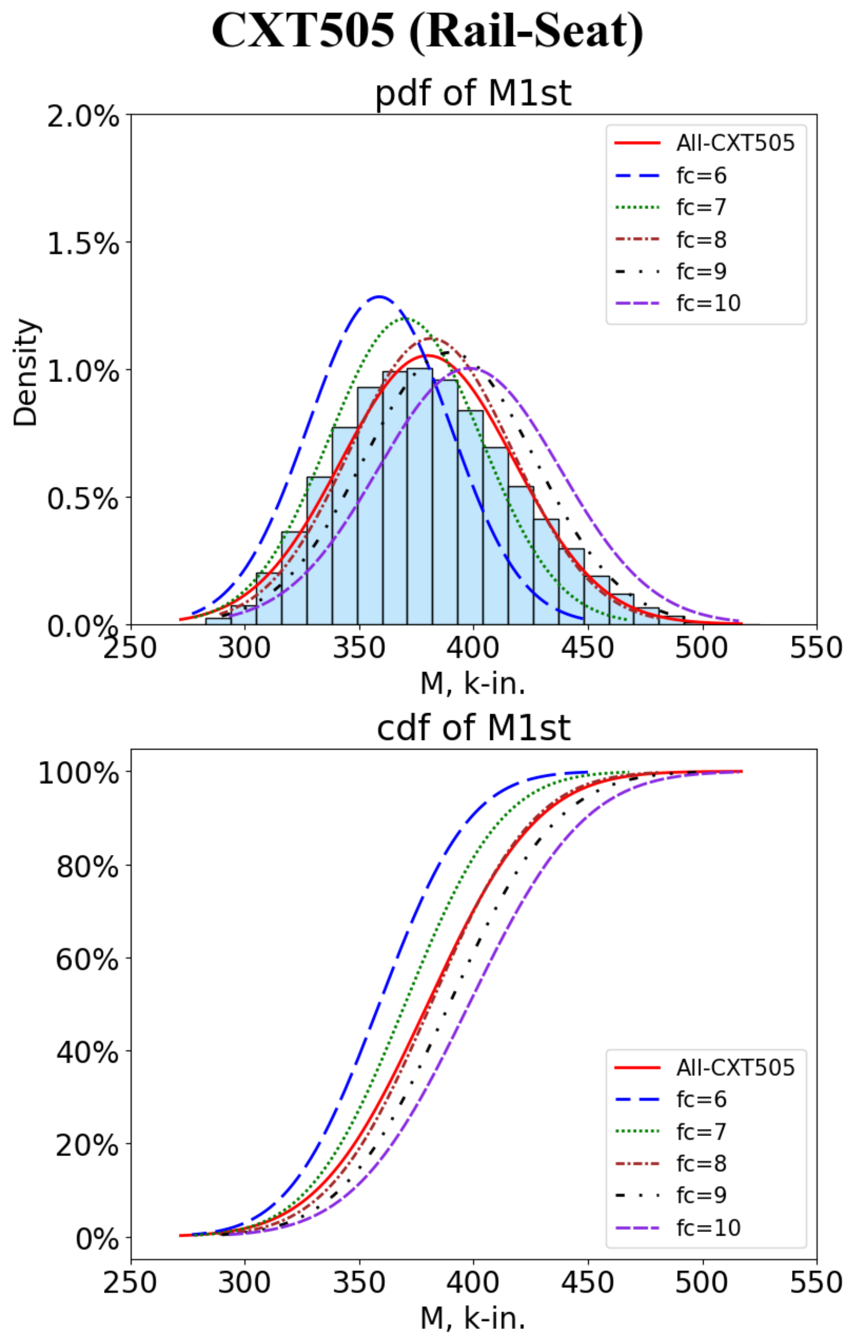

Figure D. 38 CDF and PDF plots of Concrete compressive strength (f'$_c$) for CXT 505S tie rail-seat positive at crack reached to outer layer of reinforcement moment (M$_{1st}$).

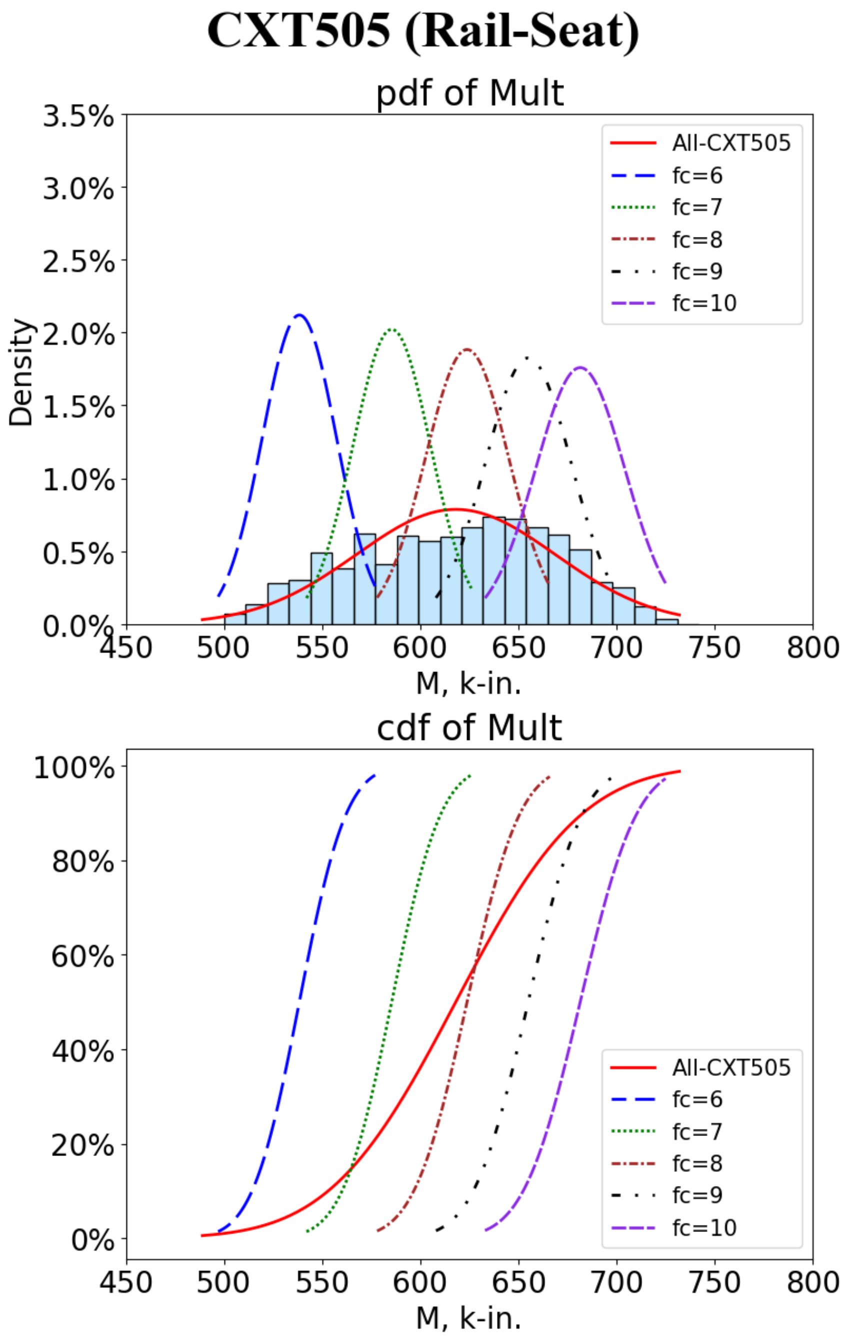

Figure D. 39 CDF and PDF plots of Concrete compressive strength (f'_c) for CXT 505S tie rail-seat positive at ultimate crack moment (M_{ult}).

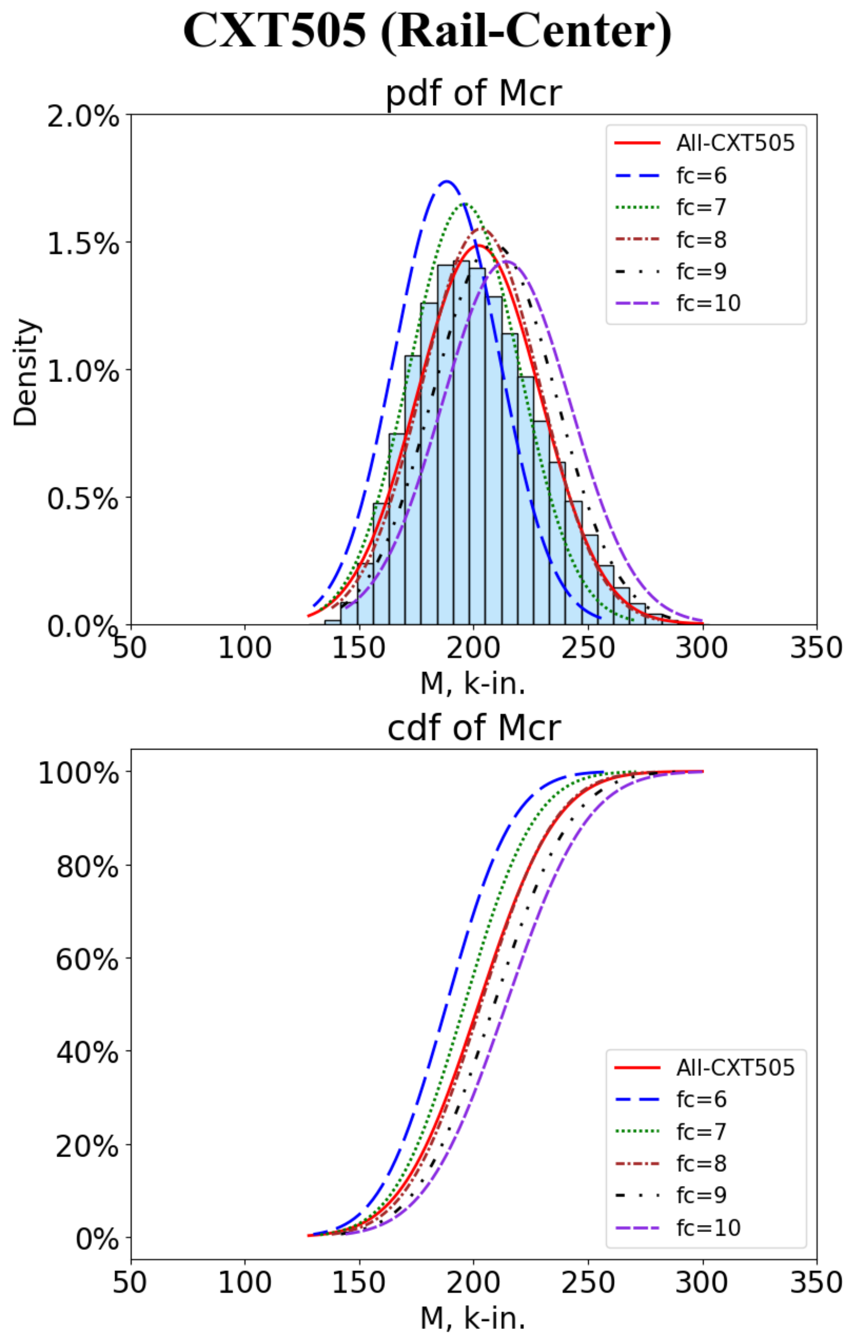

Figure D. 40 CDF and PDF plots of Concrete compressive strength (f'$_c$) for CXT 505S tie rail-center negative at first crack moment (M$_{cr}$).

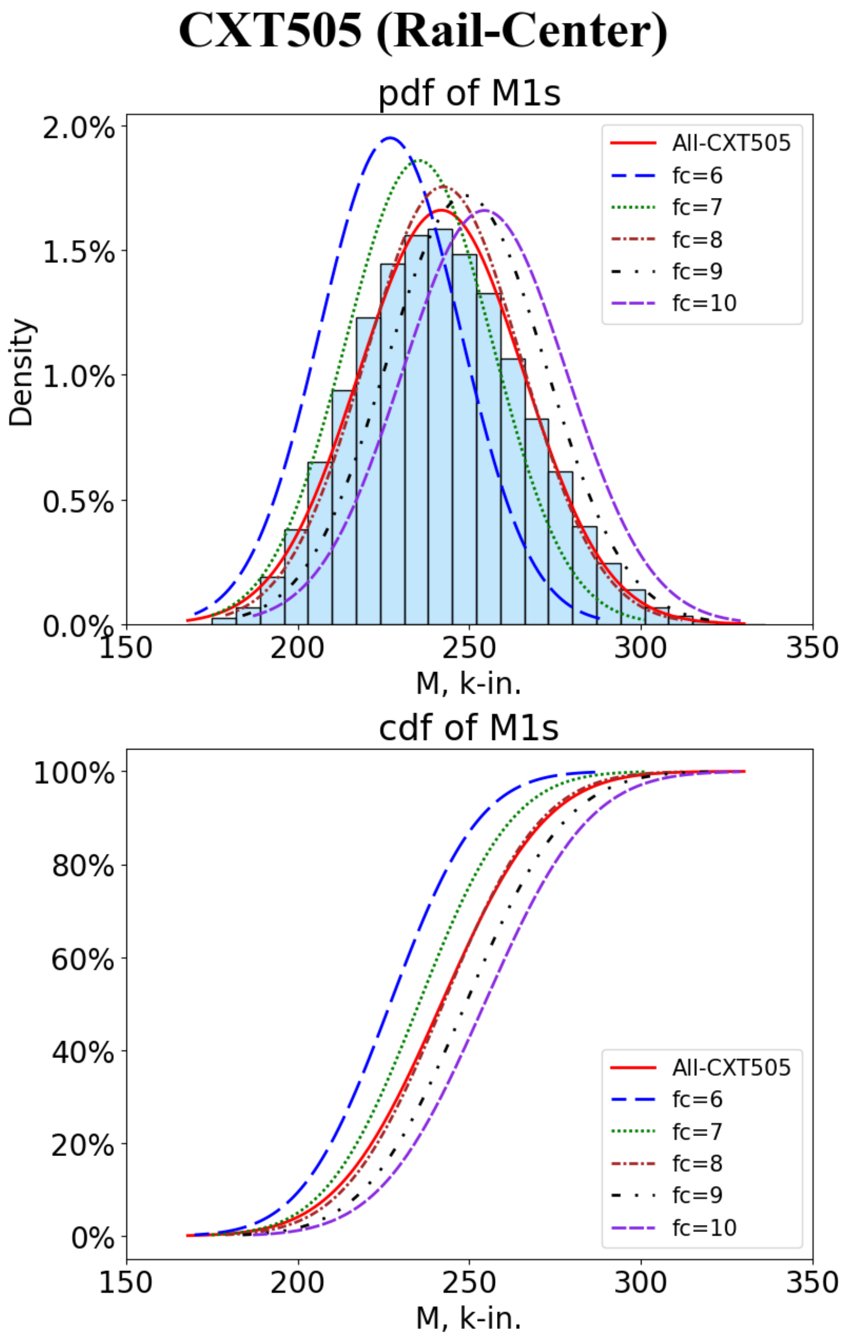

Figure D. 41 CDF and PDF plots of Concrete compressive strength (f'_c) for CXT 505S tie rail-center negative at crack reached to outer layer of reinforcement moment (M_{1st}).

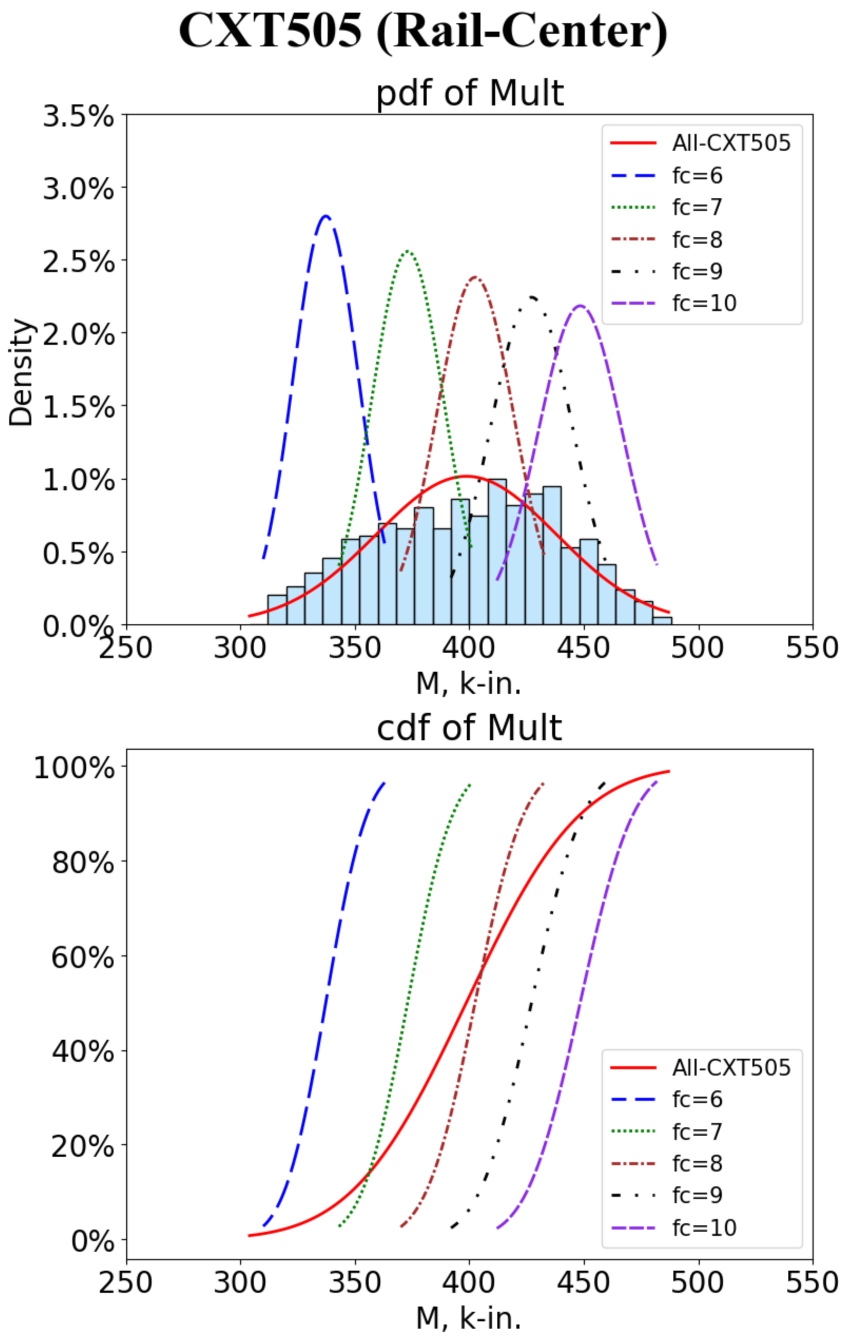

Figure D. 42 CDF and PDF plots of Concrete compressive strength (f'$_c$) for CXT 505S tie rail-center negative at ultimate crack moment (M_{ult}).

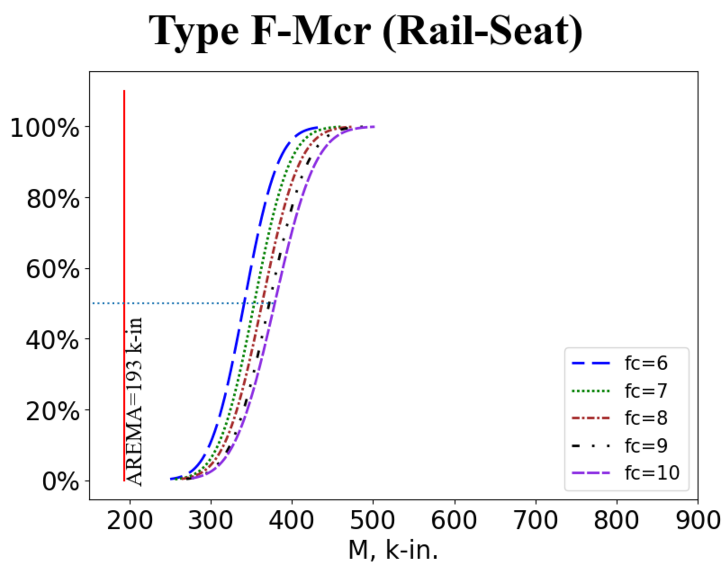

	6 ksi	7 ksi	8 ksi	9 ksi	10 ksi
Mean	341	353	363	372	378
STD	33	34	36	37	39

Figure D. 43 Comparison of AREAM design strength and rail-seat positive CDFs of Type F tie concrete compressive strength at first crack moment (M_{cr}).

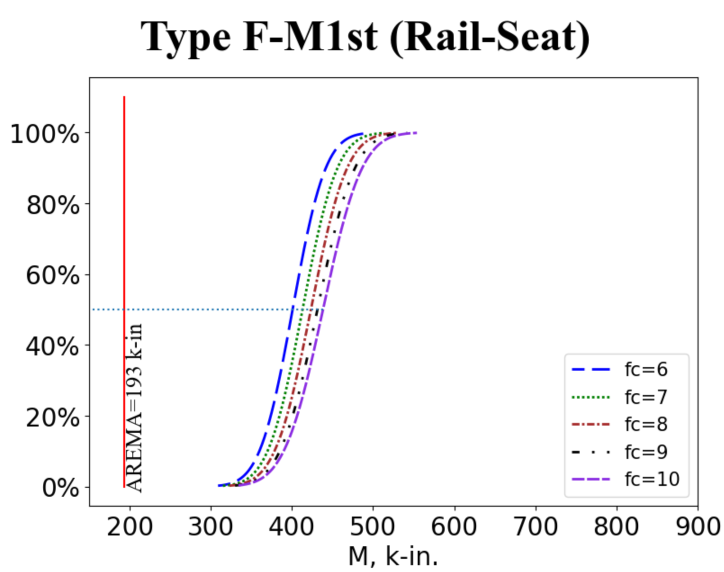

	6 ksi	7 ksi	8 ksi	9 ksi	10 ksi
Mean	400	413	423	431	438
STD	31	33	34	36	37

Figure D. 44 Comparison of AREAM design strength and rail-seat positive CDFs of Type F tie concrete compressive strength at crack reached to outer layer of reinforcement moment (M_{1st})

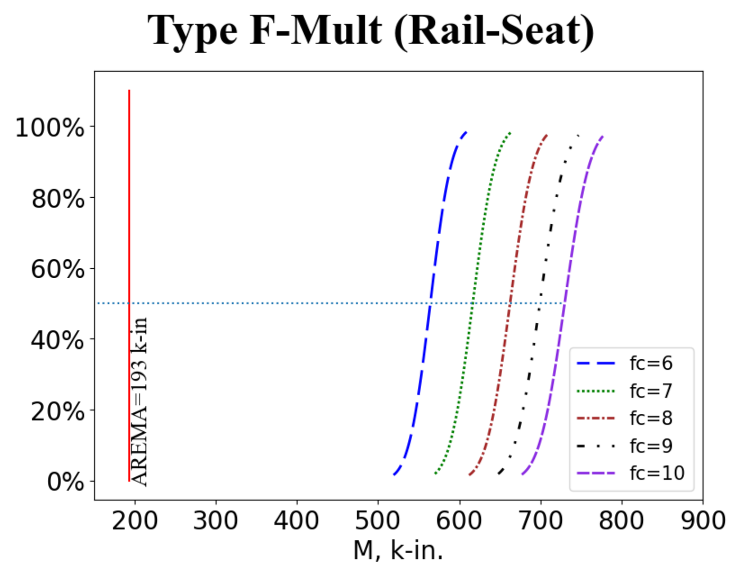

	6 ksi	7 ksi	8 ksi	9 ksi	10 ksi
Mean	564	616	662	699	729
STD	20	22	23	24	24

Figure D. 45 Comparison of AREAM design strength and rail-seat positive CDFs of Type F tie concrete compressive strength at ultimate crack moment (M_{ult}).

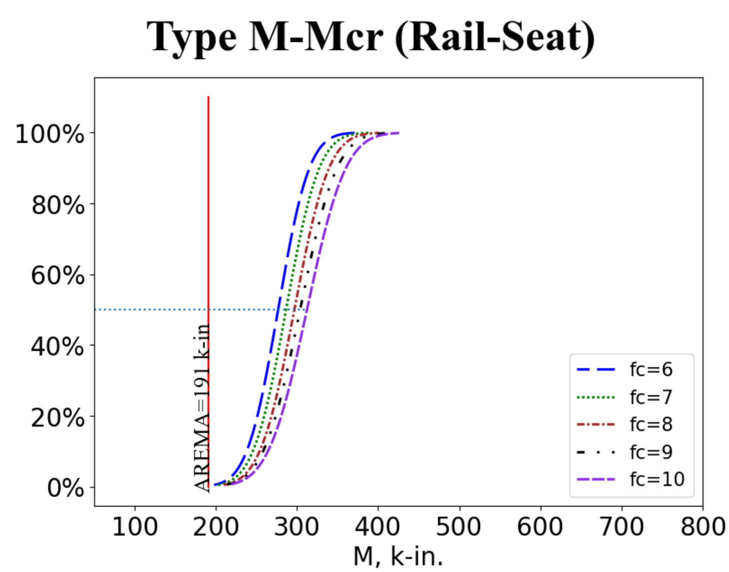

	6 ksi	7 ksi	8 ksi	9 ksi	10 ksi
Mean	276	286	296	303	312
STD	30	31	33	35	37

Figure D. 46 Comparison of AREAM design strength and rail-seat positive CDFs of Type M tie concrete compressive strength at first crack moment (M_{cr}).

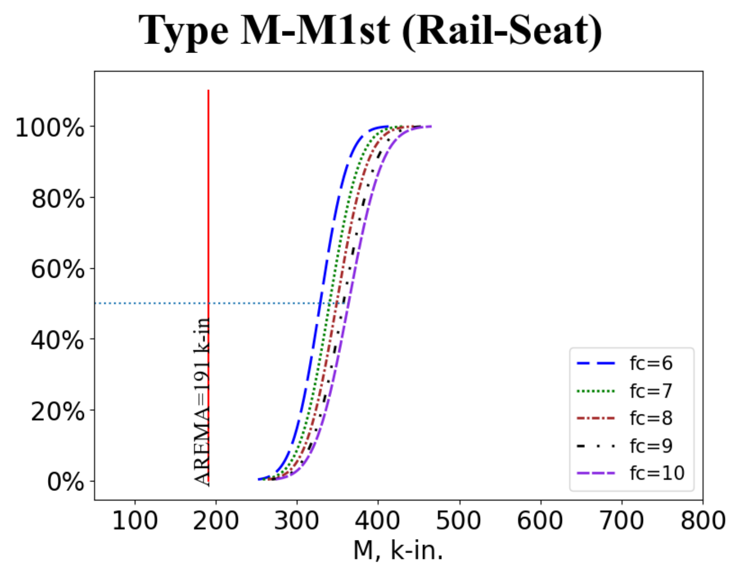

	6 ksi	7 ksi	8 ksi	9 ksi	10 ksi
Mean	328	340	348	357	363
STD	27	29	30	31	32

Figure D. 47 Comparison of AREAM design strength and rail-seat positive CDFs of Type M tie concrete compressive strength at crack reached to outer layer of reinforcement moment (M_{1st}).

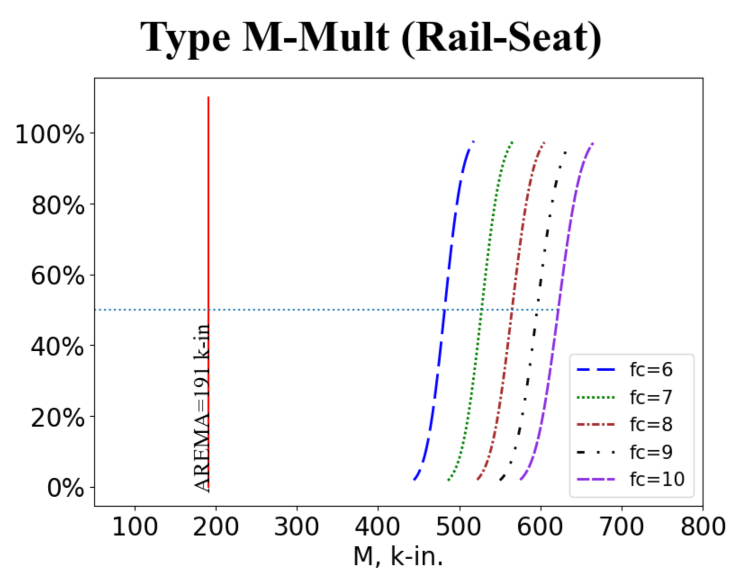

	6 ksi	7 ksi	8 ksi	9 ksi	10 ksi
Mean	481	527	564	595	621
STD	18	19	20	21	22

Figure D. 48 Comparison of AREAM design strength and rail-seat positive CDFs of Type M tie concrete compressive strength at ultimate crack moment (M_{ult}).

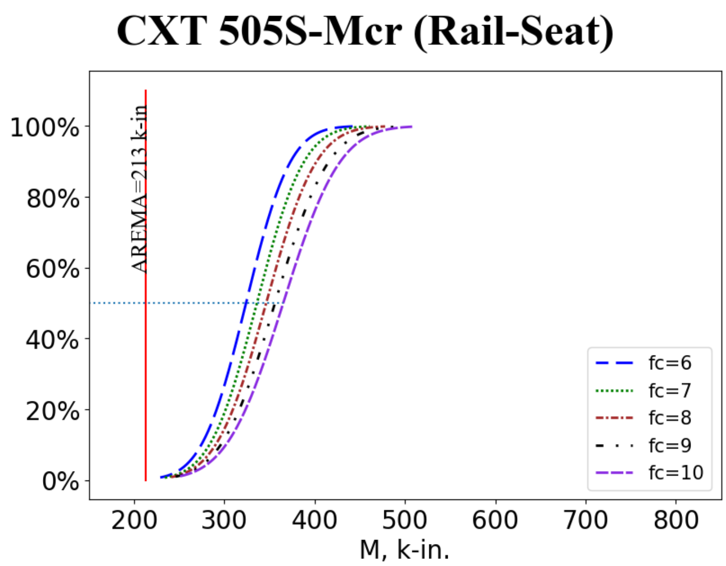

	6 ksi	7 ksi	8 ksi	9 ksi	10 ksi
Mean	323	336	346	356	365
STD	38	40	43	46	49

Figure D. 49 Comparison of AREAM design strength and rail-seat positive CDFs of CXT 505S tie concrete compressive strength at first crack moment (M_{cr}).

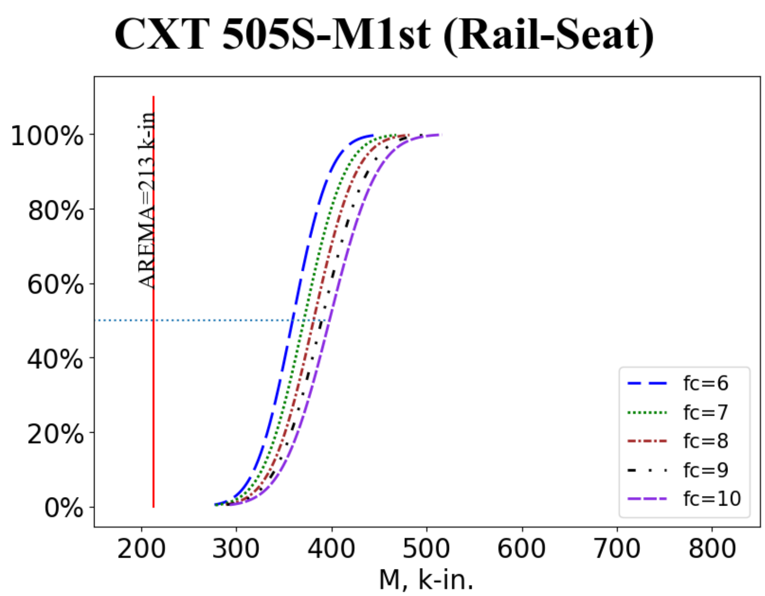

	6 ksi	7 ksi	8 ksi	9 ksi	10 ksi
Mean	358	370	381	389	397
STD	31	34	35	37	39

Figure D. 50 Comparison of AREAM design strength and rail-seat positive CDFs of CXT 505S tie concrete compressive strength at crack reached to outer layer of reinforcement moment (M_{1st}).

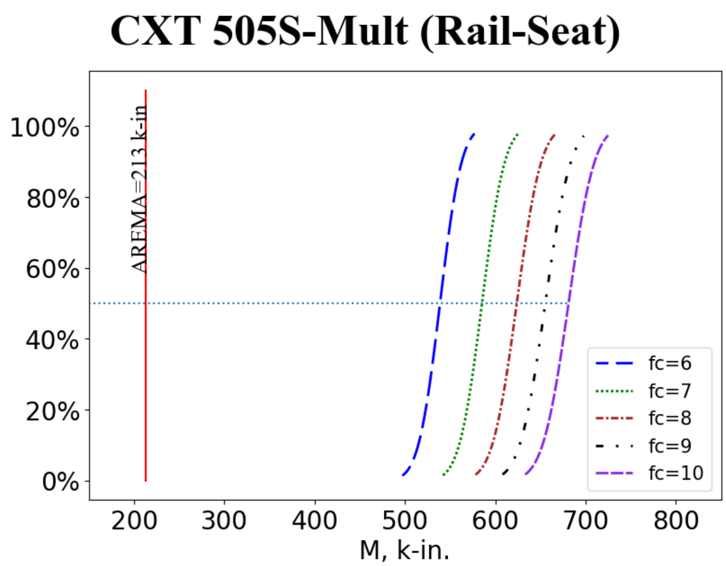

	6 ksi	7 ksi	8 ksi	9 ksi	10 ksi
Mean	538	585	623	655	681
STD	18	19	21	22	22

Figure D. 51 Comparison of AREAM design strength and rail-seat positive CDFs of CXT 505S tie concrete compressive strength at ultimate crack moment (M_{ult}).

Table D. 1 Summary of Monte-Carlo simulated rail center negative and rail seat positive moment with eccentricity variance

Rail-Center								
Concrete Compressive Strength, ksi			6	7	8	9	10	Averaged Difference
Moment at crack height reaches to first level of reinforcement, M_{1st} (k-in.)	CXT 505S	e-	-214.96	-223.41	-230.91	-237.39	-242.99	-4.5%
		e	-226.21	-234.61	-241.91	-248.09	-253.43	
		e+	-238.95	-247.55	-255.05	-261.38	-266.85	5.4%
	Type F	e-	-156.01	-162.96	-168.73	-173.45	-177.43	-6.4%
		e	-167.06	-174.27	-180.29	-185.23	-189.41	
		e+	-176.32	-183.79	-190.09	-195.30	-199.70	5.5%
	Type M	e-	-189.63	-196.95	-203.27	-208.59	-213.15	-4.2%
		e	-197.74	-205.43	-212.11	-217.72	-222.58	
		e+	-205.55	-213.61	-220.66	-226.61	-231.74	4.0%
Ultimate Moment, M_{ult} (kip-in.)	CXT 505S	e-	-320.20	-355.54	-384.45	-408.61	-428.99	-4.6%
		e	-337.21	-372.94	-402.71	-427.57	-448.46	
		e+	-353.93	-390.74	-421.35	-446.86	-468.23	4.7%
	Type F	e-	-200.42	-227.00	-249.69	-269.02	-285.44	-6.5%
		e	-215.44	-243.24	-266.97	-287.14	-304.24	
		e+	-230.48	-259.54	-284.35	-305.42	-323.25	6.6%
	Type M	e-	-283.74	-314.33	-339.46	-360.16	-377.47	-5.0%
		e	-299.18	-331.02	-357.17	-378.72	-396.74	
		e+	-314.86	-347.99	-375.19	-397.61	-416.35	5.1%
Rail-Seat								
Moment at crack height reaches to first level of reinforcement, M_{1st} (k-in.)	CXT 505S	e-	367.30	378.58	388.55	397.13	404.65	2.7%
		e	357.02	368.30	378.33	387.29	395.19	
		e+	352.73	364.96	375.90	385.87	394.84	-0.6%
	Type F	e-	409.18	421.80	432.95	442.33	450.41	2.9%
		e	397.49	409.81	420.66	429.78	437.63	
		e+	385.79	397.82	408.38	417.24	424.86	-2.9%
	Type M	e-	340.42	351.54	361.33	369.62	376.80	3.6%
		e	328.59	339.42	348.94	356.98	363.95	
		e+	316.77	327.33	336.57	344.37	351.13	-3.6%
Ultimate Moment, M_{ult} (kip-in.)	CXT 505S	e-	557.50	605.30	644.33	676.21	702.61	3.3%
		e	538.47	585.37	623.76	655.21	681.33	
		e+	519.70	565.61	603.34	634.34	660.13	-3.3%
	Type F	e-	586.47	641.01	686.26	723.39	753.77	3.5%
		e	565.38	618.72	663.11	699.73	729.87	
		e+	544.49	596.61	640.11	676.18	706.03	-3.5%
	Type M	e-	501.55	548.22	586.61	618.18	644.59	3.8%
		e	481.90	527.48	565.06	596.00	621.87	
		e+	462.48	506.98	543.72	574.04	599.37	-3.8%